New Measurement of ^{39}Ar Lifetime and Projected Sensitivities for Time-Varying Signals with the DEAP-3600 Detector

by

Gurpreet Kaur

A thesis submitted to

the Faculty of Graduate and Postdoctoral Affairs

in partial fulfillment of the requirements

for the degree of

Doctor of Philosophy in Physics

Ottawa-Carleton Institute of Physics

Department of Physics

Carleton University

Ottawa, Ontario, Canada

April 21, 2023

Abstract

DEAP-3600 is a single-phase dark matter experiment searching for direct detection of elastic nuclear scatters of the dark matter candidate, WIMPs, with 3279 kg of liquid argon. In addition to the elastic interaction of the dark matter, theories also predict the modulation in this signal rate with time which is not expected in the backgrounds in the experiment. Observing this modulation signal will extend the sensitivity of the WIMP search in the experiment. The DEAP detector has recorded more than 3 years of physics data, and the absolute stability of the detector over the time of data collection allows the analysis of event rates in the detector data, which complements many other interesting analyses, such as a precise measurement of the lifetime of the ^{39}Ar isotope. The 878 days of live time are used to measure the ^{39}Ar lifetime by fitting the trigger rates with a decay model describing the data. The result, the first measurement to directly observe the decay curve of ^{39}Ar, shows a lifetime of 438 $\pm$ 10 (stat) $\pm$ 8 (syst) years, in tension with the literature value of 388 $\pm$ 4 years. A detailed systematic study of the detector is also performed to understand data that will contribute to the sensitivity of the detector for the modulation of the nuclear signal. This study indicated the requirement of a detector threshold of 5 keV or less to observe the annual modulation in the nuclear recoil signal. The DEAP experiment would need to collect new data at this lower hardware threshold and a more complete understanding of the detector backgrounds would be required.

Acknowledgements

First and foremost, praises and thanks to God, the Almighty, for His showers of blessings throughout my life and in this research work to complete it successfully.

I would like to express my deep and sincere gratitude to my research advisor, Dr. Mark Boulay for giving me the opportunity to work with the DEAP collaboration and providing invaluable guidance and support throughout this research and since my first day at Carleton University. The dynamism, vision, sincerity, and motivation you provided have deeply inspired me. I have learned the great methodology and experiences to carry out the research and to present the research works as clearly as possible. It was a great privilege and honor to work and study under your guidance.

It is my proud privilege to express my gratitude to worthy members of the DEAP collaboration, review committee members for this analysis, Dr. Aksel Hallin, Dr. Chris Jillings, Dr. Simon Viel, and Dr. Shawn Westerdale for their encouraging attitude, brilliant comments, and offering valuable suggestions for my research work. Thank you, Dr. Marcin Kuzniak, Dr. Robert Stainforth, and Dr. Shawn Westerdale, for your help in getting started with the analysis in DEAP. Thanks for the help with the coding questions. It helped me a lot to grow as a researcher.

I would like to thank the whole DEAP collaboration, it is a great team to work with, thank you for the feedback provided by everyone in the weekly group meetings and during collaboration meetings. I am very thankful to Dr. Pierre Gorel, Dr. Sean

Daugherty, and Dr. Tina Pollmann for helping with detector stability studies and answering the DAQ-related questions. Thank you to Dr. Bjoern Lehnert for sharing the electron recoil background model.

I owe a big thanks to my fellow collaborators at Carleton University for their continuous encouragement, support, and help. Thank you, Dr. Pushparaj Adhikari, Dr. Susnata Seth, Dr. Matthew Dunford, and Dr. Roxanne Turcotte for your expert advice on various topics of analysis. I would to thank my fellow graduate and undergraduate students, Shivam Garg, Andrew Erlandson, Michael Perry, Bansari Vyas, Spencer Haskins, Kazmir Sobotkiewich, Akhil Maru, and Andres Bigentini for the breaks from analysis and for making research more enjoyable with the long talks. I am grateful I made so many friends during the course of this study.

I am extending my heartfelt thanks to my family for their acceptance and patience during the discussion I had with them on research work and thesis preparation. The endless love from my grandparents, Ujagar Singh and Bhajan Kaur, I lost you both during this journey but you are alive in my heart. I know your teachings and blessings are always with me. I am extremely grateful to my parents, Harmeet Singh and Kuldeep Kaur for their love, understanding, prayers, continuing support, caring, and sacrifices they made for educating and preparing me for my future. Also, I express my thanks to my siblings, Kamaljeet Kaur and Gurjeet Singh for their support, this would not have been possible without you both. I would also like to thank my friends Aditi Bhardwaj and Ram Singh for their constant cheering, and support.

Finally, my thanks go to all the people whose names have been missed out but who supported me to complete the research work directly or indirectly.

Statement of Originality

The research work presented in this thesis is the result of the studies performed by the author from the DEAP-3600 experiment data with the help of collaboration.

The DEAP-3600 collaboration is presently a team of more than 100 researchers who have worked very hard for the design, construction, commissioning, and operation of the experiment over the last 15 years and more. The author joined the experiment five and a half years ago when the experiment was running in a good state and completed about one year of data taking. The main contributions from the author towards the experiment include the analysis of data for the ^{39}Ar lifetime measurement, detector stability studies, data quality testing, data taking, and DAQ expert activities. The original contributions towards the data analyses are highlighted as follows with the indicated coordination from the collaboration.

The event rate algorithm was prepared for the various analyses discussed in this thesis as described in chapter 5 is the author's own work where the data variables discussed in the various sections are taken from the experiment analysis codes. The validation of the algorithm was further done with the use of calibration data from the experiment. The decay fit model describing the low energy ^{39}Ar is made and finalized with the excellent feedback from experts on the experiment, Dr. Aksel Hallin, Dr. Chris Jillings, Dr. Simon Viel, and Dr. Shawn Westerdale in the review meetings. The contribution of different parameters in the model that include the rate of events

containing Cherenkov light and the fraction of various event types in selected regions are determined from the data-driven and Monte Carlo studies by the author. The electron recoil backgrounds are constrained in the study using the detailed model made by the collaborator Dr. Bjoern Lehnert with the help of collaboration for the electron recoil background paper [1].

In chapter 6, the data selection process presented in the form of several checks has been used in the experiment to prepare the run lists. The author's contribution includes performing the quality checks on more than 3 years of data mentioned in section 6.2 with the help of the collaborators in data quality sprints. Some additional run selection criteria are defined in the following sections of the chapter to finalize the dataset for the analyses that contain the cross-checks for the precise event counts and livetime measurements. The light yield of the detector is determined from the Gaussian fits on the gamma peaks of ^{40}K, and ^{208}Tl peaks. The calculated light yield values the compared to the output of the energy response code written by collaborator Dr. Stefanie Langrock, and the light yield values measured from ^{39}Ar fittings are estimated from this processor. The light yield of the detector is plotted as a function of time from these different sources. The total trigger rates are evaluated from data in the selected region of interest after making corrections for the light yield changes and including the trigger time cut at 32 μs to remove pre-light from the previous triggers in the data. This trigger time cut value and dead time calculations are decided after various rounds of discussion with the experts, Dr. Pierre Gorel, and Dr. Matthew Dunford, and with the help of the review committee for this analysis.

Chapter 7 presents the analysis results from ^{39}Ar lifetime measurement. The fitting of trigger rates with the decay fit model and validation checks for the verification of the fit output is done by the author. The results are discussed in detail with the

experts in the experiment. The systematic uncertainty calculations performed by the author entirely are described in this chapter. Results from the ^{39}Ar lifetime analysis are presented with the final steps needed before turning the analysis to publication.

In the second part of this thesis, the calculations are done to estimate the sensitivity of the DEAP-3600 experiment toward the annual modulation of the WIMP recoil signal. The calculations for the differential recoil rates in liquid argon at the constant Earth velocity are already performed by the collaborator Dr. Shawn Westerdale. The contribution of the author is to implement the time dependence component from the Earth's velocity in this computation. The differential recoil rates are measured as a function of days in the year, and total recoil rates are evaluated with the current fiducial volume of the argon in the detector for various detector threshold values. This analysis predicts the modulation of the recoil signal in the liquid argon. The comparisons are also shown by the author for the current detector systematic uncertainty calculated in the other part of the thesis to the modulated rates.

The studies showing the very good stability of the DEAP-3600 detector during the period of data taking are presented in the appendix A. The author has written this document with the help of experts on various topics in collaboration to determine the trendline for different stability parameters.

The contributions from other sources, primarily the DEAP-3600 collaboration is correctly referenced in the thesis where relevant. The author also confirms that this work has not been submitted to any institution in whole or in part to any previous degree application. After the finalization of results from the ^{39}Ar lifetime analysis, it will be published in form of a research paper by the DEAP-3600 collaboration.

Gurpreet Kaur

April 21, 2023

Acronyms

ADC Analog to Digital Converter. xxv, 50–53, 70, 87, 88, 109–115, 125, 261

AV Acrylic Vessel. xxi, xxxvi, 40–43, 45, 46, 56, 59, 60, 64, 72, 156, 157, 221, 270, 271

DAQ Data Acquisition. xv, xxii, xxvi, xxix, xxxvi, 3, 6, 48–51, 53, 63, 69, 70, 74–78, 80, 87, 93, 95, 97, 99, 102, 103, 109, 121, 122, 124, 126, 136, 140, 144, 155, 159, 161, 163, 165, 180, 259–261, 268–270

DTM Digitizer and Trigger Module. 6, 48, 50, 75, 78, 162

FB Filler Blocks. xxi, 40, 41, 56, 59

LAr Liquid Argon. x, xv, xx, xxxvii, 2, 3, 5, 24–26, 28, 35, 36, 40, 42, 44, 45, 54–56, 59, 60, 64, 66, 72, 146, 217, 221, 232–234, 247, 249, 253, 254, 260, 266, 268, 270, 272, 279, 281–285

LG Light Guide. xxi, 40–42, 56, 59, 72

PE Photoelectrons. xi, xxii–xxv, xxix–xxxi, xxxiii, 48, 50, 53, 54, 59, 64, 65, 67, 68, 86–89, 93, 100, 108, 109, 111–115, 118–120, 123, 125, 129, 145, 158, 168, 170, 176, 178, 182, 194, 217, 218, 221, 223, 259, 260, 285

PMT PhotoMultiplier Tube. x, xv, xx, xxi, xxxvi, xxxvii, 3, 27, 28, 35, 40–50, 53, 56, 59, 63–66, 72, 76, 78, 111, 116, 118, 155, 157, 167, 260, 268, 272, 274, 276, 278–285

PSD Pulse Shape Discrimination. xxxviii, 24, 25, 27, 29, 35, 51, 52, 54, 66, 232, 258, 287

ROI Region Of Interest. xii, xvi, xvii, xxiii–xxvi, xxviii, xxix, xxxi, xxxiii, 85–97, 100, 102, 103, 117, 119, 120, 122–126, 129, 137, 139–146, 149, 150, 152, 153, 158, 171, 176–180, 184, 186, 192, 201, 204, 209, 210, 217–223, 226, 227, 229–231, 259, 264

Contents

List of Tables

List of Figures

Chapter 1

Introduction

The field of particle physics has been highly advanced in the last century, it has a great contribution to the theory of evolution from the physics perspective. The model which describes the world around us is called "The Standard Model" of particle physics. It includes elementary particles which are very well known like electrons, photons, Higgs particles, quarks, and many more. With the help of the standard model, we can explain how things happen in nature, for example, we can understand: why and how particles get a mass, why we daily interact with photons or light, why the sun burns, etc. Some of the most astonishing scientific measurements in the world are predicted with extreme accuracy within the framework of this model. Nevertheless, there are a lot of things in our universe that this model cannot explain. There is still work to do, things to understand, and stimulating open questions to address.

The existence of the hypothetical form of matter called dark matter is one of these questions that scientists are trying to answer for several decades. There is strong evidence from the various observations that suggest the presence of some unknown type of matter in the universe. The detection of this type of matter will answer questions like why the universe contains more mass than luminous matter and

asymmetry of matter and anti-matter. There are many experiments working in space, on the surface of the Earth, and in underground laboratories to detect the existence of dark matter in different ways. The motivation to detect dark matter and evidence of its existence is discussed in chapter 2.

The DEAP-3600 project is searching for direct detection of the WIMP (Weakly Interacting Massive Particle) considered a possible candidate for dark matter. This detector uses more than 3 tonnes of liquid argon (LAr) to detect the scintillation signal from the interaction of dark matter with the argon nucleus. The 3.3 tonnes of argon was extracted from the atmosphere and instrumented in a low background detector underground to search for the interaction of the dark matter with the argon as the target material. In addition to the direct detection of dark matter, the DEAP-3600 experiment is trying to extend the boundaries for the detection of annual modulation in the WIMP signal which is another famous technique predicted from the theory for the indirect signal of dark matter existence. Detailed studies of the detector systematics are required related to measuring the time-dependent event rates with the goal of determining sensitivity to the annual modulation of the dark matter particle rates. The research work of my thesis is contributing to the DEAP-3600 project and studies are done to constraint the detector stability systematics for the WIMP modulation analyses. These systematic studies are important to determine the sensitivity of the detector towards the search of annual modulation in the WIMP signal such that the detector systematics are well understood and are in proper control while looking for time-varying signals in data. The systematic studies also allowed us to observe the decay curve of ^{39}Ar directly and measure its lifetime because of the ultra-pure argon and very small backgrounds in the DEAP-3600 detector. Atmospheric argon mainly consists of the stable isotope ^{40}Ar (99.6%) with a small amount

of radioactive isotope ^{39}Ar created from the cosmogenically interactions, and is 8.2 x 10^{-14}% in abundance [2]. The ^{39}Ar beta decays to stable isotope ^{39}K with the half-life of (263±3) years, and Q-value of (565±5) keV as described in the literature [3]. This value for the lifetime of ^{39}Ar was measured in 1965 through the indirect method of argon ratios when the existence of a third isotope of argon ^{38}Ar was not known. The specific activity of ^{39}Ar is very carefully measured in the DEAP-3600 collaboration with the value (0.964 ± 0.001 (stat) ± 0.024 (syst)) Bq/kg$_{atmAr}$ [4]. The direct measurement of ^{39}Ar lifetime from the DEAP-3600 dataset is the bulk of the thesis work. Also, a part of the topic of this dissertation is to study the possibility of an annual modulation of event rates when WIMPs interact with the argon nuclei in the detector.

1.1 Outline

The study of event rates also contains very interesting analyses like the measurement of ^{39}Ar isotope lifetime from the DEAP-3600 data. The beta decay from ^{39}Ar is a major background in all the detectors using LAr as the target material as given in chapter 3. More details about the experimental setup of the DEAP-3600 detector with LAr as target material are given in chapter 4. In this thesis, I have developed an algorithm to analyze the rate of various event types in the DEAP data from their time information as discussed in chapter 5. This algorithm measured the rates of different types of events with time on a weekly bin basis. In the DEAP-3600 experiment, the Data Acquisition (DAQ) is done through the electronic trigger system. As a part of the calibration system for the light detector PhotoMultiplier Tubes (PMTs), the test pulses are injected periodically at a known value of frequency to test proper functioning and data taking. To validate the algorithm, the trigger rates of the

calibrated periodic triggers are analyzed. These measured event rates are quite stable. For further authentication of the algorithm, the rates of the triggers corresponding to the decay of ^{39}Ar isotope in the detector are calculated with the use of the selection cuts to eliminate any sources of background in the dataset from other scintillation light. A fit model is described in chapter 5 that well explains the DEAP-3600 data in the ^{39}Ar beta decay energy region. The various data components are parameters from the fit model and are evaluated from the data and Monte Carlo (MC) studies. These include the determination of low-energy triggers containing Cherenkov light and acceptances of various cuts included in the study with their variation over time. The electromagnetic recoil (ER) backgrounds are constrained in this analysis from the ER background model in the experiment. The data selection criteria were adopted to remove any instrumental effects and to choose only good physics data for the research. These data quality techniques are discussed in chapter 6. In addition to the data quality testing, this chapter also includes the study of primary systematic uncertainties from the detector about very negligible uncertainty on event count, small livetime discrepancy, and stability in the light yield of the detector with time. The trigger rates for the ^{39}Ar are plotted with the rate algorithm after adding correction from the small shift in the energy response over time. The analysis for the evaluated ^{39}Ar rates is discussed in chapter 7 where the data model is fitted to the calculated rates for the lifetime measurement of this isotope from more than 3 years of the DEAP-3600 dataset. The systematic uncertainty of the lifetime measurement is also investigated in detail from various sources.

After verifying the rate algorithm and various systematics in the DEAP-3600 data, this thesis explores the potential of studying the annual modulation of WIMPs in the DEAP-3600 detector, with an emphasis on constraining the relevant systematic

uncertainties as mentioned in chapter 8. The calculations are done for the nuclear recoil rates expected in the LAr target material. The event rate of nuclear recoils is measured at different threshold values, and the minimum detector threshold required to record the modulation in the signal is determined.

The summary of the results from the analysis is highlighted in chapter 9 with the future steps. The outcome from the ^{39}Ar analysis showed the measured lifetime of this isotope from DEAP-3600 physics data is 438 $\pm$ 10 (stat) $\pm$ 8 (syst) years. The detector systematic studies are performed in the detail. The corrections are applied to the data for some systematics that can change the event rates and cumulative systematic uncertainty from other detector effects is included in the analysis. There are some final next steps suggested for this analysis to include the systematic from detector components which can change the uncertainty on the mean value of this measurement by some percent. This present result from the direct measurement of a lifetime is 5σ away from the indirect measurement, 388 $\pm$ 4 years, done in past. The calculations are performed to estimate the sensitivity of the detector to measure the annual modulation of the WIMP signal which conveys the maximum detector threshold at 5 keV to record this modulation. Also, the amplitude of the modulation signal and its comparison with the detector's systematic understanding shows that the average rates will be limited by the statistics with the current fiducial volume at 3 tonnes of target mass. A large detector and more target volume are required to measure the modulation signal.

1.2 Nomenclature

There are several terms used in this thesis that is mainly used in particle physics and other fields of science. The clear nomenclature for the terms used in this thesis and

analysis is briefed below.

- A waveform is the timing and energy charge information saved from any physics event, test pulses, or instrumental background in the detector.
- The decay of any isotope refers to the emission of energy from the element.
- An trigger in the experiment is any occurrence in the detector that causes the DAQ system to trigger and record at least the timestamp information in the Digitizer and Trigger Module (DTM) system.
- An event in the experiment is any occurrence that triggers the DAQ system and full waveform information is saved on the data disks.
- The pulse or peak in the waveform shows the trigger in the detector when some information is saved in the data system.
- The sub-peaks in the waveforms occur when more than one events occur by coincidence in the same trigger window.
- A run is recorded through the continuous operation of the DAQ system.

Chapter 2

Theory of Dark matter

Dark matter is the hypothetical invisible form of matter that makes up a large part of the universe. In contrast to ordinary matter, it doesn't interact with electromagnetic force and hence is non-luminous. Thus, it is called dark matter because it is not visible. The important characteristics we know about this form of matter are its gravitational effects on visible matter [5], and its existence in abundance. Dark matter makes up about 27% of the universe and the universe we know which includes all stars, galaxies, and other baryonic matter in the universe is estimated to account for 5% of the total content in-universe. This leads scientists to think about something that we cannot see and is yet affecting the motion of galaxies and the basic structure of our universe. This form of matter provides the extra non-luminous mass in the universe and hence generates the additional gravity needed by the different mass bodies in space to stay intact. The presence of this form of matter is not described in the Standard Model of particle physics [6]. The direct detection of dark matter is the motivation for constructing the DEAP-3600 project, more details about the theory of dark matter are discussed in this chapter.

2.1 Evidence of dark matter

There are many shreds of evidence recorded in the past century that proved the existence of dark matter which also predicts there is a large amount of it around us and everywhere in the universe. In the time period before the 1930s, there was moderate confirmation of the presence of some other components of mass in the universe. The classical mechanics and statistical theorems used to describe the motion of the galaxies not depicting the lower limits on the masses of the galaxies. The strong first evidence of dark matter was observed by the astronomer, Fritz Zwicky in early 1930 supporting the existence of non-luminous matter in the Coma galaxy cluster [7, 8] in 1937 which does not interact with the baryonic matter and can not be seen. He suggested the presence of large matter than seen in the galaxies [9] in 1942. In the convincing mass measurement of this cluster, he found a discrepancy of about 400 times lesser luminous mass in the galaxy in comparison to mass observation reported from the theories in classical mechanics.

There have been many proofs collected since these measurements by Zwicky which support the existence of non-luminous dark matter, the important pieces of evidence include peculiarity in the galactic rotation curves, gravitational lensing around far objects than expected from the visible matter, and structure in the cosmic microwave background. In our universe the galaxies are continuously rotating about their galactic centers; however, the luminous matter seen in these galaxies is not enough for their rotational motion, there is some mass present within them that provides the additional gravitational pull to hold them together. Similarly, the motion of galaxies in the clusters also indicated the presence of an additional form of matter. A brief description of this evidence is discussed further in the following sub-sections.

2.1.1 Peculiarity in galactic rotation curves

The rotational speeds of objects containing mostly luminous mass with respect to their position relative to the center of galaxies can be seen through the galactic rotational curves. According to the Virial theorem of classical mechanics, the kinetic energy hence the velocity, v, of an object can be related to the gravitational potential energy acting on the object and varies as a function of the radial distance, r, from the central gravitational pull as shown in equation (6) in [7], also shown in the equation (2.1) below,

$$v = \frac{(GM)^{\frac{1}{2}}}{r^{\frac{3}{2}}} \tag{2.1}$$

where G is the universal gravitational constant with value 6.6E-11 $\mathrm{Nkg^{-2}m^2}$, and M is the heavy mass present at the central position. The behavior expected for the rotational velocity curves is such that the velocities are higher near the dense galactic center due to the majority of luminous mass there, followed by decreased velocities as the distance from the center increases. However, in the 1970s, the peculiar effect was recorded in reality in the shape of the rotational velocity of spiral galaxies by astronomer Vera Rubin et al [10–13]. In the observations from the NGC 3198 curve (as shown in figure 2.1) in measurement from [14], it was noticed that the rotational velocity of galaxies increases near the center and then remains constant till its edges.

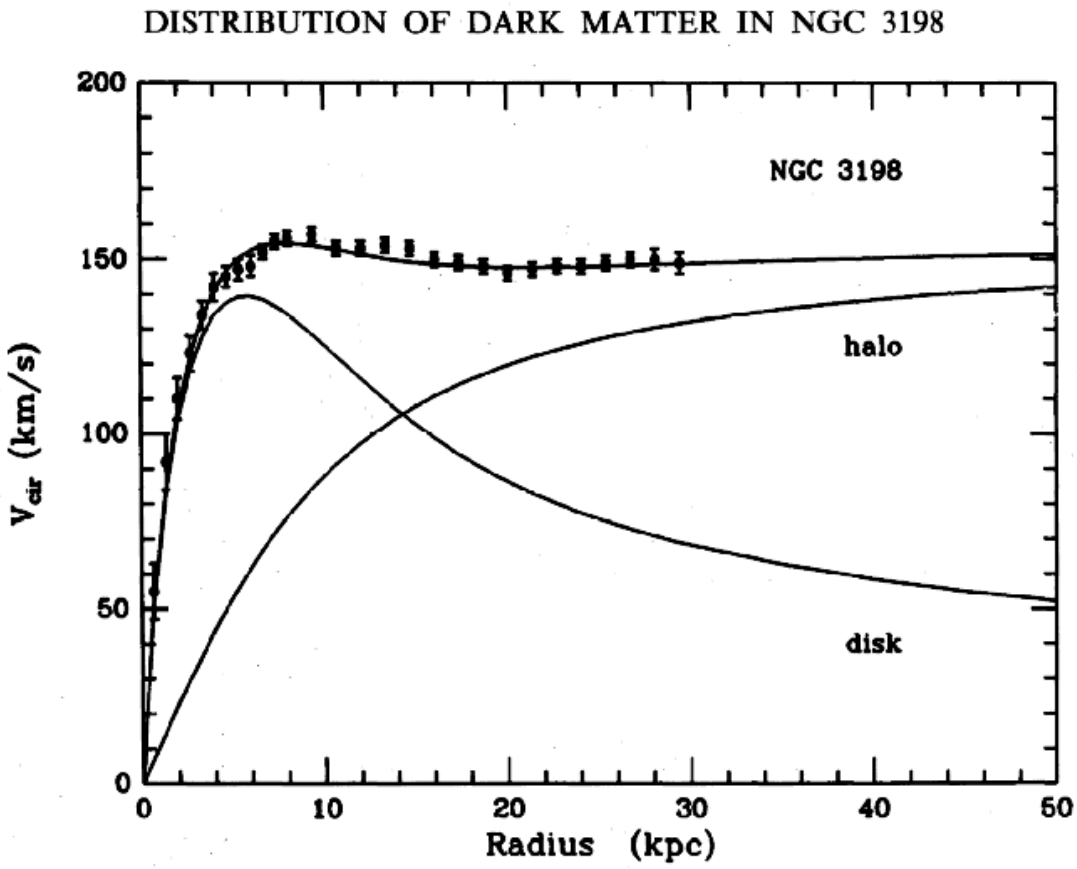

Figure 2.1: The galactic rotational velocity curve of NGC3198 [14]. The measured galactic rotational velocity is labeled with NGC 3198, whereas the expected velocities are labeled by disk. The presence of non-luminous mass is labeled by the halo curve.

Stars that are near the edge of the galaxy have greater rotational velocities than expected. These measurements showed the presence of some non-luminous mass halo in the galaxies which contribute to the total mass and affect the rotational velocity curves. As presented in figure 2.1, the addition of the halo of dark matter balances the lack of rotational velocity of the disc at the higher radial distance.

2.1.2 Gravitational lensing - The bullet cluster

The other evidence of dark matter is observed from the gravitational lensing effect of the Bullet Cluster which comprises two colliding galactic clusters. Gravitational lensing occurs when any massive celestial body such as a galaxy cluster, or black hole, causes space-time curvature due to the wrapping effect of their gravity on space-time and hence causes light around it to bend visibly as shown in figure 2.2.

Figure 2.2: The first infrared image from NASA's James Webb Space Telescope showing the distant universe so far. This is galaxy cluster SMACS 0723 with thousands of galaxies – including the faintest objects ever observed in the infrared. The gravitational lensing of electromagnetic light can be clearly seen in this image [15].

This effect is the same as the bending of light by a lens and can be used as the method to measure the mass of the object by the equation (2.2) from [16],

$$\theta = \frac{4GM}{rc^2} \tag{2.2}$$

where θ is the amount of bending in light due to the gravitational lensing effect by the object of mass M, r is the radial distance between the mass and the light ray, and G and r are the gravitational constant and speed of light respectively. This bending of electromagnetic light around the Bullet Cluster is elaborated in paper [17].

The bullet clusters were studied by the Chandra X-ray observatory which showed that the centers of masses do not coincide with the locations of luminous matter predicting significant evidence for the presence of a reasonable amount of non-luminous dark matter. Similar evidence of dark matter through gravitational lensing is published by Douglas et al in [18]. The presence of a very large non-luminous type of matter is suggested in the study of the bullet cluster where the collision of galaxies was studied by the Magellan IMACs Telescope and an x-ray image taken by the Chandra X-ray Observatory shown in the figure 2.3. There is about a 7:1 ratio of dark matter plus the galaxy constituents to the amount of plasma predicted by the bending of light in this case.

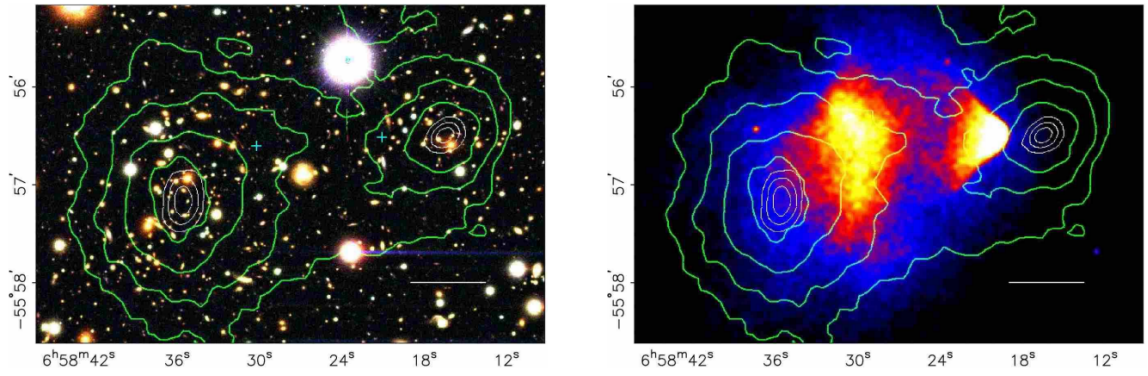

Figure 2.3: The example of bullet cluster from [18]. The observation was taken from the Magellan IMACs Telescope (left) and Chandra X-ray Observatory (right). The gravitational centers from the gravitational lensing are shown in the green contours.

The gravitational lensing is observed in the several flavours as discussed in [19]. The presence of a very dense mass in the center causes space-time to warp strongly

and light travels multiple times around the lens, and is deflected toward the observer. In weak lensing where less amount mass is present on the way, the distortion of light is small and can be resolved by the linear transformation of the sky.

2.1.3 Cosmic Microwave Background structures

The other evidence of dark matter's existence is indicated by the Cosmic Microwave Background (CMB) of the early universe. The early universe started from a very highly dense state that expanded and accelerated in all directions as explained by the big bang theory. The measurement of light from the early universe for a very short time after the matter recombination when elementary electrons combined with protons to the bound states, can be presented in the form of a CMB model (see figure 2.4) which predicts the isotropic temperature with very small changes in the scale μK [20].

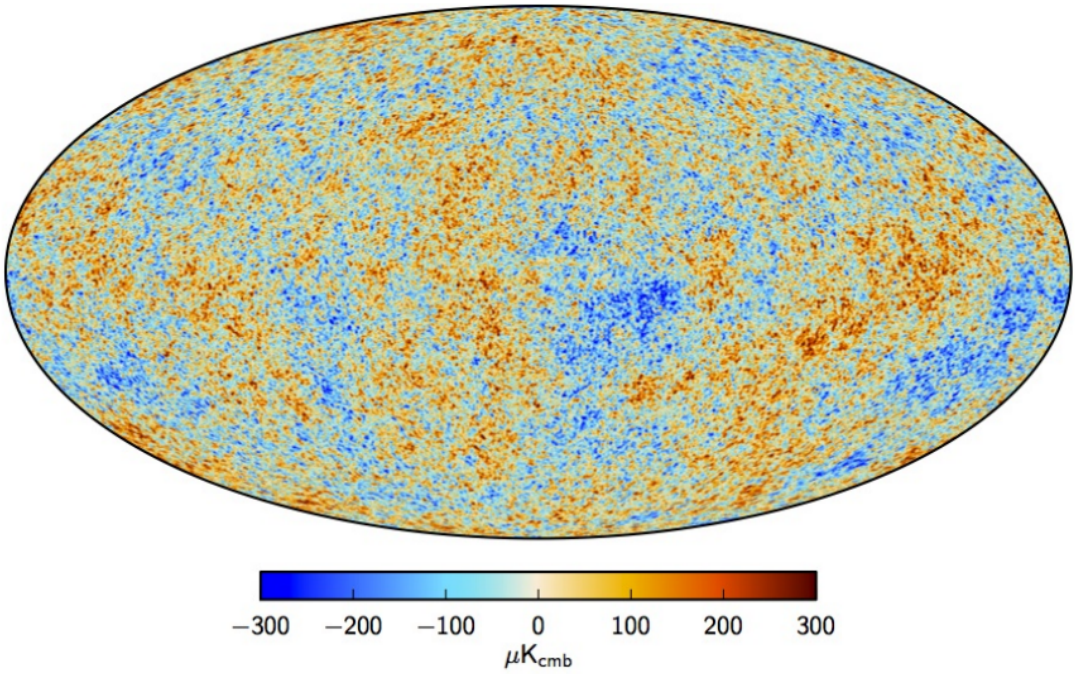

Figure 2.4: The CMB map derived for the energy density of the universe [18], the warmer clusters have the high density of matter with the variation in temperature in the scale of μK.

The anisotropy in the temperatures from the CMB structure provides a lot of information about the early universe which tests the cosmological models and predicts the energy density of the universe from the different individual contributions of luminous mass density, dark energy density, matter density, etc. The parameters indicated from this model are also fitted with the data recorded by the Plank collaboration which showed about the 26% of dark matter in the composition of the universe along with only ∼5% visible baryonic matter [20]. The results from the Plank experiment are in great agreement with the results from the bullet cluster analysis [18]. This strongly supports the hypothesis of dark matter.

Regardless of the large abundance of this form of matter, it has not been experimentally detected yet but there have been a lot of experiments working over the last two-three decades to discover the nature of this matter which are discussed in

the following sections.

2.2 Dark matter candidates

There are many measurements that point to the existence of dark matter, however, the nature of this dark matter has not yet been observed by any experiment. Theoretical models suggest the particle nature of the dark matter with several live examples and properties [21,22]. The candidates under study for the dark composition are WIMPs, Massive Compact Halo Objects (MaCHOs), axions, neutrinos, and gauge bosons as dark photons.

2.2.1 Weakly Interacting Massive Particles, WIMPs

One popular candidate considered for the dark matter is weakly interacting massive particle (WIMP), suggested by many theories like Supersymmetry which is not predicted by the Standard model of particle physics [23]. As the name suggests, this proposed candidate is expected to be a heavy particle with mass in the order of MeV/c^2 to TeV/c^2 [24]. The other characteristics include the interaction of these particles with baryonic matter through weak force and gravity only. However, the WIMPs are themselves from a non-baryonic class such that they are not made of protons and neutrons. The effect of gravitational force on the atomic scale is really very small so the possible way to detect these particles is through weak interaction of these particles with normal matter. The WIMP particle can scatter an atomic nucleus and the energy deposited from the recoiled nucleus could be detected to verify the existence and interaction of these particles. The recoiled nucleus energy can be recorded from the ionization or scintillation.

In the present study, the physics data from the DEAP-3600 experiment is used

which is looking to detect the recoil energy from the elastic scattering of WIMPs with the liquid argon nucleus (see chapter 4 for the details from the experiment). The signal from the WIMP interaction in the DEAP-3600 experiment is expected in the nuclear recoil band where the nucleus and hence the argon atom is expected to recoil with some energy transferred from the elastic scattering of the WIMP with the target argon in the detector.

2.2.2 More candidates of dark matter

Other theories predict the composition of dark matter from Massive Compact Halo Objects (MaCHOs) which are very less likely to be considered as the possible candidate. This is based on the observations from several projects such as the MACHO project [25] and the measurements from the Hubble Space Telescope which predicts that the total mass of these objects is low to account for the missing dark matter in the universe [26]. The upper bound on the mass of these particles is roughly 10^{70-71} eV [27] and hence falls under the category of electron recoils.

Also, the candidacy of axions, light pseudo-scalar particles, gives the solution to the Strong CP problem in the Standard model but since their mass is still unknown so research is underway to determine if they could be the missing dark matter [28]. The approximated mass range for axions predicted by the theories is scaled from a few μeV to meV [22, 29] which makes them the candidates of dark matter in the electron recoil energy region.

The neutrino oscillations experiments showed the mass oscillations in atmospheric and solar neutrinos, therefore, at least two neutrinos in the Standard Model are massive [30, 31]. The oscillation parameters results in the mass of neutrinos being greater than at least 50 meV hence making it a possible candidate for dark matter,

however, the Pauli exclusion principle suggests that no fermion in this mass range can be the dominant component of the galaxy. Moreover, the massive neutrinos (also called Sterile neutrinos) could be considered dark matter candidates [27, 32] with a mass range from keV to MeV. The direct detection of this type of dark matter is not quite possible because of suppressed couplings with the noble targets, and possible decay into the active neutrino and photon [33]. This type of dark matter candidate can exist in the nuclear recoil energy region and hence will be rejected from the background models of the direct detection experiments.

The other present theories in the dark matter also predict the existence of dark matter through a new gauge boson called dark photon where a light thermal WIMP (either fermion or scalar) with the mass range in MeV can interact with the Standard Model particles using this mediator that kinetically mixes with the usual photon [33]. The scattering of the target nucleus with the WIMP direct detection is suppressed in this case, and this type of dark matter can be searched in the fixed target detectors. In addition, this type of dark matter exists in the electron recoil energy region. The direct detection experiments are also increasing their sensitivities for this dark matter candidate [34].

With the recent discovery of the gravitational waves by the LIGO collaboration [35], there is increased interest in considering primordial black holes as candidates for dark matter as well. This type of dark matter is not an elementary particle and needed a physics explanation beyond the Standard Model.

2.3 Dark matter experiments and current status

There are mainly three modes of detection used by the current experiments in search of particle dark matter, to observe the interaction of dark matter with the baryonic

matter from the standard model as shown in figure 2.5. The circle in figure 2.5 represents the interaction and the black arrow shows the flow of time in the various search modes.

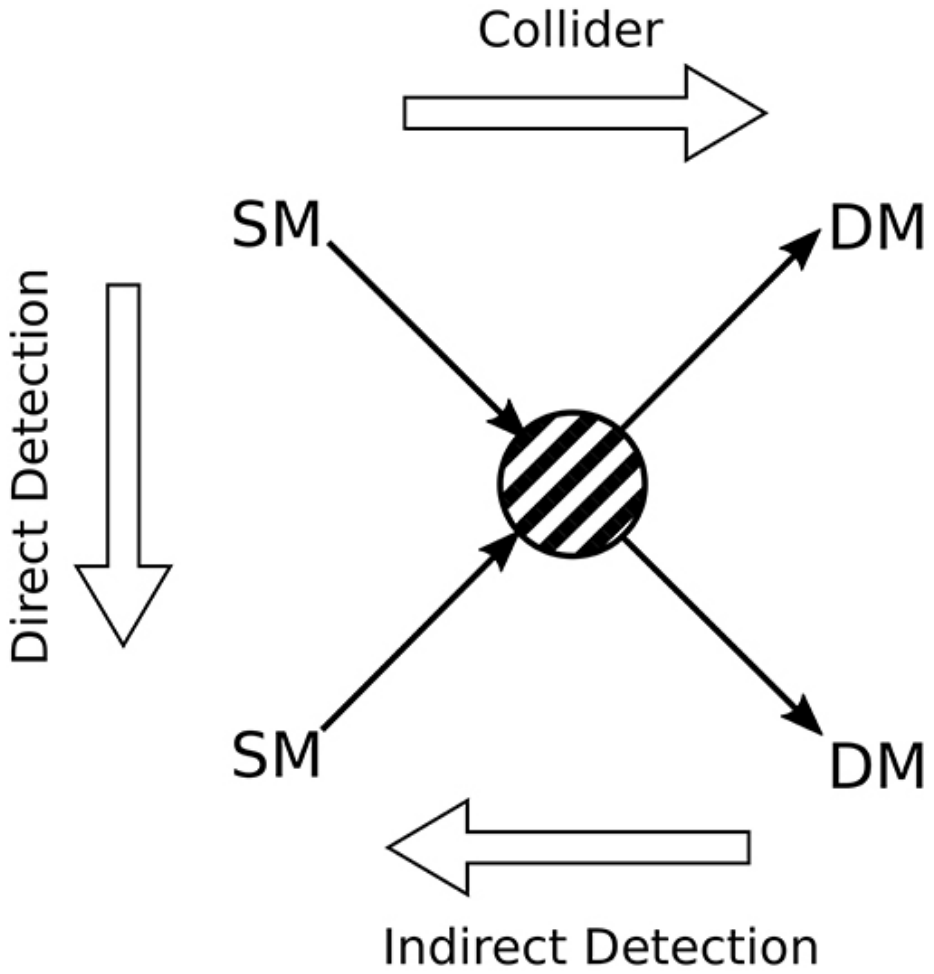

Figure 2.5: The dark matter detection channels from the current experiments [36].

2.3.1 Collider searches

In the particle collider searches the experiments are working to study the creation of the dark matter particle and antiparticle pairs from the annihilation of the high-energy particles. If the dark matter particles escape the detector, the missing transverse momentum of these particles can be used to determine the characteristics of dark

matter [36].

2.3.2 Indirect searches

In the indirect searches, the scientists are looking for the annihilation of the dark matter particles that will produce the Standard Model particles in the result [37], and the mass and cross-section of the observed daughter particles can be used to infer the properties of the parent dark matter candidates. In the study of dwarf galaxies with high mass-to-light ratios, gamma-ray searches from the galactic center have high abilities for proving and detecting the annihilation of dark matter. The studies are also looking for the annihilation of dark matter particles into Standard model particle and antiparticle pairs, the observation of the antiparticles can provide evidence for the dark matter existence experiments.

2.3.3 Direct searches

There have been many experiments working in laboratories to look for the direct detection of dark matter particles. These experiments are looking for the scattering of the Standard Model particles by the dark matter particles, through nucleus interactions [38]. In these interactions, the dark matter imparts some energy to the target nuclei, and thus the observed energy from the target nuclei with various methods can infer the properties of dark matter particles. Many direct detection experiments are only searching for elastic scattering through the interaction of dark matter with the baryonic matter in which the recoiling nucleus emits absorbed energy in the form of radiation, heat dissipated, and ionization signals. DEAP-3600 is an example of an experiment that is looking for the signal of a recoiling argon nucleus through its generation of scintillation light. The technical details for the scattering of the target nucleus with dark matter are discussed in the following section.

2.3.3.1 Scattered nuclear recoil energy

The kinematics of an elastic collision between a dark matter particle of mass m_χ with the target nuclei allows the calculation of recoil energy (E_R) from the scattered nucleus of mass M [39], which is given in the equation (2.3) below,

$$E_R = \frac{\mu_\chi^2 v^2 (1 - \cos\theta_{cm})}{M} \tag{2.3}$$

where θ_{cm} is the scattering angle in the center of the mass frame, v is the relative velocity between the WIMP and nucleus, and μ_χ is the reduced mass for the system such that,

$$\mu_\chi = \frac{m_\chi M}{m_\chi + M} \tag{2.4}$$

The recoil energies for the interaction can vary in the range of 1-100 keV for WIMP masses of 10-1000 GeV/c^2. Therefore, dark matter detectors are made for low energy sensitivity in search of dark matter.

2.3.3.2 Nuclear recoil rate

The rate of WIMP scattering events in any dark matter detector will be low because of the weak cross-section of WIMP nucleon interaction. The differential nuclear recoil event rate per unit detector mass for the weak interaction of WIMP particles and Standard model particles in a given detector is the product of several quantities [40], and can be written in the following equation (2.5),

$$\frac{dR}{dE_R}(E_R, t, m_\chi, \sigma) = \frac{n_\chi}{M} < v\frac{d\sigma}{dE_R} >= \frac{\rho_\chi}{M m_\chi}\int_{v_{min}}^{\infty} v f(v,t)\frac{d\sigma}{dE_R}(v, E_R)dv \tag{2.5}$$

where n_χ is the number density, ρ_χ is the local dark-matter density which recent estimates 0.3 GeV/cm^3 [38], $\frac{d\sigma}{dE_R}$ is a differential cross-section of the elastic scattering, $f(v,t)$ is normalized time dependent WIMP speed distribution, v_{min} is the incoming minimum WIMP speed which recoils a nucleon with energy E_R (discussed in equation (8.17)).

The dark matter rates are often written in the units of counts per day (cpd) per kg of detector per keV of the recoil energy spectrum, the rates are also sometimes expressed as dru, differential recoil units. The total recoil rate (also called tru) for WIMP-nucleon scattering, R, for any detector working at an energy threshold (E_T) can be calculated from the integration of differential event rate over the energy window E_T to overall energies,

$$R(t, m_\chi, \sigma) = \int_{E_T}^{\infty} (\frac{\rho_\chi}{M m_\chi} \int_{v_{min}}^{\infty} v f(v,t) \frac{d\sigma}{dE_R}(v, E_R) dv) dE_R \tag{2.6}$$

The nuclear recoil energy range expected for a dark matter interaction is 1 keV to 100 keV [40]. In the detectors using noble liquids as the targets material, the nuclear recoil produced less energy than the electronic recoil of the same energy, and the amount of energy transferred to a nucleus from a WIMP particle is usually measured in keVnr (keV nuclear recoil) which can be measured in terms of keVee (keV electron equivalent). These energy units are related through the scintillation efficiency parameter, $\mathcal{L}_{eff}$ as,

$$E_{keVee} = E_{keVnr} \mathcal{L}_{eff} \tag{2.7}$$

The scintillation efficiency, $\mathcal{L}_{eff}$ is measured as the ratio of electronic recoils energy to nuclear recoils energy for the range [7.1 - 117.8] keVee of nuclear recoils which results

[0.243 - 0.349] [41].

2.3.4 WIMP annual modulation

In addition to searching for individual dark matter scatters, modulation of the rate of interactions with the time of year is expected due to the annual modulation in the nuclear recoil rate with respect to time. If the WIMP halo has a net zero velocity with respect to the Galactic center, the Sun moving in the galactic plane will have a relative velocity ($\sim$ 230 km/s) with the WIMP halo, and hence Earth, as shown in the figure 2.6.

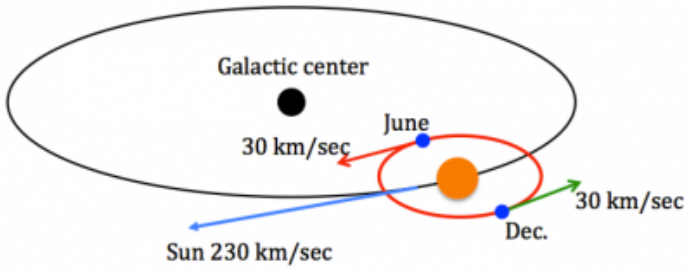

Figure 2.6: The diagram shows the rotation of the Sun (yellow) around the Galactic center (black), and hence the rotation of Earth (blue) around the Sun and Galactic center which causes the relative velocity of the Sun with respect to non-rotating WIMP halo, the picture is taken from [42].

Thus, the velocity distribution in equation(2.6) is time-dependent because of the rotation of Earth around the sun, and galactic center in the presence of dark matter WIMP wind, this will cause the sinusoidal or annual modulation in the nuclear recoil signal, with maximum magnitude in the month of June and minimum nuclear rate in the month of December [43]. The orbital motion of the Earth will be in direction of the disk rotation in the month of June which gives more interaction of WIMPs with the target nuclei and maximum relative velocity of Earth. However, in the month of December, the direction of rotation of Earth will be opposite to the rotation of the

Sun around the Galactic center hence less nuclear recoil rate is expected. The Earth's orbit is inclined at ∼60° relative to the plane of the Galactic disk.

Most of the backgrounds in all the dark matter detectors are not expected to show the sinusoidal modulation in the signal, therefore, annual modulation is a significant signature of the existence of dark matter [43]. Moreover, the sensitivity to the annual modulation of the dark matter for any detector depends upon the various factors from equation (2.6) which includes both particle physics model and flux of the dark matter particles, also scattering cross-section or type of the target material. Many dark matter experiments use the simpler case of the astrophysical model called the Standard Halo Model (SHM) for the distribution of dark matter where the WIMP halo is considered an ideal gas following the Maxwellian velocity function, on contrary, some theories also consider the non-uniform distribution of dark matter in sub-halos [44]. In any case, the event rate varies as a function of time. For the simple assumptions for WIMP halo distribution, the expected modulation in the recoil signal can be written in form of equation (2.8), where,

$$\frac{dR}{dE}(E,t) \approx S_0(E) + S_m(E)\cos\omega(t-t_0) \tag{2.8}$$

Here, $S_0(E)$ is the time average rate at any energy E and time t, $S_m(E)$ is the modulation amplitude with the fractional modulation, $S_m(E)/S_0(E)$ less than 10% for the dark matter model, $\omega = 2\pi/\text{year}$, and t_0 is the expected peak modulation time on 2nd day of the ∼June month.

Likewise, the annual modulation of the WIMP nuclear recoil signal, theories also predicts the diurnal modulation in the recoil rates due to the rotation of Earth about the Sun but the amplitude of this modulation is anticipated to be much smaller than the annual modulation because the rotational velocity of Earth on its own axis

is very small (near ∼0.5 km/s) in comparison to its orbital velocity around Sun (∼30 km/s). There are many experiments only focusing on the detection of the annual modulation in the WIMP signal. A variety of detectors are using solid crystal as the target material for the annual modulation signal but there is no information available for the sensitivity of the LAr target material for the search of this signal. A part of the thesis work is to perform the sensitivity study of the detector for the search of annual modulation in the nuclear recoil signal, which is discussed in more detail in chapter 8. This study showed the requirement of a low energy threshold of keV or less to detect annual modulation signal in argon, and PSD technique used in the DEAP-3600 experiment does not provide strong discrimination against nuclear recoils and electron recoils at this threshold value. Therefore, the annual modulation in the signal for argon can be contributed from any type of the WIMP candidates discussed in section 2.2.

There exists significant evidence suggesting the presence of unknown dark matter in the universe and the WIMPs are a well-motivated candidate for this. The DEAP-3600 experiment is searching for the elastic scattering of WIMPs with the LAr through the detection of the scintillation light coming from the particle's interaction, more details of the DEAP-3600 detector are discussed in chapter 4.

Chapter 3

Signal generation in liquid argon for dark matter detection

The DEAP-3600 detector uses ∼3279 kg of argon as the target material because of its inert nature, high stopping power against ionizing radiation, and sensitive background suppression for electromagnetic backgrounds using the Pulse Shape Discrimination (PSD) technique (section 3.2). The scintillation characteristics of LAr are discussed in this chapter. Moreover, the beta decay of the ^{39}Ar isotope is the major background in the LAr target material [45]. ^{39}Ar isotope is mainly produced by the interaction of cosmic rays with atmospheric argon. The studies of the properties of this isotope could give a piece of very useful information for the experiments using LAr target material. The theory of production and decay of ^{39}Ar isotope is also detailed in the second half of this chapter.

3.1 Scintillation in argon

The signal generation in argon is such that when an incoming dark matter candidate scatters the Ar nuclei or electrons from the Ar atoms leaving the atom in the excited state. The deposited energy in the recoiling atoms can result in the combination of atoms into the excited states forming excimer states from surrounding atoms [46]. The observed energy from the collision is then emitted by the excimers to the ground state in the form of scintillation light with a wavelength of Vacuum Ultra-Violet (VUV) region, 126.8 nm (at 85 K temperature) [47] as shown in the figure 3.1.

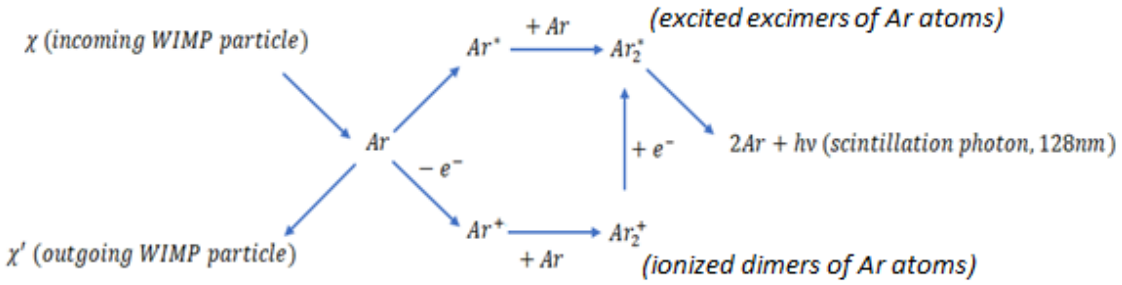

Figure 3.1: The excimer states in LAr either from the excitation of argon atoms (shown with * symbol) or from the ionization of the atoms (shown with + symbol), following subsequent bonding with a neutral argon atom, and decay of VUV light photon.

The light from the decay channels of excimers (Ar_2^*) made from the excited atoms called exciton (Ar^*) and ionized dimers created in the ionization of atom (Ar^+) are not the same. The lowest energy state of excimers in noble gases is a singlet spin state and a triplet spin state. The ground state in the liquid argon has a spin state, S = 0. The singlet states in the excimers have spin, S = 0, and they freely decay to the ground state with a lifetime in a few nanoseconds, $\tau_s < 6.2$ ns due to allowed transition as per selection rules (ΔS = 0). However, in the case of a triplet state with spin, S = 1, this decay to the ground state of the liquid argon atom state is forbidden

due to the conservation of angular momentum, and selection rules. The triplet state decays radiatively to the ground state with the equation (3.1), thus it decays to the ground state with the lifetime, $\tau_t = (1300 \pm 60)$ ns [47].

$$Ar_2^+ + e^- \rightarrow Ar^{**} + Ar \tag{3.1}$$

$$Ar^{**} \rightarrow Ar^* + Heat \tag{3.2}$$

$$Ar^* + Ar \rightarrow Ar_2^* \tag{3.3}$$

Also, in the ionization decay of dimers, the introduction of a new electron is involved which can have a spin value independent of the spin of the recombination atom because it is likely possible that the ionized and recombination of electrons are not the same.

The difference in the lifetime of singlet and triplet decay drives to the techniques of PSD through which one can differentiate the signal from nuclear and electron recoils which are discussed in section (3.2). The fraction of singlet states to triplet states generated is very different from electron recoil events and nuclear recoil events. Moreover, the decay photons from the scintillation light in both processes are absorbed by the thin layer of tetraphenyl butadiene (TPB) and transmitted to the PMTs in the DEAP-3600 experiment. The scintillation photons are generated in the VUV region and need to be wavelength shifted to the Visible region through TPB where PMTs are sensitive. This procedure is explained further in chapter 4.

3.2 Pulse Shape Discrimination

The Pulse Shape Discrimination technique is very popular in experiments to distinguish the scintillation signals from the particles with different decay times [48]. In the

DEAP-3600 experiment, this technique is used to separate the nuclear recoils from the electron recoils in the liquid argon target material. The LAr allows strong discrimination for these recoils than any other noble liquid such as Xenon, and Neon [45]. This discrimination power is greater than 10^8 at the low threshold of 10 keV which eliminated the electron and gamma backgrounds in the argon.

The nuclear recoils produce more ratio of singlet to the triplet dimers in comparison to electron recoils, and this fraction depends on the type of the particle. Thus, the overall time distribution of photons is very different in both cases. This can be seen in the amount of light decayed in the early part of the recorded waveform (called prompt light), if there is more light released in the early part indicates the singlet state decay in comparison to triplet light decay which gives a small signal in the whole part of the waveform, and hence indicates the nuclear recoils to the electron recoils as shown in the figure 3.2.

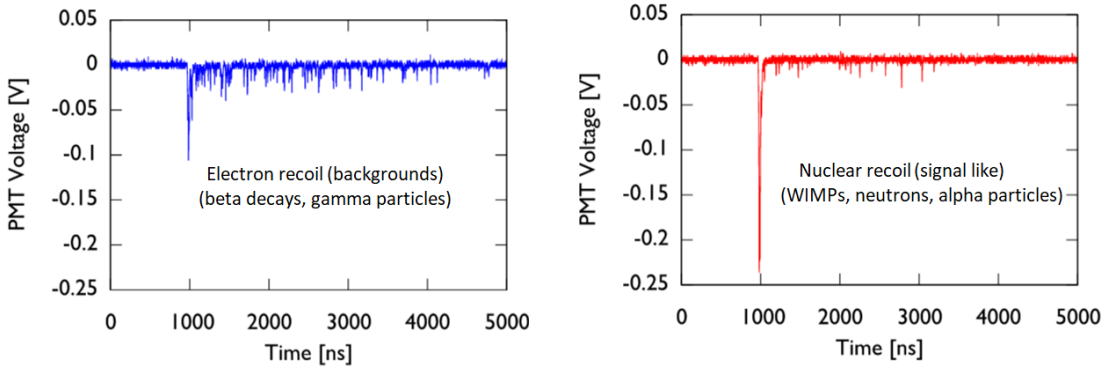

Figure 3.2: Example of electron recoil (blue), and nuclear recoil (red) signal from the recorded PMT voltage in DEAP-3600 detector. The rapid decay of the more singlet state excimers can be seen in the early part of the signal in the right plot.

This provides excellent discrimination between two types of recoils. Also, when the fraction of the scintillation light in the early part of the signal waveform to the full waveform is plotted as a function of deposited energy (or Photoelectrons discussed

in section 5.2.1), two clear bands of electron and nuclear recoils can be seen in the fprompt variable (or PSD variable, see section 5.2.2) and energy space. The nuclear recoils exist at fprompt value ∼0.7 and electron recoils exist at fprompt value ∼0.3, as shown in figure 3.3 from DEAP-3600 dark matter search publication [6], with WIMP search region shown in red where no events were recorded in 231 days of physics data. There are bands in the plot corresponding to the high rate of ERs and NRs. The neutron-induced NRs are from the calibration source data. The fprompt distribution is not obtained for the single neutron-induced NRs because they exist in the coincidence of ERs and Cherenkov light. Therefore, the simulated AmBe source is compared to the observed fprompt distributions. Thus, by applying a cut on the fprompt, and energy, one can distinguish the low-energy WIMP-Ar signal from the other electromagnetic backgrounds in the detector.

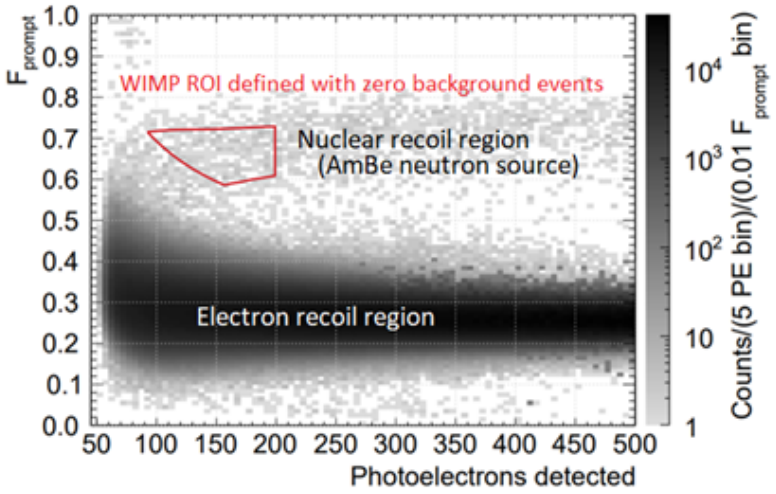

Figure 3.3: The fprompt variable versus photoelectrons detected for the Americium-Beryllium (AmBe) neutron source data taken in the DEAP-3600 detector with two bands of nuclear and electron recoil bands, and WIMP region of interest in red.

3.3 ^{39}Ar production and decay in detector

Argon is the third-most abundant gas in the atmosphere of Earth with about 0.93% of the atmosphere by volume, and 1.3% of the atmosphere by weight. It exists in the atmosphere mostly in form of stable isotopes, ^{40}Ar, ^{36}Ar, and ^{38}Ar with abundances 0.9960, 0.0033, and 0.0006 respectively [2]. The naturally occurring isotope, ^{40}Ar has a prime source of production from the radioactive decay of ^{40}K by electron capture. When the cosmic rays from the atmosphere interact with argon, three long-lived radioactive isotopes ^{39}Ar, ^{37}Ar, and ^{42}Ar are formed, with the highest specific activity for ^{39}Ar with the value ranging from 0.95 to 1.01 Bq/kg [49,50]. The specific activities for the other two isotopes are low and hence their abundances are very small in comparison to ^{39}Ar in the atmosphere [2], however, it depends upon the lifetime of these isotopes. The radioactive isotope, ^{39}Ar is produced mainly with the neutron capture and subsequent neutron emission.

$$ {}^{40}_{18}Ar_{22} + n \rightarrow {}^{41}_{18}Ar_{23} \rightarrow 2n + {}^{39}_{18}Ar_{21} \tag{3.4} $$

and, also by reaction,

$$ {}^{40}_{18}Ar_{22} + n \rightarrow {}^{39}_{17}Cl_{22} + d, \tag{3.5} $$

$$ {}^{39}_{17}Cl_{22} \rightarrow {}^{39}_{18}Ar_{21} + e^{-} + \bar{\nu}_e \tag{3.6} $$

The neutron capture on ^{38}Ar also produces ^{36}Ar to a very small extent,

$$ {}^{38}_{18}Ar_{20} + n \rightarrow {}^{39}_{18}Ar_{21} + \gamma \tag{3.7} $$

The beta decay of argon isotope, ${}^{39}_{18}Ar_{21}$ with 21 neutrons to the stable isotope of potassium, ${}^{39}_{19}K_{20}$ is shown in equation (3.8) with the Q value of decay at (565±5) keV [51].

$$ {}^{39}_{18}Ar_{21} \rightarrow {}^{39}_{19}K_{20} + e^{-} + \bar{\nu}_e \tag{3.8} $$

The beta decay energy spectrum for ^{39}Ar measured from the DEAP-3600 experiment is shown in figure 3.4.

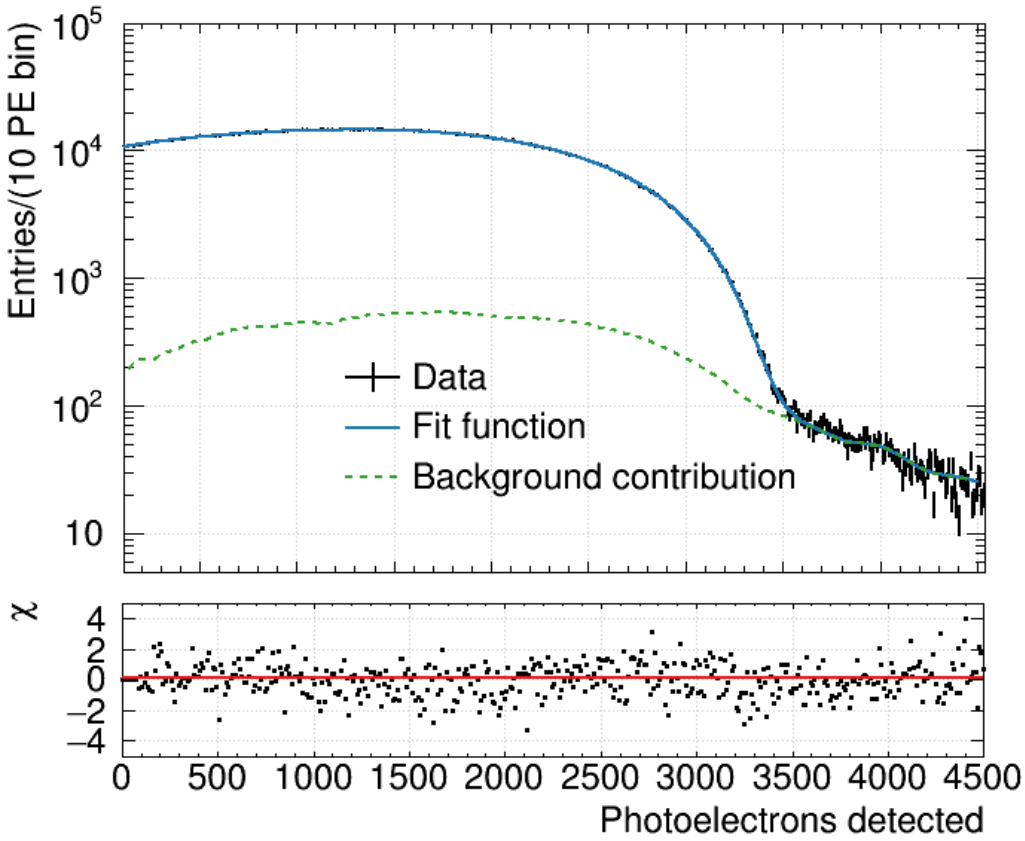

Figure 3.4: ^{39}Ar beta spectrum fit model (blue) in DEAP-3600 fitted to the data (black) with the very agreement. The expected backgrounds from the other gamma rays and pile-up events are shown in green.

3.4 Lifetime of ^{39}Ar isotope

The Q value for the decay of ^{39}Ar isotope is known, and there were several measurements for the lifetime of this isotope. The half-life of ^{39}Ar was firstly estimated in 1937 to be 4 minutes with insufficient evidence in the study of radioactivity with the bombardment of high energy neutrons [52, 53]. This estimate was disproved by Brosi et al in 1950 while investigating the beta spectrum for this isotope and they gave the lower limit with the half-life of ^{39}Ar greater than 15 years [51]. The half-life and mass measurement of ^{39}Ar was later presented by them in a different publication in 1952, where the argon was produced in the nuclear reactor from KCl, purified for 3 samples of the measurements. The mean half-life of ^{39}Ar was calculated from the three independent measurements with value (265 $\pm$ 30) years from the determination of the isotope ratios, with the values ranging from 240 to 290 years [54]. There were some sources of error mentioned while taking measurements which are related to the purification of the samples and the absorption rates of the beta ray spectrometer used, though the corrections were applied for the spectrometer. The other value for the half-life for the decay of ^{39}Ar used in the literature was 325 years [55]. This value was used in the year 1960 in a meteorite experiment to determine the spatial constancy of the cosmic radiations within the solar system by measuring the radioactivity of meteorite stones fallen on the Earth. The ratio of the ^{37}Ar to ^{39}Ar production rates was measured and compared for different meteorite samples, and 35 days half-life of ^{37}Ar and 325 years half-life for the ^{39}Ar were satisfying the measurements.

The most commonly used value for the half-life of ^{39}Ar isotope is 269 years which was estimated in 1965 from the isotope ratios of ^{39}Ar, and ^{42}Ar with ^{37}Ar [3]. These are the updated measurement that corresponds to a lifetime of ^{39}Ar isotope with a value of 388.1 $\pm$ 4.3 years. The half-life of the ^{37}Ar was measured as (35.1 $\pm$

0.1) days from its decay by producing the samples in the reactor and purifying the samples, and measuring the decay in proportional counters. The half-lives of ^{39}Ar, and ^{42}Ar obtained from the mixture of ^{37}Ar, ^{39}Ar, and ^{42}Ar atom ratios as, ^{37}Ar:^{39}Ar, and ^{37}Ar:^{42}Ar, however, the absolute number of atoms for individual isotopes were not calculated. The counting efficiency of the detector and systematic preparation of the samples were included in the study which gave the uncertainty of 3 years on the half-life of ^{39}Ar though the values from different samples varied from 253 to 288 years. These measurements were done with the assumption of the natural abundance of atmospheric argon in form of ^{40}Ar and ^{36}Ar with the ratio of branching fractions 296 with the uncertainty of 2 to 3%, which were only known that time. The complete branching ratios of the atmospheric argon isotopes and abundance were measured in 1971 by Melton et al [56] that showed the presence of the third isotope, ^{38}Ar with a low abundance of (0.064 ± 0.01)%.

The method used to measure the half-life of ^{39}Ar through mass spectroscopy with the indirect technique of recording the ^{40}Ar to ^{36}Ar ratios is discussed by Baksi et al [57] in 1996. This resulted in a half-life measurement of the ^{39}Ar to be (276±3) years with 3% change from previous measurements, however, the authors suggested some improvements in the apparatus for the more precise measurements eliminating some errors atmosphere contamination which occurred while taking this data. In the nuclear data sheets from 2018 [58], the half-life of ^{39}Ar is suggested to be (268 ± 8) year, only with enlarged uncertainties. Therefore, a re-measurement for the half-life of ^{39}Ar is required before considering it as a dating tool [59].

Before this work, there has been no direct measurement of the ^{39}Ar half-life made by directly observing its decay curve. The production and decay of the ^{39}Ar in the atmosphere are in a steady state, this isotope is both short-lived to produce

a strong signal and long-lived because of its expected long lifetime. DEAP-3600 detector has shielded from the many cosmic ray particles due to overburden, however, the presence of neutrons underground through the detector components or survived cosmic rays causes the production of ^{39}Ar isotope, which is the dominant background in the detector at the rate of $\sim$ 3000 Bq, the event energies existing in the electron recoil band. If the event rates for the ^{39}Ar isotope decays are studied carefully and precisely by controlling and correcting for all the systematics in the DEAP-3600 detector with time, then the fitting of the correct event rates with the radioactive decay model can provide a direct measurement for the lifetime of this isotope. One part of this thesis is to determine the event rates of ^{39}Ar isotope decays in DEAP data and fit the evaluated with the radioactive model that defines the data to measure the lifetime of this isotope which will contribute to many fields using Argon-Argon and Argon-Krypton dating. Also, this measurement will provide useful information for future large-scale experiments using liquid argon as the target material. More details on the analysis of DEAP-3600 data for lifetime measurement of ^{39}Ar isotope are discussed in chapter 5, 6 and 7.

Chapter 4

DEAP-3600 experiment

The DEAP-3600 experiment is a dark matter experiment designed to use 3600 kilograms of LAr as the target material in an acrylic cryostat to search for the direct detection of dark matter candidate WIMPs [60]. This is a single-phase experiment in which the scintillation light emitted from the interaction of dark matter particles with the argon nucleus is recorded. The DEAP-3600 experiment has projected sensitives to cross-sections of 10^{-46} cm^2 for the spin-independent scattering of 100 GeV/c^2 massive WIMPs on argon nucleus with a fiducial exposure of 3 tonne-years.

4.1 Brief history of DEAP project

The concept of the DEAP-3600 experiment with the pulse shape discrimination technique (section 3.2) was proven by its prototype DEAP-1 experiment. The DEAP collaboration firstly utilized 7 kg of LAr with the setup of two PMTs in 2006 to prove the PSD method as a useful method to discriminate electron recoil background signals from nuclear recoils of argon (for the WIMP-like particle energies) [45]. The operation period of the DEAP-1 experiment was completed in 2007 and its next-generation de-

tector DEAP-3600 was constructed in the SNOLAB research laboratory at Creighton Mine in Lively, Ontario, with a much larger size and mass of LAr but it operated under the same principle. In this chapter, the details of the DEAP-3600 detector with its physical design and scintillation process will be described with a brief overview of the underground research facility where the experiment is operated.

4.2 SNOLAB underground research laboratory

The current experiments searching for rare processes such as dark matter interaction and properties of the neutrinos like neutrinoless double beta decay require laboratory locations that are background free, or in reality, the backgrounds should be very negligible, as low as possible, and fully understood. The DEAP-3600 experiment is located in the cleanroom laboratory at SNOLAB. This cleanroom laboratory provides an almost background-free environment to record the extremely rare physical interaction with a class 2000 which means there is a concentration of a maximum of 2000 airborne particles larger than the 0.5 μm per cubic foot of air [61]. SNOLAB lab facility is the expansion of the existing clean lab facility constructed originally for the Sudbury Neutrino Observatory (SNO) solar neutrino experiment [62] in the 1990s, results of which were awarded the Nobel Prize, jointly awarded in 2015 [63]. After the SNO experiment, the SNOLAB underground lab has expanded substantially, and in addition to the dark matter and neutrino physics experiments, SNOLAB also hosts many biological underground experiments in the total cleanroom area of 5000 m^2. The Cube Hall area in the SNOLAB facility is the second-largest hall in the cleanroom with a cube of 15 m and a staircase and height for a crane [64]. The diagram for the map of the SNOLAB facility is given in Figure 4.1.

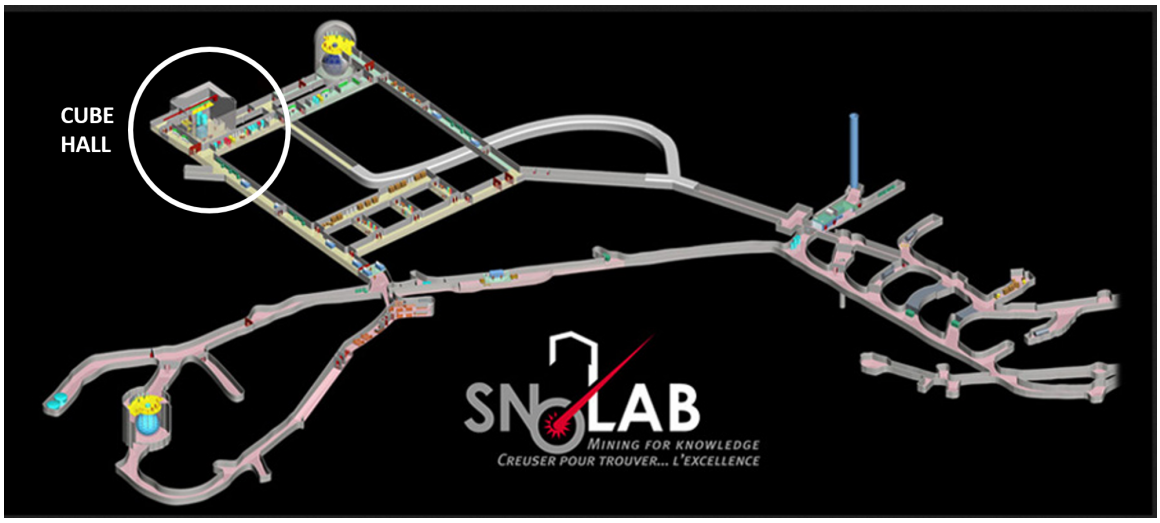

Figure 4.1: A map of the SNOLAB underground facilities. DEAP-3600 experiment resides in the Cube Hall, highlighted in the top left corner of the diagram.

SNOLAB is one of the preeminent deep underground laboratories located 2 km underground (which is 6000 meters water equivalent) at the Vale Creighton Mine near Sudbury, Ontario, Canada [65]. This underground lab facility has a clean laboratory with an area of 5000 m^2 and a volume of 37000 m^3 [64]. The overburdened rock at the SNOLAB provides shielding from cosmic radiation. High-energy cosmic rays interact with the atmosphere and create showers of secondary particles such as neutrons, protons, and electron secondaries by many orders of magnitude. The muons produced in the cosmic ray showers can penetrate kilometers of rock and hence, the deep underground facilities like SNOLAB provide the best protection against these particles, resulting in muon flux is $0.27/m^2/day$ [64].

The other gamma and neutron backgrounds underground come from the elemental composition of the norite rock formation in the lab which results in the small dust and radiological backgrounds from gammas of Potassium (1.2%), Uranium (^{238}U which is 1.2ppm), and Thorium (^{232}Th which is 3.3ppm) [61]. The flux of the various gammas rays from the norite rock was measured in the lab during the SNO

experiment installation, summarised in the table 4.1.

Table 4.1: The measured gamma flux for various energies from the gammas emitted in the norite rock surrounding SNOLAB.

Energy [MeV]	Flux [gamma/m^2/day]
4.5-5	510 $\pm$ 220
5-7	360 $\pm$ 220
> 7	180 $\pm$ 90
> 8	< 20

The estimated flux of the thermal neutrons from the rock is 4144.9 neutrons/m^2/day, and the fast neutron flux is 4000 neutrons/m^2/day. The radon gas amount in the SNOLAB air from the combined measurement for ^{220}Rn and ^{222}Rn is measured to be 123 Bq/m^3 [61].

4.3 The DEAP-3600 detector: Overview

The main features of the DEAP-3600 detector design include the single-phase target, radiopure acrylic cryostat, and raw materials used in the construction with the optimized electronics for scintillation detection and low data rates. The graphic design of the DEAP-3600 detector is shown in figure 4.2.

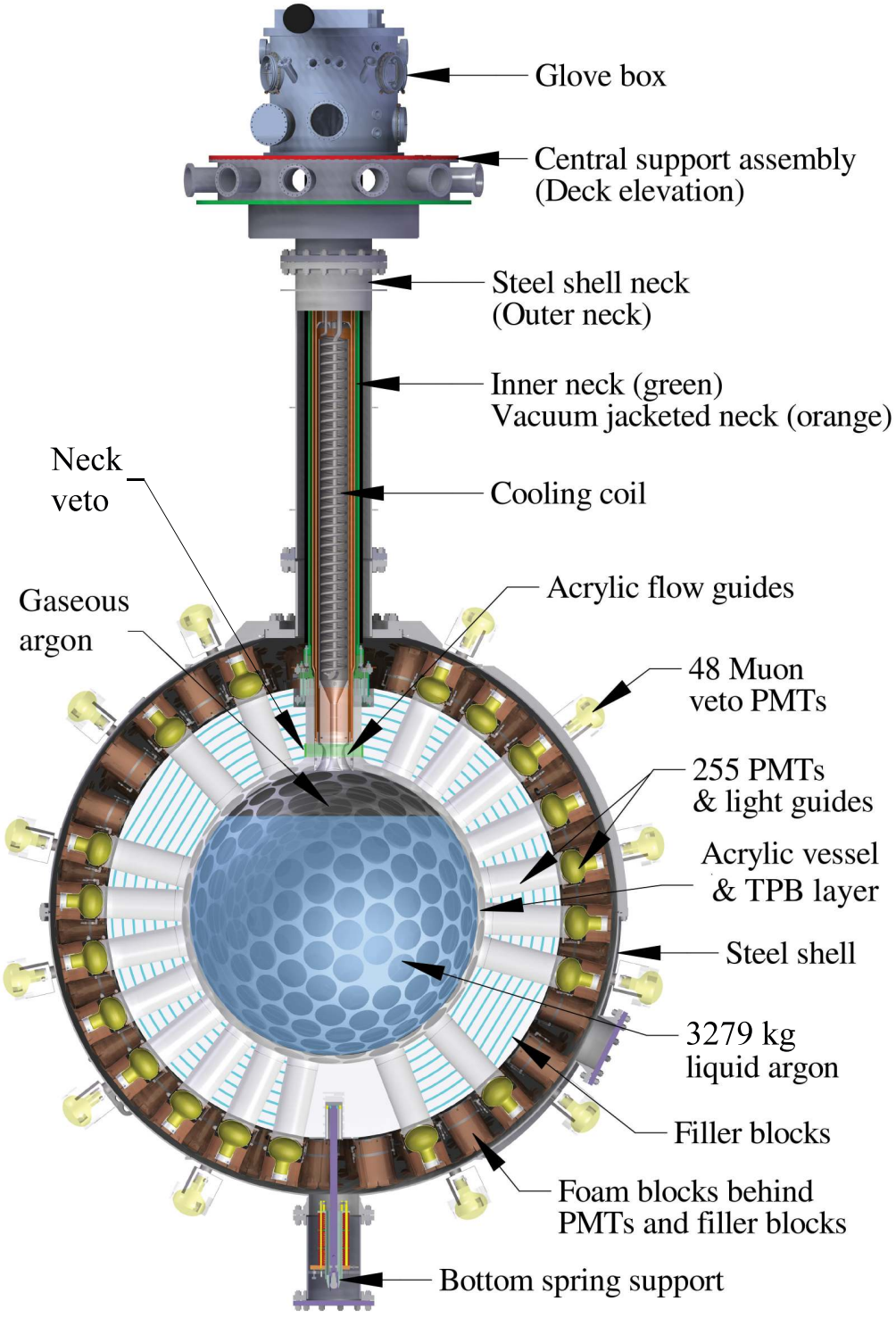

Figure 4.2: Schematic diagram of DEAP-3600 detector with different components.

The inner component of the detector is an acrylic cryostat, a spherical-shaped 5 cm thick Acrylic Vessel (AV). The inner radius of the AV is 85 cm which can hold 3600 kg of LAr target mass. The scintillation light signal from AV travels to the 255 LAr PMTs surrounding the AV through the cylindrical acrylic light guides (LGs) which are 45 cm in length and are bonded directly to the vessel. The LGs provide the shielding from neutrons and connect the AV with the 255 detectors PMTs to transmit the signal. The PMTs used in the detector are Hamamatsu R5912-HQE (high quantum efficiency) PMTs with the 8-inch diameter and 23% quantum efficiency at a wavelength of 400 nm [66]. Neutron shielding in the sphere is also provided by the filler blocks (FBs) which are made from the layers of high-density polyethylene and polystyrene and filled in the space between LGs. There is a 3 μm thick coating of 1,1,4,4-tetraphenyl1,3-butadiene (TPB, $C_{28}H_{22}$) wavelength shifter on the inner surface of AV to change the wavelength of argon scintillation light in the vacuum ultraviolet (VUV, peaked at the 128 nm) to the visible light region (peaked at ~420 nm) which is transmitted to the PMTs through the LGs.

The inner detector setup described above is placed in stainless steel consisting of a spherical shell and the outer neck as shown in figure 4.2. There is a cooling coil mounted in the neck that uses liquid nitrogen (LN_2) to cool the LAr, and the glove box at the top of the neck allows the insertion and extraction in a radon-free environment. The outer steel shell is submerged in the ultra-pure water tank of 7.8 m in diameter and there are 48 Hamamatsu R1408 PMTs on the steel shell serving as a muon veto see section 4.4. The water tank provides the shielding from external radiation sources and muons that passes through the detector and surrounding components. Selected photos from the DEAP-3600 picture album [60] during the construction of the detector are shown in figure 4.3.

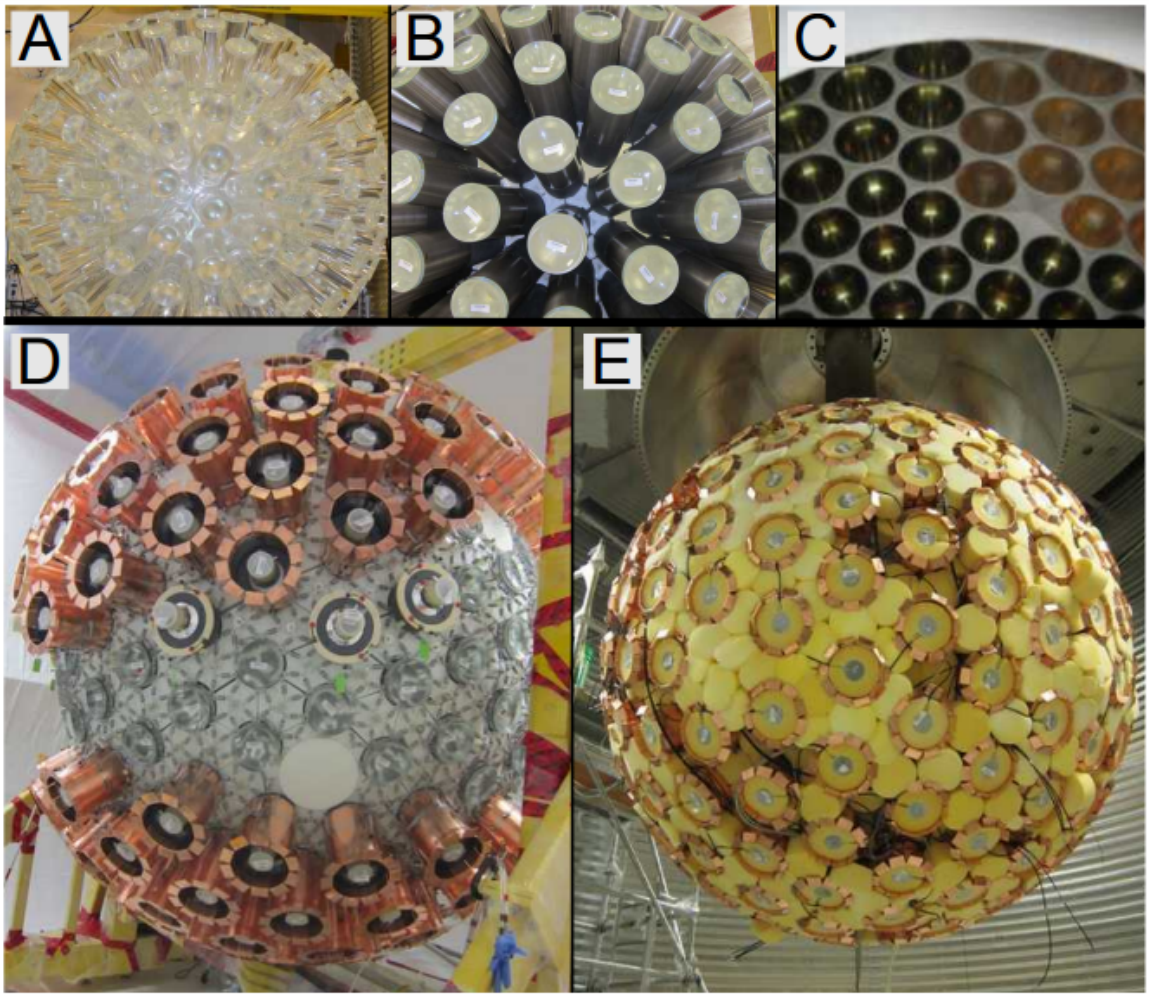

Figure 4.3: Some pictures of DEAP-3600 construction taken from research paper [60]. A) The AV after bonding on the LGs. B) Reflectors and magnetic shielding installed around LGs. C) View from inside the detector with the white Tyvek and most PMTs installed on LGs. D) Detector with FB installed and during PMT installation. E) Detector with all PMTs installed and during backing foam installation.

4.3.1 Detector material and properties

The detector is made up of many different materials. All the materials selected for the construction are verified and tested to be extremely radiopure, to ensure the purity of the detector signal to reject the background signals that will mimic the WIMP signal. The detailed construction and detector setup with the materials used in the

detector formation can be found in the reference [60].

Some of the materials used in the detector set up such as the acrylic sphere and the stainless steel shell are specifically chosen for the structure stability and optical demands of the experiment, however, there may introduce a few radioactive backgrounds. The AV sphere and LGs are made up of Acrylic or poly(methyl methacrylate) (PMMA) which was selected because of its easy manufacturing and optical properties with a long attenuation length of order 1 m or greater [67] which is 90% transparent to the light emitted by the wavelength shifter [68] with some loses due to reflection. Therefore, the introduction of radioactive materials was under full control during its building process. The TPB layer on the inner surface covers the 9 m^2 of the AV which is also radiopure to prevent the alpha decays from the bulk that would produce the background triggers. The base chemicals used for the production of this layer were certified with 99% or greater purity.

The air in SNOLAB contains some amount of radon from the rock surroundings (as mentioned in the section 4.2) and its long-lived daughter can accumulate on any part of the detector during the setup. Thus, the air exposure in the lab was kept to the minimum value during the assembly of the various detector components, and the inner surface of the AV was resurfaced before completion to remove the potential particles to get in contact with the bulk LAr. The other components of the detector integrated for its operation such as LAr and PMT glass could also introduce radioactive backgrounds which are mitigated from the proper understanding of the detector in the detailed background model discussed in the section 4.6.

4.4 Light detection and calibration

The light detection system in the DEAP-3600 experiment consists of different sets of PMTs for recording the scintillation light from bulk argon decays in the AV, alpha and background decay in the neck region of the detector, and muons in an outer water veto. The basic principle of a PMT is discussed in the following paragraph.

PMTs Photomultiplier tubes (PMTs) are light detectors that detect single photons through the light-sensitive photocathode. It consists of a vacuum tube with an input window, a photocathode, focusing electrodes, an electron multiplier, and an anode sealed into an evacuated glass tube. When a photon strikes the photocathode, it ejects an electron called a primary electron through the photoelectric effect. The electric fields are generated within the PMT due to supplied high voltage which drifts the primary electron to the dynodes. Secondary electrons are ejected from the dynodes when the primary electron strikes the first dynode and hence electron amplification takes place in the PMT as a result of the drift of secondary electrons to the other dynodes until all the electrons are collected on the anode plate. The electrons are amplified by a factor of 10^7 which leads to the detection of single photons possible through the electronic signal. The schematic diagram of the PMT action from the Hamamatsu photonics is shown in figure A.14.

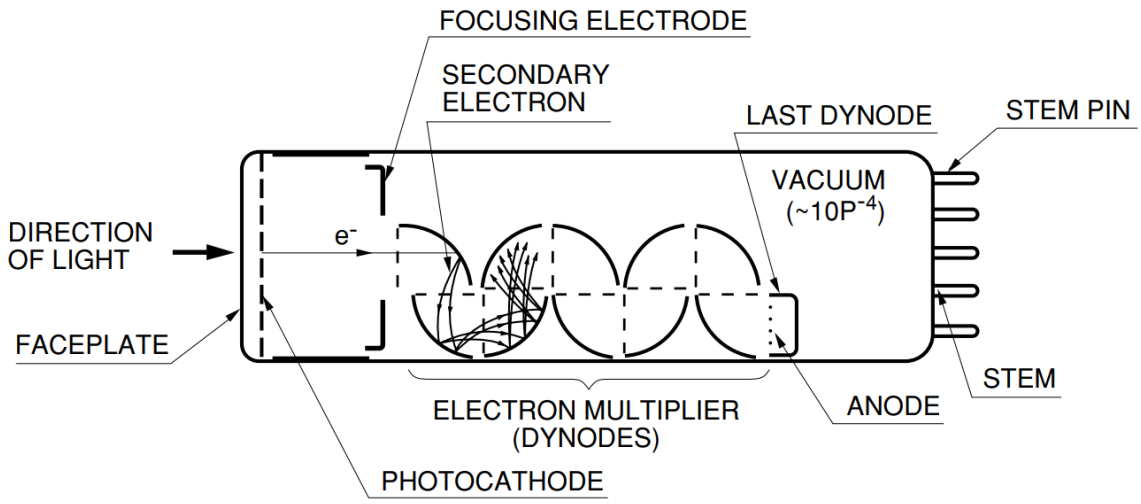

Figure 4.4: The diagram of the Hamamatsu PMT construction from [69].

Afterpulsing in the PMTs Afterpulsing in the PMTs refers to the pulses which occur at the end of the signal output. These are small amplitudes most of the time but can be as large or sometimes larger than the primary pulse. These pulses are from the positive ions in the residual gases in the PMTs which causes delayed pulses from drifting and ejection of electrons that pass to the dynode chain. The delayed pulses from the afterpulsing have a time difference from the nominal signal in hundreds of nanoseconds to the microseconds. In the DEAP-3600 experiment, there are several energy estimators defined to reduce and neglect the effect of these after pulsing signals from the standard recorded signals (see section 5.2.1 for details).

4.4.1 LAr PMTs

As discussed in the section 4.3, there are 255 LAr PMTs used in the detector set up which are Hamamatsu R5912 8 inch diameter HQE PMTs [66] selected for their high photon detection efficiency and low dark noise rates, and good timing properties. The detailed study of the PMTs characteristics used in the detector can be found in

the reference [60]. During operation, the PMTs temperature doesn't vary a lot, so their noise rates are approximately constant. This stability neglects any systematics uncertainty from the effect of thermodynamics on their action. The stability of the LAr PMTs over time of data taking is discussed in the appendix A.

4.4.2 Neck veto system

The neck of the AV is wrapped with the 100 Kuraray Y11 (200M) wavelength shifting optical fibers that record the light signals from the alpha and Cherenkov light backgrounds in the neck part of the detector. The length of the fibers is between 2.6 m to 3.3 m, and the end parts of each fiber are collected in bundles of 50 and optically coupled to four Hamamatsu high quantum efficiency PMTs.

4.4.3 Muon veto system

The muon system in the detector is made of 48 Hamamatsu R1408 PMTs connected on the outer surface of the steel shell as mentioned in the section 4.3 and is immersed in the water tank. There is a muon flux of $0.27/\mathrm{m}^2/\mathrm{d}$ at the SNOLAB and to reduce the effect of these small backgrounds the muon veto PMTs are added to the system. Whenever an incoming muon survives the overburden of the lab and passes through the water tank, it will produce the Cherenkov light in the tank [70] which is recorded by these PMTs. After creating the Cherenkov light in the water tank these particles usually cause the scintillation light in the AV from the secondary neutrons, and if the detector records the signal from these muon PMTs and inner LAr PMTs at the same time, those triggers are categorized as muon particles and are not used in the data. The neutrons are indistinguishable from the WIMP signals however these particles are rejected up to some fraction using the muon veto system, there are about $\sim$0.162% of all the triggers are caused by the muons. The Monte Carlo studies from

the DEAP-3600 collaborators show the muon veto system has a detection efficiency of greater than 96% for the muon particles above 1 GeV. The schematic diagram for the distribution of veto PMTs around the steel shell is shown in figure 4.5.

4.4.4 Calibration systems

There are different calibration systems used around the detector setup to regulate the PMT action and understand detector response. The calibration for the optics of the detector is done by diffusing the laser ball source, which was deployed into the detector before it cooled down to take data. This calibration was done to determine the optical response of the detector materials. There is an array of the fiber optic cables that are uniformly installed around AV and connected to the LED drivers in the detector to regulate and record the PMT performance as a function of time [60]. These optic fibers are called the acrylic and aluminum reflector fiber (AARF) system and are useful to determine the energy response of the detector (see section 5.2.1).

To calibrate the response of the detector with the various radioactive sources, the external radioactive calibration sources are deployed outside of the steel shell of the detector [6]. The stainless steel tubes (A, B (not visible), C, and E), and a circular high-density polyethylene tube F as shown in the figure 4.5 are used to deploy the radioactive sources around the detector.

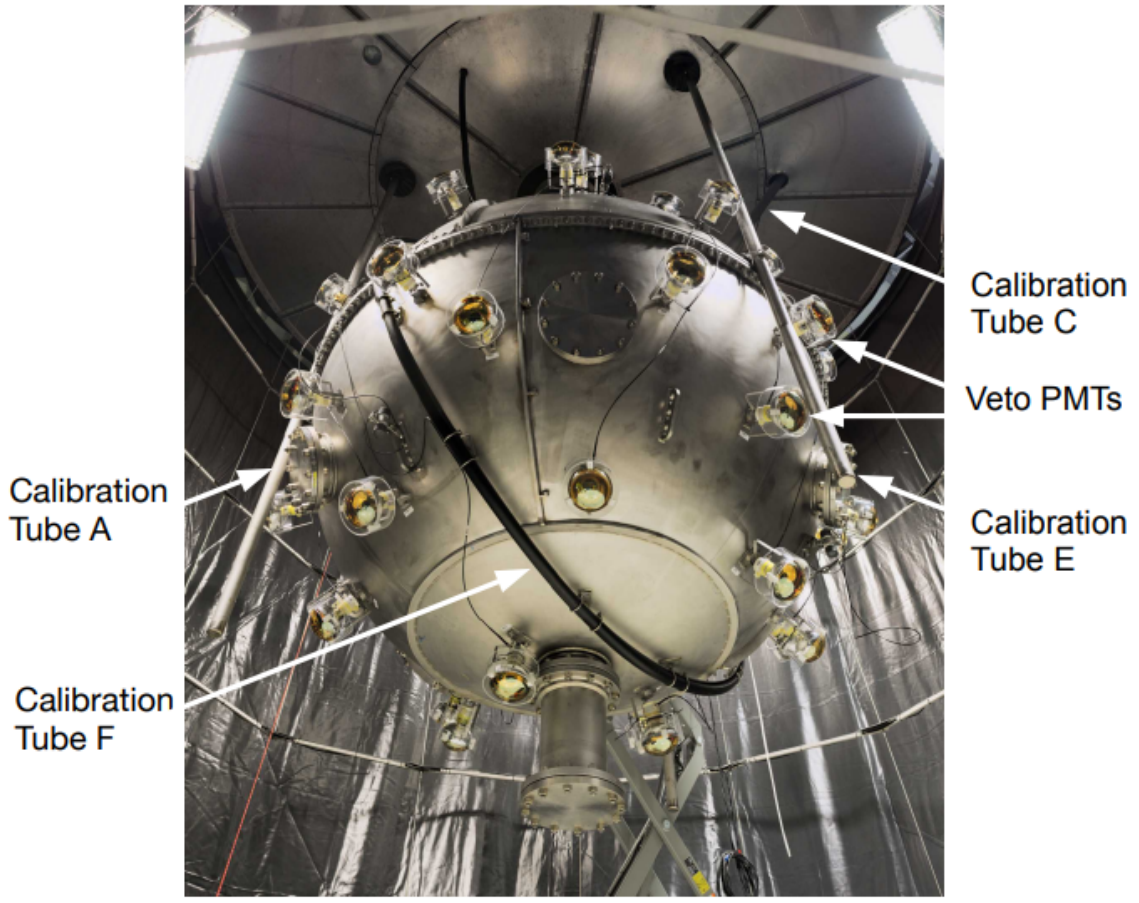

Figure 4.5: The water shield tank of the DEAP-3600 detector with the calibration tubes A, B (not visible; in the background), C, E, and F as indicated. The 48 PMTs attached to the steel shell are used for the muon veto system [60].

A ^{22}Na source is tagged to observe the energy scale, resolution, and position response of the setup. This is done through the timing of the pulses in the two tagging PMTs (which record the scintillation light from gamma particles emitted from the source) with respect to the detector response for ^{39}Ar betas and ^{22}Na gammas. In addition to this, a tagged americium-beryllium (AmBe) neutron source is used to report the response for the neutron-induced nuclear recoils similar to the interactions from the WIMPs. The tagging of PMTs in this case is done such that when an alpha

emitted from the decay of ^{241}Am captures the nucleus of ^{9}Be, its releases a neutron and a gamma particle. The PMT thresholds are set in the scale to tag emitted neutrons from the gamma particle.

The report of the gamma interactions is calibrated from the ^{208}Tl decays for the Cherenkov light produced in the acrylic. Moreover, the intrinsic activity of ^{39}Ar beta decays form an additional energy spectrum which is further used to understand the energy distribution and position reconstruction for a wide range of PEs in the detector since the distribution of these events is uniform in the argon.

4.5 Electronics and trigger system

The electronic system in the DEAP-3600 experiment is mainly supported by the DAQ system which is housed on 3 computer racks. The PMT signals are collected and analyzed by a Digitizer and Trigger Module (DTM) in the DAQ, which decides whether to trigger the event readout. The simplified diagram for the DAQ is shown in figure 4.6.

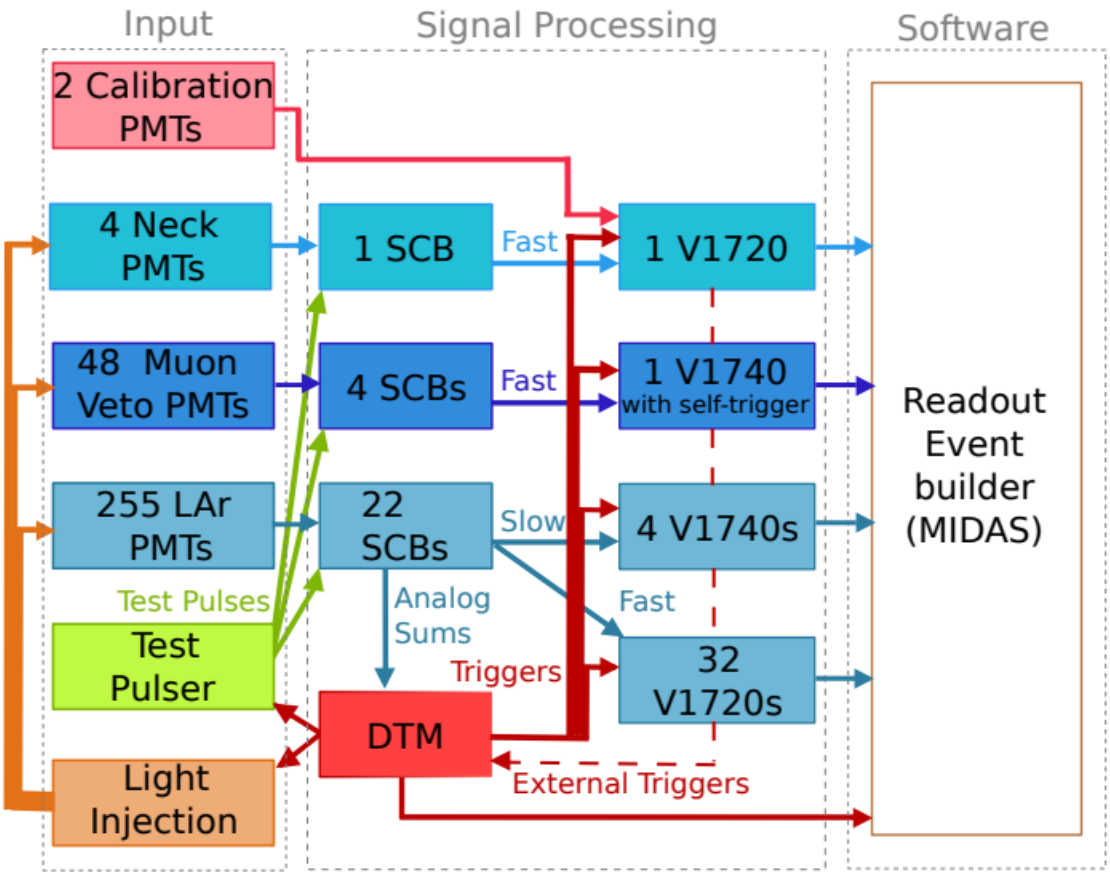

Figure 4.6: The data acquisition system for DEAP-3600 experiment with various components.

There are a set of digitizers and triggers collected in the different boards that are used to record the signals from the PMTs. A detailed description of various DAQ components is given in the following sections.

4.5.1 Signal conditioning boards

The light signal from the different PMTs in the detector is connected to the DAQ through the 27 custom Signal Conditioning Boards (SCBs). The SCBs are designed at the TRIUMF laboratory and built at the University of Alberta. Every SCB in the system can hold up to 12 PMTs. The 255 inner detectors PMTs are connected to 22

SCB boards, the 48 muon veto PMTs are dedicated to 4 SCBs, and there is one SCB for the neck veto PMTs. The SCBs decouple the applied high voltage, thus providing high voltage protection, and shape the signals from the PMTs through 12 identical channels. The output from every 12 channels is summed to create an analog sum (ASUM) for each SCB and used in the digitizers and DTM to test the pulses.

4.5.2 Digitizers

The output from the SCBs are processed through the two sets of 36 CAEN digitizers. The 32 CAEN V1720 modules are used to record the fast pulses from the high gain channels which are designed to get high signal-to-noise for single PEs. These V1720 digitizes sample the signal at 250 MHz. There are 4 CAEN V1740 modules that have lower gain amplifiers which allow a wider dynamic range of the signal amplitude. These V1740 digitizes sample the signal at 62.5 MHz. The continuous analog pulses from the PMTs are converted to discrete digital signals through digitizers which distribute the signal waveforms in the time bins which is the inverse of the sampling rate and the process is called analog to digital conversion (ADC). For example in V1720s, the time bins are sampled like $1/(250\text{x}10^6)$ which is 4 ns, and for V1740s, the time bins are $1/(62.5\text{x}10^6)$ which returns 16 ns. All the digitizers are then connected to readout computers in the DAQ. The physics data used in the ^{39}Ar lifetime analysis are recorded from the V1720 digitizers.

4.5.3 Trigger system

The DTM in DAQ makes the trigger decision, provides the instructions to the master clock to synchronize digitizers, trigger digitizers, and external calibration systems, and controls the data collection if the DAQ is overloaded [60]. The trigger system in the DAQ works on the basis of trigger sources and logical trigger outputs. The DAQ

system is taking data using the following triggers settings,

1. Physics trigger
2. Periodic trigger
3. Muon Veto trigger

The DAQ is recording the data continuously from the digitizers using the two rolling integral windows called a narrow window (150 ns) and a wide window (10 µs) to search for the signal pulses. The DAQ triggers to record the signal waveforms in two ways depending upon the trigger source. If the external trigger sources such as periodic triggers from the pulse pattern generator and external calibration light pulses are fired in the system, the DAQ is triggered to save the data as guided by the sources. However, for the actual physics trigger to occur, the integrated charge in the narrow window must surpass 1000 ADC counts, which refers to the standard threshold of the DAQ system. When either of the two conditions is met the signal waveforms are saved in the DAQ such that the information is written for the 2.5 µs before the trigger and 13.5 µs after the trigger, producing a waveform of 16 µs of data. This approach is adopted to calculate an approximate fprompt (see section 5.2.2) at the trigger level to reduce the data since this experiment is mostly interested in low-energy and high-fprompt data for the WIMP search, so most of the ER data are prescaled. Each trigger source can be connected to many trigger outputs, all configured differently for example if the trigger is classified as a periodic trigger (discussed in section 5.4) then that DAQ is forced to trigger with no threshold. The output from the trigger setup is then sent to the DAQ computers for further processing.

The triggering algorithm decides the output depending on the value of the total charge in the narrow and wide windows. The PSD parameter (Trigger Fprompt),

which is the ratio of the energy deposited in the narrow to wide windows is calculated from the rolling windows in the trigger monitors and using this information along with the narrow charge (Eprompt), the waveform is constructed in one of the five different trigger regions. The two-dimensional space of the trigger regions as a function of the energy of the narrow window and PSD parameter is shown in figure 4.7.

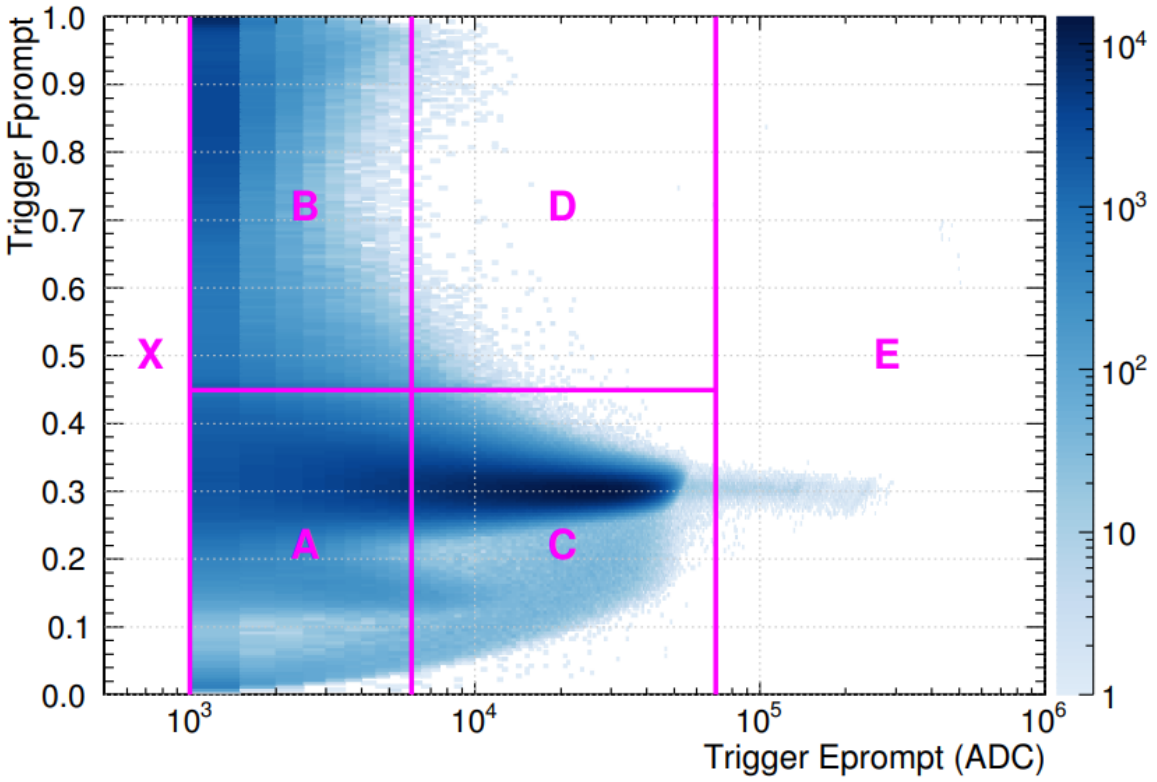

Figure 4.7: The trigger energy in the narrow window plotted as a function of trigger fprompt from a physics run [60]. The different trigger regions are highlighted in pink boxes.

The triggers in region X are very low energy and not recorded with the detector threshold at 1000 ADC, and the other 5 regions are all recorded with separate trigger sources. The digitizers read all the triggers in regions A, B, D, and E, and the full information related to the triggers is saved. The periodic triggers are running at the frequency of 40 Hz and the test pulses are added at the rate of 1 Hz such that

the remaining 39 Hz are invested to monitor PMTs. The muon veto self-triggers are recorded by the veto PMTs. The total trigger rate in the detector is 3200 Hz. The physics trigger in region C saves data with some prescaling as discussed in the following section.

^{39}Ar Prescaling The region C in DEAP-3600 trigger settings is called prescaled region because the electron recoil band in DEAP-3600 data falls in this energy region (explained in section 4.7). The ^{39}Ar beta decays are dominant in the energy spectrum and are emitted at a very high rate which is approximately 3000 Hz out of the total event rate which contains the single ^{39}Ar decay triggers, as well as the pile-up ^{39}Ar decays with itself and other low energy triggers [60]. Therefore, to save disk space only 1 out of 100 triggers that fall in this energy region are saved in the system although the digitizer information for all the triggers.

The trigger energy regions considered for the present study are A and C, hence the corrections are made for the selected dataset to account for the prescaling effect (see section 5.7 for event count in rate algorithm). However, to understand the data more precisely the event contributions from low energy region X are included in the fit modeling (section 5.8), and detected lower energy triggers are extrapolated in the study with the example run recorded at a lower detector threshold of 150 ADC (section 5.9).

Trigger Efficiency The trigger efficiency for selecting events as a function of energy is also investigated from different analyses. There are some instrumental restrictions therefore the trigger efficiency is not 100% for very low-energy triggers. There is a strong dependence of fprompt on trigger efficiency. The DAQ system fails to detect some low energy triggers in the reconstructed energy or PE (PE variable is an amount

of the total measured number of photoelectrons that are produced by an event, see section 5.2.1 for the definition of PE, energy estimator), and above a PSD parameter value (fprompt) value of 0.10. However, the trigger response at the standard threshold is greater than 99% efficient in detecting the different kinds of particles at various energies above 200 PE. In the current study for lifetime measurement of ^{39}Ar, the trigger efficiency is 100%.

4.6 Backgrounds in detector

The overburden shielding in the SNOLAB stops many cosmic rays and cosmic-induced particles to enter the DEAP-3600 detector. However, the radioactive decay components in the detector decay and causes some backgrounds. The dominant backgrounds in the DEAP-3600 occur from the decay of ^{39}Ar, beta, and gamma-ray interactions with the LAr, which can be significantly separated from the WIMP nuclear recoil region using the PSD parameter (see section 3.2), and is used as the region of interest for the ^{39}Ar lifetime study. That being said there still exists some fraction of triggers from different sources that can mimic the WIMP nuclear recoil signal, and occur in the electron recoil region as well. The DEAP-3600 background model is designed to categorize the background triggers as discussed in the following sections.

4.6.1 Electromagnetic recoils

The electromagnetic recoil (ER) events are mainly contributed from the internal and external beta and gamma ray interactions, which include decay from the ^{39}Ar, ^{85}Kr, and other radioactive decays. The sources of these backgrounds are detailed in [1] and briefly discussed as under.

4.6.1.1 Internal sources

These sources are uniformly distributed in the bulk LAr. The triggers from these sources are emitted in the following decays.

^{39}Ar and ^{42}Ar/^{42}K The ^{39}Ar decays are used in the lifetime study in this thesis while it is dominant background in the DEAP-3600 experiment. The ^{39}Ar isotope has a Q value of 565 ± 5 keV and decays to the stable ^{39}K. The details about the production and decay of ^{39}Ar is given in section 3.3.

The ^{42}Ar is another rare isotope and a long-lived radioactive isotope of argon with a Q value of 599 ± 6 keV that undergoes beta decay with a half-life of 32.9 years through cosmic interactions. The daughter product of this decay is ^{42}K with a half-life of 12.36 hours and Q value of 3525 ± 0.2 keV, which also undergoes a beta decay to form a stable ^{42}Ca. However, the activity of ^{42}Ar is four times lesser than the activity of ^{39}Ar in magnitude, thus the low energy spectrum in DEAP-3600 is dominated by ^{39}Ar [1].

^{85}Kr The beta decay from ^{85}Kr isotope to stable ^{85}Rb isotope is another possible background in the ER recoil band within the LAr bulk. It has a half-life of 10.8 years [71], and a Q value of 687.0 keV [1]. The specific activity of ^{85}Kr depends upon the purification of the LAr, and no evidence of its existence is yet recorded in DEAP-3600 data. Moreover, for this analysis, the upper limit of ^{85}Kr is tested at different values to estimate the systematic uncertainty on the lifetime of ^{39}Ar, see section 7.3.8.1 for more details.

^{220}Rn and ^{222}Rn in LAr The ^{220}Rn and ^{222}Rn have the half-life of 55.6 s and 3.8 d respectively. These radioactive decays are from the activity of ^{238}U and ^{232}Th chains

which are the main sources of background from LGs and PMTs. However, the ER background is mainly contributed by the beta decay of ^{214}Bi and ^{208}Tl which have high Q values of 3270 keV and 4999 keV, respectively. The ^{222}Rn chain below ^{210}Pb with a half-life of 22.2 years is not considered in the background model since it does not reach the equilibrium in the dataset [1].

4.6.1.2 Backgrounds from different surfaces

The backgrounds from the TPB and acrylic surface are mainly contributed by the decay of ^{210}Pb which emits the beta and gamma rays [72]. Also, for LAr the daughter of ^{210}Pb isotope, ^{210}Bi with a Q value of 1162 keV is background in the ER region [1].

4.6.1.3 External sources

The complete summary of the external backgrounds is given in [1], and the dominant external components of the background model are briefed below.

Backgrounds in bulk AV, LG, and FB The beta and gamma rays in the LAr from the AV are emitted from the radioactive isotopes ^{226}Ra in the decay chain of the ^{238}U decay and ^{232}Th decay, the decay chains of ^{232}Th and ^{238}U are given in figure 4.8 and figure 4.9 respectively. The radon is eliminated from the stainless steel and freezes at the cold outer AV surface.

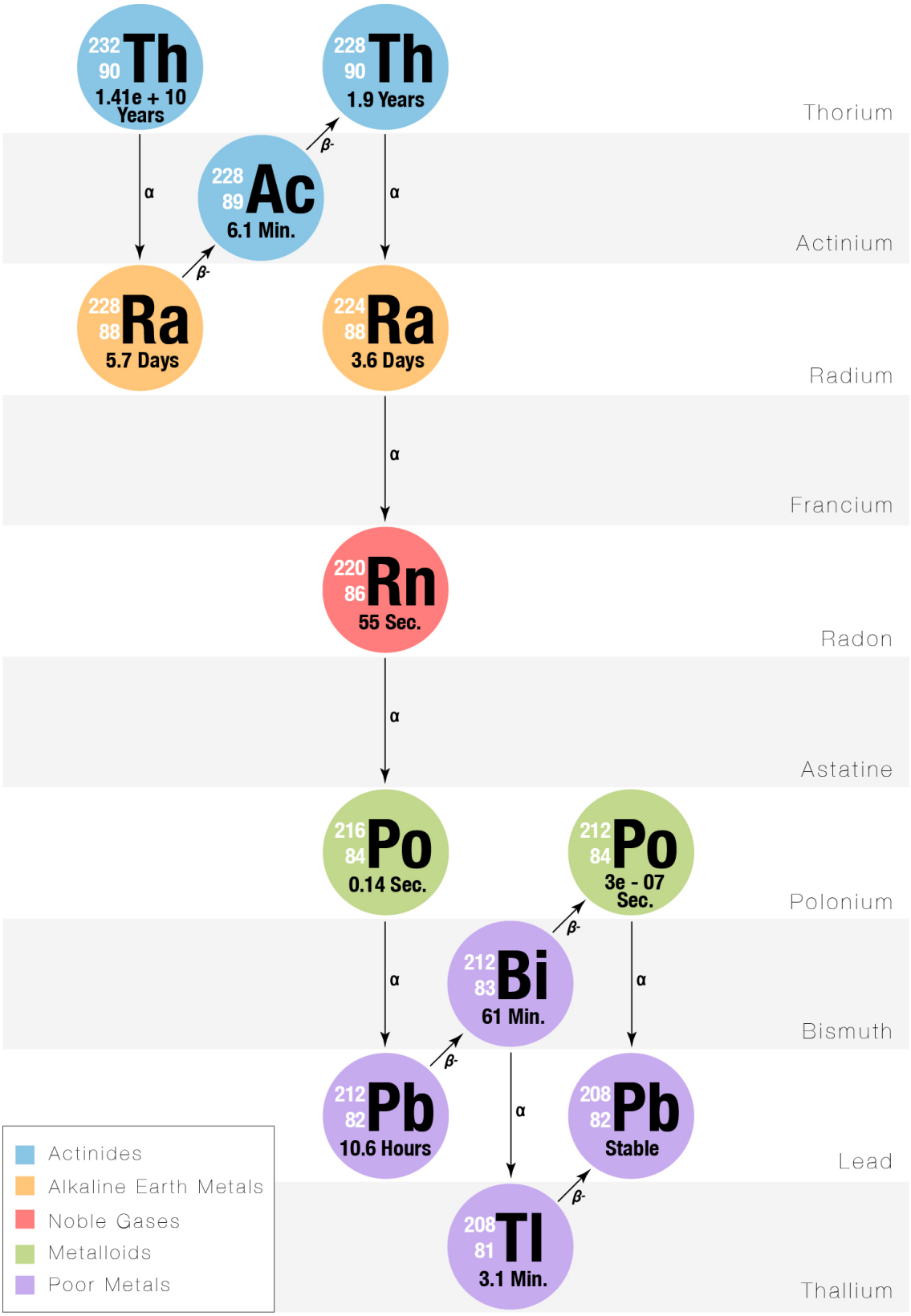

Figure 4.8: The schematic of ^{232}Th decay chain with half-life of nuclides [73].

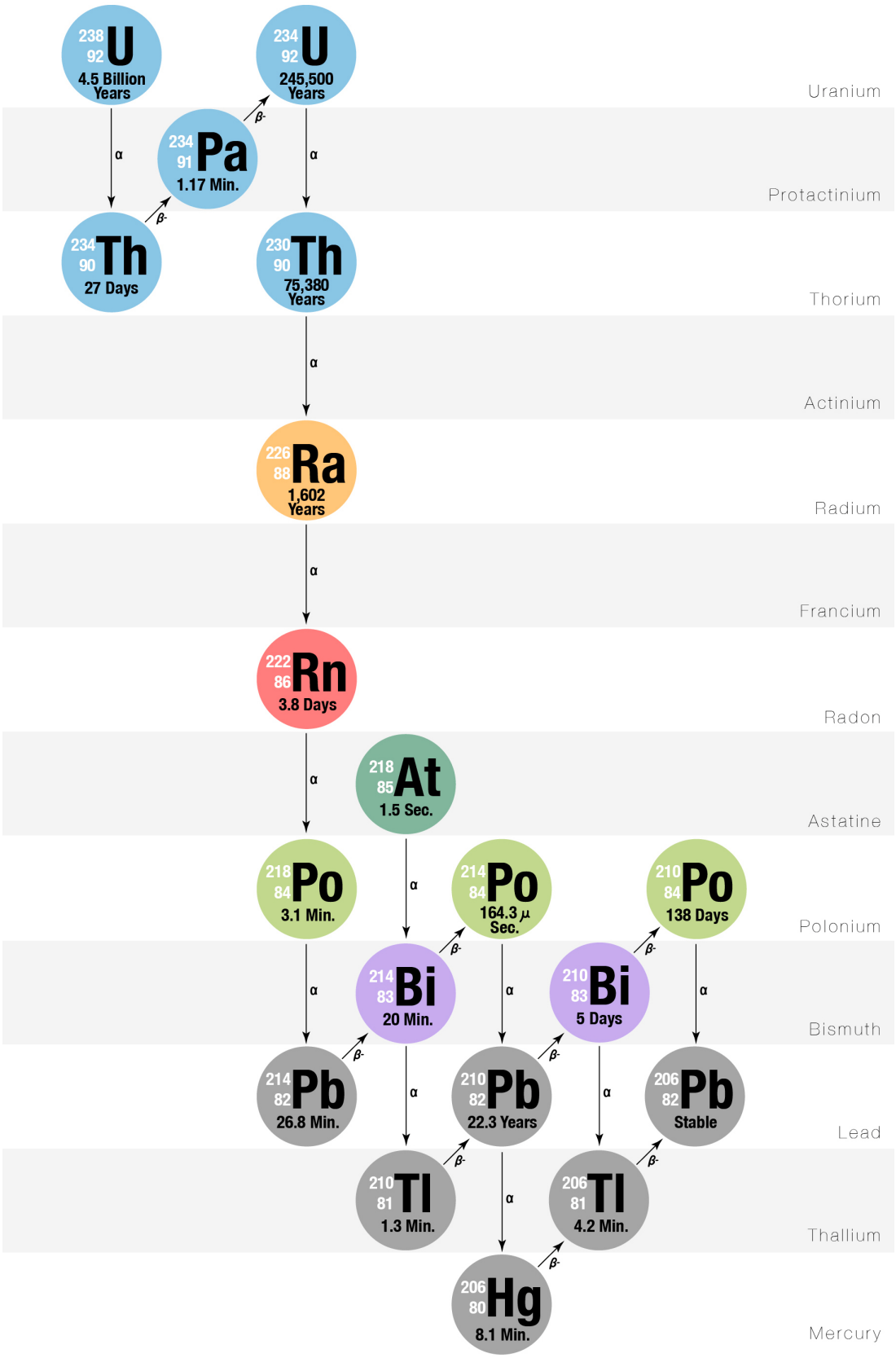

Figure 4.9: The schematic of ^{238}U decay chain with half-life of daughter nuclides [74].

The low energy gammas from ^{40}K in the LGs and PMTs generate 1.4 MeV gamma rays. Also, the gamma rays from the ^{208}Tl has an effect on the PE spectrum above 2.6 MeV. The LG, and FB can pass some low-energy gamma rays because of their geometry. However, the very low gamma rays like ^{210}Pb do not contribute significantly.

Backgrounds from PMTs and Stainless Steel Shell There are different components of PMT, glass, inner components, and mounting systems have been studied in detail for their background contribution and summed in the background model [1]. Neutrons are created from the PMT glass in (alpha,n) reactions, which can then be thermalized and captured by surrounded materials and emit gamma rays, for example, from ^{226}Rn, ^{232}Th, and ^{40}K. Moreover, the stainless steel shell is far from the active volume but has high-energy gamma rays which are also traced in the background model in the experiment. The summary of the backgrounds in the detector from all the different sources is given in the following table 4.2.

Table 4.2: The summary of the different ER backgrounds in the detector with the sources and corresponding isotopes creating the backgrounds.

Background Source	Isotopes
Internal Sources, LAr bulk	^{39}Ar, ^{42}Ar, ^{42}K, ^{85}Kr, ^{214}Bi, ^{212}Bi, ^{214}Pb, ^{212}Pb, and ^{208}Tl
LAr surface	^{210}Pb, and ^{210}Bi
External Sources, bulk AV, LG, and FB	^{214}Pb, ^{214}Bi, ^{210}Pb, ^{210}Bi, ^{228}Ra, ^{228}Ac, ^{212}Pb, ^{212}Bi, ^{208}Tl, and ^{40}K
PMTs and Stainless Steel	^{214}Pb, ^{214}Bi, ^{210}Bi, ^{228}Ac, ^{212}Pb, ^{212}Bi, ^{208}Tl, ^{40}K, and ^{60}Co

4.7 Prescaling in DEAP-3600

In the WIMP search, the electron recoils are background and it is not necessary to record the complete waveform information for all events. Therefore, only the timestamp information of every 99 triggers out of 100 triggers is saved, and the full waveform of every 100^{th} event in the electron recoil band is recorded in the disk, which is mainly beta decays of ^{39}Ar isotope. This reduction of file format in saved data is called Prescaling in the DEAP-3600 experiment which keeps the data files small and saves the disk space without losing all the information about the electron background triggers since the electronics would otherwise not support the high trigger rate from decay triggers of ^{39}Ar. In the current analysis, the effect of prescaling is corrected by multiplying the selected prescaled triggers by a factor of 100 to keep the statistics the same for the prescaled and non-prescaled triggers, more details for this will be discussed in chapter 6.

4.8 Current status and hardware updates

The detector was first filled with LAr in June 2016, and the first running period of the detector was from June to July 2016. A contraction of a cryogenic seal in the neck region allowed leakage of nitrogen from the high pressure in the nitrogen from within the steel shell which poisoned the argon in AV while penetrating into it. The liquid argon was thus boiled off and the detector was filled with liquid argon of mass (3279 $\pm$ 96) kg, and dark matter search data was taken in stable conditions from November 2016 to March 2020. The detector was emptied and warmed for hardware upgrades after three years of operation after this. The detector is being upgraded with the latest cooling tower and Pyrene coating on the inner neck region to prevent

the dominant neck backgrounds and make it dust background free. The physics data taken during the second fill of the detector is being analyzed in the experiment with the WIMP detection and is also used in the current thesis for the measurement of ^{39}Ar isotope as discussed in the following chapters.

Chapter 5

Rate algorithm and analysis variables

A rate algorithm is prepared to calculate the rate of any type of trigger with time for various analyses. The function describing the trigger rate within the selection cuts is developed in this chapter to measure the ^{39}Ar lifetime and evaluate uncertainty on the measurement from different parameters in the function. The data variables used in the DEAP-3600 experiment and the selection of the region of interest for the ^{39}Ar are also given in this chapter.

5.1 Rate algorithm

The trigger rates for any trigger type are calculated by taking the ratio of the total trigger counts in selected energy region passing data cleaning cuts to the total livetime after all the corrections applied for the time when the detector was not taking data, such that,

$$\text{Total trigger rate (R)} = \frac{\text{Total Trigger Count}}{\text{Total livetime}} \tag{5.1}$$

In DEAP-3600 data is recorded continuously on the timestamp information level, however, the rate algorithm in the lifetime analysis will typically bin the data by week. The algorithm is designed to plot the rate on a weekly bin basis since DEAP has more than 3 years of physics data for different analyses and considering the bin width of a week for filling rates results in enough statistics for the error estimation and statistics are too low to bin more finely. The algorithm defined above was then tested by calculating the rates of known calibration triggers, called periodic triggers which are given in section 5.4, and further validated and used to plot rates of ^{39}Ar triggers 5.7. Before coming to the details and usage of this algorithm for the trigger rate calculations for the periodic and ^{39}Ar triggers, a brief introduction to the data analysis variables used in the DEAP-3600 experiment is discussed in the following section.

5.2 Data variables in the DEAP

In the DEAP-3600 experiment, the main data is collected in waveforms which are the output of all the PMTs producing the current pulses of corresponding scintillation photon light observed in the detector. There is a remarkable amount of information present in these waveforms processed by a single trigger. The analysis of this data is done by using the different parameters and variables designed for extracting the useful characteristics for the triggers which are recorded whenever DAQ is triggered by any event, either through the physics processes like the decay of ^{39}Ar isotopes and interactions of WIMPs with ^{40}Ar nuclei or by the internal calibration triggers.

In this section, the variables used in the experiment are described along with their values for the purpose of selecting different types of triggers in physics data.

5.2.1 Photoelectrons (PE)

The PE parameter is the measure of the reconstructed charge which represents the total number of the PE contained in the scintillation light pulse. The PE value of each pulse in the waveform is evaluated from the property of a single photoelectron (SPE) for every PMT and corresponds to the number of detected photons in an event.

In data taking in DEAP-3600, there are two to three PMT calibration runs (about 10 minutes in length) performed daily using the AARF system (discussed in section 4.4.4). This system is made of acrylic fibers distributed uniformly near the ends of 20 (out of 255) of the LAr PMTs around the light guides across the AV. The end of these fibers has reflective aluminum; for AARF calibration runs 435 nm light is injected through these fibers which reflects off the end towards the closest PMT. The reflected light is partially observed by the PMT and partially redirects into the detector. The SPE variable is used to read out the average charge for PMTs, and then PE is calculated from the charge of each identified pulse divided by the PMT SPE charge. The PE spectrum of ∼24 hour-long physics data is shown in figure 5.1. The majority of triggers in DEAP-3600 are in the low fprompt region known as the electron recoil band.

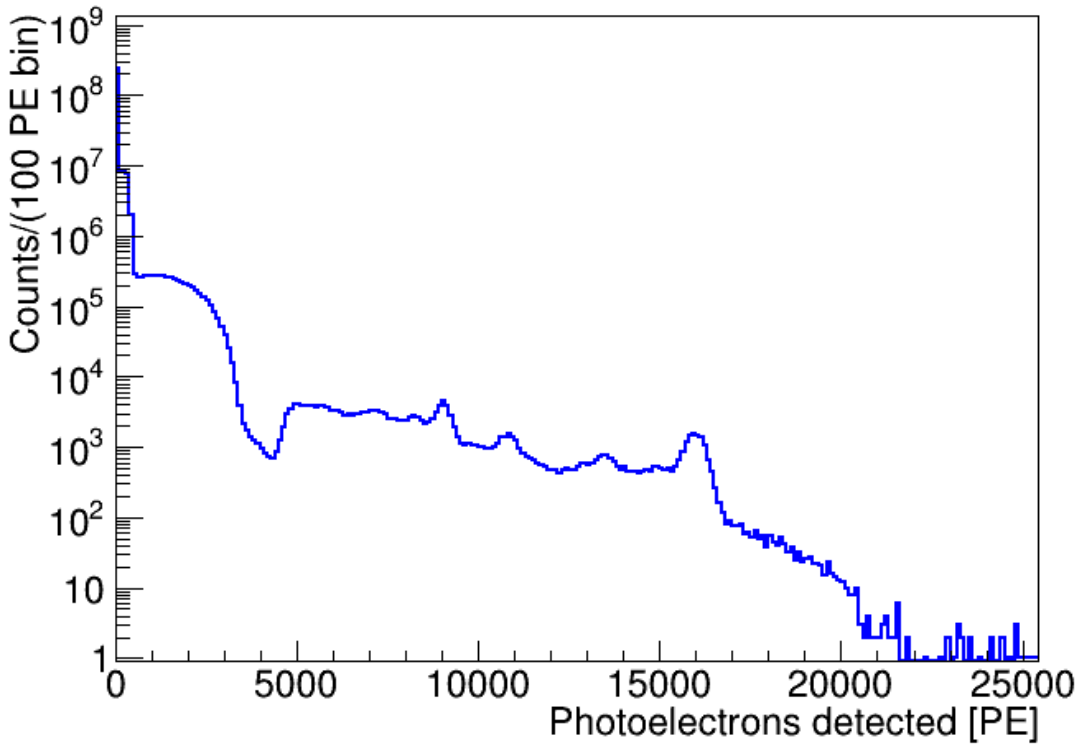

Figure 5.1: The PE spectrum of the physics data measured in the DEAP-3600 experiment. The region from ∼500 to 4000 PE is prescaled for the ^{39}Ar decays (the corrections for the prescaling effect are applied later for this analysis). The peak at ∼9000 PE shows the ^{40}K gamma decay with energy 1461 keV, the peaks at ∼11000 PE and ∼13500 PE in the spectrum are due to 1765 keV and 2204 keV gammas from ^{214}Bi decays, and the gamma decay peak for ^{208}Tl with energy 2614 keV is shown in the spectrum at ∼16000 PE.

There are two different energy estimators used in DEAP-3600, one is called qPE which is without corrections for PMT afterpulsing and late light which can lead to erroneous values of PE, and the other is called nSCBayes with afterpulsing corrections. The nSCBayes energy estimator was used in this analysis (and shown in figure 5.1). The use of this estimator is important to understand the energy response, and hence the light yield of the detector because the contribution from the late light pulses is removed for this variable while reconstructing data which results in the more

pure data. However, neither of these energy estimators accounts for the change in the light yield of the detector which is discussed in more detail in section 6.4.

5.2.2 fprompt

The fprompt is the PSD variable used in the DEAP analysis which is defined for each trigger as the fraction of the charge collected from all the LAr PMTs in the prompt window (or the pulse time, first 150 ns of a waveform) to the total charge of the trigger in the waveform (or the trigger time, over 10 μs of a waveform), such that,

$$\text{fprompt} = \frac{\int_{t_0}^{t_{150ns}} Q(t)\,dt}{\int_{t_0}^{t_{10\mu s}} Q(t)\,dt} \tag{5.2}$$

where t_0, t_{150} ns, and t_{10} μs are the beginning time, prompt time, and trigger time of the waveform, and Q(t) represents the charge quantity. The relative timing of the PMTs is calibrated with the help of fast laser sources which results in the overall time resolution of 1.0 ns [6]. The fprompt parameter is an excellent PSD variable to distinguish the electron recoils from the nuclear recoils and low-energy Cherenkov light in the liquid argon.

The example of a DEAP-3600 data waveform is shown in figure 5.2. The fprompt integration windows are highlighted in different colors where red is the 150 ns (prompt) window, blue is the 10 µs (wide or late) window and purple is the overlap of the two windows.

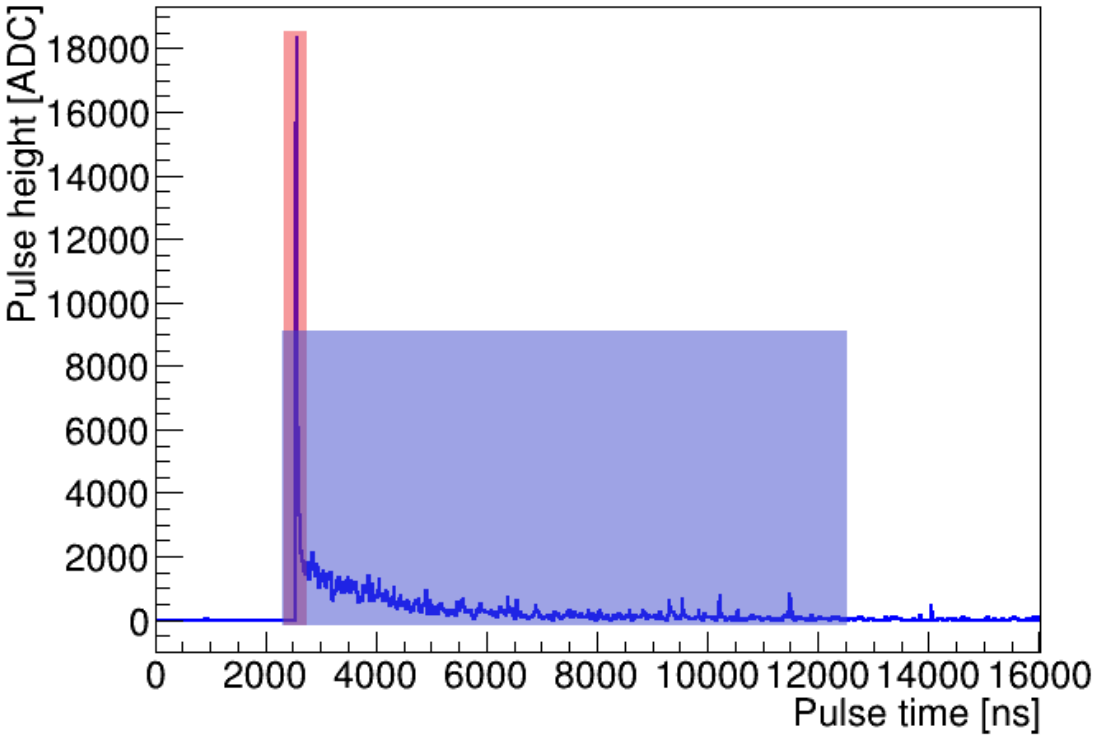

Figure 5.2: An example of a standard waveform from the DEAP-3600 experiment data with the fprompt integration windows overlaid. The prompt window can be seen in red, the wide window can be seen in blue, and where the two windows overlap can be seen in purple.

Also, the fprompt ratio together with the PE energy estimator can be used to build a two-dimensional parameter space in which the nuclear recoil band and electronic recoil bands can be identified separately as shown in the figure 5.3. The fprompt region selected for the ^{39}Ar trigger rate study is below 0.41, which is specifically taken to consider only the ^{39}Ar decay triggers only, and also reject the blinding region from the data as discussed in section 6.2.4.

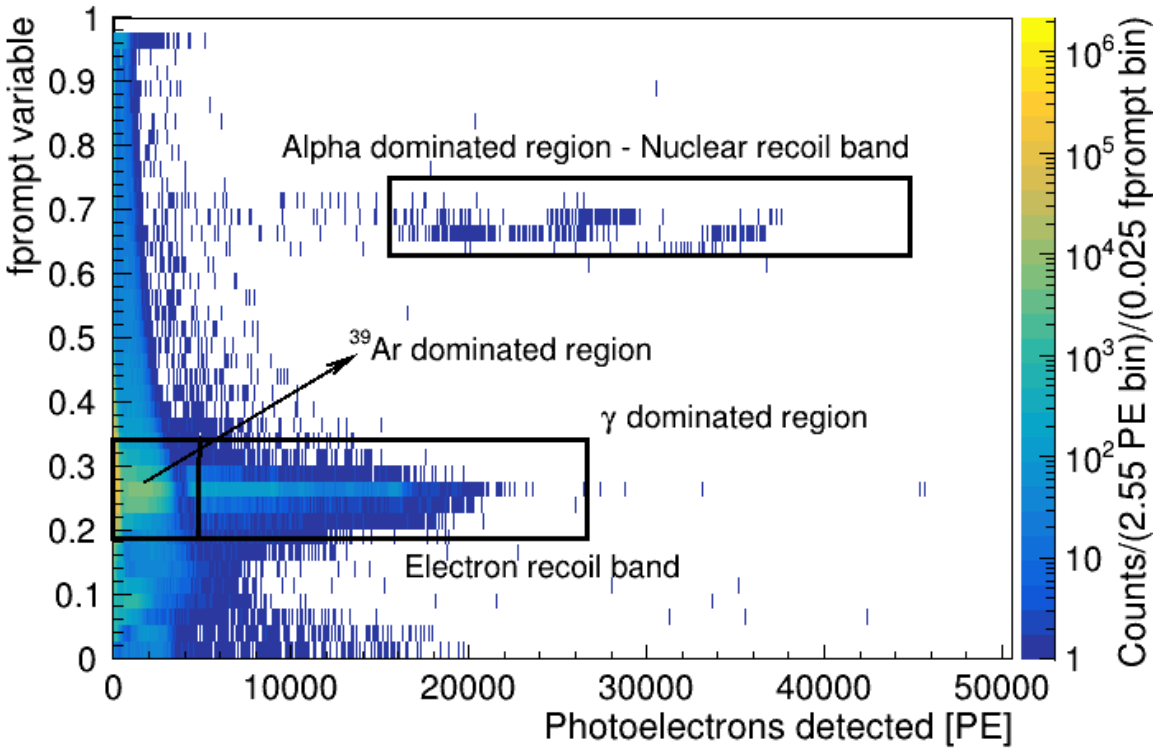

Figure 5.3: The 2D distribution of fprompt variable versus PE detected for a physics run which is an example of Pulse-shape discrimination in the DEAP-3600 experiment. Livetime and pileup cuts have been applied. The nuclear recoil band (at fprompt 0.70) and the electronic recoil band (at fprompt 0.30) are distinguished as shown.

5.2.3 Trigger selection cut variables

The overall trigger rate in DEAP-3600 is dominated by ^{39}Ar beta decays, but it also has contributions from beta, and alpha backgrounds, and some instrumental or non-physics triggers. Some sets of variables and cuts can be used to select the different trigger types from the physics data. For example, a certain set of trigger cuts are used to select the ^{39}Ar triggers and to reject these background triggers which are caused by the decay reactions of radioactive components present in and around detectors such as Uranium and Thorium decay chains, etc. in section 5.5.

The trigger rates for any trigger type are plotted by counting the triggers passing the set of cuts and the time passed while taking the measurement. These cuts are designed to reduce the backgrounds to the maximum level. The cut variables include the simple parameters which account for very low-level information such as charge and counting statistics and as well as parameters that use very high-level statistics utilizing fits, charge corrections, multivariate analysis, and machine learning. The next subsections contain the details of these cut variables used in the analysis.

5.2.3.1 Removal of non-physics triggers

The rejection of non-physics triggers from the physics data is performed with the use of two basic data-cleaning variable cuts. However, for the validation of the rate algorithm explained in section 5.1, the periodic triggers from the calibration sources are used as discussed in section 5.4. The variables to select non-physics triggers from the physics data are elaborated on in the following sections.

calcut The calcut variable is a bitmask variable used to reject the non-physics triggers. The designed flags with the calcut parameter decide if the triggers recorded are good to be included in physics analysis, or if it removes the bad triggers due to instrumental effects and inefficiencies in the DEAP-3600 DAQ system. There are different possible reasons why the triggers may be flagged to be not appropriate for analysis. These reasons are given in the table 5.1 below, with the corresponding values of bits and flags deciding the state of every single trigger.

Table 5.1: The list of all calcut bit masks used in trigger selection cuts in DEAP-3600 analysis. Smart QT (SQT) is an algorithm that is applied in the V1720 digitizers to encode waveforms.

Bit	Hexadecimal	Description
0	0x1	Any V1720 pulse had a bad baseline
1	0x2	Any V1720 pulse reached 0 ADC (saturation)
2	0x4	Failed to find a good calibrated trigger time
3	0x8	This is a PPG trigger[1]
4	0x10	Trigger is recorded soon after a PPG, could be noise trigger[1]
5	0x20	DAQ were running busy and suppressing readout of digitizers
6	0x40	Trigger/digitizers are out of sync
7	0x80	Trigger timestamps are appearing out-of-order
8	0x100	There are no digitizers in the trigger[2]
9	0x200	There are no digitizers in the trigger[2]
10	0x400	Trigger came from a non-physics trigger source
11	0x800	SQT info was used for a non-SPE-like pulse[3]
12	0x1000	SQT info was used for a pulse where the charge integral was truncated[3]
13	0x2000	SQT info was used for a pulse[3]$>$ 1000 pC
Cut Value	0x31f8	Removes any instances of bits 3, 4, 5, 6, 7, 8, 12 and 13

[1] Not good for physics analyses
[2] Generally due to pre-scaling
[3] Rather than ZLE

The standard value of the calcut variable used in the physics analysis (in bitwise hexadecimal notation) is 0x31f8 which removes the triggers matching the bits 3, 4, 5, 6, 7, 8, 12, or 13. These flags show the triggers such as a PPG trigger during which the DAQ was not calibrated correctly, or if the DAQ system was failing due to specific reasons. The benefit of having these defined flags in the variable design is that we can remove different kinds of physics/non-physics triggers that are sometimes causing the hurdle in the actual triggers. For example, the extra flag with bit 1 can be used to remove the triggers when the ADC value falls and hence no correct indication of

the energy of the trigger can be concluded.

dtmTrigSrc The dtmTrigSrc variable is a bitmask variable that identifies the triggers that are intentionally triggered and hence indicates the source of the trigger in the data. For every type of triggered event written in the data, this variable is added as a flag which shows if the recorded trigger is a trigger from an external calibration source or from some internal pulse generator, or if it is from the physics trigger contained in one of five different regions in prompt scale. The list of primary flags for this variable is given in table 5.2 below.

Table 5.2: List of dtmTrigSrc bitmasks used in trigger selection cuts in DEAP-3600 analysis

Bit	Hexadecimal	Description
2	0x2	Internal periodic trigger
7	0x40	Internal periodic trigger, following exponential distribution
8	0x80	External calibration trigger
11	0x400	Low energy, low fprompt trigger
12	0x800	Low energy, high fprompt trigger
13	0x1000	Medium energy, low fprompt trigger
14	0x2000	Medium energy, high fprompt trigger
15	0x4000	High energy trigger
16	0x8000	Minimum bias trigger
Cut Value	0x82	Removes any instances of bits 2 and 8

The bit-wise values currently used with this parameter are instances from bits 2 and 8. As explained in the table, these two-bit values correspond to removing events with the period or external calibration triggers. The internal triggers include the triggered triggers from periodic triggers used to calibrate the signal recording from the system. The external trigger corresponds to the triggers from the muon veto system in the DEAP experiment. The bit value 13 can be used for selecting the

^{39}Ar triggers from the physics data which corresponds to the medium energy and low fprompt trigger region from the physics data. As discussed in the section 4.7, the ^{39}Ar triggers fall under the electron background recoil region, and the triggers falling in this region are suppressed by a factor of 100 to reduce the data size. The prescaled triggers selected with this bit value are scaled up by a factor of 100 again to remove prescaling and get an actual number of ^{39}Ar triggers.

Thus to reject any non-physics triggers from the study, the calcut and dtmTrigSrc variables are used with the values, (!(calcut&0x31f8)) and (!(dtmTrigSrc&0x82)).

5.2.3.2 Removal of low energy background triggers, fmaxpe variable

The fmaxpe variable is designed to remove the low-energy backgrounds such as Cherenkov light triggers from the physics data. This variable is defined as the fraction of the charge measured by the PMT with the greatest charge to the total charge in the trigger. Thus, this variable is defined similarly to the fprompt variable except for the numerator here is taken as the maximum light seen by the single PMT in place of light seen by all the PMTs, moreover, this variable is correlated with the low energy triggers. The low energy light triggers contain a very amount of light observed by the few PMTs and maximum light always went through the single PMT. Chereknov events are localized within the acrylic and so tend to have one high-charged PMT.

Low energy triggers can be produced isotropically from within the LAr and from the inner surface of the AV like the decay of ^{39}Ar contains low fmaxpe value. The triggered events with mostly Cherenkov light are emitted from the PMT LGs or PMT glass with high fmaxpe value, this is because a trigger occurring close to the LG will result in most of the light going to a single PMT only, thus producing the high fmaxpe value. The fmaxpe cut variable with the upper limit at $\leq$0.4 is used in the ^{39}Ar trigger rate analysis. This is one of the standard sets of cuts used for the dark

matter search in DEAP. More details on the use of this cut for rejecting Cherenkov light are discussed in the section 5.9.

5.2.3.3 Removal of pile-up events

The pileup in the DEAP data occurs when two or more events accidentally occur in the same trigger window. The trigger rate in the detector is very high which results in a high pile-up of events. The rate of these pile-up events is more than 165 Hz as estimated from the ^{39}Ar triggered events with a total rate of 3300 Hz. There are different kinds of decay with different energies that can arise in the pile-up. Therefore, many variables are designed in the collaboration to remove these pile-up events which include subeventN, numEarlyPulses, deltat, and trigger time. However, for the lifetime study of ^{39}Ar decays no pile-up cut variable is used, only the deltat cut variable (section 5.2.3.3) is used to verify the rate algorithm and fit output considered in section 6.6, and 7.1.3 respectively. These cuts are used to select the single low-energy Cherenkov triggers which are included as an important pile-up in the analysis as discussed in section 5.9. The definition and role of these different variables are discussed below.

subeventN The subeventN variable is designed to identify the number of sub-peaks in a waveform signal in the trigger window of 16 μs. This variable is the yield of a Multi-trigger processor in the DEAP-3600 analysis code, which scans through the full waveform to look for the multiple pulses generated from a coincident trigger. It can be used with the various integral values which represent the number of interactions or pulses found in the waveform in the same trigger window, however, it is purely made to select only the triggers with single pulses in the summed waveforms. For example, subeventN=1 implies the single big pulse signal in the waveform. Similarly, the

subeventN variable with values 2, 3, etc. indicates the double, triple, etc. coincidence decays in the waveforms with some timing and energy conditions in the waveforms. An example of two distinct sub-triggers in the waveform is shown in figure 5.4.

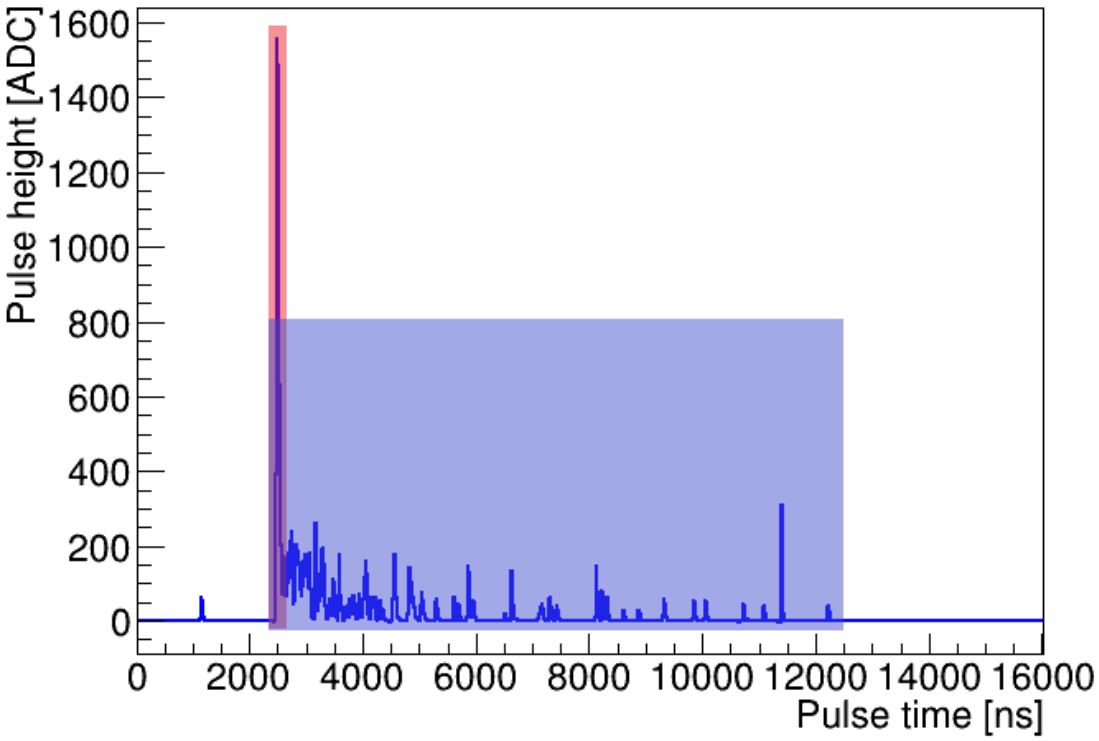

Figure 5.4: An example of two distinct sub-triggers in the waveform from DEAP-3600 data. The prompt window can be seen in red, the wide window can be seen in blue, and where the two windows overlap can be seen in purple.

numEarlyPulses The numEarlyPulses variable measures the number of pulses and sub-pulses present in the pre-trigger region of the trigger window before the initial pulse of the waveform. When the trigger rate is very high like in DEAP-3600 there is always some possibility of leaking of the previous trigger light in the next trigger window which sometimes triggers the DAQ and gives rise to pulses in the pre-trigger window or this extra energy would be added in the second trigger that causes the

deformation of energy of the trigger. However, sometimes the little deformation in the energy spectrum of any observed trigger can also generate these early pulses because only a portion of the total charge is measured hence they are not always the pile-up of decays.

The triggers passing this cut variable are calculated from the charge processor. Similar to the subeventN variable, this can be used with various integral values indicating the number of sub-pulses found in the pre-trigger window of 1600 ns of the waveform, before the full pulse trigger. There are various values of early pulses tested at the experiment level, and it is recommended to use triggers with a maximum of 3 early pulses in the pre-trigger window, this number is based on the trigger topologies and the charge distribution of the triggers. An example of the waveform flagged by numEarlyPulses greater than 1 can also be seen in figure 5.4.

deltat The deltat variable is the difference in the timestamp of trigger time for the current trigger to the precedent trigger. This variable is used to remove the triggers which occur very close to each other in time. As for the early light issue, if the two triggers occur very close in time there would be a high chance of leaking of late light of the first trigger in the integration window of the next trigger, which outputs a pile-up spectrum otherwise. The following trigger could be either of the same type or any other type such as periodic, calibration, or muon veto trigger in addition to physics. Also, even without leaking late light the trigger system itself has some dead time, and so isn't fully efficient for short deltat values.

The DTM clocks in DAQ are working at a periodicity of 16 ns. Thus, the minimum time difference between any two triggers is 16 ns. Moreover, the deltat distribution of successive physics triggers can also be inferred from the dominant source activity like the decay of ^{39}Ar which gives the exponential distribution rate

for deltat. Due to the effect of additional internal, external, and periodic triggers operating at different rates and piling up offered by the after pulsing of PMTs, the exponential distribution of deltat no longer remains exponential below deltat with a value of 20 μs which is due to piling up from triggers happening in rapidly after one another. Various studies in the experiment suggested that a minimum cut value of the deltat variable at 32 μs is needed to remove any pre-light from the previous trigger.

eventTime The trigger time parameter measures the time of the first main pulse peak trigger in the waveform. The studies show that the typical well-calibrated trigger in the DEAP-3600 DAQ occurs around 2500 ns, thus a trigger time cut between the time values between 2250 to 2700 ns is suggested to select good physics triggers. The lower cut at 2250 ns is the pre-trigger pile-up cut which basically means removing the tail of the previous triggers which have been missed by other pile-up cuts like numEarlyPulses and deltat cut. The upper time limit at 2700 ns is defined to remove any post-trigger pile-up cut. The function of trigger time is strongly correlated to the subeventN cut.

The values used for these data cut variables are further mentioned in the upcoming sections for selecting different trigger types, periodic triggers, ^{39}Ar decay triggers, or triggers corresponding to low energy Cherenkov light, while calculating their trigger rates.

5.3 Trigger time cut from deltat variable and dead time calculations

The deltat cut variable is used to remove any photoelectrons which might be contributed from the scintillation light of the previous trigger in the detector, and the triggers which may have occurred very close in time. This cut is included as a cross-check of the trigger rate calculations for different trigger types, periodic and ^{39}Ar decays. To account for the triggers removed by this additional cut, an equal amount of dead time is included in the livetime calculations for plotting trigger rates precisely. The dead time corrections are determined in the algorithm (5).

As mentioned in the section 5.2.3.3, the deltat cut at 32 μs scans over all the triggers in the data file and removes the triggers where the time difference between two consecutive triggers is less than 32 μs such that if the trigger time of the second trigger is less than 32 μs from its prior trigger. The cut value for the deltat variable is particularly selected from the understanding of the hardware DAQ system, the minimum cut value at 32 μs is long enough to remove pre-light irrespective of any trigger type in the detector.

The dead time, Δt_{dead} with the introduction of a deltat cut value, Δt_{cut} is evaluated for any run number in the physics data by looping over each and every trigger in the data without making any prior cuts and adding their deltat (Δt) value.

Algorithm 1 Algorithm to calculate the dead time (Δt_{dead}) for any deltat cut (Δt_{cut})

```
if Δt ≤ Δt_cut then
    Δt_dead += Δt
else
    Δt_dead += Δt_cut
end if
```

The corrected livetime, L_{corr}, is calculated by subtracting the dead time, Δt_{dead}, determined in the algorithm (5) from the real-time of any run number, L, such that,

$$\text{Corrected Livetime}(L_{corr}) = L - \Delta t_{dead} \tag{5.3}$$

This corrected livetime is used to calculate the trigger rates for the periodic triggers which are discussed in the sections 5.4, and trigger rates for ^{39}Ar decay isotopes triggers after making corrections to the energy based on the response and light yield of the detector, refer to the following section 6.6 for more details.

5.4 Rate of periodic triggers

The rate algorithm from equation (5.1) is authenticated from the calibration triggers in the physics dataset. The calibration triggers used for the verification are periodic pulse triggers which are injected into the trigger system of DAQ to monitor the timing information of the digitizers and recorded data to maintain the synchronization of DTM and all PMT channels. These pulses are added to the system regularly at the frequency of 40 Hz, and the output pulses are prescaled with a factor of 40, hence only one out of the 40 waveforms are saved in the database and system. The result of the rate algorithm should return the periodicity of 1 Hz for these triggers.

The internal periodic triggers can be extracted from the physics dataset using the dtmTrigSrc variable (see section 5.2.3.1 for details) with a bitmask value of 2 (as indicated in the table 5.2), and since there is a prescaled factor of 40 while recording these triggers, therefore an additional cut variable, dtmTrigOut is used to select these triggers. The dtmTrigOut variable results in the trigger output of different triggers in the DAQ system. Thus, the triggers which are passing the data selection cuts,

1. (dtmTrigSrc&0x2)

2. (dtmTrigOut&0x40000000)

are used to calculate the rates of these periodic triggers. The measured number of periodic triggers, N, in the physics run numbers passing dtmTrig cuts are then normalized by the corresponding livetime information, L, in order that,

$$\text{Periodic trigger rate} = \frac{N}{L} \tag{5.4}$$

The calculated ratios hence rates of these triggers are plotted in the weekly bin basis as presented in figure 5.5, such that each data point in the figure shows the rate of periodic triggers in one week of the dataset. The calculated periodic trigger rates are constant over time as expected since these triggers are generated for calibration purposes with a known constant frequency of 40 Hz.

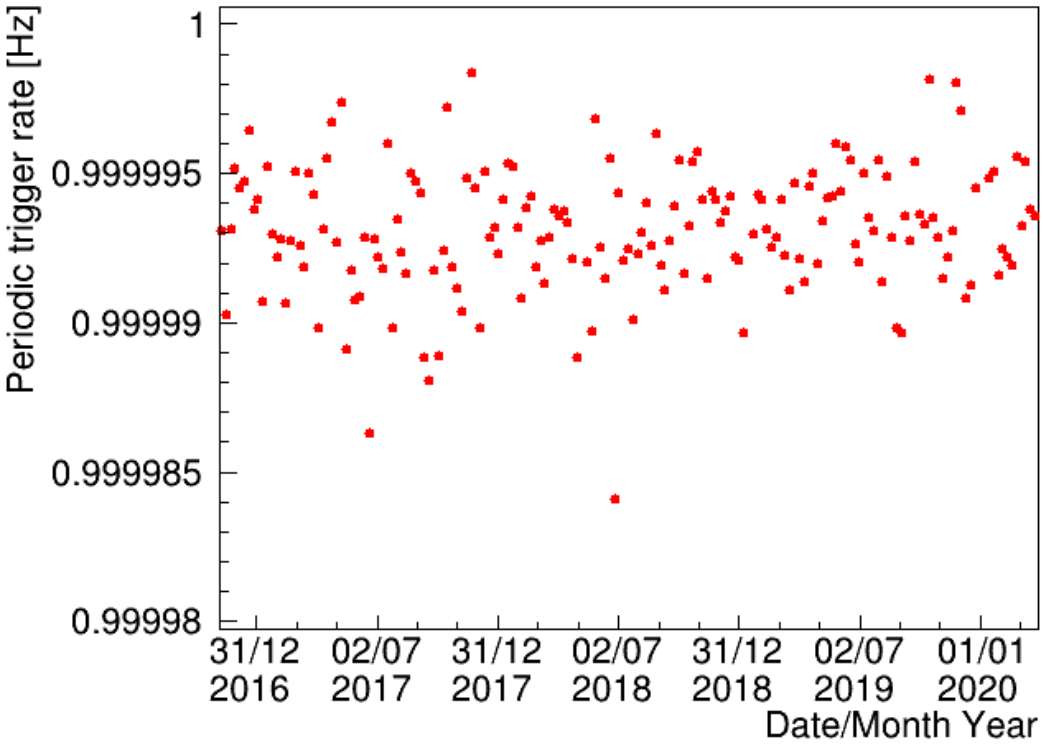

Figure 5.5: The rate of periodic triggers in weekly time bins, each point in the graph represents one week of the periodic data rate introduced in the DAQ system for the calibration of the digitizer time information.

The one-dimensional distribution of the calculated periodic rates in the above figure is shown in figure 5.6. The measured rate of periodic triggers from the rate algorithm is 1 Hz on average and is very precise as expected.

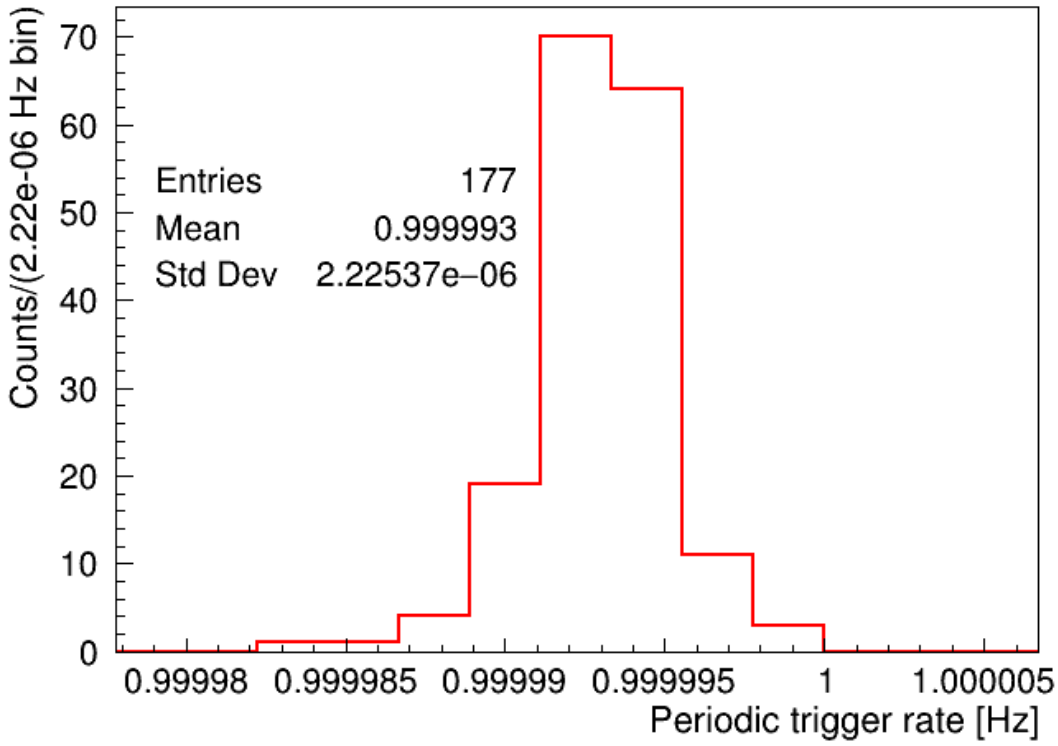

Figure 5.6: The one-dimensional distribution of the rate of periodic triggers. The mean value of the distribution is 1 Hz which signifies the precise measurement of rates by the equation (5.4). The width of the distribution is 2.2E-06 Hz which shows a very small spread of calculated periodic trigger rates.

The trigger rate calculations for periodic trigger type are also done by including an additional deltat cut at 32 μs to test the dead time calculations explained in section 5.3. The periodic trigger type is non-random, and its frequency at 1 Hz is already known from the trigger settings. If the deltat cut is added with the cut value at 32 μs, it will reject the periodic triggers where the trigger time difference between the two successive triggers is less than 32 μs, it will return $N_{\Delta t}$ number of periodic triggers, however, an equal dead time can be removed from the livetime corresponding to these removed triggers, such that periodic trigger rate will be 1 Hz again if evaluated from

the total periodic triggers passing cuts and corrected livetime, L_{corr}, moreover,

$$\text{Periodic trigger rate with deltat cut } = \frac{N_{\Delta t}}{L_{corr}} \tag{5.5}$$

The comparison of the calculated trigger rate for periodic triggers without and with a deltat cut after making dead time corrections is conveyed in figure 5.7.

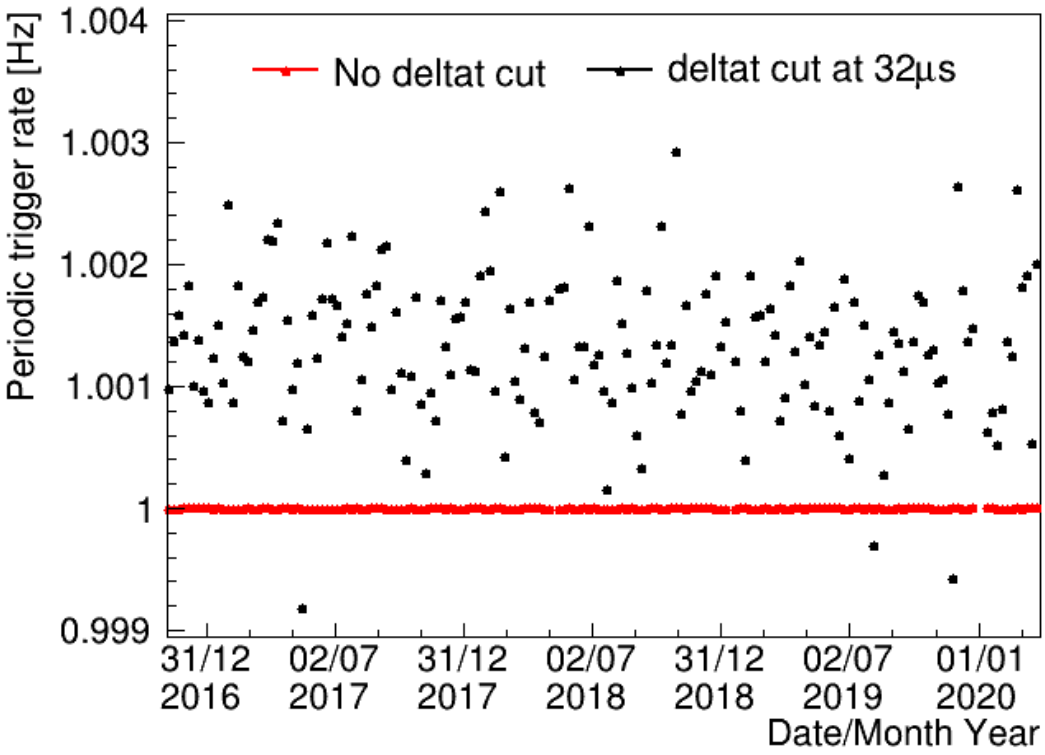

Figure 5.7: The periodic trigger rates calculated for the full dataset without and with using a deltat variable, trigger time cut at 32 μs to examine the dead time calculations from the algorithm (5) in the study. The measured trigger rates with the additional deltat cut value are consistent with calculations from no deltat cut within 0.2% of residuals from the expected rate of 1 Hz.

5.4.1 Residuals of periodic trigger rates for very high trigger time cut values

The periodic trigger rates are analyzed with the deltat cut varying from 32 μs to 500 μs. The measured trigger rates are constant over time but there are some small residuals recorded in the calculated rates which summed up and hence increased with the increment in the deltat cut, especially for the very higher values. These residuals are recorded after applying the dead time corrections to the real livetime information. The residuals of the average periodic trigger rates calculated with different deltat cut values from the expected trigger rate of 1 Hz are presented in figure 5.8. The error bars on the residuals are from the spread in the one-dimensional distribution of the evaluated trigger rates.

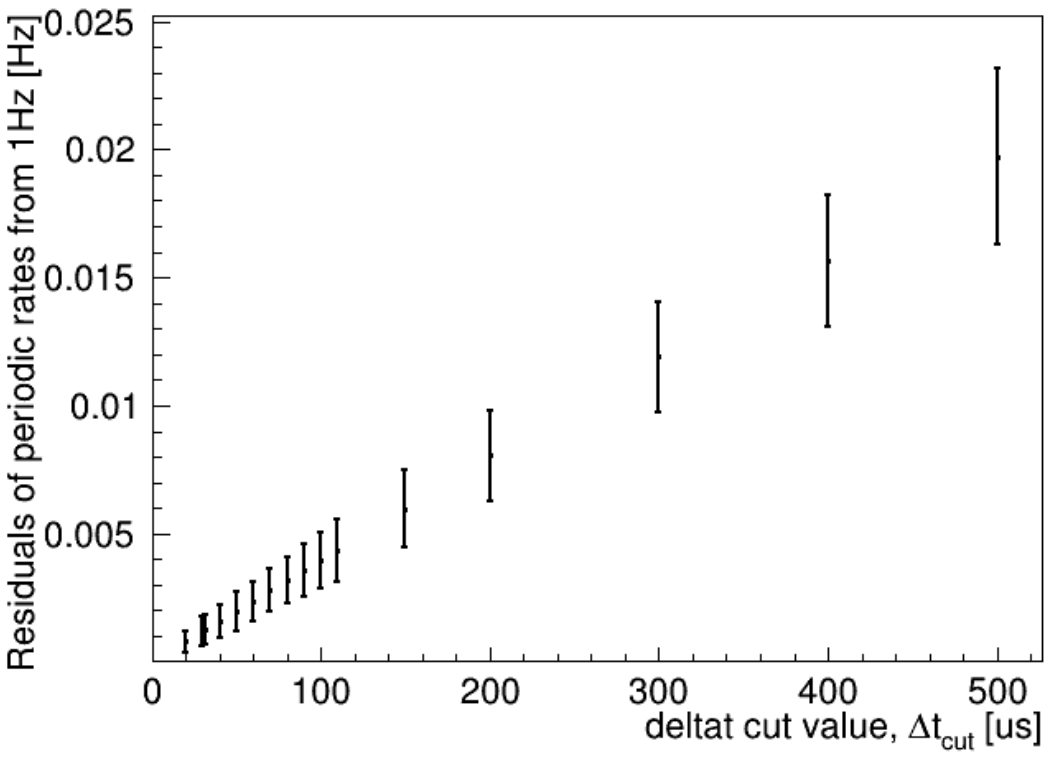

Figure 5.8: The residuals of the periodic trigger rates from the expected rate of 1 Hz are plotted as a function of different deltat cut values. The increase in the residuals indicates systematic uncertainty in the deltat variable for higher trigger time cut values. Moreover, the residuals are less than 0.5% for the deltat cut less than and equal to 110 μs which is used as a cross-check in the study.

The deviation seen in the rates is yet unexplained. This issue could be explained with the biasing of the data for a very long deltat cut value which selects the two consecutive triggers which are very spaced such that a large of fraction data is removed from the analysis. For example for a deltat cut at 500 μs, there is only 20% of total data available after this additional cut. The other possible reason could be due to a systematic uncertainty associated with the deltat variable that adds up for the longer deltat cut values. The deltat cut suggested at 32 μs has a very small residual which does not affect the results from the present analysis. Therefore, the deltat cut at 32

μs is used for the nominal result for the ^{39}Ar trigger rate analysis. For the consistency test of the calculated trigger rates and lifetime measurement, the deltat cut up to 110 μs is used since the residuals are again very small with a value less than 0.5% for this cut limit.

Therefore, plotting the trigger rates for periodic trigger type verifies the technique adopted in the rate algorithm which is further used for the investigation of rates of ^{39}Ar triggers in the next sections.

5.5 Cut selection for ^{39}Ar triggers from data

The basic low-level cuts, and ^{39}Ar selection region cuts used in the study of lifetime measurement are,

1. (!(calcut&0x31f8))
2. (!(dtmTrigSrc&0x82))
3. fmaxpe$\leq$0.4
4. fprompt$\leq$0.41

Only low-level cuts are used for the rejection of non-physics and noise triggers so that more data, hence, statistics can be taken into study. However, to reject any type of systematics which could have occurred from the prescaling and saturation in the physics dataset, a properly defined energy region of interest is used. The process of selecting the ROI for ^{39}Ar analysis is given in the section 5.6.

5.6 Selection for ROI from energy scale

In addition to these data cleaning cuts discussed in section 5.5, the cuts are used with the PE scale for the selection of the ROI. The only part of the full PE spectrum of the physics data in DEAP-3600 (as shown in the figure 5.1) is 700 to 1200 PE to neglect the systematic uncertainties in the dataset. The highlighted energy ROI for the study is given in figure 5.9. The lower limit at 700 PE is selected to reject any systematic due to prescaling effect of the trigger settings (see section 4.7 for details). The upper bound for the PE scale is selected to reject the systematic from the saturation of the ^{39}Ar decay triggers in the trigger system which are discussed in the section below.

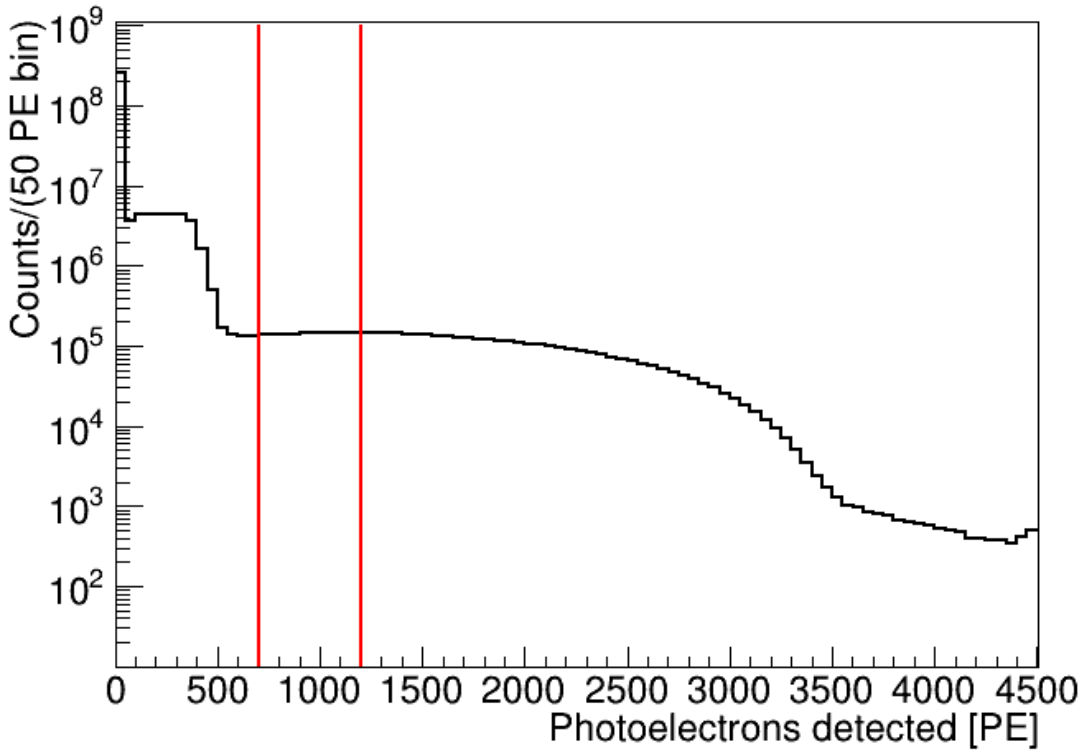

Figure 5.9: The PE spectra for the ^{39}Ar region from 0 PE to ∼4500 PE in the physics run. The ROI region is shown within red lines from 700 to 1200 PE. The lower limit of 700 PE is selected to neglect systematic prescaling in the trigger system. The upper limit at 1200 PE is selected to remove the systematic from the saturation of energy.

5.6.1 Saturation of energy in ^{39}Ar region

The saturation of trigger energies stands for the condition when the observed energy of the scintillation light is underestimated by any of the channels in the trigger system because of the baseline settings of the DAQ. As discussed in the section (4.5.3), the waveforms of the scintillation light are recorded by measuring its deviation from the baseline voltage in ADC scale. The baseline for recording the scintillation light is set to ∼3980 ADC since it was expected at the beginning of the experiment that the magnitude of the recorded light would not go beyond this baseline threshold.

However, in reality, there are some data pulses recorded where the energy released by the scintillation light in the decay of ^{39}Ar isotope is certainly above the fixed baseline voltage, and hence the recorded energies corresponding to these pulses are underestimated. Therefore, the PE calculation for these clipped ^{39}Ar decay triggers is not correct. To avoid this effect of the clipping in the ^{39}Ar triggers, a comprehensive study of the calcut variable is performed.

The baseline information and length (in ADC scale) of the pulses in the waveforms of DEAP-3600 data can be easily retrieved from the database using the calcut variable. The extra flag with bit 1 is used with the standard value of the calcut variable (calcut&0x31f8) to separate the ^{39}Ar triggers where the energies were saturated during data collection, such that the value of the calcut variable to select these triggers is (calcut&0x31fa). The PE distributions of the saturation decay triggers are further used to select the upper limit for the ^{39}Ar energy spectrum in the analysis. In figure 5.10 an example of the PE scale for triggers for different calcut values is presented. The triggers passing the standard calcut value are given in blue color, and triggers failing the standard calcut variable are mainly electronic noise, and hence non-physics triggers are given in deep blue color. The triggers failing the calcut variable with an extra saturation flag are shown in the red color which dominates the tail part of the ^{39}Ar beta decay spectrum. The selected ROI for the study is given in the green lines.

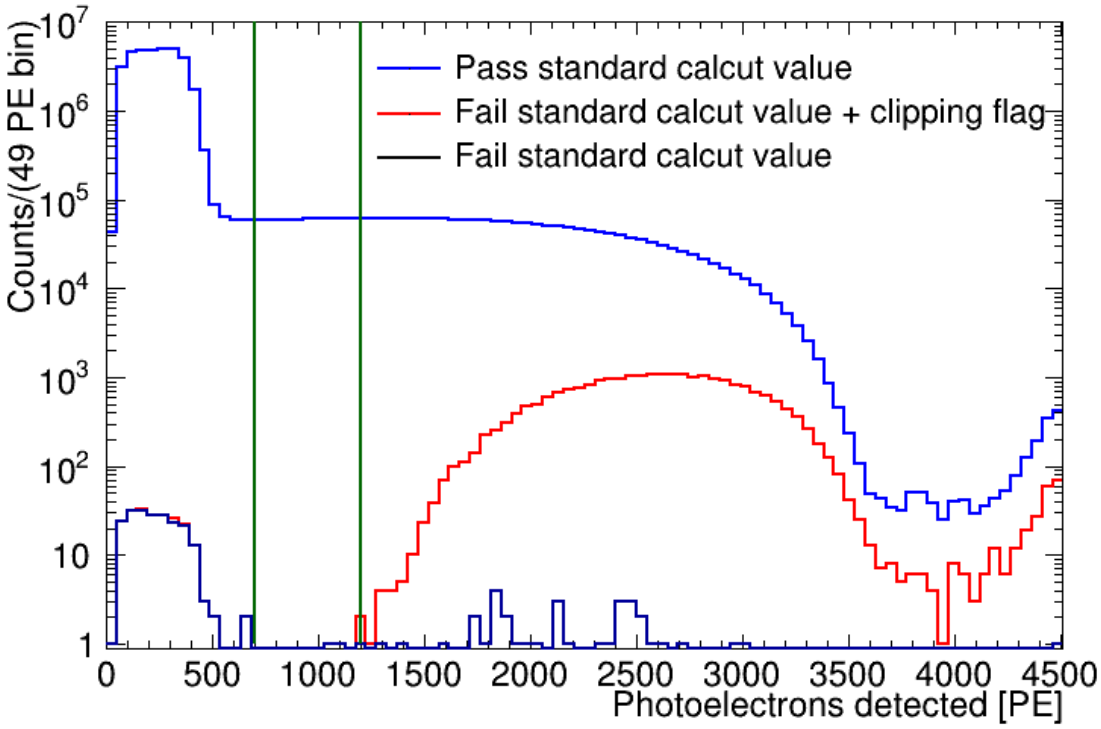

Figure 5.10: The PE distribution of triggers passing and failing different calcut bitwise values. The triggers passing and failing the standard calcut value, (!(calcut&0x31f8)) and (calcut&0x31f8) are given in blue color, and deep blue color respectively. The triggers failing the standard calcut value plus the extra clipping flag, (calcut&0x31fa) are shown in red color and present mostly at the end of the spectrum. The ROI selected for the study is given by the area within two green lines.

Thus, the best suitable ROI selected for the study rejecting any possible known systematic from the detector trigger settings, the two-dimensional space of fprompt and PE is highlighted in the figure 5.11. In addition to the basic low-level cuts mentioned in the section 5.5, the extra cut value for the energy selection, 700 $\leq$ PE $\leq$ 1200, is applied to the physics data recorded in run numbers for the taking the good sample of ^{39}Ar decay triggers for the lifetime study.

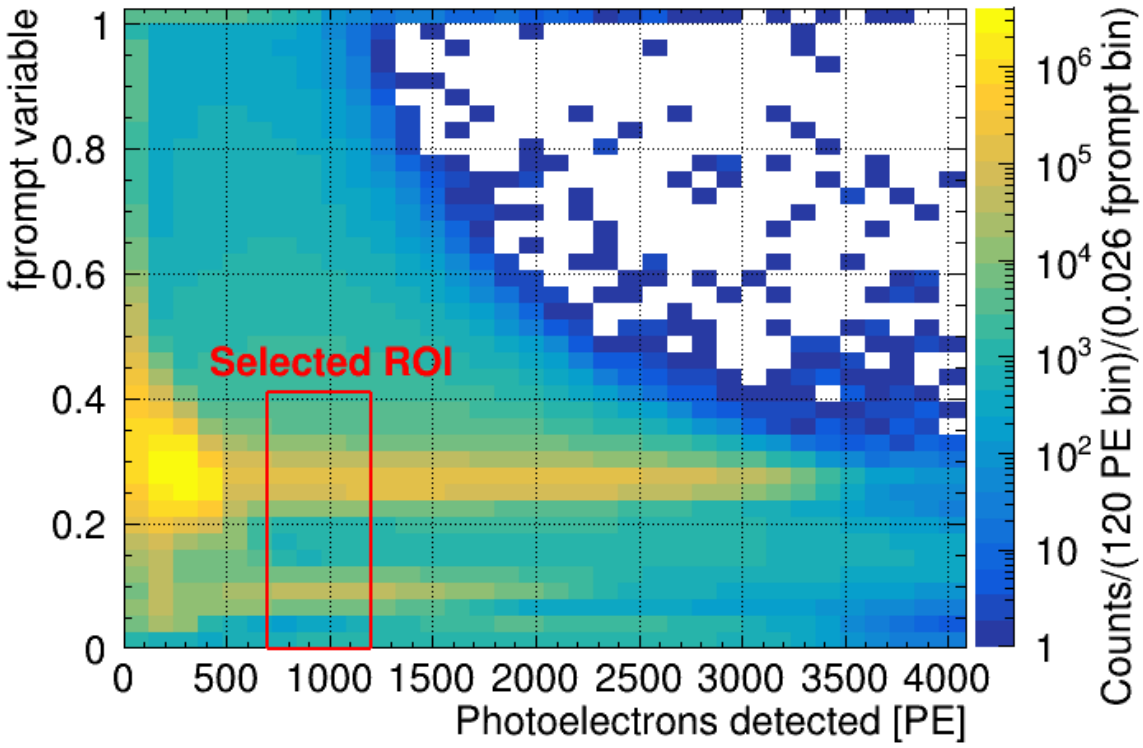

Figure 5.11: The ROI selected for the study highlighted in the red box presented in the two-dimensional distribution of fprompt variable versus detected for a physics run.

The band at low fprompt is from pile-up events, and it is included in the analysis to avoid uncertainty related to cut efficiency.

5.7 Rate of ^{39}Ar triggers

The lifetime for the decay of ^{39}Ar isotope is calculated from the physics data by fitting the rate of these triggers passing the data cleaning cuts (given in the section 5.5) in the selected suitable ROI where the detector systematics and backgrounds are negligible to affect the results. The fit model used in the study is discussed in section 5.8. The ROI is selected to include only the prescaled triggers (see section 4.7) from

ER band in the study, however, there is always some rare probability of non-prescaled triggers leaking into the ROI. Therefore, the total triggers in the ROI can be written as,

$$\text{Total } ^{39}\text{Ar decay triggers in ROI} = \text{NP} + \text{P*F} \tag{5.6}$$

where NP is the number of the non-prescaled triggers which are the low-energy triggers just before the prescaling region, P is the number of triggers that fall under the prescaling region, and F is the correction factor applied for the prescaling so that the same statistics will be kept for the trigger calculation. The triggers in the low fprompt with medium energies are prescaled by the factor of 100, thus the correction factor, F is simply 100. Also, the ROI for the study is selected such that we will have a negligible contribution to these low-energy triggers however for the exact number of the triggers, a little contribution was added.

The prescaled and non-prescaled triggers are selected separately using the following cuts,

1. ((dtmTrigSrc&0x1000) $>$ 0) $\Rightarrow$ Prescaled triggers
2. ((dtmTrigSrc&0x1000) $<=$ 0) $\Rightarrow$ Non-prescaled triggers

Thus, after using the data cleaning cuts on the data, two additional cuts are used to distinguish the ^{39}Ar triggers that fall in the prescaled region (low fprompt and medium energy) and non-prescaled region.

Also, a little variation in the energy response of the detector over time (discussed in section 6.4.1) caused one more correction to the calculation for the trigger rates of ^{39}Ar decays. The trigger rate is calculated on run by run basis after this correction and plotted on the weekly bin level. Moreover, the details for the trigger calculations

are given in the chapter 6, and systematic studies for the measurement of a lifetime from the calculated trigger rates are given in chapter 7.

5.8 Decay fit equation derivation for ^{39}Ar

In this section of the thesis, we will determine the decay fit model to fit the calculated trigger rates of ^{39}Ar to measure the lifetime of this isotope from the DEAP-3600 dataset for a selected region of energy (see section 5.6 for more details). There are different contributions included in the fit model which account for the single ^{39}Ar triggers and pile up of ^{39}Ar events which other low energy events in the same energy region. The low-energy triggers possible in the DEAP-3600 detector are as follows.

5.8.1 Low energy triggers in ROI

The low energy part of the DEAP-3600 physics data spectrum contains mainly the following types of triggers,

1. The very low energy triggers are not detected by the detector because the threshold of the detector is 15-20 keVee
2. The low-energy triggers that are detected and recorded by the detector
3. The triggers correspond to decay of ^{39}Ar nuclei
4. The triggers correspond to decay of ^{85}Kr nuclei
5. The triggers which correspond to the other backgrounds in the electron recoil region
6. The noise triggers or other non-physics triggers occurring in the detector electronics (if any)

In addition to the decay triggers of ^{39}Ar, the low energy part of the spectrum from DEAP data (as shown in figure 5.1) also consists of a coincidence of ^{39}Ar with itself and any other trigger type. This is due to the high rates of the scintillation light triggers observed in the large target mass. The contribution of coincidence of ^{39}Ar decays with itself and low energy Cherenkov triggers are the dominant ones from all the pile-up. However, for the precise measurement of the ^{39}Ar lifetime, the pile-up of ^{39}Ar decays with other low-energy triggers are studied in the detail.

To derive the fit function for the lower energy triggers in DEAP, let us start with the trigger rates (R) at the lower energies (E) which can be written in the following equation,

$$\frac{dR}{dE} = \sum_i A_i * \frac{dR_i}{dE} \tag{5.7}$$

where i represents the different types of triggers and A_i is the initial activity.

As discussed above in section 5.6, the detector systematic and DAQ response results in us choosing the subpart of the ^{39}Ar decay spectrum with energy range 700 to 1200 PE as ROI, where the response of the detector is well understood for the lower energy region. Therefore using this region of energy as the stable ROI for the lifetime study, the equation for the trigger rates in the low energy can be written as,

$$R(t) = \int_{E_l}^{E_h} (\frac{dR}{dE}) dE = \int_{E_l}^{E_h} \sum_i (A_i * \frac{dR_i}{dE}) dE \tag{5.8}$$

where, R(t) is the rate of triggers observed at time t in the selected energy window, and, E_l and E_h are the lower and upper bounds for the selected energy region. This energy ROI also rejects any very low energy trigger which is triggered by the detector or not detected at all. The triggers in this energy region are occurring from

^{39}Ar decays, ^{85}Kr decays, and some little contribution of backgrounds and triggers which corresponds to the decay of ^{39}Ar piled up with any other decays.

Activity of ^{85}Kr in the DEAP-3600 data The ^{85}Kr beta decays to ^{85}Rb, a stable isotope of Rubidium by the following equation (5.9),

$$^{85}_{36}Kr \rightarrow ^{85}_{37}Rb + e^{-} + \bar{\nu}_e \tag{5.9}$$

The half-life of decay of ^{85}Kr is ∼10.7 years [71], and Q value of 687 keV, however no evidence of ^{85}Kr contribution is yet recorded in the DEAP data [1]). A constant upper limit of 1.5 mBq/kg is used for the activity of ^{85}Kr contribution in the ER background model previously in the experiment. Although its contribution to the total trigger rate from the detector is very small, a constant upper limit for the ^{85}Kr contribution will provide the uncertainty in the lifetime calculation of ^{39}Ar isotope. The effects from the ^{85}Kr activity on the ^{39}Ar lifetime is studied by considering several upper limits which are discussed in the section 7.3.8.1.

There are very negligible triggers expected from the other electromagnetic backgrounds in the selected ROI, hence it is considered as a fixed parameter in the decay fit model which is discussed in detail in section 5.13. The selection of a stable energy region is not enough for the ^{39}Ar triggers since the pure physics data from the detector contains periodic triggers and some non-physics triggers as well. Hence the following basic data-cleaning low-level cuts from the section 5.5 are used in the analysis. Adding the above cuts in the study with the energy cut window modifies the rate equation (5.8) as follows,

$$R(t) = \sum_{i=1}^{4}(\prod_{j=1}^{4} \epsilon_{i,j}(t) R_i(t)) \tag{5.10}$$

Moreover, expanding the equation,

$$R(t) = R_1(t) * \prod_{j=1}^{4} \epsilon_{1,j}(t) + R_2(t) * \prod_{j=1}^{4} \epsilon_{2,j}(t) + R_3(t) * \prod_{j=1}^{4} \epsilon_{3,j}(t) + R_4(t) * \prod_{j=1}^{4} \epsilon_{4,j}(t) \tag{5.11}$$

The definition of all different terms in the equation are,

- R(t) is the recorded trigger rate of ^{39}Ar isotope at time t in the detector after cuts
- R_1(t), R_2(t), and R_3(t) is the rates for the single, double, and triple ^{39}Ar decays respectively. The double, and triple ^{39}Ar decays are where the two, and three ^{39}Ar isotopes decay simultaneously to give a signal trigger in the same trigger window.
- R_4(t) is the rates of coincidence triggers where ^{39}Ar scintillation light piled up with any low energy Cherenkov light trigger in the same trigger window

The additional terms, $(\prod_{j=1}^{4} \epsilon_{i,j}(\mathrm{t}))$ where i varies from 1 to 4, account for the ^{39}Ar fractions, event multiplicity, and software efficiency of the cuts used in the study for selecting different trigger types. The fractions of different ^{39}Ar triggers are fixed in the fit model from the energy cuts in the analysis and given in detail in section 5.10. The event multiplicities are fixed in the fit model as no changes were made to the detector and DAQ setup throughout the data taking, and the time dependence for the software efficiency cuts is also included to account for any systematic related to these variables. The definition of all $(\prod_{j=1}^{4} \epsilon_{i,j}(\mathrm{t}))$ where i vary from 1 to 4, are,

- $\epsilon_{1,1}(\mathrm{t}) = \epsilon_{1,1}$ is the fraction of the single ^{39}Ar triggers in ROI after energy cuts at [700, 1200] nSCBayes

- $\epsilon_{1,2}$(t) is software efficiency of the single ^{39}Ar triggers in ROI after fmaxpe cut at [0.0,0.4]
- $\epsilon_{1,3}$(t) is software efficiency of the single ^{39}Ar triggers in ROI after fprompt cut at [0.0,0.41]
- $\epsilon_{1,4}$(t) or $\epsilon_{1,4}$ is the multiplicity of the single ^{39}Ar triggers
- $\epsilon_{2,1}$(t) = $\epsilon_{2,1}$ is the fraction of the double ^{39}Ar decays in ROI after energy cuts at [700, 1200] nSCBayes
- $\epsilon_{2,2}$(t) is software efficiency of the double ^{39}Ar decays in ROI after fmaxpe cut at [0.0,0.4]
- $\epsilon_{2,3}$(t) is software efficiency of the double ^{39}Ar decays in ROI after fprompt cut at [0.0,0.41]
- $\epsilon_{2,4}$(t) or $\epsilon_{2,4}$ is the multiplicity of the double ^{39}Ar decays
- $\epsilon_{3,1}$(t) = $\epsilon_{3,1}$ is the fraction of the triple ^{39}Ar decays in ROI after energy cuts at [700, 1200] nSCBayes
- $\epsilon_{3,2}$(t) is software efficiency of the triple ^{39}Ar decay triggers in ROI after fmaxpe cut at [0.0,0.4]
- $\epsilon_{3,3}$(t) is software efficiency of the triple ^{39}Ar decays in ROI after fprompt cut at [0.0,0.41]
- $\epsilon_{3,4}$(t) = $\epsilon_{3,4}$ is the multiplicity of the triple ^{39}Ar decay triggers
- $\epsilon_{4,1}$(t) = $\epsilon_{4,1}$ is the fraction of the ^{39}Ar and Cherenkov pile up triggers in ROI after energy cuts at [700, 1200] nSCBayes

- $\epsilon_{4,2}(t) = \epsilon_{4,2}$ is software efficiency of the ^{39}Ar and Cherenkov pile up triggers in ROI after fmaxpe cut at [0.0,0.4]

- $\epsilon_{4,3}(t) = \epsilon_{4,3}$ is software efficiency of the ^{39}Ar and Cherenkov pile up triggers in ROI after fprompt cut at [0.0,0.41]

- $\epsilon_{4,4}(t) = \epsilon_{4,4}$ is the multiplicity of the ^{39}Ar and Cherenkov pile up triggers

The software efficiency for the pile-up of ^{39}Ar and Cherenkov scintillation light is studied from the toy MC, without the time dependence since this background is not expected to vary with time. The values of the trigger multiplicity parameters are known from the DAQ settings, and software efficiency terms are evaluated from the toy MC studies as discussed in sections 5.10 and 5.11. Also, including a electromagnetic background trigger rate, R_{bg}, the fit model from equation (5.11) becomes,

$$R(t) = R_1(t) * \prod_{j=1}^{4} \epsilon_{1,j}(t) + R_2(t) * \prod_{j=1}^{4} \epsilon_{2,j}(t) + R_3(t) * \prod_{j=1}^{4} \epsilon_{3,j}(t) + R_4(t) * \prod_{j=1}^{4} \epsilon_{4,j} + R_{bg} \tag{5.12}$$

R_{bg} is added as a constant from the electronic recoil region, and hence ROI, which is constrained from the result of other analyses in the experiment with value 1.65 Hz (described in the section 5.13). However, the effects of floating this parameter in the fit model are also studied for any uncertainties related to the ER background as discussed in chapter 7.

5.8.2 Poisson probability for different trigger types

In this section the fit equation (5.12) is expanded as follows. Using Poisson statistics, we can write the probability of occurrence of any k triggers in the time interval δt as,

$$P(k) = \frac{(R_{^{39}Ar}(t) * \delta t)^k * \exp(-(R_{^{39}Ar}(t) * \delta t))}{k!} \tag{5.13}$$

where $R_{^{39}Ar}(t)$ is the trigger rate for the ^{39}Ar isotopes at any time t. For the calculation of rates of single ^{39}Ar decay triggers, the probability of the occurrence of single ^{39}Ar decay triggers (with no coincidence or pile up at all) using the Poisson statistics is,

$$P(0) = \frac{(R_{^{39}Ar}(t) * \delta t)^0 * \exp(-(R_{^{39}Ar}(t) * \delta t))}{0!} \tag{5.14}$$

which gives probabilities of single ^{39}Ar decay triggers as,

$$P(0) = \exp(-(R_{^{39}Ar}(t) * \delta t)) \tag{5.15}$$

Therefore, the trigger rates for single ^{39}Ar decay in time interval δt is,

$$R_1(t) = R_{^{39}Ar}(t) * P(0) = R_{^{39}Ar}(t) * \exp(-(R_{^{39}Ar}(t) * \delta t)) \tag{5.16}$$

Similarly, the probability of occurrence of two, and three ^{39}Ar decay triggers in the same trigger window, δt, is given by P(1) and P(2) respectively, and also,

$$P(1) = (R_{^{39}Ar}(t) * \delta t) * \exp(-(R_{^{39}Ar}(t) * \delta t)) \tag{5.17}$$

$$P(2) = \frac{(R_{^{39}Ar}(t) * \delta t)^2 * \exp(-(R_{^{39}Ar}(t) * \delta t))}{2!} \tag{5.18}$$

The trigger rates for double and triple ^{39}Ar decays can be written in the form,

$$R_2(t) \quad = \quad R_{^{39}Ar}(t) \ * \ P(1) \quad = \quad R^2_{^{39}Ar}(t) \ * \ \delta t \ * \ \exp(-(R_{^{39}Ar}(t) \ * \ \delta t)) \tag{5.19}$$

and,

$$R_3(t) \quad = \quad R_{^{39}Ar}(t) \ * \ P(2) \quad = \quad \frac{R^3_{^{39}Ar}(t) * \delta t^2 * \exp(-(R_{^{39}Ar}(t) * \delta t))}{2} \tag{5.20}$$

Thus, using the Poisson statistics the trigger rates of single, double, and triple ^{39}Ar coincidence decays can be calculated. Also, the pile-up corresponding to the coincidence of ^{39}Ar decay light with the low energy Cherenkov light can be written in the form,

$$R_4(t) = R_{^{39}Ar}(t) * \exp(-(R_{^{39}Ar}(t) * \delta t) * R_{Cherenkov}(t) * \exp(-(R_{Cherenkov}(t) * \delta t)) * \delta t \tag{5.21}$$

where $R_{Cherenkov}(t)$ is the rate of triggers corresponding to the low energy Cherenkov scintillation light in the detector. The Poisson probability for selecting only the single ^{39}Ar triggers and single Cherenkov triggers are used.

In DEAP-3600, the total trigger rate from all the raw physics data without any cuts applied is about 3300 Hz. The length of the trigger window used in the DEAP-3600 DAQ system is 10.028 μs long, and the total trigger rate is very small as compared to the reciprocal of the time window, or $R_{^{39}Ar}(t) * \delta t \ll 1$. The factor $\exp(-(R_{^{39}Ar}(t) * \delta t))$ gives as ~94.72% of single decays, and ~5.28% of pile-up events

for the full energy spectrum. However, the pile-up events are mainly present at the tail of the ^{39}Ar spectrum. The trigger rate at the low energy region in the ROI from equation (5.12) is as under,

$$R(t) = [R_{^{39}Ar}(t) * \prod_{j=1}^{4} \epsilon_{1,j}(t) + R^2_{^{39}Ar}(t) * \delta t * \prod_{j=1}^{4} \epsilon_{2,j}(t) + \frac{R^3_{^{39}Ar}(t)}{2} * \delta t^2 * \prod_{j=1}^{4} \epsilon_{3,j}(t) +$$
$$R_{^{39}Ar}(t) * R_{Cherenkov}(t) * \delta t * \exp(-(R_{Cherenkov}(t) * \delta t)) * \prod_{j=1}^{4} \epsilon_{4,j}] *$$
$$\exp(-(R_{^{39}Ar}(t) * \delta t)) + R_{bg} \quad (5.22)$$

The dominant fraction of ^{39}Ar pile-up is present at higher energies (at about ∼3500 PE in figure 5.9) than the selected ROI, therefore, the contribution of the pile-up are expected to be very low in the selected energy region.

5.8.3 Radioactive decay of ^{39}Ar isotope

The ^{39}Ar isotopes decays randomly to stable ^{40}K isotope. The radioactive decay equation is given by,

$$R_{^{39}Ar}(t) = R_{^{39}Ar} * \exp(\frac{-t}{\tau_{^{39}Ar}}) \quad (5.23)$$

where, $R_{^{39}Ar}$ is average rate of ^{39}Ar isotopes at time, t=0, and $\tau_{^{39}Ar}$ is the lifetime for the radioactive decay of ^{39}Ar isotope. Therefore, the fit model from equation (5.22) can be expressed in the form of equation (5.24) which gives the fit function to fit the trigger rates of ^{39}Ar isotope from the DEAP-3600 detector data.

$$R(t) = [R_{^{39}Ar} * \exp(\frac{-t}{\tau_{^{39}Ar}}) * \prod_{j=1}^{4} \epsilon_{1,j}(t) + R^2_{^{39}Ar} * \delta t * \exp(\frac{-2t}{\tau_{^{39}Ar}}) * \prod_{j=1}^{4} \epsilon_{2,j}(t) + \frac{R^3_{^{39}Ar}}{2} * \delta t^2 *$$

$$\exp(\frac{-3t}{\tau_{^{39}Ar}})*\prod_{j=1}^{4}\epsilon_{3,j}(t)+R_{^{39}Ar}*\exp(\frac{-t}{\tau_{^{39}Ar}})*R_{Cherenkov}(t)*\delta t*\exp(-(R_{Cherenkov}(t)*\delta t))*$$
$$\prod_{j=1}^{4}\epsilon_{4,j}]*\exp(-(R_{^{39}Ar}*\exp(\frac{-t}{\tau_{^{39}Ar}})*\delta t))+R_{bg} \quad (5.24)$$

This equation has two independent parameters for the measurement of a lifetime, and the activity of ^{39}Ar at the beginning of the dataset. The physics data included in the study were collected from 4 November 2016 to 27 March 2020 (see chapter 6 for more details). Thus, the initial time in the fit function is used as the start time of the dataset, hence the $R_{^{39}Ar}$ is the activity of ^{39}Ar at the beginning of the dataset, November 2016, and $\tau_{^{39}Ar}$ is the lifetime for the radioactive decay of ^{39}Ar isotopes. The rate for the low energy Cherenkov light triggers, $R_{Cherenkov}$(t) from the DEAP-3600 detector and physics data to be included in the fit model 5.24 is evaluated in the section 5.9.

5.8.4 Summary table for the fit model parameters

The various parameters used in the ^{39}Ar decay fit model derived in the equation (5.24) are summarized in the table 5.3. Also, the values of the fit parameters used in the study are given in the third column, more details about the evaluation of different parameters are discussed in the following sections.

Table 5.3: List of fit parameters used to model the decay of ^{39}Ar isotope from DEAP-3600 dataset.

Fit Parameter	Definition	Value used in the analysis
$R_{^{39}Ar}$	Rate of ^{39}Ar triggers in start of dataset	Independent parameter
$\tau_{^{39}Ar}$	Lifetime of ^{39}Ar triggers	Independent parameter

Continuation of Table 5.3		
Fit Parameter	Definition	Value used in the analysis
$R_{Cherenkov}(t)$	Rate of triggers containing the Cherenkov light in DEAP-3600 detector, extrapolated to zero threshold condition	538.1 ± 3.9 Hz, evaluated from the dataset
R_{bg}	Rate of ER background triggers in ROI	1.65 Hz, constrained from the ER paper for backgrounds in ROI
δt	Trigger time window	10.028 μs, in the DAQ settings
$\epsilon_{1,1}$	Fraction of the single ^{39}Ar decay triggers in the selected energy region out of the total spectrum	0.21, from the analytical spectrum and MC
$\epsilon_{1,2}(t)$	Efficiency of selecting single ^{39}Ar decay triggers in ROI with fmaxpe cut, in [0.0,0.4] fmaxpe region	1.0000000 ± 0.0000016, from data and MC
$\epsilon_{1,3}(t)$	Efficiency of selecting single ^{39}Ar decay triggers in ROI with fprompt cut, in [0.0,0.41] fprompt region	1.0000000 ± 0.0000050, from data and MC
$\epsilon_{1,4}$	Multiplicity of the single ^{39}Ar triggers	1, in the DAQ settings
$\epsilon_{2,1}$	Fraction of the double ^{39}Ar decay triggers in the selected energy region out of the total spectrum	0.20, from the analytical spectrum and MC
$\epsilon_{2,2}(t)$	Efficiency of selecting double ^{39}Ar decays in ROI with fmaxpe cut, in [0.0,0.4] fmaxpe region	1.0000000 ± 0.0000065, from data and MC
$\epsilon_{2,3}(t)$	Efficiency of selecting double ^{39}Ar decays in ROI with fprompt cut, in [0.0,0.41] fprompt region	0.9099 ± 0.0033, from data and MC
$\epsilon_{2,4}$	Multiplicity of the double ^{39}Ar decays	0.5, in the DAQ settings
$\epsilon_{3,1}$	Fraction of the triple ^{39}Ar decay triggers in the selected energy region out of the total spectrum	0.19, from the analytical spectrum and MC
$\epsilon_{3,2}(t)$	Efficiency of selecting triple ^{39}Ar decay triggers in ROI with fmaxpe cut, in [0.0,0.4] fmaxpe region	1.000000 ± 0.000037, from data and MC

Continuation of Table 5.3		
Fit Parameter	Definition	Value used in the analysis
$\epsilon_{3,3}$(t)	Efficiency of selecting triple ^{39}Ar decay triggers in ROI with fprompt cut, in [0.0,0.41] fprompt region	0.860 ± 0.039, from data and MC
$\epsilon_{3,4}$	Multiplicity of the triple ^{39}Ar decay triggers	0.33, in the DAQ settings
$\epsilon_{4,1}$	Fraction of pile-up containing the ^{39}Ar and Cherenkov light in the selected energy region out of the total spectrum	0.21, from toy MC
$\epsilon_{4,2}$	Efficiency of selecting ^{39}Ar and Cherenkov light pile-up in ROI with fmaxpe cut, in [0.0,0.4] fmaxpe region	1.00, from MC
$\epsilon_{4,3}$	Efficiency of selecting ^{39}Ar and Cherenkov light pile-up in ROI with fprompt cut, in [0.0,0.41] fprompt region	1.00, from MC
$\epsilon_{4,4}$	Multiplicity of the triggers containing the ^{39}Ar pile up with Cherenkov light	0.5, in the DAQ settings

Monte Carlo studies There are two types of MC simulations used in the analysis. The decay energy spectrum of ^{39}Ar isotope is convoluted from the analytical spectrum as described in the section 5.10. A toy MC is made to estimate the fraction of the different decays in ROI which includes the fit parameters, $\epsilon_{1,1}$, $\epsilon_{2,1}$, $\epsilon_{3,1}$, and $\epsilon_{4,1}$. Also, the pile-up spectrum of ^{39}Ar with the low energy Cherenkov spectrum is made from the same toy MC technique which helped to calculate the values for $\epsilon_{4,2}$, and $\epsilon_{4,3}$ in the fit model.

The second type of MC used in the analysis includes the GEANT4 [75] simulations where the detector setup and its optical properties are implemented in the RAT framework [76], based on the ROOT [77], and the response of the detector is

recorded for the simulated samples of ^{39}Ar. The gammas simulations are performed from this framework to full low energy Cherenkov spectrum from the ^{40}K and ^{208}Tl isotopes in the PMTs at different detector thresholds. Moreover, the absolute value of the efficiency of the cuts included in the analysis, fmaxpe, and fprompt are calculated from these simulated samples as discussed in section 5.11. In addition, the values from the fit model evaluated from the toy MC using the analytical spectrum are also verified from the simulated samples in the RAT environment.

5.9 Rate of triggers containing Cherenkov light

The coincidence rate of ^{39}Ar with the low energy Cherenkov light, $R_4(t)$ is included in the fit function in the terms of rates of single $R_{^{39}Ar}$ triggers and rate of triggers that contain Cherenkov light, $R_{Cherenkov}(t)$, after investigating these trigger rates in the dataset over time with detector conditions described as follows.

5.9.1 Cuts used to select the triggers containing Cherenkov light

The rate of single triggers giving Cherenkov light from the dataset was calculated by using the Cherenkov selection cuts given below,

1. (!(calcut&0x31f8))
2. (!(dtmTrigSrc&0x82))
3. fmaxpe>0.4
4. fprompt>0.8
5. subeventN == 1

6. deltat$\geq$20000

7. numEarlyPulses$\leq$3

8. eventTime [2250,2700]

The first two cuts are used as data cleaning cuts to reject any non-physics triggers from the dataset. The fmaxpe cut at greater than 0.4 and fprompt cut at region greater than 0.8 was used to select the trigger window for the Cherenkov scintillation light.

The triggers for Cherenkov light in the data are distinguished from the other recoils on the basis of their scintillation nature. The argon scintillation light within liquid argon is expected to be highly isotropic such that the maximum fmaxpe value of its recoil triggers is very small. This study was done by other collaborators where it is suggested to use the fmaxpe variable as the discriminator for Cherenkov and alpha backgrounds. Figure 5.12 shows the distribution of the fmaxpe variable for physics run in DEAP-3600 data. The red vertical line represents the separation region for Cherenkov light on the right side of the distribution.

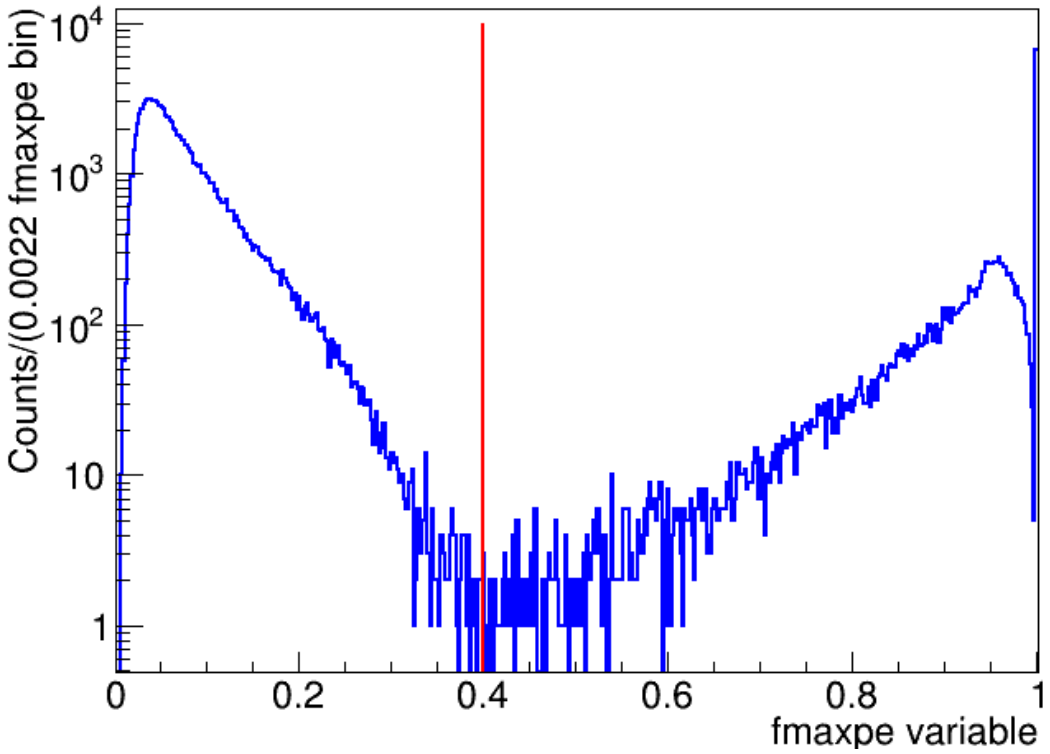

Figure 5.12: The fmaxpe variable distribution for a physics run after the livetime cut, (!(calcut&0x31f8)), (!(dtmTrigSrc&0x82)), subeventN==1, deltat>=20000, and numEarlyPulses<=3. The vertical red line gives the cut value used for the selection of the Cherenkov region.

Also, the fprompt and fmaxpe distribution in figure 5.13 gives the separate regions of the ^{39}Ar electron recoil region and Cherenkov region in physics data. The fprompt variable values greater than 0.8 give the maximum single Cherenkov scintillation light, this lower limit is set for Cherenkov light selection to reject any alpha particles. The data cuts from 5 to 8 are the pile-up cuts used to select only the single Cherenkov light triggers.

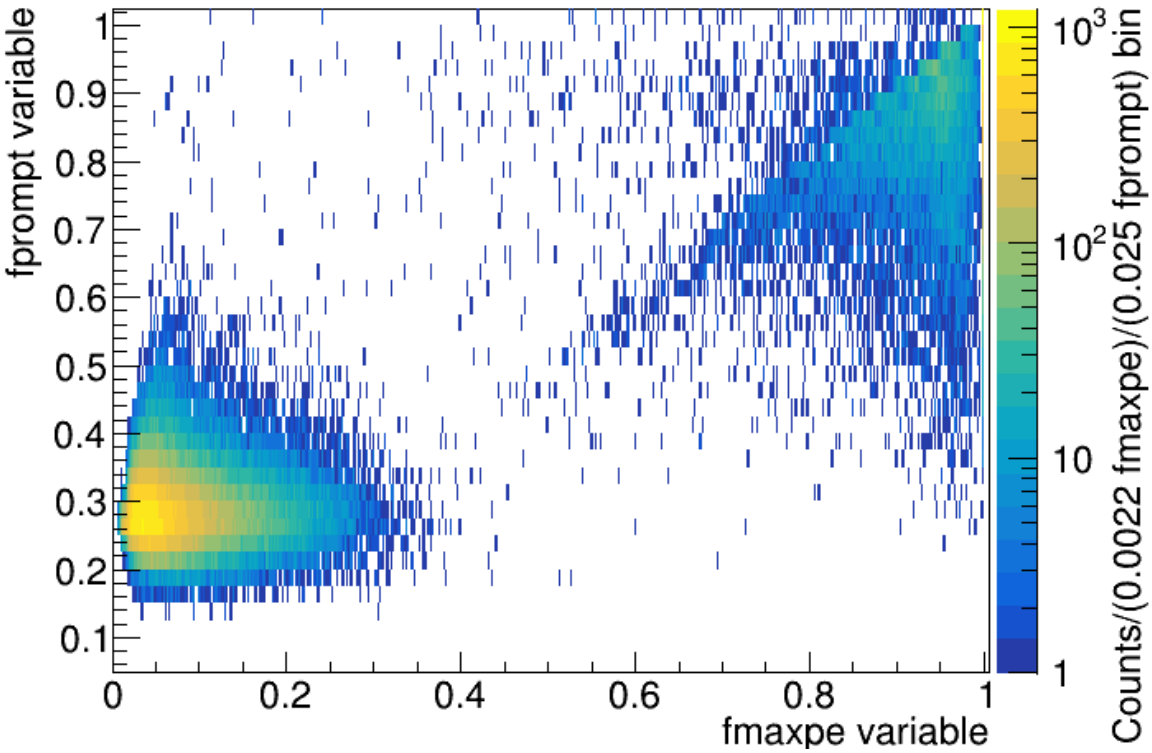

Figure 5.13: The distribution of fmaxpe and fprompt variables for a physics run in DEAP-3600 after the livetime cut, (!(calcut&0x31f8)), (!(dtmTrigSrc&0x82)), subeventN==1, deltat>=20000, and numEarlyPulses<=3. The fmaxpe value at 0.4 clearly distinctions between the Cherenkov region and the fprompt value greater than 0.8 contains maximum Cherenkov particles.

5.9.2 Cherenkov light spectrum from data

The Cherenkov spectrum from plotted from the first run number 18721 in the dataset is shown in figure 5.14.

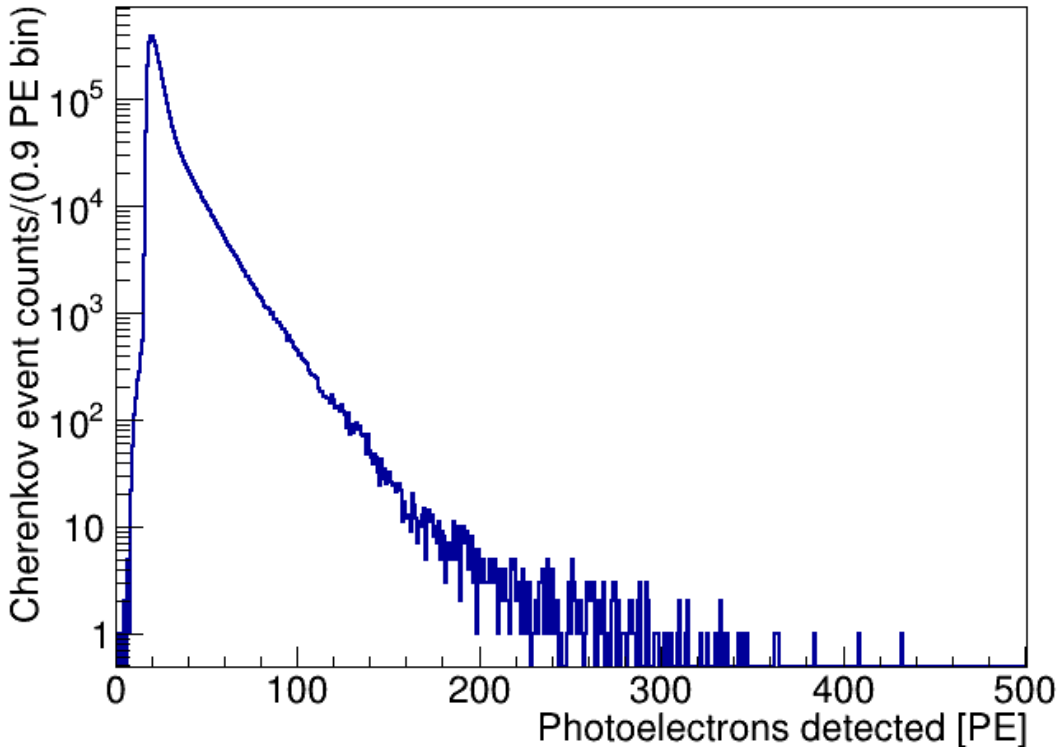

Figure 5.14: PE distribution of Cherenkov trigger counts from physics run number 18721, first run in the database.

This spectrum gives the PE distribution for the single triggers when the Cherenkov light is passing the data selection cuts discussed at the beginning of this section. Also, normalizing the Cherenkov spectrum from figure 5.14 with the livetime information of the same run number, the PE spectrum for the Cherenkov rates is given in figure 5.15. The major contribution to the Cherenkov rates is from the lower energy triggers with a PE value of less than 30 PE. The maximum energy Cherenkov triggered event seen from the data is all below 500 PE.

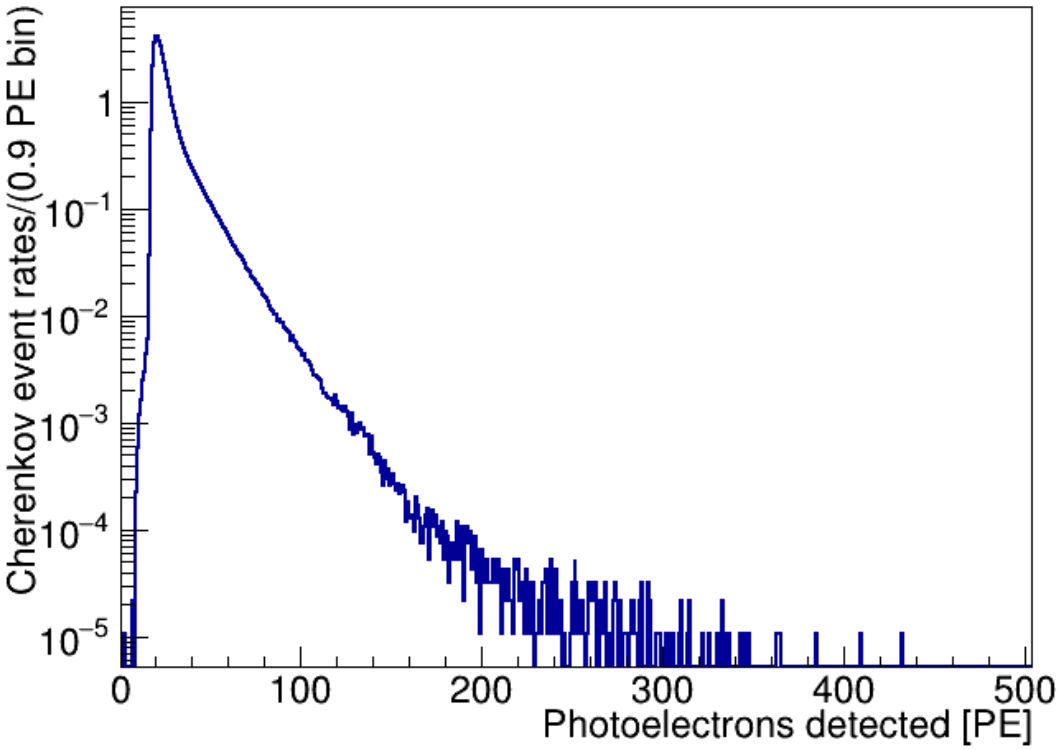

Figure 5.15: PE distribution of Cherenkov trigger rates from physics run number 18721 after normalizing the spectrum with the livetime of the run.

However, these figures do not show the full Cherenkov spectrum because the standard trigger threshold for the DEAP-3600 DAQ was set at 1000 ADC such that we were not sensitive to the very low energy triggers below 20 PE. In reality, the Cherenkov spectrum goes much down below the 20 PE with the threshold energy of electrons to produce Cherenkov light. Therefore, the triggered rates for Cherenkov scintillation are presented in figure 5.15 need the correction for the threshold effects at the lower energy part of the spectrum. The variation in the Cherenkov light trigger rates without this lower threshold correction over time is shown in figure 5.16.

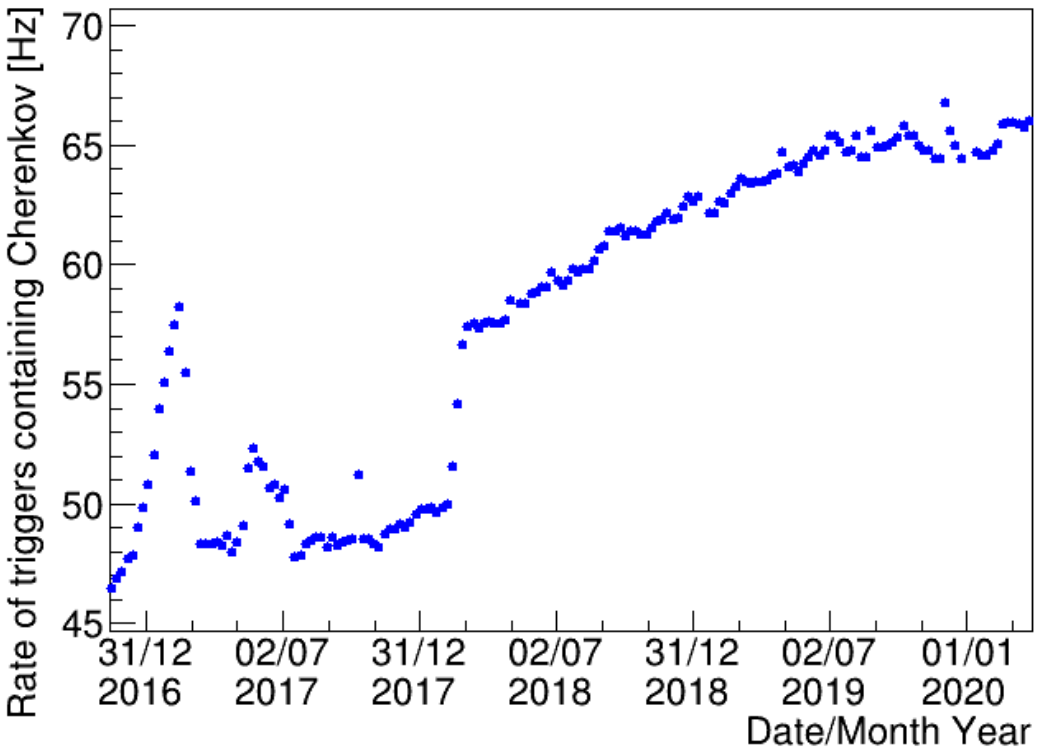

Figure 5.16: The calculated Cherenkov light trigger rates from data at the standard detector threshold at 1000 ADC; the corrections are needed for the lower part of the spectrum to get the exact Cherenkov light rates.

The Cherenkov light rates are calculated for each run number from the dataset and plotted with time on a weekly bin basis such that each bin in the figure above represents the Cherenkov light trigger rate in the week over the year. The rates are varying over time from 46 Hz in the first week of the dataset to 66 Hz in the last week of the dataset before applying any lower threshold corrections.

5.9.3 Lower threshold normalization for the full Cherenkov spectrum

The standard physics data in DEAP-3600 was taken at the lowest possible trigger threshold of 1000 ADC where the trigger system is absolutely 100% efficient. How-

ever, for the complete Cherenkov spectrum, the lower energy response must be known. Chereknov light will be generated in acrylic above a threshold energy of 174.6 keV, and in PMT glass above 126.1 keV (as discussed in section 4.4.3). To evaluate the full spectrum down to zero threshold, MC calculations were used and matched to the above-threshold spectra. In general, the Cherenkov triggers are having energies varying from 0 to 160 PE maximum as seen from figure 5.14 which shows the Cherenkov spectrum from physics data.

As mentioned earlier with the detector threshold at 1000 ADC we are not able to see any triggers below 15 PE, therefore, the MC simulations were performed at different detector thresholds to get the full Cherenkov spectrum with the lower energies. The detector threshold was set at 150 ADC, 50 ADC, and 0 ADC (such that we can attain the zero threshold condition for the detector to see very energy triggers), and the simulated Cherenkov spectrum from the ^{40}K gammas and ^{208}Tl (both at PMT glass) were compared as shown in figure 5.17.

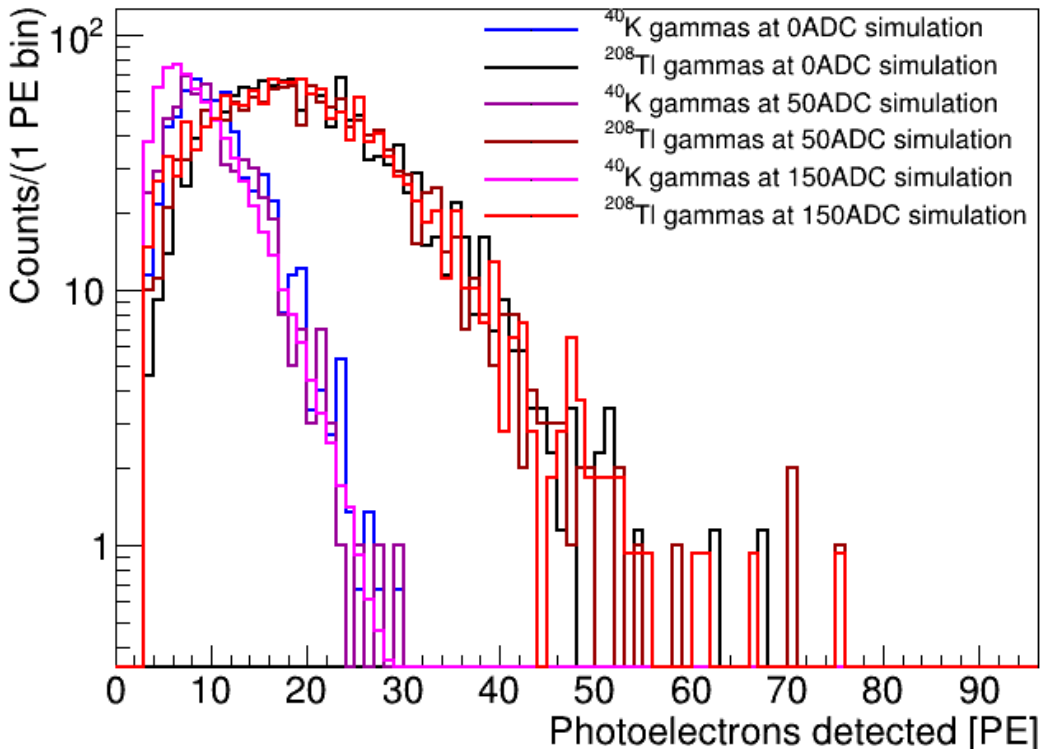

Figure 5.17: The MC simulations for ^{40}K and ^{208}Tl gammas at different detector thresholds. The simulations were performed to obtain the lower threshold needed for the full Cherenkov energy spectrum at low energies.

The Cherenkov spectrum from the simulated ^{40}K gammas peaked at ∼8 PE, and for simulated ^{208}Tl gammas, it peaked at ∼20 PE. The Cherenkov spectrum from two different gammas sources is very little affected at the three different tested lower trigger thresholds. The lower trigger threshold at 150 ADC returns the full Cherenkov spectrum at very energies like other threshold values.

This threshold value was chosen specifically because some physics data was taken at this threshold value with the DEAP trigger system some time ago for other studies (which showed this trigger threshold value at 150 ADC is the best lower threshold we can get with the trigger settings at the DEAP-3600 experiment). The

Cherenkov spectrum was plotted from the physics data taken at a lower threshold value 150 ADC (given in figure 5.18) while the same Cherenkov trigger selection cuts were used.

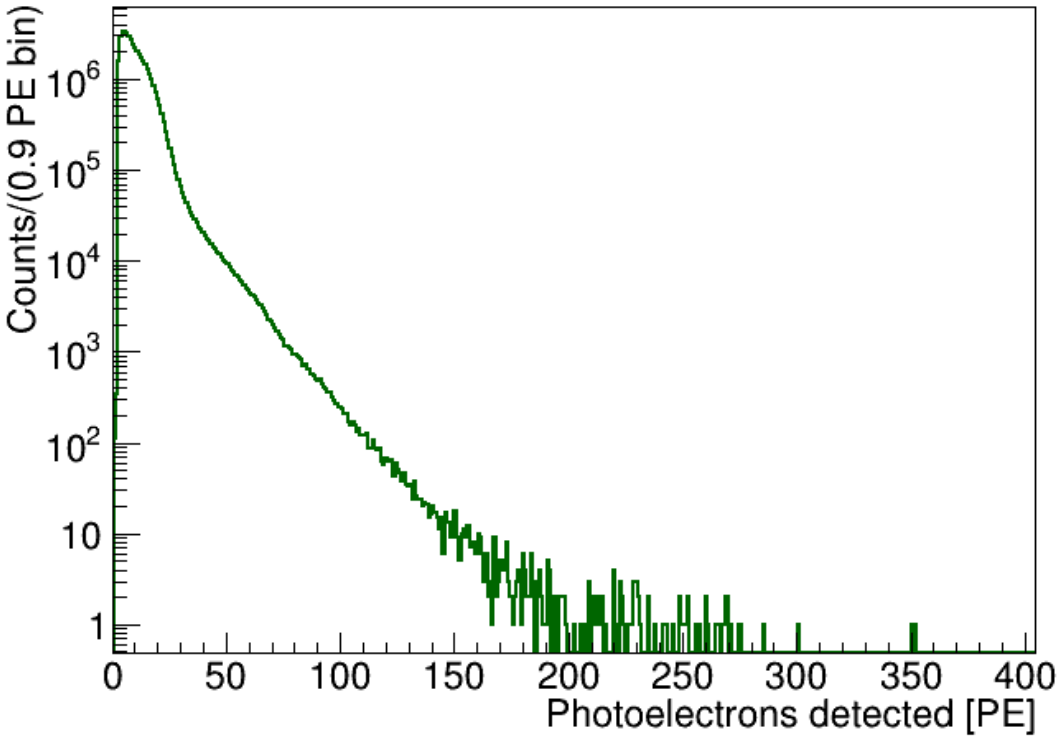

Figure 5.18: PE distribution of Cherenkov trigger counts from physics data taken at lower trigger threshold at 150 ADC.

The Cherenkov spectrum from a lower threshold 24 hours of data peaked at a 4 PE value and the lower energy trigger we got from this spectrum is at 1 PE which is the pretty much lower energy Cherenkov light trigger we can record with a physical detector. As seen in the figure 5.19 the obtained Cherenkov spectrum from data at lower detector threshold 150 ADC matches well with the spectrum obtained from the MC simulations at the lower energies.

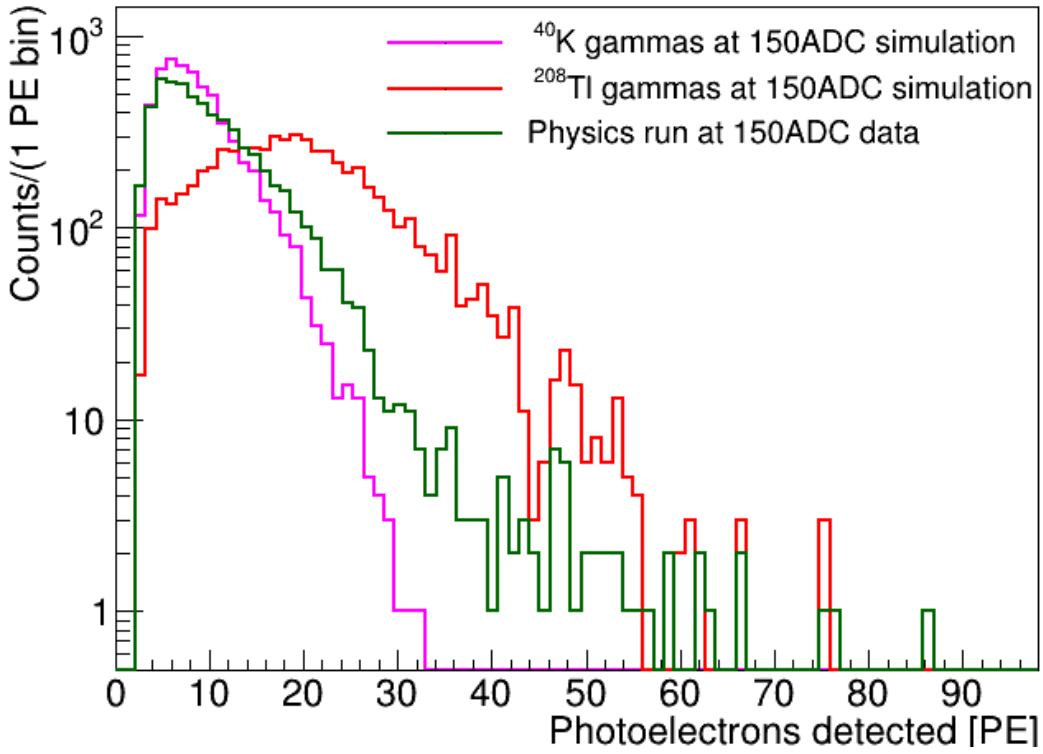

Figure 5.19: PE distribution of Cherenkov trigger counts from physics data and MC simulations for ^{40}K and ^{208}Tl gammas at lower trigger threshold at 150 ADC.

Assuring the Cherenkov spectrum from the physics data at a lower threshold to be correct and real, the Cherenkov spectrum from the physics runs in the dataset is normalized to the spectrum in figure 5.18 at the energies 42 PE. If the Cherenkov scintillation trigger counts for any physics run are less than or greater than the Cherenkov trigger counts at 42 PE for the lower threshold run, the spectrum is scaled up or down such that it matches with the correct spectrum at 42 PE. The extra contribution from the lower energy part of Cherenkov spectra below 42 PE is added to the physics runs i.e., the integral of the Cherenkov spectrum in figure 5.18 below 42 PE minus the same integral of spectra from each and every run in the dataset is added to the physics runs to get the complete distribution of Cherenkov scintillation triggers at low energies,

and this correction is made on run by run basis. The trigger energy at 42 PE is again specifically chosen to avoid any trigger efficiency effects.

5.9.4 Cherenkov light trigger rates from threshold corrected spectrum

The Cherenkov light rates for the physics data are plotted on a weekly bin basis after applying the threshold corrections (discussed in the section above), as shown in figure 5.20.

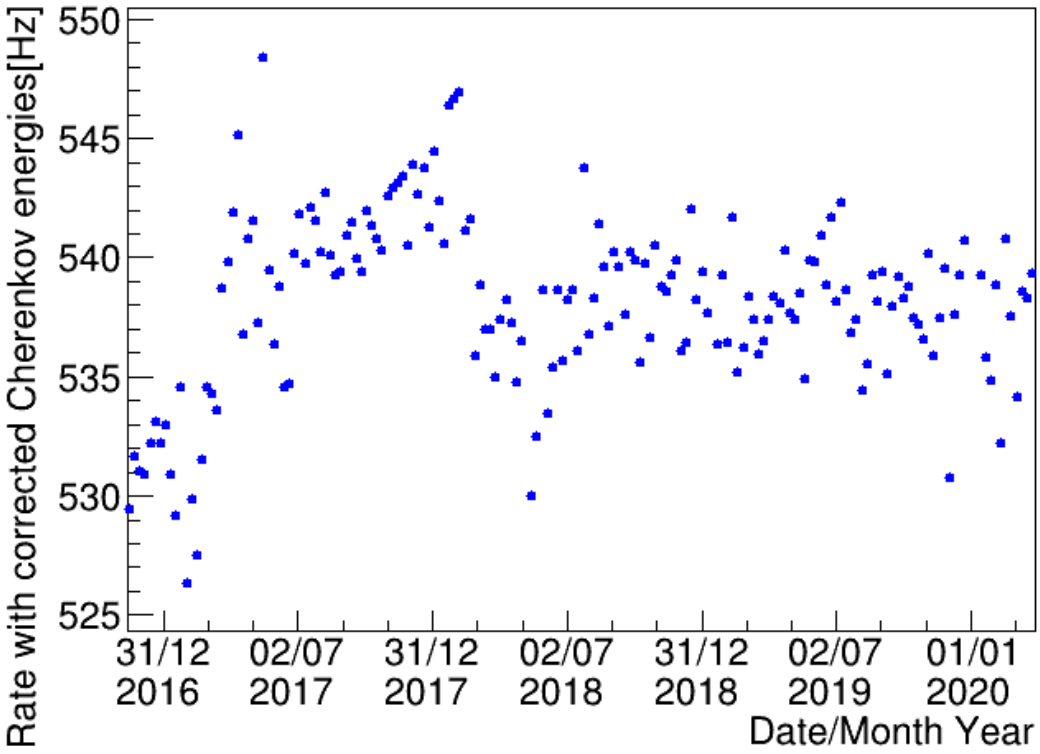

Figure 5.20: The calculated trigger rates corresponding to Cherenkov scintillation light from physics data after normalization from lower energy threshold response at 150 ADC.

These Cherenkov light rates are calculated from the threshold-corrected Cherenkov spectrum normalized with livetime information of the run numbers, where each data

point on the plot represents one week of the year. The Cherenkov light rates are mostly stable throughout the dataset as expected. The Cherenkov light triggers are only emitted from the different detector components as described in chapter 4 which remained the same during the data collection and hence rates are not varying very much with time.

The little variations observed could be because of small changes in the response of PMT additional components like light guides with the temperature of the water tank (as discussed in appendix A). The one-dimensional distribution of the relative residuals of Cherenkov light rates from the first week in the dataset is presented in figure 5.21 which showed a standard deviation of 0.7% on the relative residuals. The Cherenkov rates from the dataset will be used further in the fit model from equation (5.24) to estimate the lifetime of ^{39}Ar isotope.

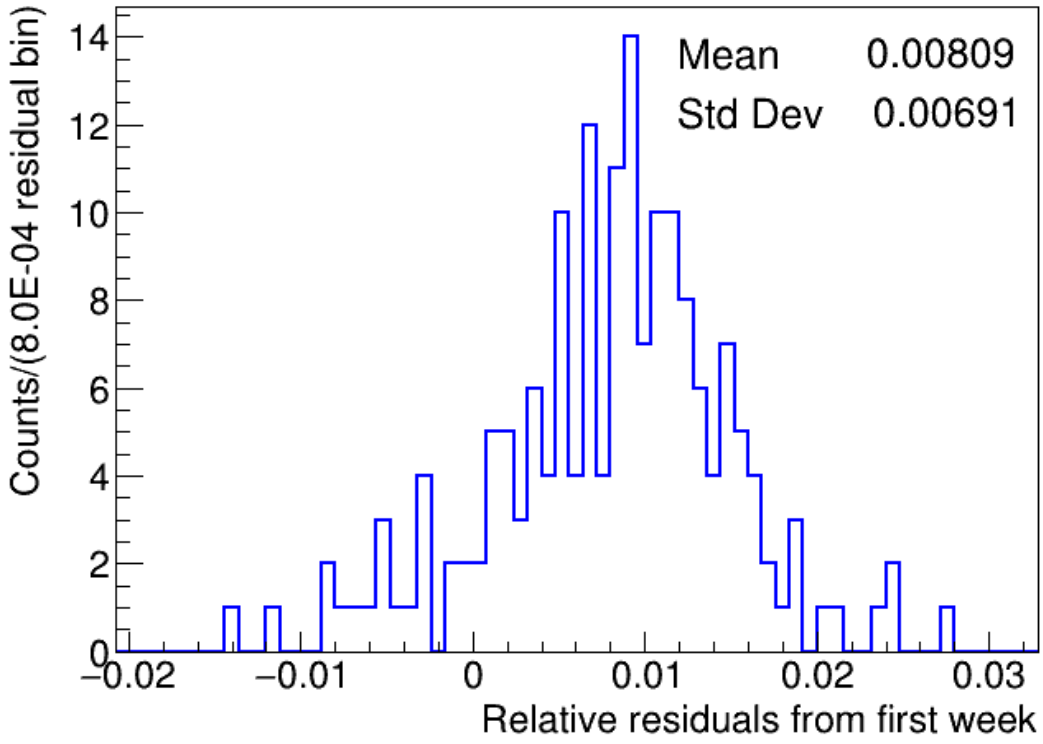

Figure 5.21: The one-dimensional distribution of relative residuals of the triggers rates corresponding to Cherenkov light from the first week in the dataset.

5.10 Fraction of single and coincidence ^{39}Ar decays in the ROI

The fraction of different types of triggers in ROI is calculated from the toy Monte Carlo simulations using the analytical spectrum for ^{39}Ar beta decay. The analytical spectrum for the beta decays of ^{39}Ar isotopes was taken from the publication by J. Kostensalo et al [78] as shown in figure 5.22. This beta spectrum shows the ground state to ground state decay of ^{39}Ar and is calculated using the microscopic quasiparticle-phonon model and the shell model with the effective interaction sdpfnow. The Q-value for this decay is (565 ± 5) keV.

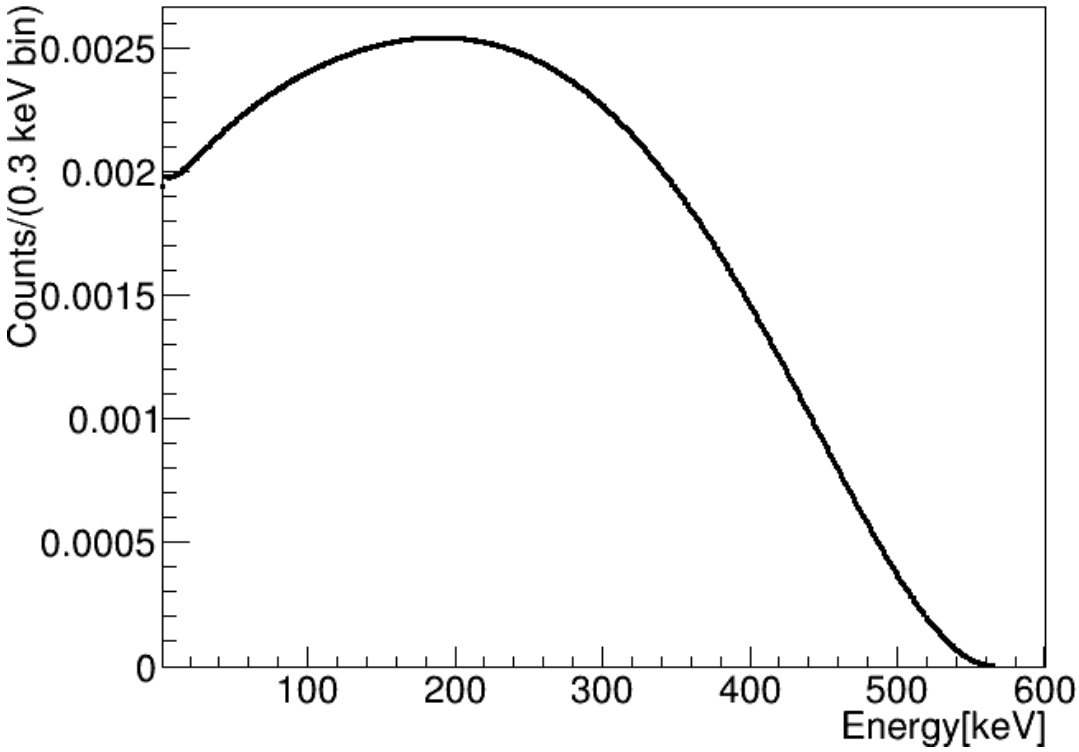

Figure 5.22: Analytical beta decay spectrum of ^{39}Ar isotopes calculated by J. Kostensalo, J. Suhonen, and, K. Zuber (KSZ) in [78].

The decay spectrum in the keV energy scale is converted to the number of PE detected by the PMTs using the energy response model of the detector discussed in the second physics paper [6] from the DEAP-3600 experiment. This model uses a Gaussian response with mean μ as follows,

$$\mu[PE] =< N_{DN}[PE] > + Y_{PE}[PE/keVee] * E[keVee] \tag{5.25}$$

where, $<N_{DN}>$ gives the average number of PE produced by the dark noise and other independent photons in the PE window, Y_{PE} is the light yield of the detector. The values for these parameters were used as given in the table 5.4.

Table 5.4: The energy response parameters for the best-fit function from a fit to ^{39}Ar triggers collected for 231 days of physics data

PE mean	$<N_{DN}>$	Y_{PE}
	(1.1 ± 0.2) PE	(6.0170 ± 0.0014) PE/keVee

The average value of the dark noise parameter and its uncertainty is taken from the second physics paper from the DEAP-3600 experiment [6] since this has a very small contribution to the total PE, and the light yield value is an average value from the more than 3 years of physics dataset as discussed in section 6.4. The energy resolution is kept constant while convolving the ^{39}Ar spectrum from the keVee scale to the PE scale. Also, to account for systematic uncertainty from the light yield and energy resolution, detailed studies are performed which are mentioned in chapter 6.

5.10.1 Spectrum for single ^{39}Ar events

Including the energy response parameter terms from table 5.4, the ^{39}Ar beta spectrum is plotted in the scale of detected PE as given in figure 5.23. The selected ROI for the study is shown in the red lines which contain 21% of the total ^{39}Ar single beta decays calculated from the spectrum, thus,

$$\epsilon_{1,1} = 0.21 \tag{5.26}$$

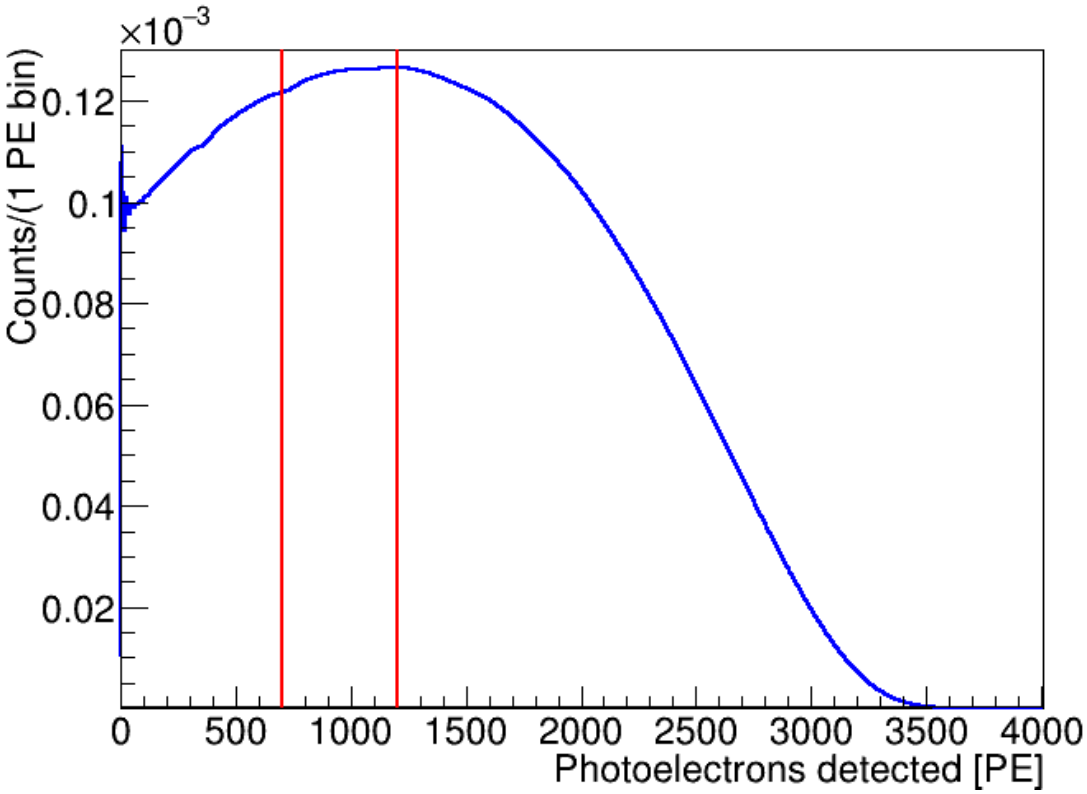

Figure 5.23: Analytical beta decay spectrum of ^{39}Ar isotopes in terms of PE detected after using energy response model of detector. The selected ROI for the study is shown in the red lines.

This value for the fraction of single ^{39}Ar in the selected energy region is verified from the MC simulated spectrum, which shows only about ∼0.3% change in the fraction. However, the uncertainty calculations are done for the $\tau_{^{39}Ar}$ measurement from this very small shift in this fraction, and considering the maximum variation of 5% on $\epsilon_{1,1}$ which are discussed in table 7.2.

5.10.2 Spectrum for coincidence of two ^{39}Ar events

The pile-up spectrum for the coincidence of two ^{39}Ar simultaneous decay triggers is calculated from the random selection of any two triggers in this spectrum from figure 5.23 and summing their energies (PE) for the total energy of the final trigger. The

spectrum in figure 5.24 shows the spectrum for the coincidence of two ^{39}Ar triggers where the full triggers happened in the DAQ trigger window and the final energies summed up completely.

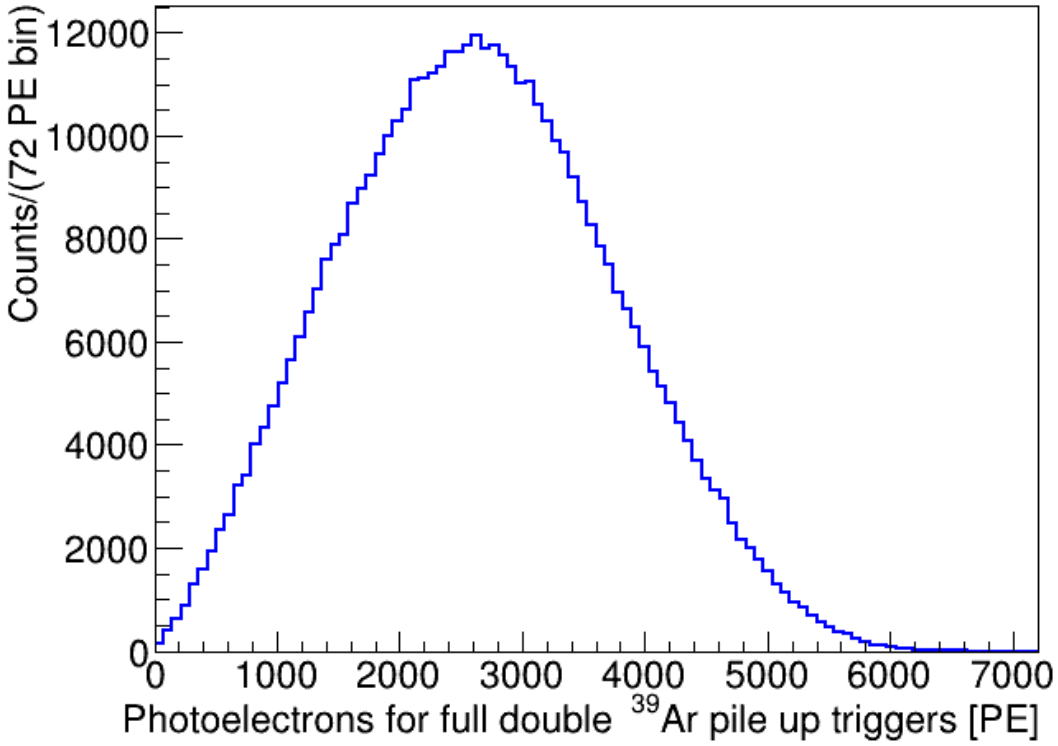

Figure 5.24: Beta decay spectrum of any two ^{39}Ar isotopes scintillating and resulting in the single trigger in the detector if scintillation light from both the triggers add up completely and is detected in the ideal case.

However, in the DEAP-3600 experiment trigger settings, the length of the trigger window is 10.028 μs. Therefore, an additional condition is applied in the toy MC such that for the second trigger only the fraction of energy falling in the time window of less than and equal to 10.028 μs is used to calculate the summed energy, and hence for calculation of total photoelectrons. The toy Monte Carlo was run for 5,000,000 triggers adding the energies of two random individual triggers in the trigger window,

this shifted the energy spectrum to the left as shown in the figure 5.25.

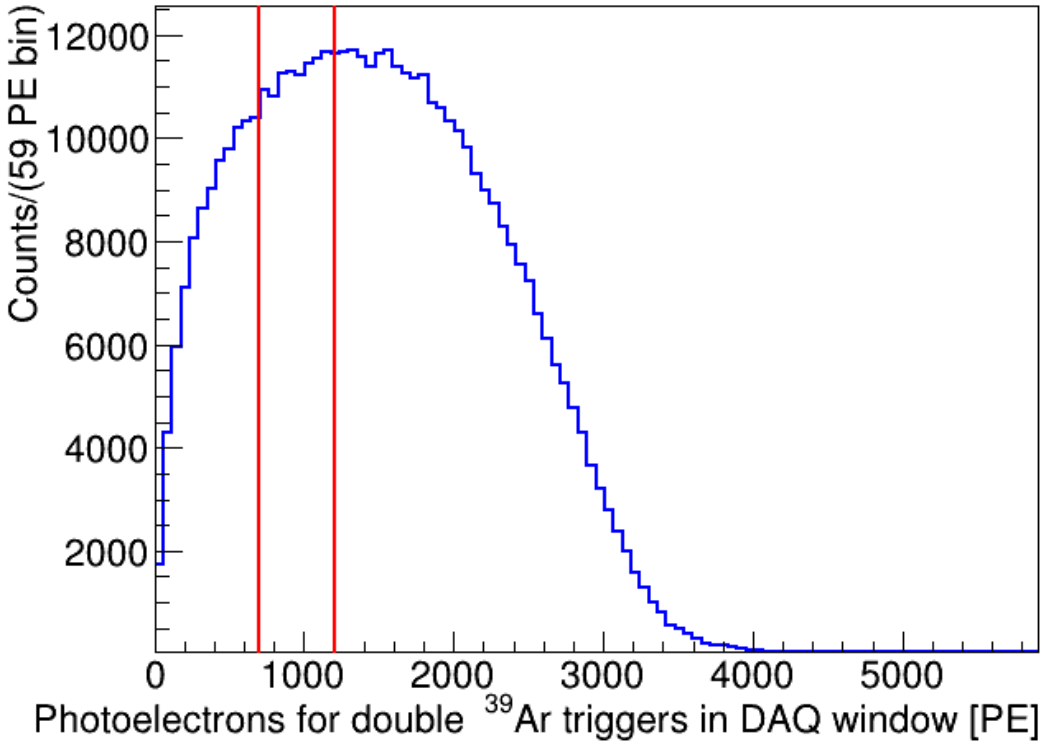

Figure 5.25: Beta decay spectrum of any two ^{39}Ar isotopes scintillating and resulting in the single trigger in the DAQ system within a trigger window of length 10.028 μs. The selected ROI for the study is shown in the red lines.

The contribution of the double ^{39}Ar decay triggers in ROI is highlighted in the red lines which contain 20% of total double pile-up in the spectrum, therefore,

$$\epsilon_{2,1} = 0.20 \tag{5.27}$$

Furthermore, to estimate the systematic uncertainty on $\tau_{^{39}Ar}$ for any deviation in this number, an additional 5% change is added to this value, which changed the lifetime measurement of ^{39}Ar by a very small fraction as discussed in table 7.2.

5.10.3 Spectrum for coincidence of three ^{39}Ar events

A similar toy MC is written and calculation is done to get the spectrum and the fraction of the triple ^{39}Ar coincidence triggers in the ROI. Any three triggers were selected at random from the spectrum in figure 5.23, and there were energies added for the final energy (or PE count) value of the piled-up trigger. The toy Monte Carlo studies showed if the complete energies of three random ^{39}Ar triggers are added to get the full pile-up spectrum for triple coincidence as given in figure 5.26, the spectrum is peaked at the 4000 PE.

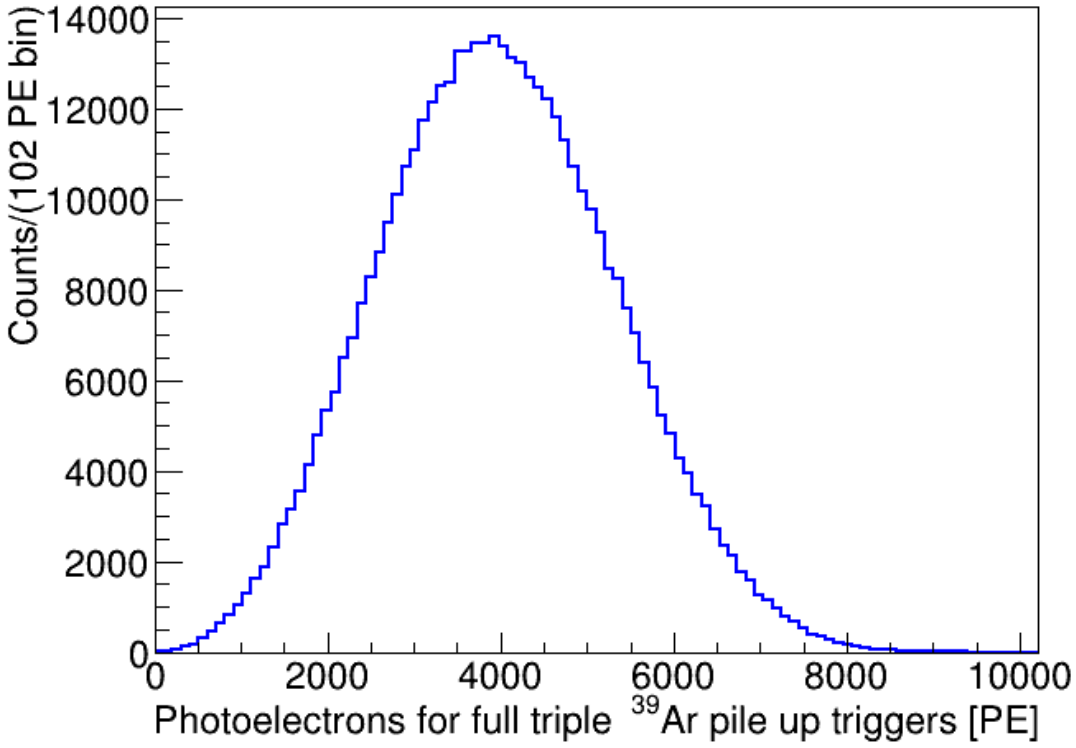

Figure 5.26: Beta spectrum of any three ^{39}Ar isotopes decaying simultaneously and resulting in the single trigger in the ideal case.

Furthermore, taking into account the length of the trigger window, 10.028 μs, and only adding the fraction of energies from the second and third trigger occurring in

this window, the triple pile-up spectra in terms of detected photoelectrons are shown in the figure 5.27.

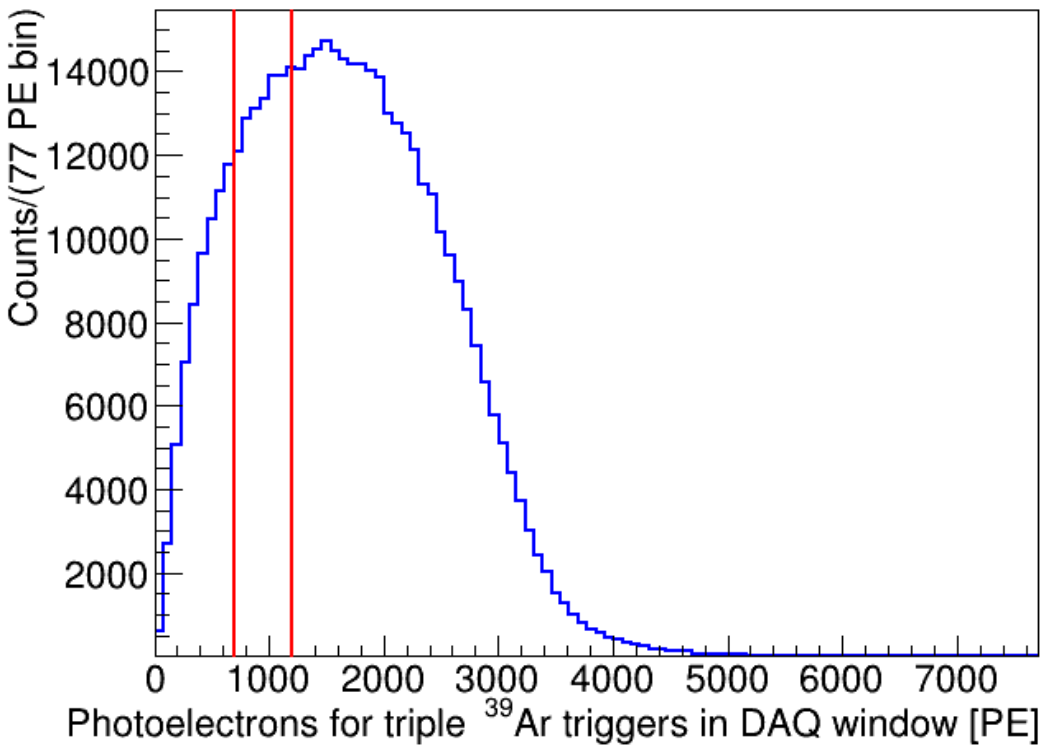

Figure 5.27: Beta decay spectrum of any three ^{39}Ar isotopes scintillating and resulting in the single trigger in the DAQ system within a trigger window of length 10.028 μs. The selected ROI for the study is shown in the red lines.

There are 19% of total triple ^{39}Ar decay triggers in the ROI as highlighted in the red line region, which gives,

$$\epsilon_{3,1} = 0.19 \tag{5.28}$$

An additional 5% change is included in the systematic studies to evaluate the uncertainty on $\tau_{^{39}Ar}$ from this parameter which shows the negligible effect as presented in table 7.2.

5.10.4 Spectrum for pile-up of ^{39}Ar with low energy Cherenkov light

The estimation of pile-up fraction for ^{39}Ar decay triggers with low energy Cherenkov triggers is calculated through similar Monte Carlo simulations. The Cherenkov spectrum obtained from the simulated gammas from ^{40}K and ^{208}Tl sources (as discussed in section 5.9) at different thresholds are compared. The Cherenkov trigger is selected at random from the Cherenkov spectrum, and the final energy of the pile-up is calculated by adding the energies of the randomly selected Cherenkov trigger with the random ^{39}Ar trigger from the spectrum in figure 5.23 within 10.028 μs for the length of trigger window.

In the energy limits for selected ROI between 700 to 1200 PE, the fraction of the piled-up triggers for the Cherenkov light coincidence with the ^{39}Ar at different lower thresholds is given in the table 5.5. However, the fraction of pile-up from this Cherenkov light with ^{39}Ar is negligibly affected by the threshold change as calculated from the MC simulations.

Table 5.5: The fraction of pile up triggers from Cherenkov light with ^{39}Ar in ROI for a trigger window of 10.028 μs

Gamma source	Lower threshold for detector		
	0 ADC	50 ADC	150 ADC
^{40}K	20.81%	20.83%	20.81%
^{208}Tl	20.79%	20.82%	20.79%

The verify the fraction of ^{39}Ar and Cherenkov triggers in data, and MC studies, the Cherenkov spectrum from the physics data taken at a low threshold of 150 ADC which is given in figure 5.18 is used again. The pile-up spectrum for the coincidence of scintillation light from low energy Cherenkov trigger and ^{39}Ar beta decay is shown in the figure 5.28 where the ROI (highlighted in within the red lines) contains 20.81%

of the spectrum, which returns,

$$\epsilon_{4,1} = 0.21 \tag{5.29}$$

Similar to the fraction of other trigger types, the systematic uncertainty is calculated from this parameter by increasing the value of $\epsilon_{4,1}$ with 5%, and there is no significant change noticed in the lifetime measurement of ^{39}Ar, the details are highlighted in the table 7.2.

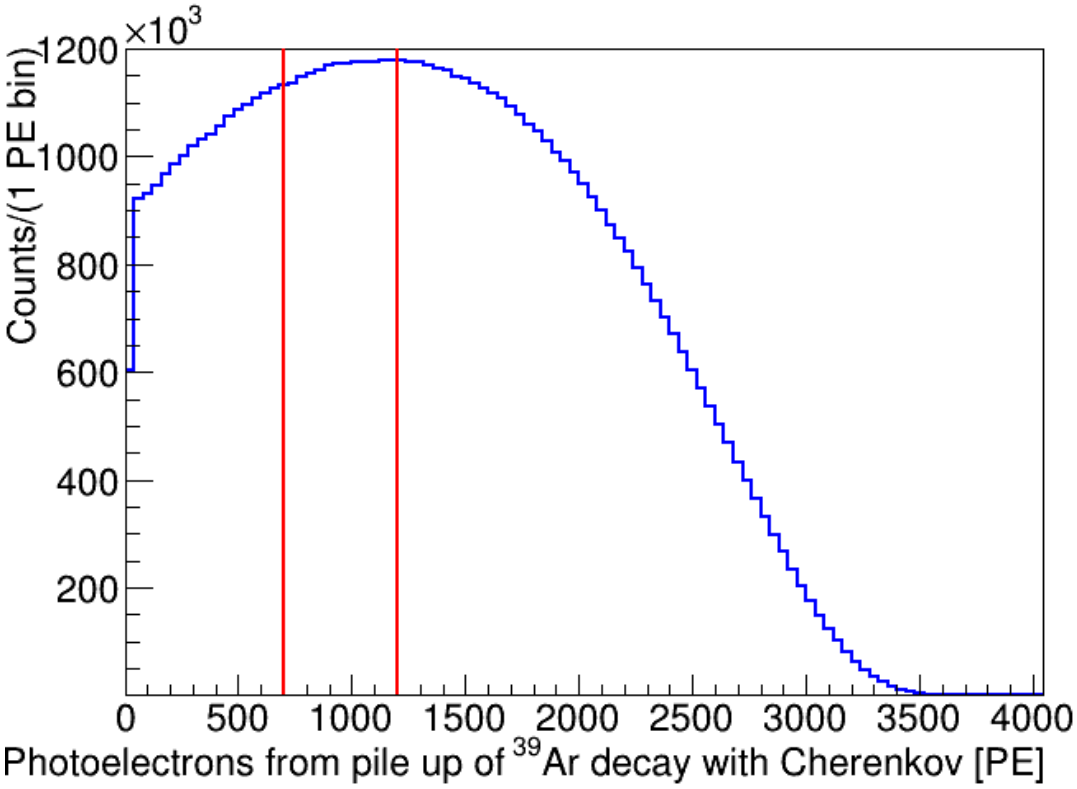

Figure 5.28: The beta spectrum for ^{39}Ar isotopes where the recorded triggers are piled up with any low energy Cherenkov light trigger in the DAQ window of 10.028 μs. The selected ROI is shown in the red lines which consist of 20.81% of this spectrum.

Thus, the fraction of various physics triggers which are in coincidence with ^{39}Ar decay triggers are calculated from the simulations and are known. These fractions are

independent of time, hence can be used as constant values in the fit function (5.24).

5.11 Software efficiency for ^{39}Ar data selection cuts

The efficiencies for the software cuts used with ^{39}Ar data in the fit function from equation (5.24) are investigated and detailed in this section. These parameters are included in the fit function such that the correct number of different trigger types are counted in the study, and to neglect any systematic from the efficiency of cuts. The efficiency is investigated over time, and the relevant uncertainties are considered for the uncertainties on the rate of ^{39}Ar triggers.

The efficiency for various data cleaning cuts used in the analysis is calculated from the simple ratio of the number of triggers passing the cut ($N_{triggerspassingcuts}$) to the total number of triggers before making the cut ($N_{triggersbeforecuts}$), therefore,

$$\text{Efficiency}(\epsilon) = \frac{N_{triggerspassingcuts}}{N_{triggersbeforecuts}} \tag{5.30}$$

The fmaxpe and fprompt cut variables are the only software cuts studied for the ^{39}Ar selection as mentioned in section 5.5. The calcut and dtmTrigSrc cut is the basic low-level cuts to remove any type of noise and other non-physics triggers in the data, thus the efficiency for these two cuts is not investigated since these variables remove only the unwanted backgrounds in the data.

In addition, fmaxpe and fprompt cut variables were used collectively while selecting ^{39}Ar triggers in the physics data, thus the product of the efficiency for these cuts is determined for the final consideration. However, the resultant number of ^{39}Ar decays in the run number would be the same irrespective of the order of the cuts used. The calculation for the variable ($\prod_{j=2}^{3} \epsilon_{i,j}(\text{t})$) for any ith type of trigger (where i can

vary from 1 to 4 for different trigger types as discussed in section 5.8.1) is written explicitly in the following way,

$$\epsilon_{fmaxpe} = \frac{N_{triggerspassingfmaxpecut}}{N_{triggersbeforefmaxpecut}} \tag{5.31}$$

and,

$$\epsilon_{fprompt} = \frac{N_{triggerspassingfpromptcut}}{N_{triggersbeforefprompt}} \tag{5.32}$$

The product of the calculated efficiencies is performed for further use in the fit model. The mean value of software efficiencies ($\prod_{j=2}^{3} \epsilon_{i,j}(\mathrm{t})$), and its time dependence, hence uncertainties ($\prod_{j=2}^{3} \sigma_{\epsilon_{i,j}}(\mathrm{t})$) for any type of trigger i are constrained separately in two separate ways. The mean value of efficiencies is constrained by the simulated MC samples of different trigger types. The acceptance of subeventN cut (section 5.2.3.2) is studied from the above method firstly (which is used for the selection of different trigger types from the data for time dependence study) from simulated samples as discussed in the section below.

5.11.1 Acceptance of subeventN cut for selecting pile-up events

The subeventN is purely used in the experiment to select the waveforms with the single pulses, and hence single triggers. If this cut is used for the pile-up, there is uncertainty on this cut given the timing and energy selection used in this processor. If the two triggers have a separation in a time difference of fewer than 40 ns, and/or if the charge of the second pulse is less than 10% of the first pulse, these pulses will not be considered separate triggers by this cut variable. To select the different types of triggers in data, the subeventN cut is used with data, such that the selection is made

only for the single, double, and triple ^{39}Ar decays initially in the corrected energy region (where the PE region between 700 to 1200 PE was modified for the change in the light yield value of detector) on run by run basis. Therefore, it is important to validate the performance of this cut for the pile-up.

The acceptance of the subeventN cut is validated from the MC samples of ^{39}Ar decay triggers which are simulated with the detector setup conditions in RAT (Reactor Analysis Tool, version 5.13.0), and with the trigger window length. The acceptance of subeventN cut for selecting single ^{39}Ar decay triggers is 100% both in MC and in data samples. However, for the selection of double and triple ^{39}Ar decays, the acceptance of this cut is different by 6% and 12% respectively. This will only affect the pre-selection of the trigger types from the dataset, however, its distribution over the time period of the dataset is very stable as required for this study.

The efficiency study for the famxpe and fprompt cuts for the selection of different event types in the ROI with its variation over the entire data set is detailed in the following sub sections.

5.11.2 Efficiency for selecting single ^{39}Ar decay events

The efficiency calculations for the selection of single ^{39}Ar decay triggers is $\sim$100% from both the simulated MC samples and physics data. Also, the trend for the product of the efficiency of both ^{39}Ar selection cuts, fmaxpe, and fprompt for the selection of these triggers in the dataset is shown in figure 5.29.

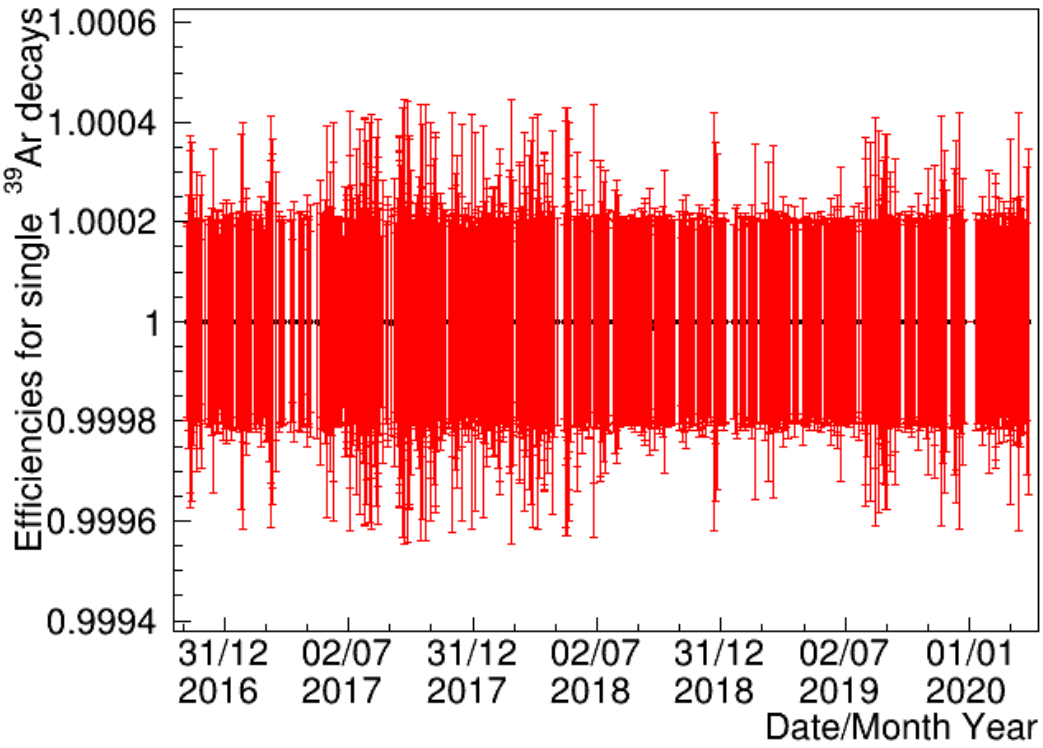

Figure 5.29: The trendline for the efficiency of cuts used in the selection of single ^{39}Ar triggers in the dataset. The acceptance for selection of single ^{39}Ar triggers is almost ∼100%.

If N_a and N_b are the numbers of events after and before applying the cuts, the uncertainties on the efficiency are calculated from the error propagation as follows,

$$\epsilon = \frac{N_a}{N_b} \tag{5.33}$$

$$\sigma_\epsilon = \sqrt{(\frac{\sigma_{N_a}}{N_b})^2 + (\frac{N_a * \sigma_{N_b}}{{N_b}^2})^2} \tag{5.34}$$

where σ_{N_a} and σ_{N_b} are the uncertainty on the number of events after and before applying the cuts respectively from the Poisson statistics, $\sigma_{N_a} = \sqrt{N_a}$, and $\sigma_{N_b} = \sqrt{N_b}$. The uncertainties on the measured efficiencies are very small, the one-dimensional

distribution of the uncertainties is presented in figure 5.30.

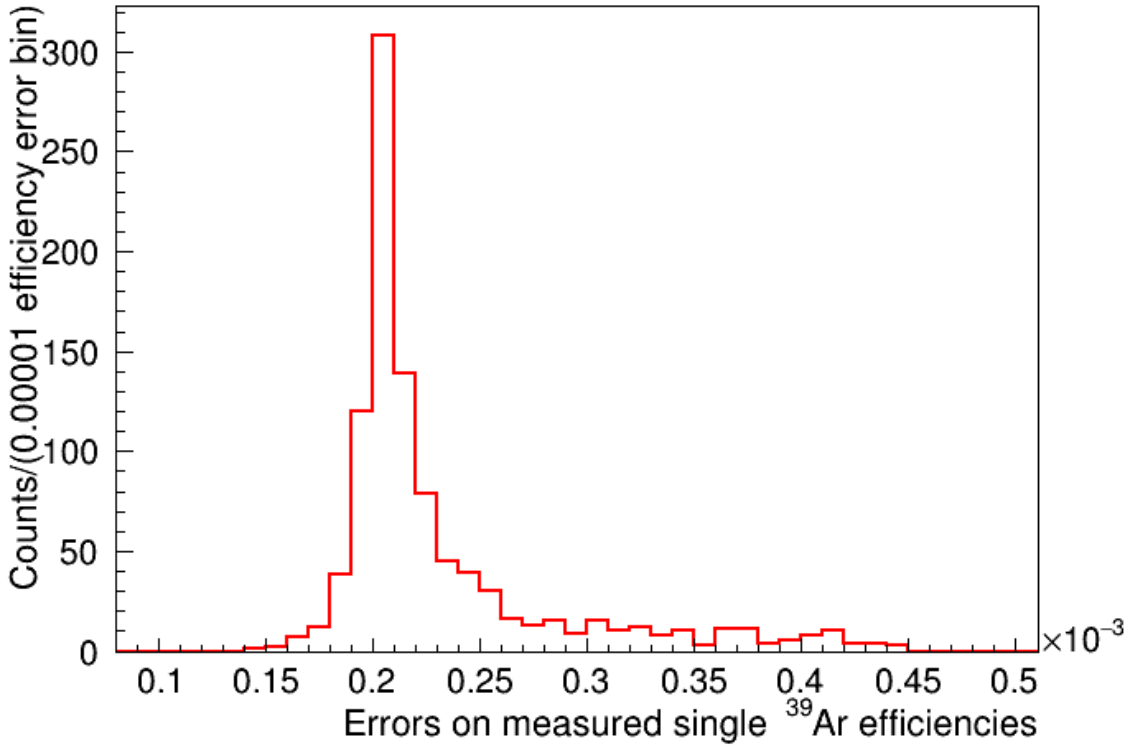

Figure 5.30: The one-dimensional distribution of the uncertainties on the measured efficiency of software cuts used in the selection of single ^{39}Ar triggers in the dataset.

Moreover, the one-dimensional distribution of the calculated efficiency provides the mean value with the uncertainty from this variable used in the fit function, see figure 5.31. As the figure suggests the mean value of the efficiency is almost 100% with the standard deviation in order of 10^{-5} which is very small hence the trigger selection in ^{39}Ar decays is very precise. The value for the variable, $\prod_{j=2}^{3} \epsilon_{1,j}(\mathrm{t})$ is,

$$\prod_{j=2}^{3} \epsilon_{1,j}(t) = 1.00000000 \pm 0.00000079 \tag{5.35}$$

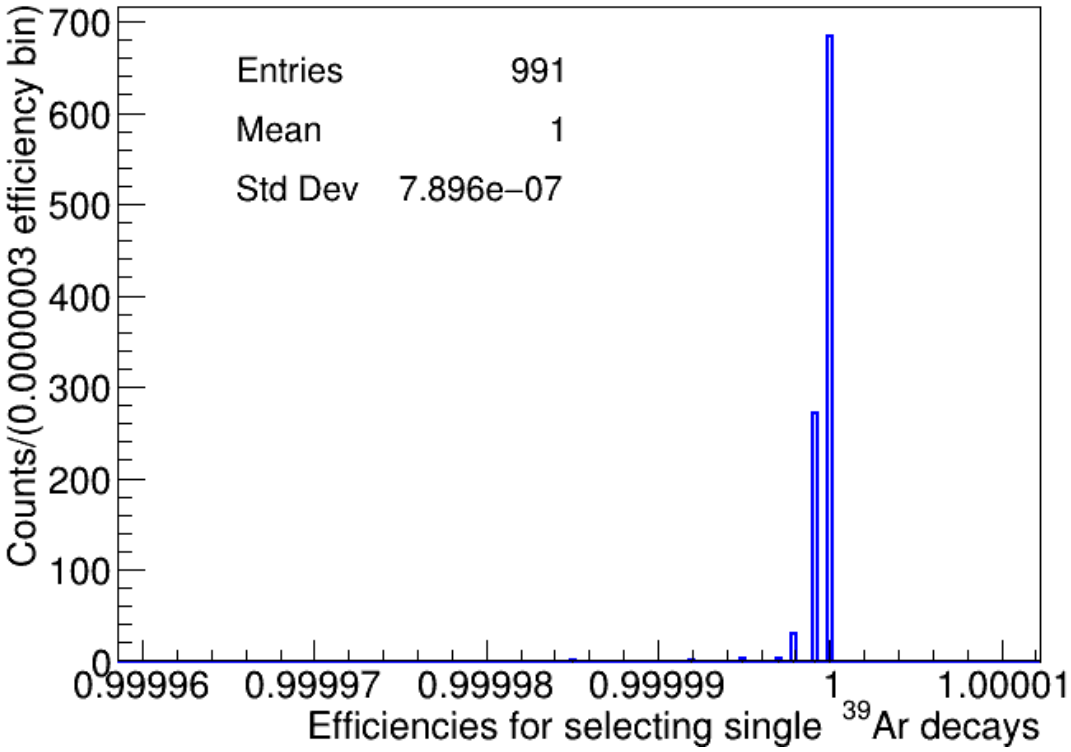

Figure 5.31: The one-dimensional distribution for the efficiencies of selecting the single ^{39}Ar triggers from the dataset using the fmaxpe and fprompt cut variables.

5.11.3 Efficiency for selecting double ^{39}Ar decay events

The average value of efficiency for selecting the double ^{39}Ar decays in the dataset using the cut variables fmaxpe, and fprompt with the initial use of subeventN cut is 85%. Also, in simulated MC samples, this number is evaluated as 90.87% $\approx$ 91%. The 6% difference in the mean value described from the pre-selection of good double ^{39}Ar decays in the data is validated from the use of subeventN==2 cut with the MC samples, which returned the same value for the efficiencies (85%) with use of this extra cut. Therefore, the mean value of $\prod_{j=2}^{3} \epsilon_{2,j}(\mathrm{t})$ is constrained in the study from

the MC samples. The average value of efficiencies is calculated from the equation,

$$\prod_{j=2}^{3} \epsilon_{2,j}(t) = \prod_{j=2}^{3} \epsilon_{2,j_{data}}(t) + (\prod_{j=2}^{3} \epsilon_{2,j_{MC}} - \prod_{j=2}^{3} \epsilon_{2,j_{mean,data}}) \tag{5.36}$$

Thus, the 6% factor is introduced from the second term in the equation. The effect of different mean values of efficiencies from data and MC is independently studied in the fit model as additional systematic, and only the variation in the efficiencies over time hence the spread of these values acts as a minor systematic for the analysis and is discussed in the section 7.3.6.3. The trend in the product of efficiency for selecting the double ^{39}Ar decays in the dataset using the cut variables fmaxpe, and fprompt with time (including 6% correction in the mean efficiency) is presented in figure 5.32.

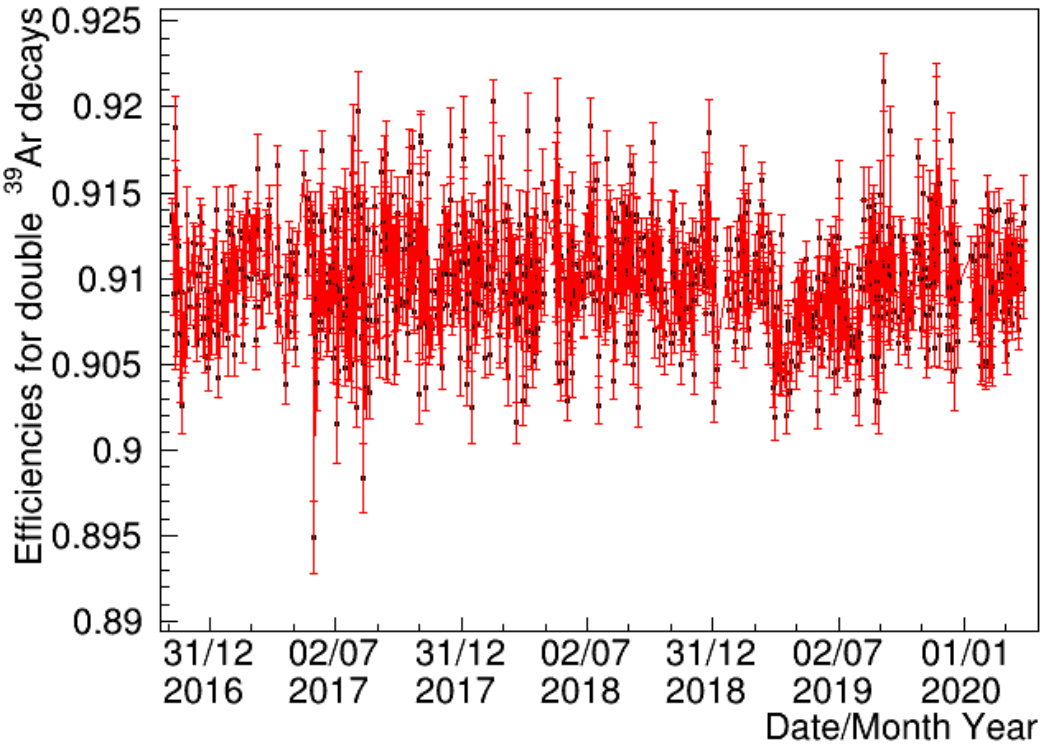

Figure 5.32: The trendline for the efficiency of cuts used in the selection of double ^{39}Ar decays in the dataset. The acceptance for selection of double ^{39}Ar triggers is around 91% which mainly indicates the 9% of double ^{39}Ar decays occur in the high window above 0.41 fprompt value.

The uncertainties on the measured efficiencies in the one-dimensional distribution can be seen in figure 5.33.

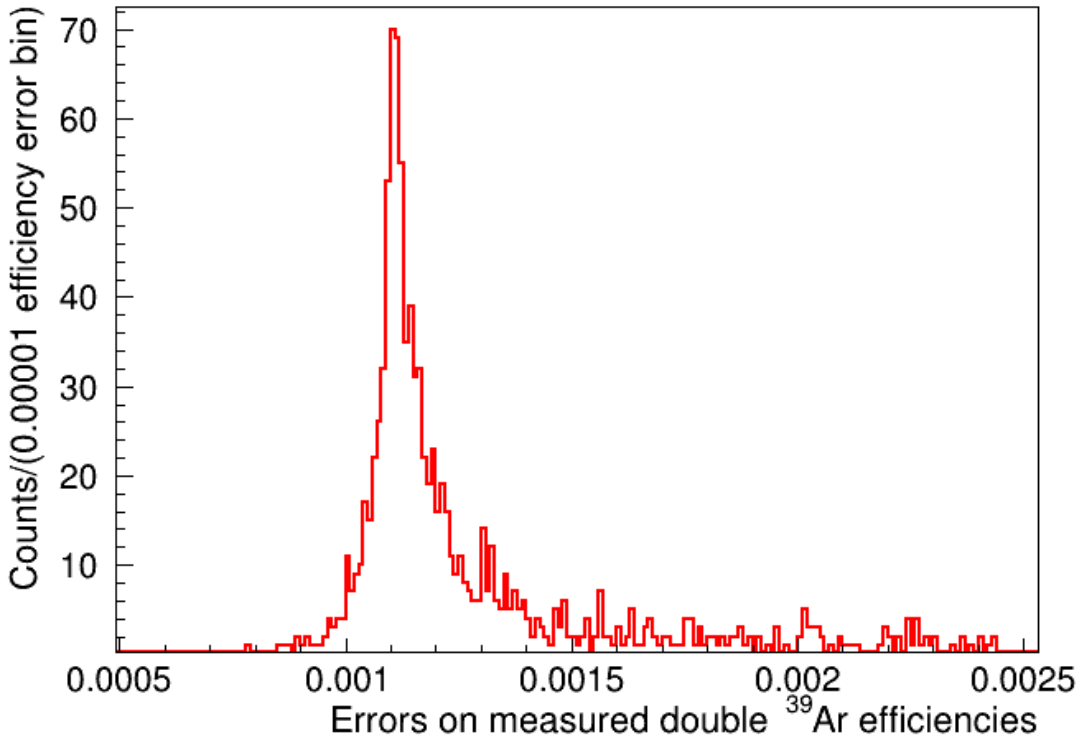

Figure 5.33: The one-dimensional distribution of the uncertainties on the measured efficiency of software cuts used in the selection of double ^{39}Ar decay triggers in the dataset.

The mean acceptance of the selection cuts for double ^{39}Ar decay triggers from figure 5.34 is 0.9099±0.0033, which implies nearly 9% of double ^{39}Ar decay triggers fall in the region in higher fprompt region above 0.41, this is mainly explained from the trigger time information.

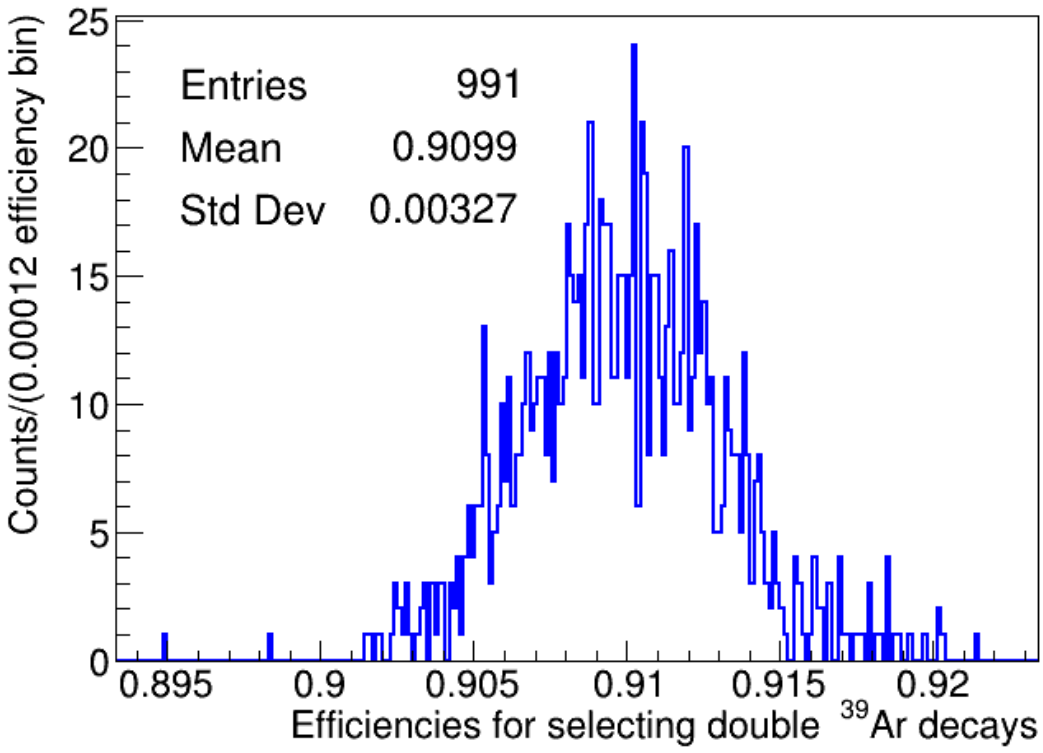

Figure 5.34: The one-dimensional distribution for the efficiencies of selecting the double ^{39}Ar decays from the dataset using the fmaxpe and fprompt cut variables.

The DAQ window in the DEAP-3600 experiment calculates the prompt time from the largest pulse always which means if the pulse with the highest charge values occurs lately in the time window (10.028 μs), the calculation of the fprompt variable returns the larger values. The correction factor of the acceptance of these triggers is thus applied in the fit function to account for the exact value of double ^{39}Ar decays in the study, although the contribution of these triggers is very small in the dataset. Therefore,

$$\prod_{j=2}^{3} \epsilon_{2,j}(t) = 0.9099 \pm 0.0033 \tag{5.37}$$

5.11.4 Efficiency for selecting triple ^{39}Ar decay events

The product of the software efficiencies for selecting the triple ^{39}Ar decay triggers is calculated in a similar way from both MC samples and data. For the selection good triple ^{39}Ar decay triggers, there is a 12% difference in the efficiencies from data and MC, but the proportion of these triggers in the ROI is very low. Also, the mean value of efficiency for selecting these triggers in the dataset is corrected by 12% which comes out to be 86.04%, and the equation to calculate the average value of cut efficiencies for triple ^{39}Ar decays are,

$$\prod_{j=2}^{3} \epsilon_{3,j}(t) = \prod_{j=2}^{3} \epsilon_{3,j_{data}}(t) + (\prod_{j=2}^{3} \epsilon_{3,j_{MC}} - \prod_{j=2}^{3} \epsilon_{3,j_{mean,data}}) \tag{5.38}$$

Thus, the 12% factor is introduced from the second term in the equation. Also, the effect of different average values of the efficiencies is included as an additional systematic in the study which does not change the lifetime of ^{39}Ar significantly, see the section 7.3.6.4 for more details. The trend line and one-dimensional distribution of efficiencies with uncertainties for selecting triple ^{39}Ar decay triggers are as shown in the figure 5.35, and 5.36 respectively.

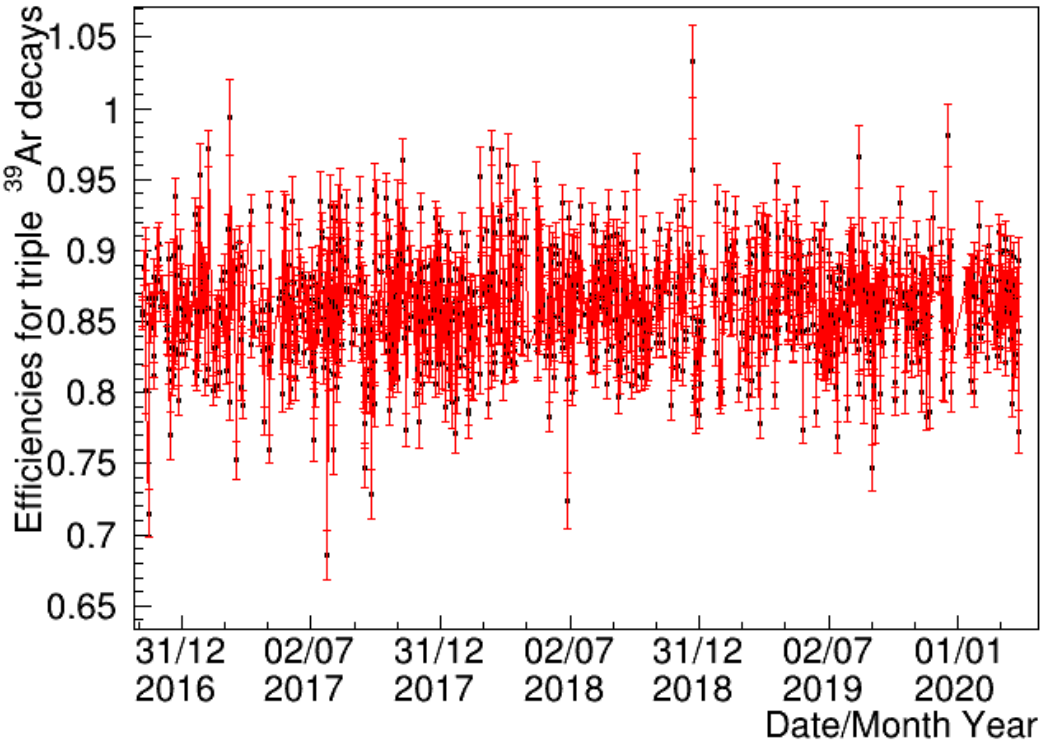

Figure 5.35: The trendline for the efficiency of software cuts used in the selection of triple ^{39}Ar decay triggers in the dataset. The acceptance for selection of triple ^{39}Ar triggers is around 86% which mainly indicates the 14% of double ^{39}Ar decay triggers occur in the high window above 0.41 fprompt value.

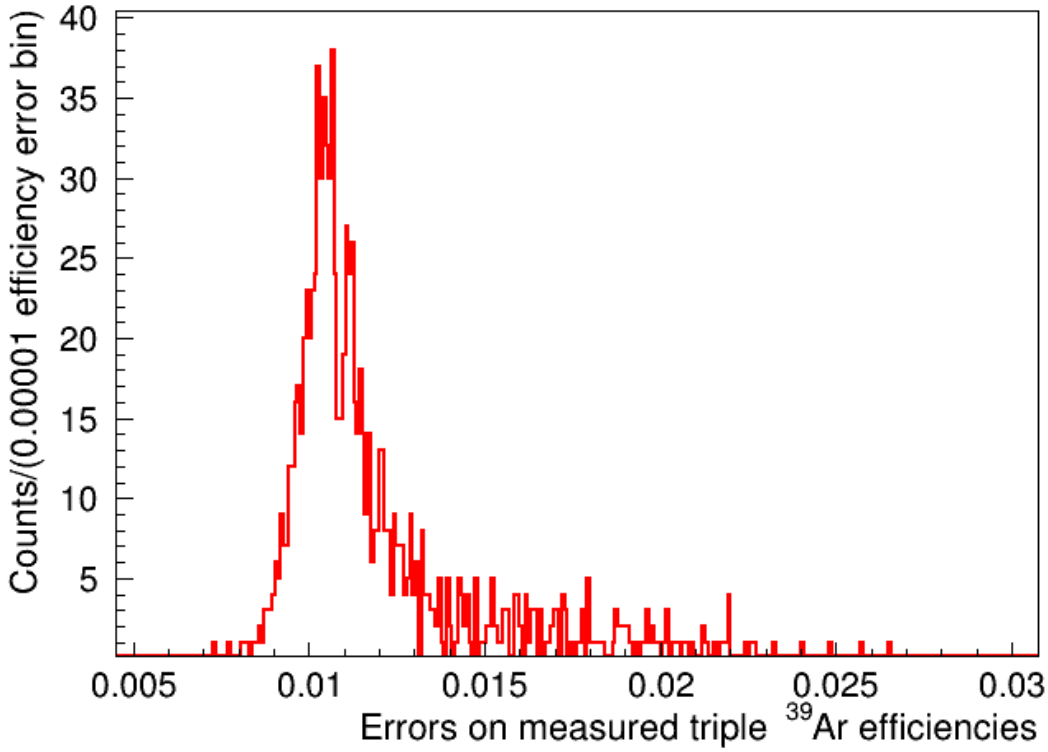

Figure 5.36: The one-dimensional distribution of the uncertainties on the measured efficiency of software cuts used in the selection of triple ^{39}Ar decay triggers in the dataset.

The acceptance for selecting the triple ^{39}Ar decays in ROI is around 86%, as conveyed by the one-dimensional distribution of the mean efficiency from figure 5.37, which gives,

$$\prod_{j=2}^{3} \epsilon_{3,j}(t) = 0.8604 \pm 0.03901 \tag{5.39}$$

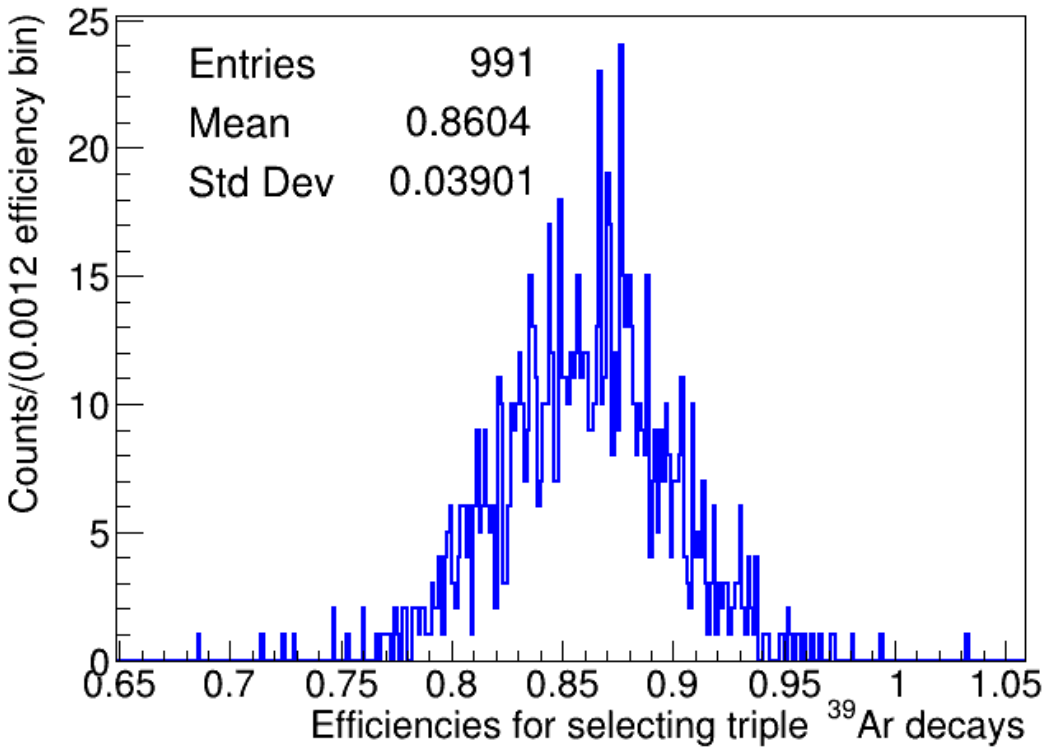

Figure 5.37: The one-dimensional distribution for the efficiencies of selecting the triple ^{39}Ar decays from the dataset using the fmaxpe and fprompt cut variables.

The lowest value of the acceptance is again explained from the time information of the waveform.

5.11.5 High fprompt values for ^{39}Ar pile up decay triggers

There are about 9%, and 14% of double and triple ^{39}Ar decay triggers respectively which are rejected with the selection of ROI. This is mainly due to the higher values of the fprompt variable for the double and triple ^{39}Ar decays that can be explained on the basis of the trigger time window distribution of the signals.

The scanning window in the DAQ which look for the largest pulse in the waveform calculated the prompt window from these pulses. If the second pulse in the

waveform has a higher charge than the first pulse then the prompt will be calculated from it such that the fprompt variable (in section 5.2.2) would have a comparatively larger numerator (which is still less than the denominator) and hence the fprompt gives the value much higher than the 0.41 which is the upper limit set for the ROI. Figure 5.38, 5.39, and 5.40 shows the trigger time distributions as a function of fprompt variable for a physics run for single, double and triple ^{39}Ar decay triggers respectively.

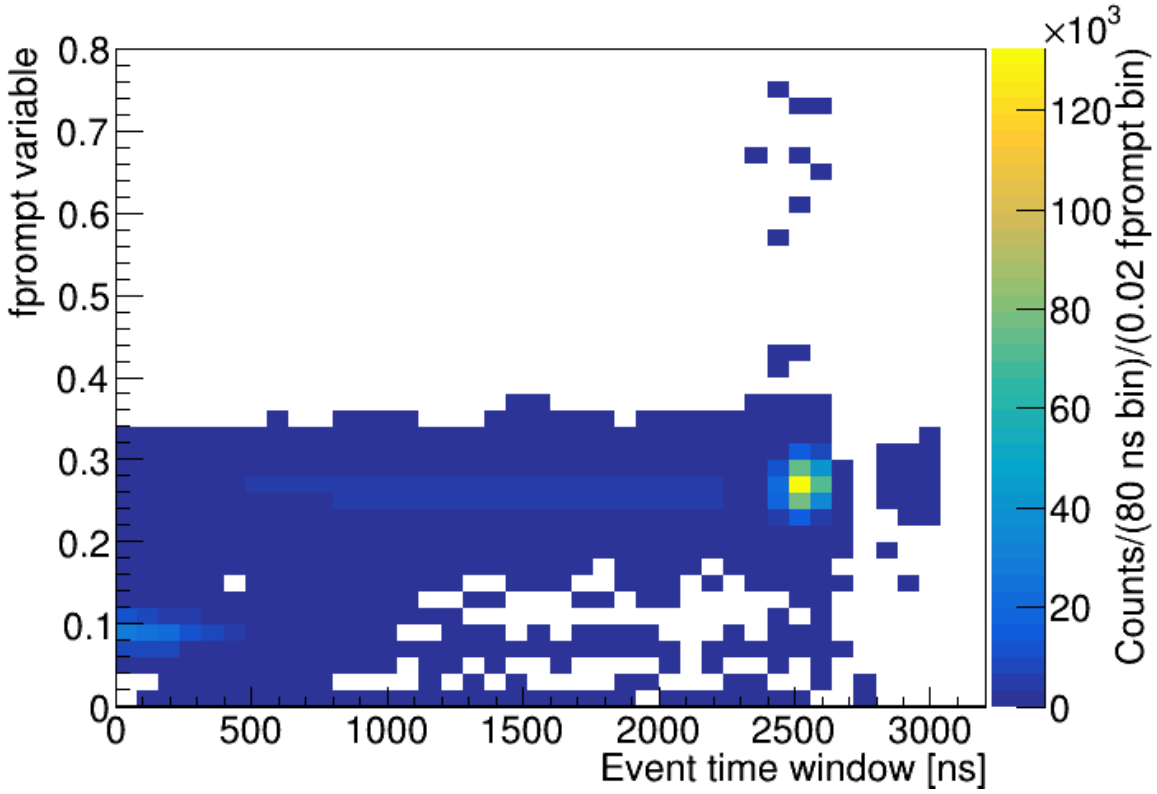

Figure 5.38: The trigger time distribution of single ^{39}Ar trigger type with respect to the fprompt variable value. The large fraction of single ^{39}Ar decay triggers occurs in the trigger window 2400 to 2700 ns.

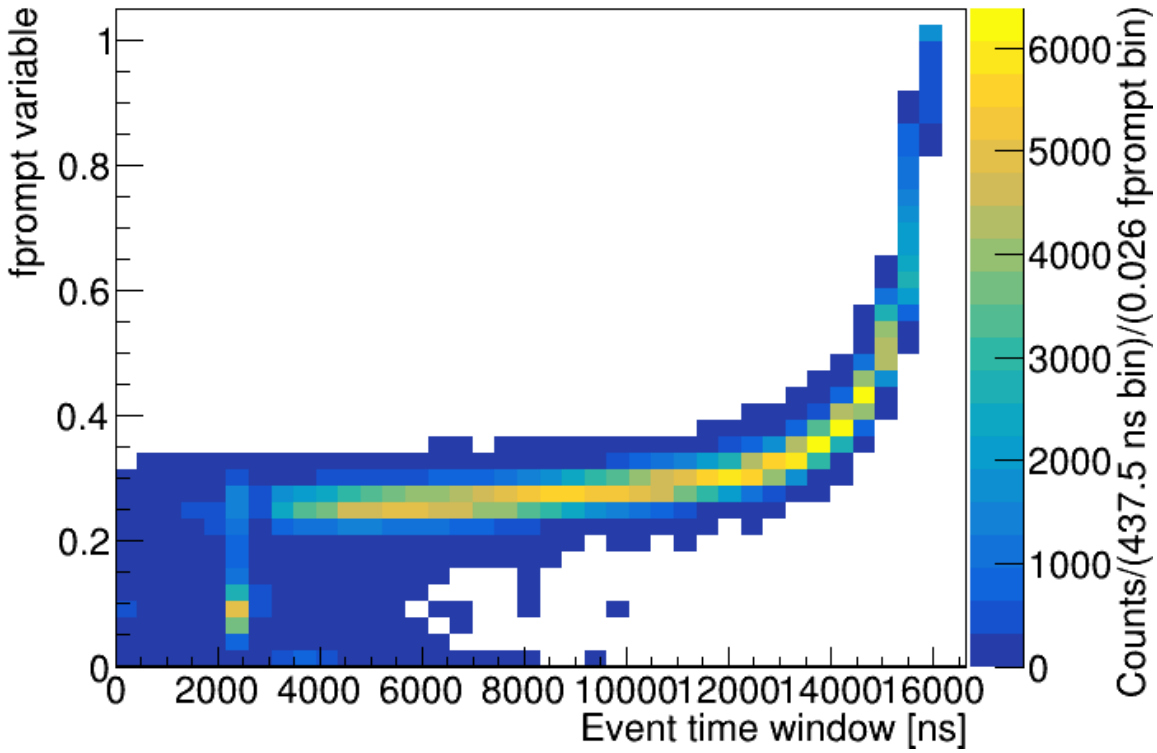

Figure 5.39: The trigger time distribution of double ^{39}Ar decay trigger type with respect to the fprompt variable value. There is about ∼9% of double ^{39}Ar decay triggers which are rejected by the selected fprompt region (0.0,0.41), falls at the end of the trigger window hence a correction factor for the fraction of these trigger types in the ROI is used in the final fit model (see equation (5.24)).

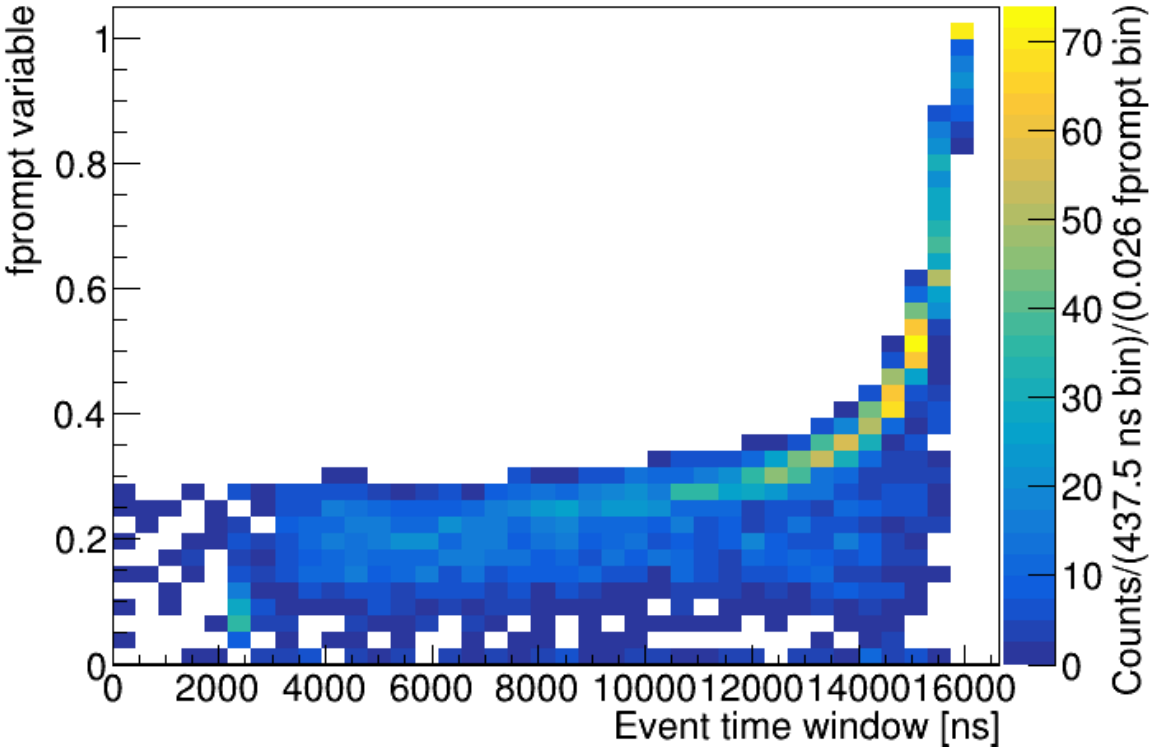

Figure 5.40: The trigger time distribution of triple ^{39}Ar decay trigger type with respect to the fprompt variable value. There is about ∼14% of double ^{39}Ar decay triggers which are rejected by the selected fprompt region (0.0,0.41), falls at the end of the trigger window hence a correction factor for the fraction of these trigger types in the ROI is used in the final fit model (see equation (5.24)).

5.11.6 Efficiency for selecting ^{39}Ar and Cherenkov coincidence triggers

The software selection efficiency for the coincidence of ^{39}Ar decay triggers with the low energy Cherenkov light in the ROI is evaluated from MC studies. The efficiency for the fmaxpe and fprompt cut variables for selecting the pile-up of low energy Cherenkov light with ^{39}Ar triggers is 100%. The fprompt region for the Cherenkov light is above the value 0.8, and hence the selection cuts return the same trigger count

in the ROI. Thus, we have,

$$\prod_{j=2}^{3} \epsilon_{4,j} = 1.00 \tag{5.40}$$

5.12 Event multiplicity for ^{39}Ar triggers

The event multiplicity parameters in the fit model from equation (5.24) are inputted from the DAQ trigger settings. There will be only one trigger recorded from the system for the pile-up of ^{39}Ar scintillation light either with itself or any other type of the scintillation light, irrespective of the number of light pulses generating the summed light or the final number of photoelectrons. The event multiplicity for different trigger types can be written in the following equation,

$$\text{Number of } ^{39}\text{Ar decays recorded in one trigger} = M_n * 1, \text{ for } n = 1 \text{ to } 3 \tag{5.41}$$

The subscript n represents the trigger type where the scintillation light in the trigger is recorded from the decay of single (n = 1), double (n = 2), and triple (n = 3) ^{39}Ar isotope simultaneously in the detector. The values for the multiplicity for different number of decays is,

$$M_1 = 1 \tag{5.42}$$

$$M_2 = 1/2 \tag{5.43}$$

$$M_3 = 1/3 \tag{5.44}$$

Therefore, the event multiplicity terms in the fit model for ^{39}Ar rates in equation (5.24) are fixed with the following values,

$$\epsilon_{1,4} = 1.00 \tag{5.45}$$

$$\epsilon_{2,4} = 1/2 = 0.5 \tag{5.46}$$

$$\epsilon_{3,4} = 1/3 = 0.33 \tag{5.47}$$

$$\epsilon_{4,4} = 1/2 = 0.5 \tag{5.48}$$

Thus, the calculated fraction of different ^{39}Ar triggers in ROI, and the event multiplicity and software efficiencies for the selection of different ^{39}Ar triggers can be constrained in the fit model from equation (5.24).

5.13 ER backgrounds in DEAP-3600

The energy spectrum for the electron recoils in the DEAP-3600 is well described in the publication [1], and is shown in the figure 5.41. This spectrum is plotted in the PE scale for consistency, and the background rates contribution from the electron recoils in ROI is investigated from this model.

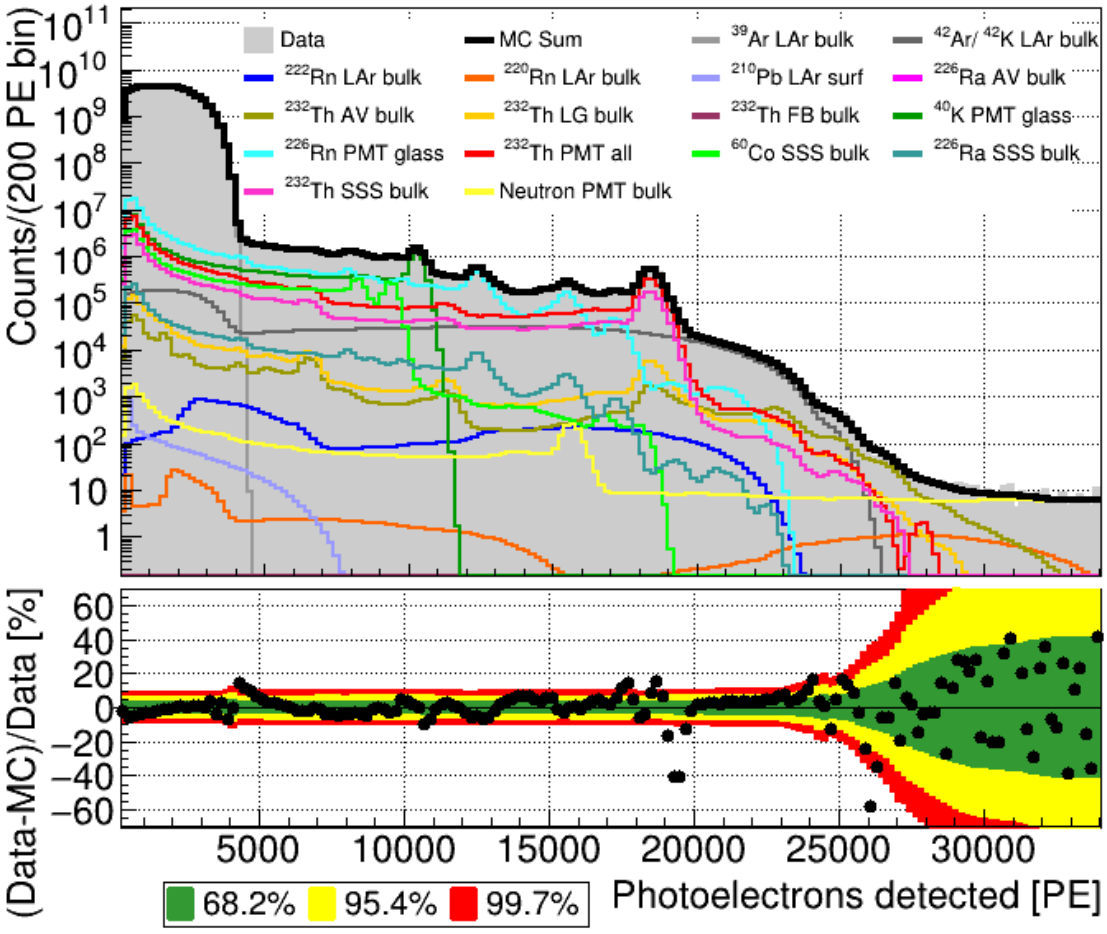

Figure 5.41: Top panel: The energy spectrum of the ER background model components with one year of dataset shaded in gray. Bottom panel: The residuals of data and MC model in percent with different confidence intervals.

The ER background rates are calculated by adding the gamma background triggers in ROI other than ^{39}Ar decays. The trigger counts for these backgrounds in ROI is determined from the subtraction of ^{39}Ar LAr bulk from the total MC sum, the difference is then normalized to the livetime of the dataset. This spectrum was plotted from the 247.2 days of the physics dataset but in the current fit model, there are about 3.5 years of the physics dataset. The ER backgrounds are mainly emitted from the different detector components which were the same and not varied

over the entire dataset hence these ER rates are expected to be constant. The other ER background rates from this calculation come out ∼1.65 Hz which is fixed in the analysis for the systematic studies, and validation studies are also performed by floating this parameter further discussed in the section 7.1.1.

5.13.1 Consistency of ER backgrounds over time

The ER backgrounds calculated in the publication [1] are evaluated from the one year of the dataset. For this analysis, the time dependence of the ER backgrounds is tested from the rates of gammas from the ^{232}Th, and ^{238}U daughter isotope.

The rates for the ^{232}Th are measured from the ^{208}Tl gamma peaks over time. The Gaussian distribution with the linear background model is fitted to the ^{208}Tl gammas peaks to extract the number of events in the peak with respect to the run numbers. The calculated events are then divided with the total livetime of the run number and rates are plotted on a weekly bin basis using the rate algorithm. The rates of the ^{208}Tl gamma peaks are shown in figure 5.42.

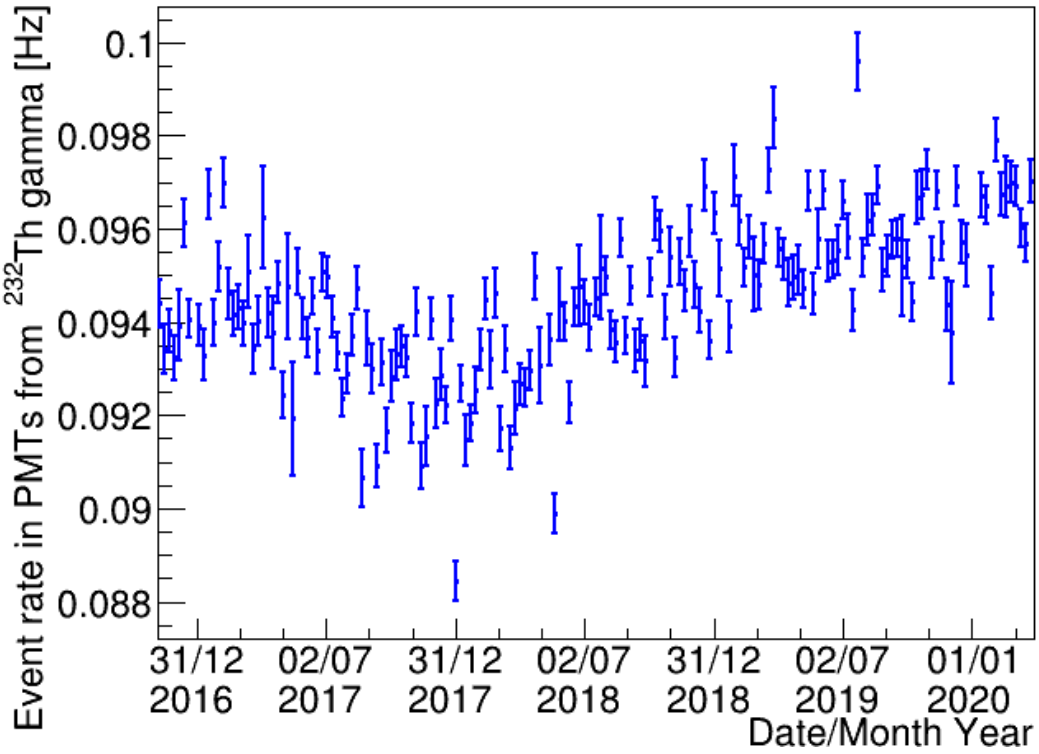

Figure 5.42: The rates of the ^{208}Tl gammas as a function of time evaluated from the area under the peak with the background subtraction.

The measured rates from the ^{208}Tl gamma peaks are pretty stable over time with a very negligible spread. Also, the one-dimensional distribution of the calculated rates for ^{232}Th is given in figure 5.43.

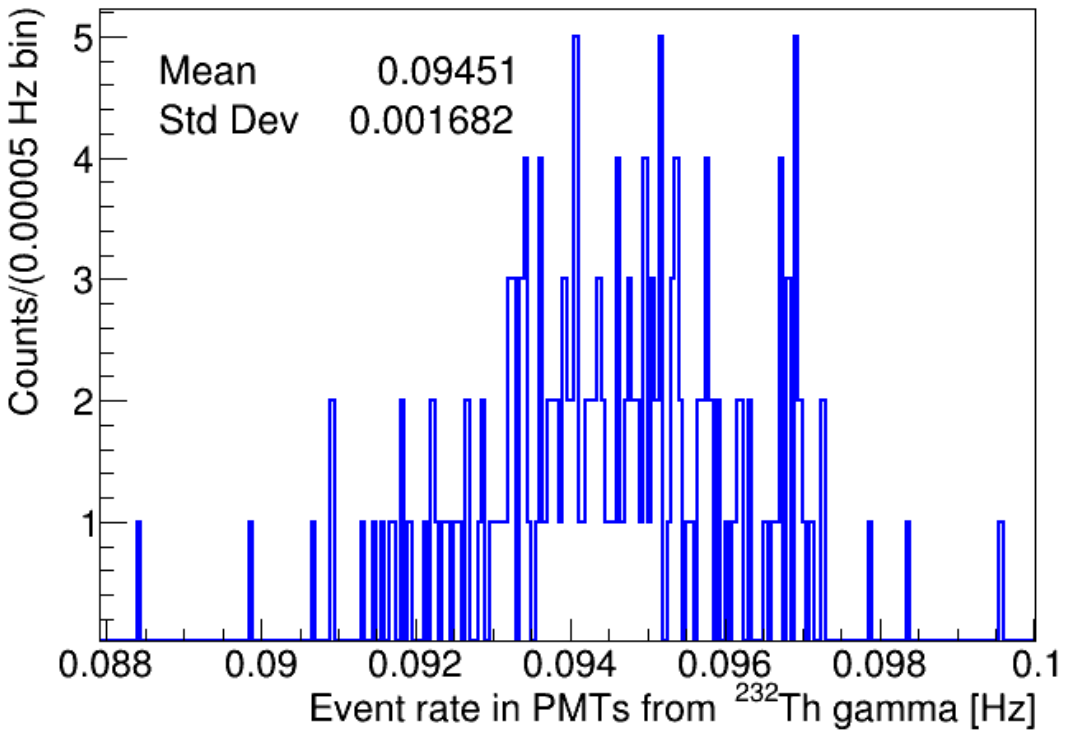

Figure 5.43: The one-dimensional distribution for the rates of ^{208}Tl gammas as a function of time evaluated from the area under the peak with the background subtraction.

The average value of the calculated rates is (0.095 ± 0.0017) Hz in the higher energy region. To estimate the fraction of these backgrounds in the ROI, the ratio of the event contribution from the ROI to the peak position of ^{208}Tl is determined using the gammas distribution from the [1]. These calculations showed the excess of 5 times the extra events in the ROI from these gammas as presented in the figure 5.44.

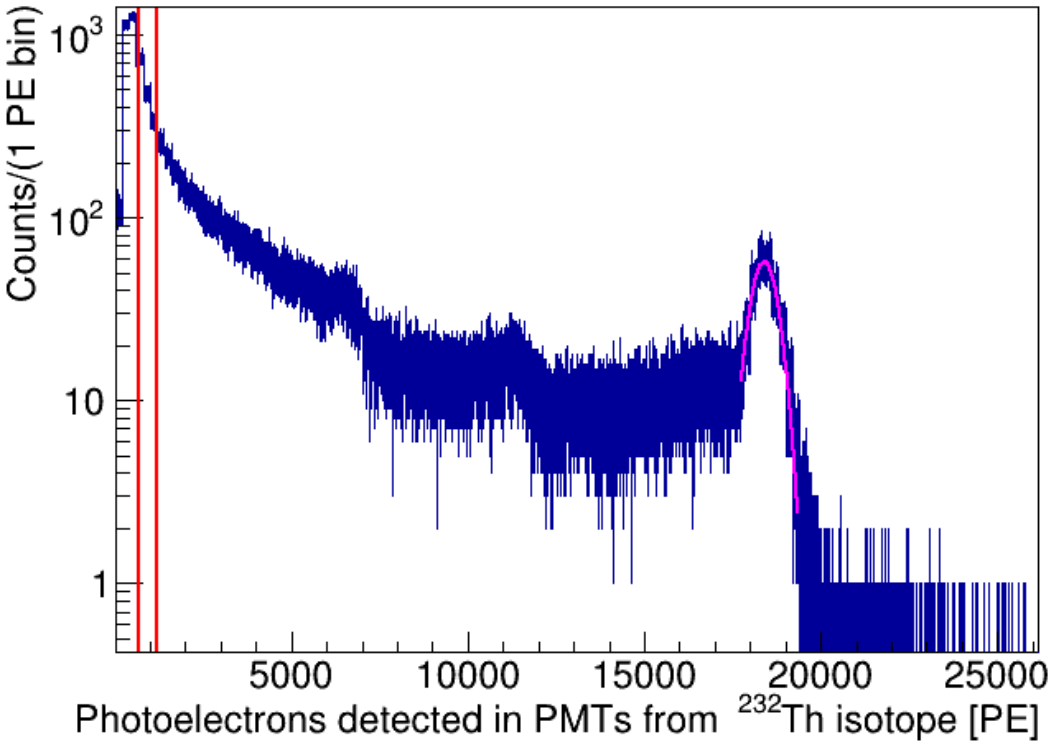

Figure 5.44: The energy distribution for the gammas of ^{232}Th chain in the ROI to the high energy region. The red lines are enclosed ROI, and the pink fit model shows the Gaussian fit to the ^{208}Tl gamma peak.

The systematic uncertainty on the lifetime of the ^{39}Ar is measured from a little change of 0.0084 Hz in the ER background term contributed from the ^{232}Th decay in the ROI in the chapter 5. To further verify the consistency of the ER backgrounds from the ^{238}U decay, the gamma rates of the ^{226}Ra peaks are plotted with a similar approach. The rate of the ^{226}Ra gamma peaks over time are given in figure 5.45.

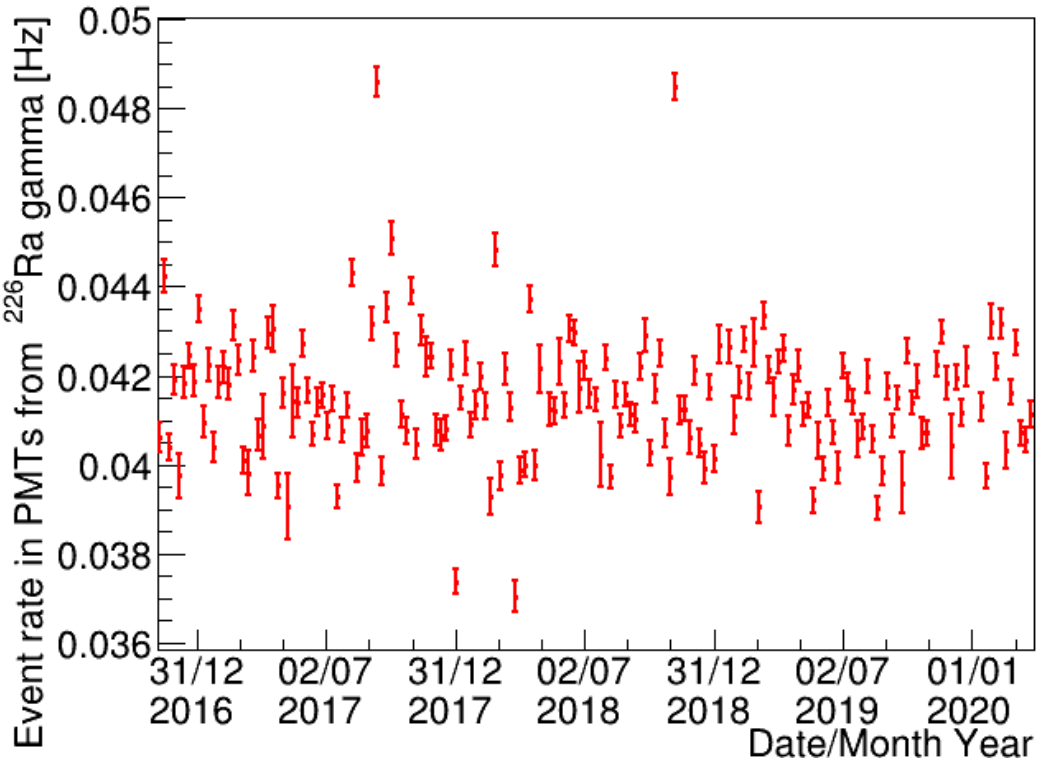

Figure 5.45: The rates of the ^{226}Ra gammas as a function of time evaluated from the area under the peak with the background subtraction.

The one-dimensional distribution of the calculated rates from ^{226}Ra gammas showed the mean value, (0.042 ± 0.0015) Hz as presented in the figure 5.46.

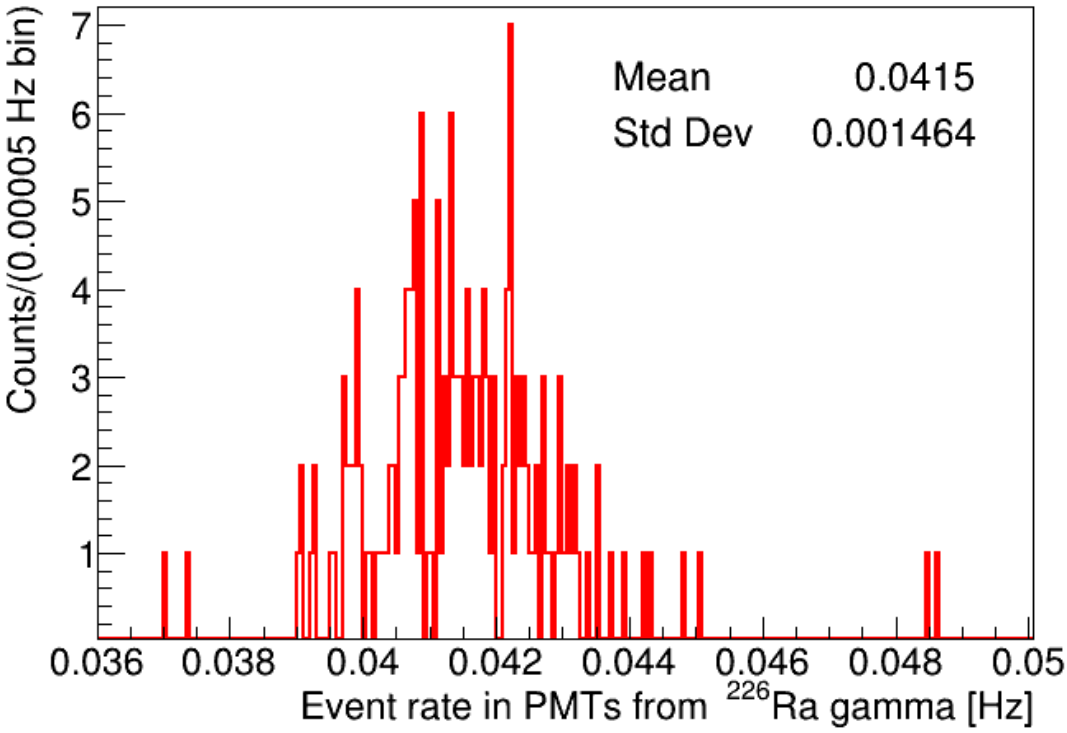

Figure 5.46: The one-dimensional distribution for the rates of ^{226}Ra gammas as a function of time evaluated from the area under the peak with the background subtraction.

Also, the energy distribution of the ^{238}U decay from figure 5.47 indicates the excess of 7 times extra rates in the ROI from this contribution of the ER backgrounds.

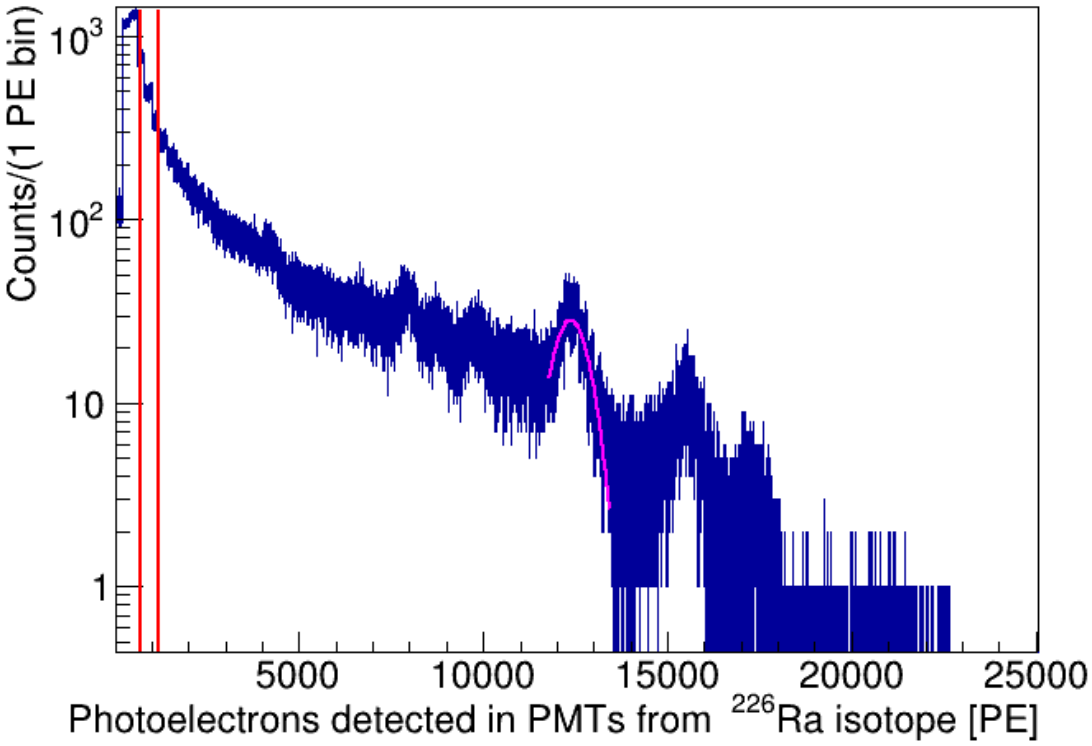

Figure 5.47: The energy distribution for the gammas of ^{238} chain in the ROI to the high energy region. The red lines are enclosed ROI, and the pink fit model shows the Gaussian fit to the ^{226}Ra gamma peak.

Similarly, the small systematic uncertainty on the lifetime of ^{39}Ar from the 0.010 Hz change in the ER background rate is evaluated in chapter 7.

Chapter 6

Data selection and systematic studies from DEAP-3600 data

This chapter discusses the data selection criteria used in the analysis and different detectors systematic which are corrected or considered as additional uncertainties in the trigger rate studies of the DEAP-3600 experiment.

6.1 Physics data included in the study

The lifetime calculation for the decay of ^{39}Ar isotope is studied from the rate of beta decay triggers from this isotope. The physics data from the DEAP-3600 detector from the running period November 2016 to March 2020 is analyzed for this measurement, which is $\simeq$3.4 years of physics dataset. Some data quality tests are performed over the recorded physics data to select the good data for the WIMP analysis and ^{39}Ar lifetime analysis. The details of the various data quality steps are given in the sections below.

6.2 Data quality testing and data selection

The detector stability was excellent throughout the whole period of data taking hence there are not any major effects from the environmental and external factors on the data. However, the little changes in the detector settings sometimes affect the data taking and hence the number of recorded triggers. The physics data from the detector passes through a number of data quality checks before getting selected for the final analysis. The data quality testing includes a few major steps discussed in the following sections.

6.2.1 Automated checks

These checks are performed by the DEAP-3600 experiment DAQ system at the end of each run. It includes information such as PMT voltages, and PMT currents which are expected to be constant or vary negligibly changed throughout the run. The automatic checks also include the testing of the timestamp information of the first and last triggers at various stages of the data recording as the timestamp information for the first and last triggers should be the same for the MIDAS system and digitizers if the timestamps don't match those physics runs are actually crashed and hence these run numbers are not included in the study.

6.2.2 Shifter checks

The monitoring of the DEAP-3600 detector functioning and its data-taking is done by the collaborators during the 24-hour long shifts. These shifts include the responsibility to keep track of detector operation and DAQ system. The DAQ shift mainly consists of taking several runs with calibration data that have been requested and starting the run with physics data and fixing the systems in case any problem occurs. At

the end of every run apart from the automatic checks, the shifter also performs some preliminary checks to test the quality of the data taken. The saved data templates are indicated depending on the data type and the shifter saves the information and questionnaire if the recorded data matches with the templates. This results in the preliminary data quality of different data types in the DEAP-3600 experiment.

6.2.3 Final data quality checks from processed data

The physics data passing the automatic checks and shifter checks are processed for the different variables and parameters used in the DEAP data analysis. The data quality processor works in parallel with other processors and plots some data quality histograms and graphs based on sub run basis which are saved in the data quality root files separately in the database. The sub-run files are summed together and used for the final data quality checks. The final data checks include the manual examination of the plotted distributions for the various parameters. The histograms and graphs saved in the data quality root files are looked up by the data quality team to give the final indication to pass the good physics data for the WIMP and other analyses.

6.2.4 Additional data quality checks

There are some other additional data quality checks performed before finalizing the final run numbers for physics analysis along with the checks discussed above sections. The additional tests involve the study of the stability of AV pressure and the stability of the liquid argon level in the AV. The temperatures of the gaseous argon are recorded using different temperature sensors at the top of the neck region and various sensors located in the filler blocks around the AV, the temperature readings from the sensors are also examined so that there are no fluctuations from the average temperature value during the run. The physics data with run numbers failing any of these stabilities are

rejected for any physics analysis. The physics runs where the acrylic and aluminum reflector fiber (AARF) calibration system was left on by mistake are also removed from the physics analysis because these runs are used to measure the average charge from the PMTs for the SPE (single photoelectron) calibration. In the addition to all these thermodynamic checks, the physics runs with some activity around the detector are rejected from the physics analysis to neglect any source of background.

The 3.4 years of physics data from the DEAP-3600 experiment has 1280 total run numbers that passed all the data quality checks discussed above. These 1280 run numbers cover 878 days of physics data. The summary of the run selection criteria used for the selection of the good physics run numbers are,

1. Must pass all automatic and manual data quality checks
2. The fill level must be stable at around 551 mm with a maximum of 10 mm variation
3. The AV pressure must be stable at around 13.75 psi with sigma 0.15 psi
4. The run must be longer than 15 minutes
5. There must be no other anomalous activity around the detector, on deck or in the electronics

Blinding of physics data in DEAP-3600 From the total dataset in the DEAP-3600 experiment, the data from 2016 to 2017 is completely open, and then collaboration decided to start taking blind data at the beginning of 2018. Blinding the data has become a common thing in many fields of research to provide the tool to reject the over-tuning or biasing of data [79]. The blinding is done in the experiment with a hidden data scheme in which a portion of data is blinded and some data is kept

open to ensure that there is enough data available to monitor the data quality later over time. The blinding of data does not have any effect on the ^{39}Ar lifetime analysis since the blinding strips are above the ER backgrounds band as shown in figure 6.1 but it resulted in keeping the upper fprompt cut at 0.41 such that only data below this cut value is included in the analysis.

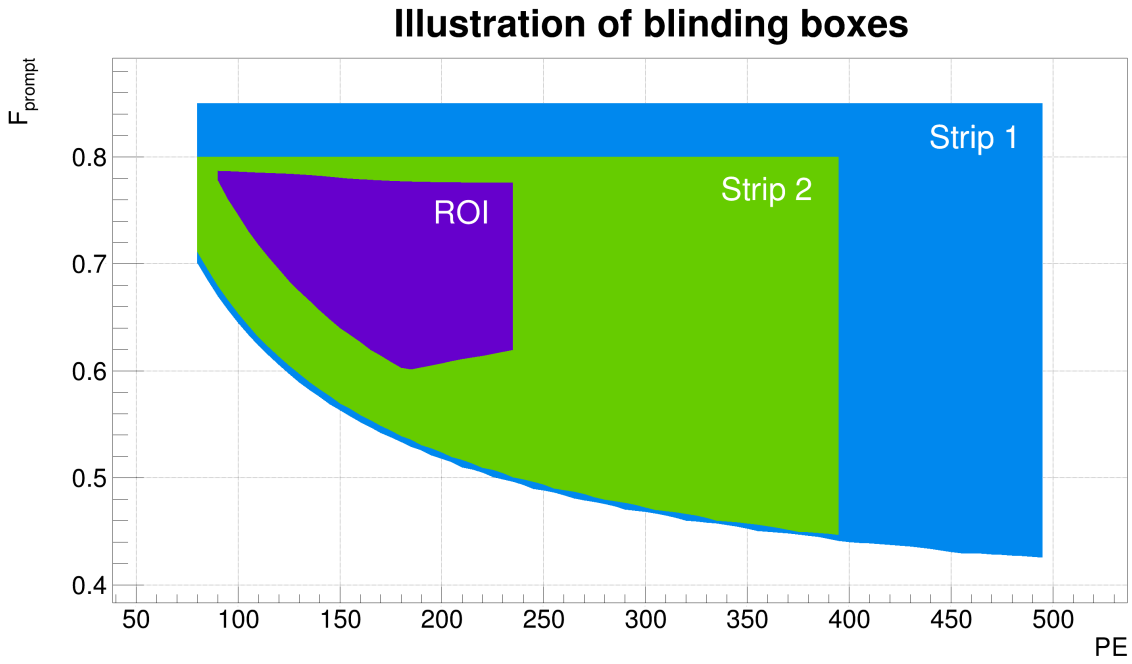

Figure 6.1: This is a set of 3 blinding regions applied to DEAP-3600 physics data. The ROI box for the WIMP signal from the elastic scattering is drawn in the center is where we plan to perform the 3-tonne year WIMP search. The x-axis shows the number of photoelectrons (PE) with the fprompt variable on the y-axis.

6.3 Extra run selection criteria for ^{39}Ar lifetime analysis

The ^{39}Ar lifetime analysis needs the precise measurement of the ^{39}Ar decays in the detector and hence includes the selection of the physics data where we can either minimize the little systematic which can affect the trigger collection by the data

acquisition system or we have to make the corrections for these changes. Thus, along with the main data quality checks discussed in section 6.2, some additional run selection criteria are used which tighten the data selection for this analysis which are discussed in the following sections. The physics data used for the trigger rates constitute 991 run numbers out of 1280 runs passing the standard data selection checks.

6.3.1 Accuracy of the trigger count in the physics runs

The data acquisition system records every light scintillation very precisely, however, the study was done to validate the correct trigger counts for ^{39}Ar decays in the later process when data is migrated from one part of the DAQ system to the database as the little variation in the trigger count with the time can affect the final calculation of the activity of ^{39}Ar isotope. While looking for the uncertainty related to the ^{39}Ar trigger counts for rate analysis we found a very small (almost negligible) discrepancy in the total triggers stored in the Couch database (or MIDAS files) and processed/reprocessed data files at Graham. The reasons for the trigger count difference are investigated in the detail.

The total number of triggers for any run number is stored in the database which returns the trigger count including the triggers from all sub-runs and periodic triggers. This trigger count is compared to the total triggers from processed/reprocessed data files and the difference between the number of triggers is plotted with respect to run numbers. We haven't expected any difference in trigger count from the two sources but unfortunately, there is some discrepancy. However, the difference in the number of trigger counts is the same in the different file formats (raw, cal, and ntuple data files). The observed trigger count difference for selected 1280 run numbers, recorded

from the database and data files is shown in figure 6.2.

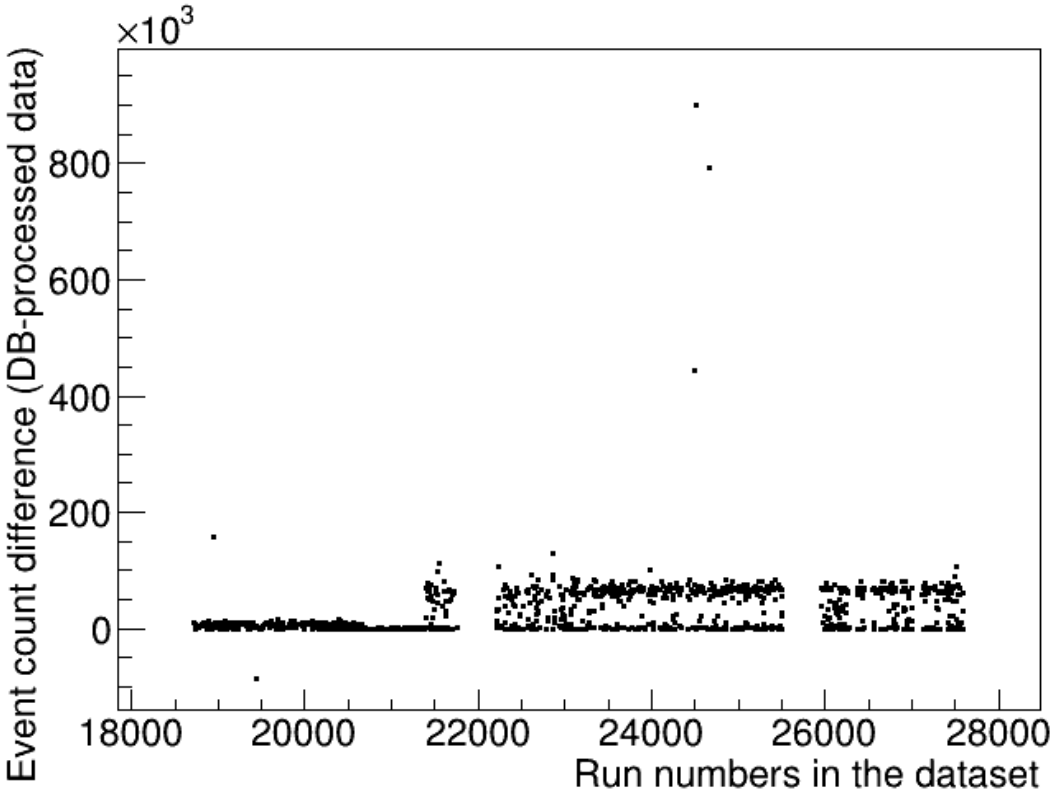

Figure 6.2: Trigger count difference from the database and processed data files with respect to run numbers in the dataset.

The physics run numbers from 18721 to 20654 have a 10000 to 12000 trigger difference. The database has more triggers as compared to other processed data files, or the data files using which the rates are plotted have 0.1 to 0.12 missed triggers per second. This difference is mainly due to the contribution of non-physics triggers in MIDAS files for these run numbers. All these non-physics triggers are from temperature readings of cooling water lines which were recorded in data from DEAP water front-end programs in the MIDAS but it is no anymore recorded in the data after run number 20654. This difference in triggers from run numbers 18721 to 20654 will be get solved after applying the data cleaning cuts and physics trigger selection

cuts mentioned in the section 5.5.

The discrepancy in trigger count is large for the blind data (as discussed in section 6.2.4) from run number 21394, this is expected because triggers are taken out while processing data files with the blinding boxes defined and used in the experiment. The rate of missing triggers for blind runs in 0.8 to 0.83 triggers/second which is on average 60k triggers missed in a typical 20-hour run. To neglect any systematic which could occur from this trigger difference in the blind dataset, the fprompt region below 0.41 is selected for the ^{39}Ar lifetime analysis, this is the ^{39}Ar region where the last blinding strip ends on fprompt scale hence there is no effect of blinding in this low fprompt region. This is the main reason to select the fprompt region [0,0.41] for this analysis. The corrections for any ^{39}Ar missed in the higher fprompt region are applied through the efficiency terms in the fit equation (5.24).

Thus, the trigger count discrepancy is explained for most of the missing triggers and corrections will be applied for this either by using the data cleaning cuts or by selecting an appropriate fprompt region of interest for this analysis. Based on this study, there were about 30 run numbers rejected from the analysis (which are mainly outliers seen in the figure 6.2), where the triggers were a little different because of one or more reasons.

There still exists some small discrepancy in trigger count (after excluding the slow control triggers etc.), with a rate of 0.006 to 0.008 triggers missed per second for all the runs. Investigating further on this, these left-out missing triggers are exactly 2 times the number of sub-runs in the runs. For example, for run number 28876 with 19 sub runs, the MIDAS file has 28265609 triggers, and the database shows 28265647 triggers, the difference of 38 triggers is 2 times the number of sub runs in this run. So MIDAS is losing 2 triggers/sub-runs somewhere. This was confirmed by the DAQ

experts that the DTM internal counter is agreeing with the number of triggers in the MIDAS file but not with the logger. Therefore, the issue is related to the logger and this trigger difference is very small and almost negligible.

To account for this little systematic related to the trigger count the relative residuals of the trigger count difference recorded in the database and data files are plotted with respect to run numbers as given in figure 6.3.

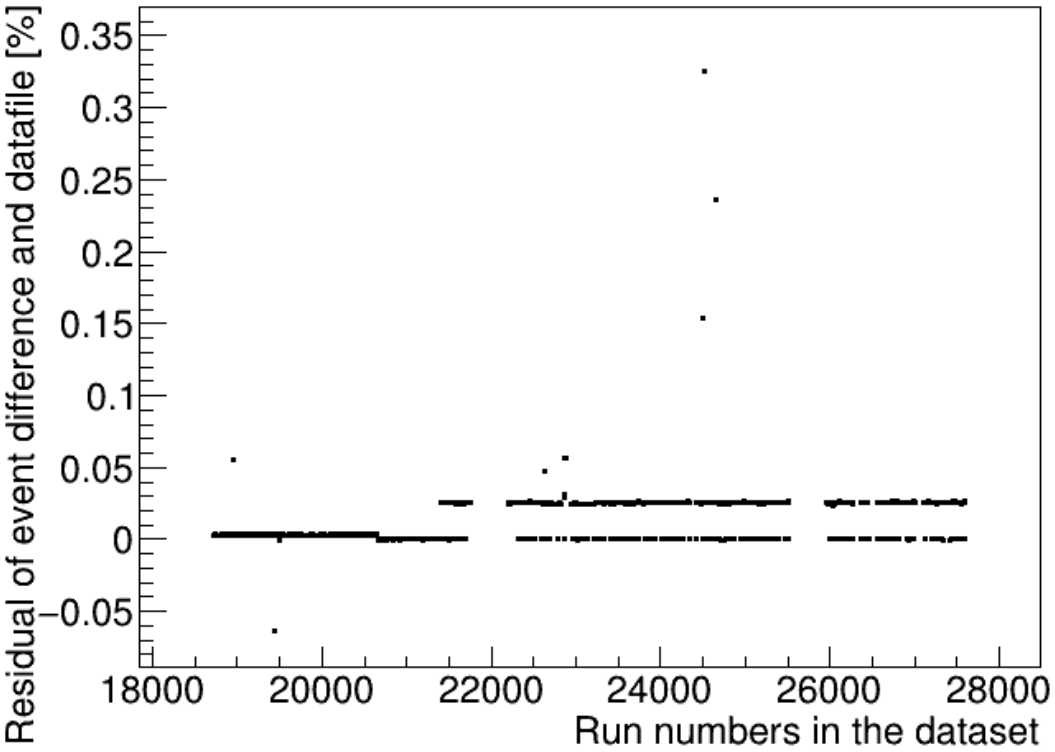

Figure 6.3: Relative residuals for the trigger count difference from the database and processed data files with respect to run numbers

However, the large trigger discrepancy can be solved as discussed above. The only small discrepancy is due to trigger count in the logger, and thus its residuals are studied for the additional systematic uncertainty with the mean value 0.00022% and sigma value 0.00012% from this systematic to calculate the total error for the lifetime

of ^{39}Ar decay. This uncertainty is measured from the one-dimensional distribution as shown in figure 6.4. The very small value of this systematic shows the well-defined precision of the DEAP-3600 DAQ system to record the scintillation light triggers.

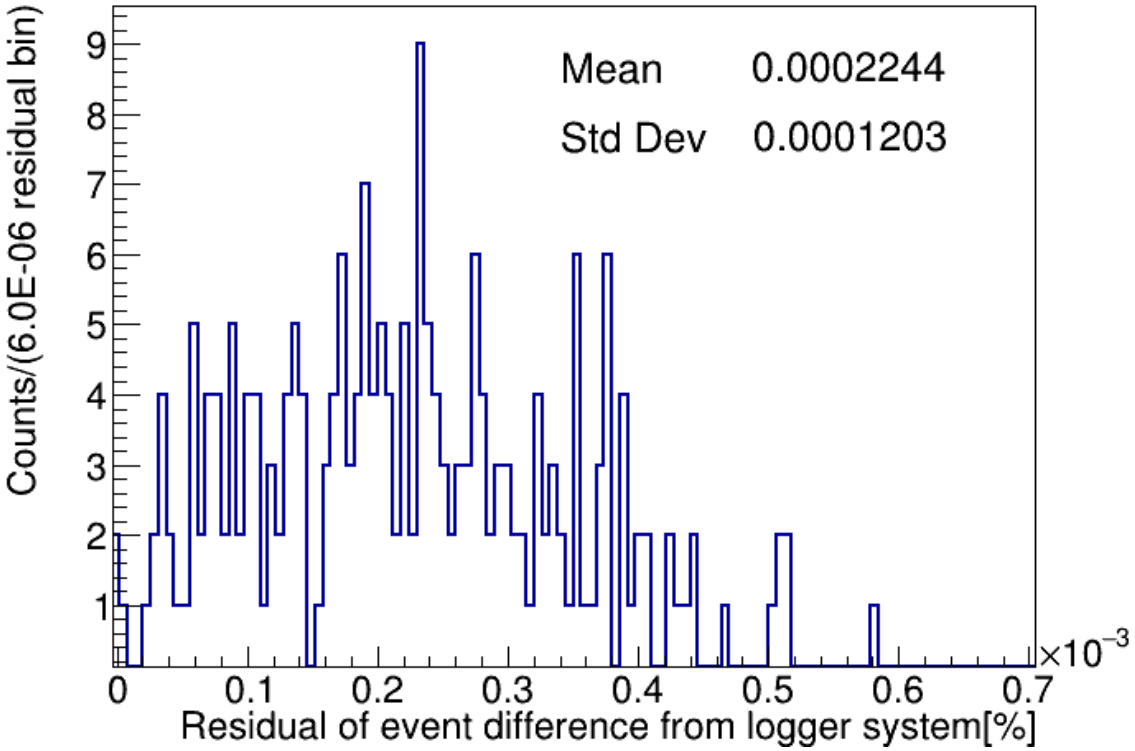

Figure 6.4: The distribution of the relative residuals for the trigger count difference from the database and processed data files because of the logger system. It has a mean value of 0.00022% with a standard deviation of 0.00012%.

6.3.2 Precise measurement of livetime for data

The ^{39}Ar decay triggers have the dominant contribution to the total trigger rate in physics data. Therefore, the run time information stored in the database should be the same as the timestamp difference of the last and first ^{39}Ar trigger in any physics run number. However, plotting the difference between the run time from the timestamp information and database with respect to run numbers showed some peaks where

these numbers are different. These run numbers are investigated further to consider this systematic in the study.

The run-time information for all the run numbers is saved in the database which returns the livetime of the run number in seconds only, including the good triggers with valid timestamp information. The livetime is calculated from the difference between the first and last good trigger of all sub-runs and adding them to the total livetime of any run number. The run time for individual sub-runs varies from 309 to 318 seconds in physics runs. To validate the livetime information for run numbers in the database, the timestamp information of the first and last trigger ^{39}Ar triggers passing the data cleaning cuts are calculated from the date and time information of the triggers. The subtraction of the timestamp of the last and first gives the run time for any physics run number.

The difference between the two run time measurements is plotted with respect to the run numbers and is shown in figure 6.5.

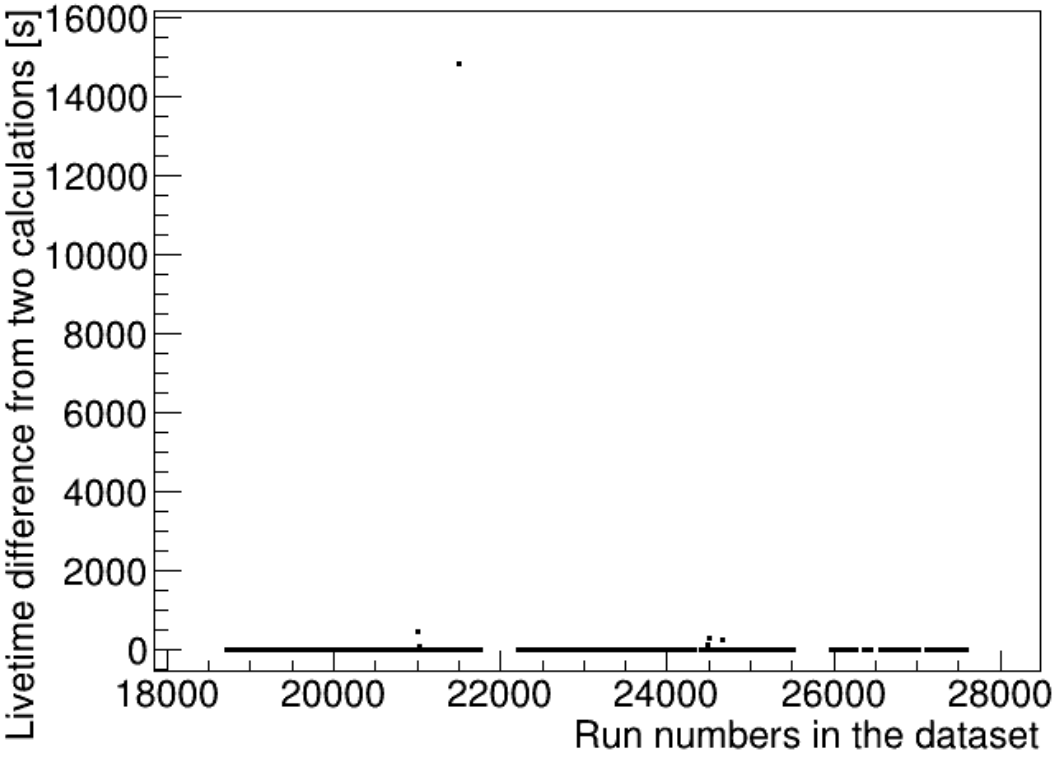

Figure 6.5: The difference in the run time measurement from the timestamp information of the first and last ^{39}Ar trigger in the data file, and livetime saved in the database from DAQ.

Detailed studies for the small mismatch of run time information are underway and a low-level group is investigating this. The relative residuals of the time difference measured in the timestamp method and database information are given in figure 6.6. However, for the ^{39}Ar lifetime analysis, there are about 20 run numbers are rejected from the analysis to neglect this systematic. The run numbers for which run time information from two different measurements agree within one second are only included in the study.

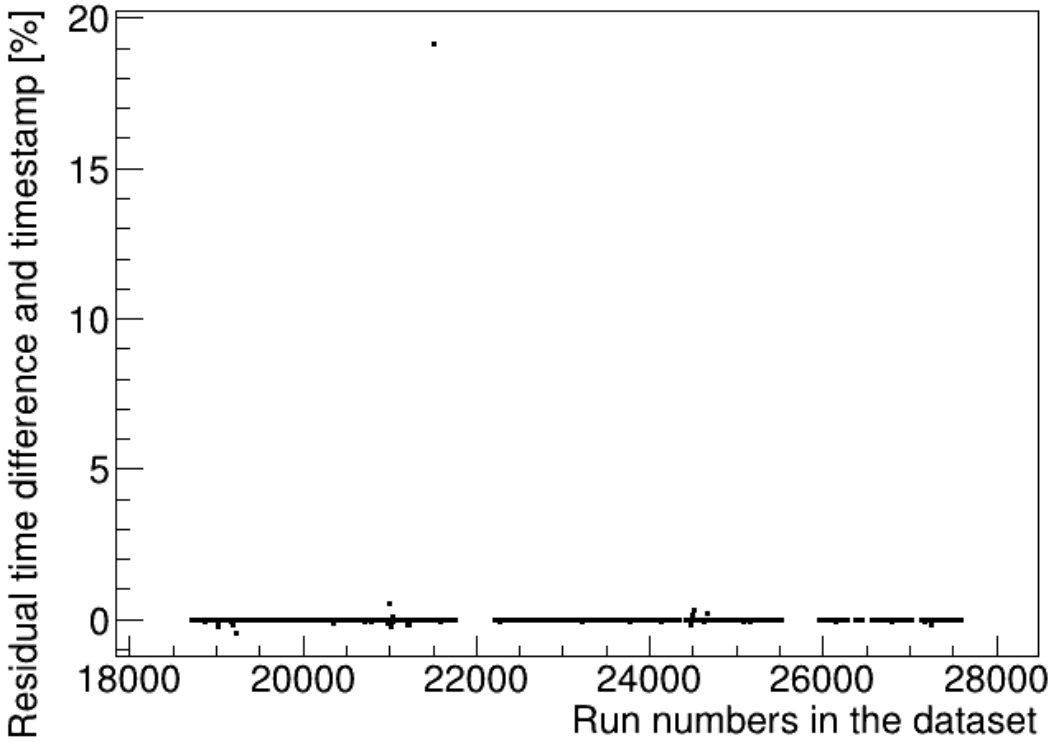

Figure 6.6: The relative residuals for the run time difference measured from the timestamp information of the first and last ^{39}Ar trigger in the data file, and livetime information saved in the database. The outlier shows largely the run time difference noticed in the database which is fixed after a detailed investigation.

This systematic is included in the ^{39}Ar lifetime study as an additional uncertainty with mean 0.00075%, which is calculated from the one-dimensional distribution relative residuals of the time difference measured in timestamp method and database information as seen in the figure 6.7.

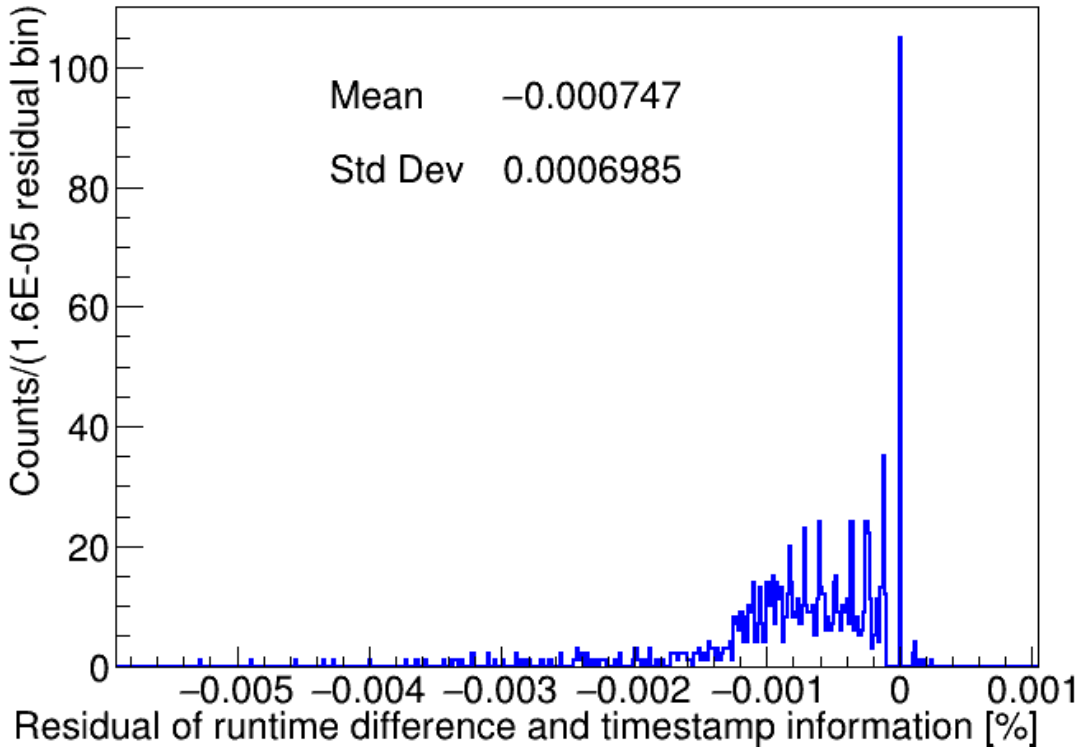

Figure 6.7: The distribution for the relative residuals of the difference in the run time measurement from the timestamp information of the first and last ^{39}Ar trigger in the data file, and database.

6.4 Light yield of detector and energy response

The other important systematic considered in the study is the small change in the light yield of the detector with time, which has a large systematic effect on the lifetime of ^{39}Ar decay measurement. The light yield of the detector is quite stable throughout the second fill dataset, however, due to the slight variations in the temperature of the outer water shield and water level, the PMTs could have a slight difference in their performance and hence changes the energy response of the detector.

The light yield of the detector is calculated by fitting the mono-energetic high gamma peaks of different radioactive sources with Gaussian fits. The gamma peak

position of radioactive decay is estimated from the mean position of the Gaussian fits and divided by the energy of the corresponding peak. The gamma peaks from ^{40}K (1426 keV), and ^{208}Tl (2605 keV) are determined and used for the light yield calculation at high energy, figure 6.8 shows an example of Gaussian fitting on the ^{40}K gamma peak for a run number.

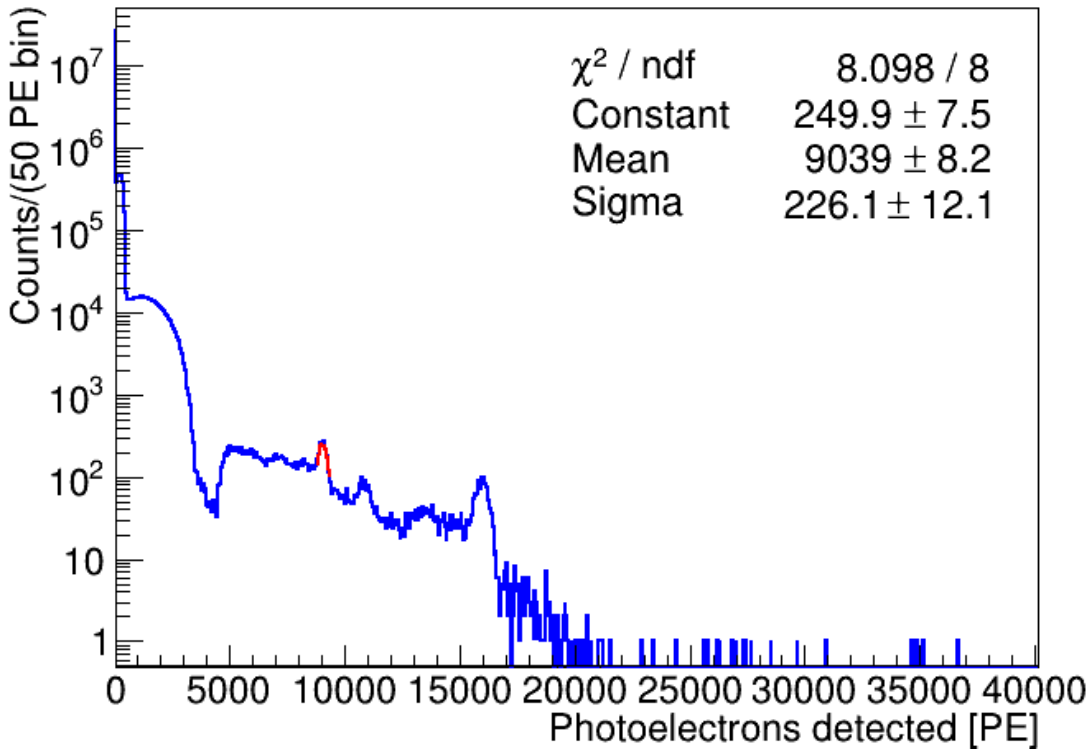

Figure 6.8: The PE distribution with the Gaussian fitting on the ^{40}K gamma peak and the fitting statistics to determine the light yield of detector for some run number.

The position of gamma peaks from the fitting mean has an uncertainty associated with it, which results in an uncertainty in the calculated light yield values. Moreover, at the low energy, the fits to the ^{39}Ar spectrum were used to calculate the light yield of the detector as discussed in section 5.10.

The trendline for the light yield of the detector calculated from the different

sources, ^{39}Ar, ^{40}K, and ^{208}Tl is given in the figure 6.9 whereas the uncertainty on these light yield values is from the uncertainties on the mean of the Gaussian fittings. The light yield of the detector is very stable over 3.4 years with a very little variation of 0.3 PE/keV. Also, the trendline for the light yield response of the detector is similar for all three sources.

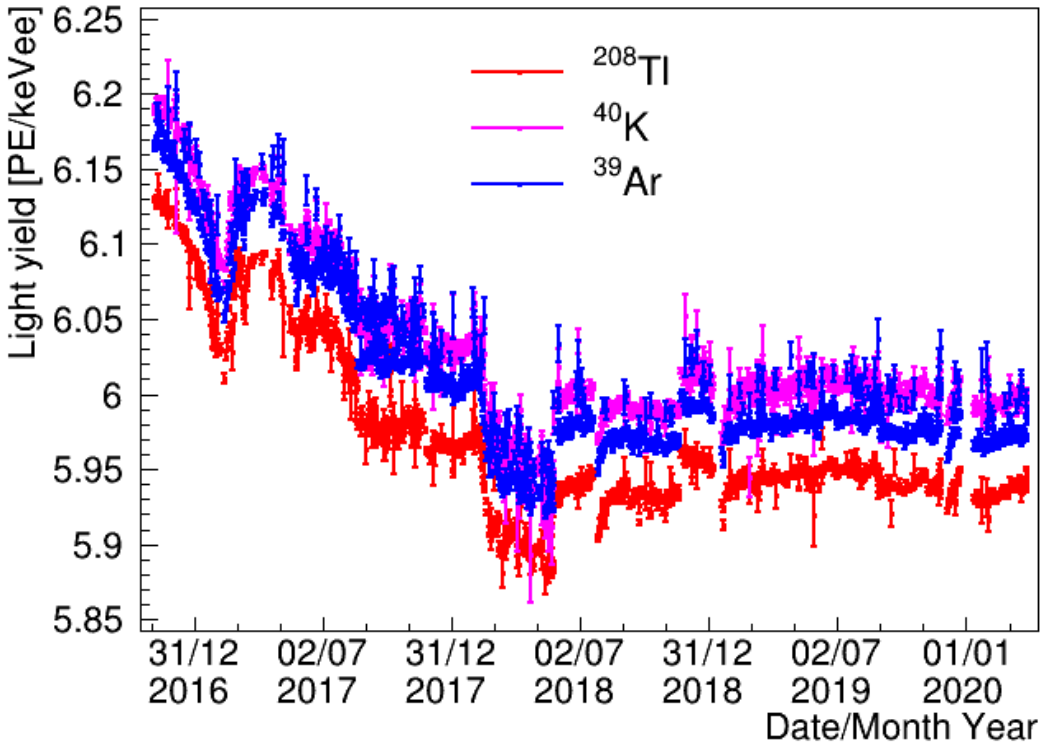

Figure 6.9: The light yield of the detector over time calculated from the gamma peaks of ^{208}Tl, ^{40}K, and from fits of ^{39}Ar spectrum.

There is an additional run selection cut applied based on the basis of fitting of the gamma peaks with Gaussian distributions. The run numbers which are shorter than 4.85 hours (with a run time less than 17505 seconds) do not have sharp gamma peaks for the ^{40}K, and ^{208}Tl, hence the fitting statistics were not enough for the calculation of the light yield values. Thus, the run numbers with a livetime of fewer

than 4.85 hours are rejected from the analysis (which counts up to 250 run numbers that were rejected from the analysis).

6.4.1 Corrections for variations in energy scale

The corrections are implemented to account for the systematic related to little variations in the energy calculation, and thus the changes in the light yield of the detector. The correction factor corresponds to the differential change in the light yield (LY) was multiplied by the trigger energies on the trigger-by-trigger basis, and hence the corrected energy region from 700 to 1200 PE is used in the analysis, such that,

$$\text{Corrected energy of trigger from run i} = \text{Energy of trigger} * \text{Change in LY for run i} \quad (6.1)$$

The change in the light yield is calculated from the ratio of the light yield of the first run number in the dataset 18721, LY_0, to the light yield of every j run number in the dataset, LY_j, such that, the light yield ratio for any run number is,

$$\text{LY ratio} = \frac{LY_j}{LY_0} \quad (6.2)$$

Also, the energy response function (section 5.10) shows the light yield calculations from three different sources are dependent. Therefore, the arithmetic mean value of the light yield ratio is evaluated from the trends in three different sources in figure 6.10 which is further used for the correction of energies of triggers.

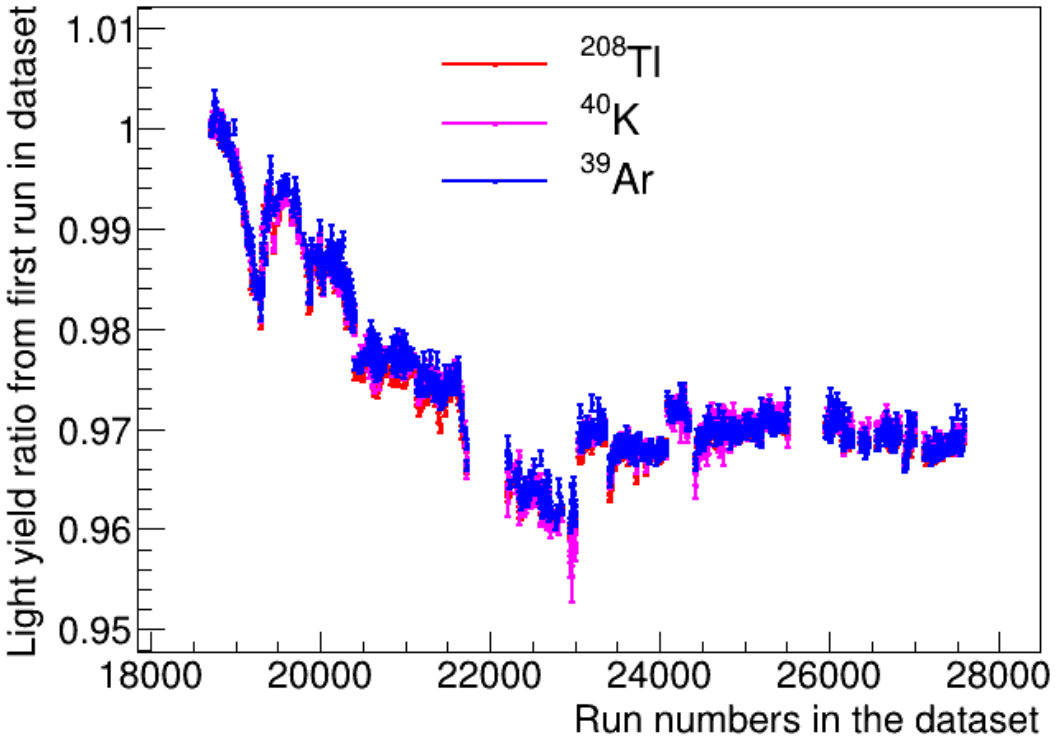

Figure 6.10: The ratio of light yield of detector for any run j to the light yield of the first run in the dataset with time. The light yield values are calculated from the gamma peaks of ^{208}Tl, ^{40}K, and from fits of ^{39}Ar spectrum.

The mean light yield ratio value, LY_{rm}, for all the run numbers in the dataset, are determined from the equation (6.3) as shown in figure 6.11,

$$\text{Mean LY ratio}(LY_{rm}) = \frac{r_{^{208}Tl} + r_{^{40}K} + r_{^{39}Ar}}{3} \tag{6.3}$$

where, $r_{^{208}Tl}$, $r_{^{40}K}$, and $r_{^{39}Ar}$ are the change in the light yield from starting of the dataset, calculated from ^{208}Tl, ^{40}K, and ^{39}Ar peaks respectively. This mean LY ratio is used for the correction of the energy of triggers in the dataset, and ^{39}Ar trigger rates are plotted from the corrected trigger energies, selecting the triggers falling the ROI which is described in the section 6.6.

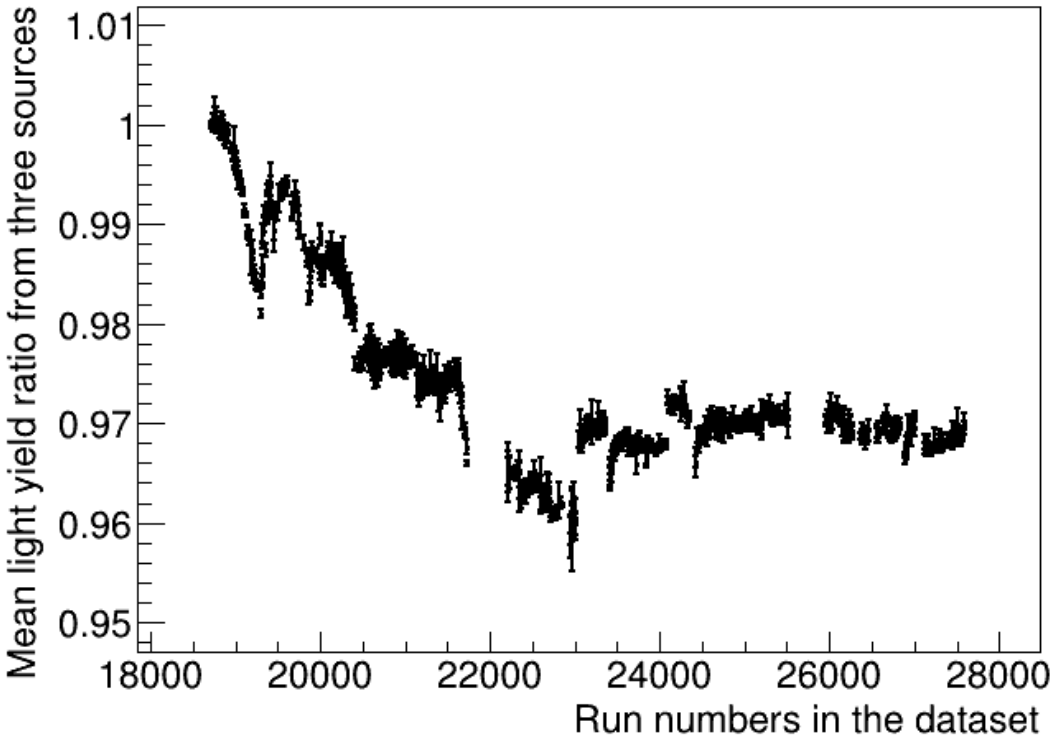

Figure 6.11: The mean LY ratio is calculated from three different sources over time to correct for the little variations in the energy response of the detector.

6.4.2 Systematic uncertainty from energy scale corrections

There are two uncertainties related to the mean light yield ratio calculations, firstly the statistical uncertainties related to the position of the gamma peak which is basically the error on the mean of the Gaussian fittings used for the determination of the light yield values for every three trends. The statistical uncertainty on the mean light yield ratio is given by the equation (6.4),

$$\text{Statistical uncertainty on mean LY ratio}(\sigma_{statLY_{rm}}) = \sqrt{(\frac{\sigma_{^{208}Tl}}{3})^2 + (\frac{\sigma_{^{40}K}}{3})^2 + (\frac{\sigma_{^{39}Ar}}{3})^2} = \frac{\sqrt{\sigma^2_{^{208}Tl} + \sigma^2_{^{40}K} + \sigma^2_{^{39}Ar}}}{3} \quad (6.4)$$

Secondly, the systematic uncertainties which occur because of the selection of different gamma peaks or sources for light yield calculation such as ^{208}Tl, ^{40}K, and from fits of ^{39}Ar spectrum. The systematic uncertainty on the light yield measurement is measured from the standard deviation of the light yield ratio from the mean ratio as given in the following equation (6.5),

$$\text{Systematic uncertainty for LY ratio}(\sigma_{sysLY_{rm}}) = \frac{\sqrt{(r_{^{208}Tl} - LY_{rm})^2 + (r_{^{40}K} - LY_{rm})^2 + (r_{^{39}Ar} - LY_{rm})^2}}{2} \quad (6.5)$$

The total uncertainty on the LY_{rm} is determined by adding the statistical uncertainty (calculated from 6.4) and systematic uncertainty (calculated from 6.5) in the quadrature. The final uncertainty on the differential change in the light yield is shown in figure 6.11, and is given by,

$$\text{Total uncertainty on } LY_{rm} = \sqrt{\sigma^2_{statLY_{rm}} + \sigma^2_{sysLY_{rm}}} \quad (6.6)$$

In addition to the corrections applied for the energy changes, the uncertainties on the differential change on the energy response, and hence the calculated total relative uncertainties from the mean as presented in figure 6.12 is also considered in the study.

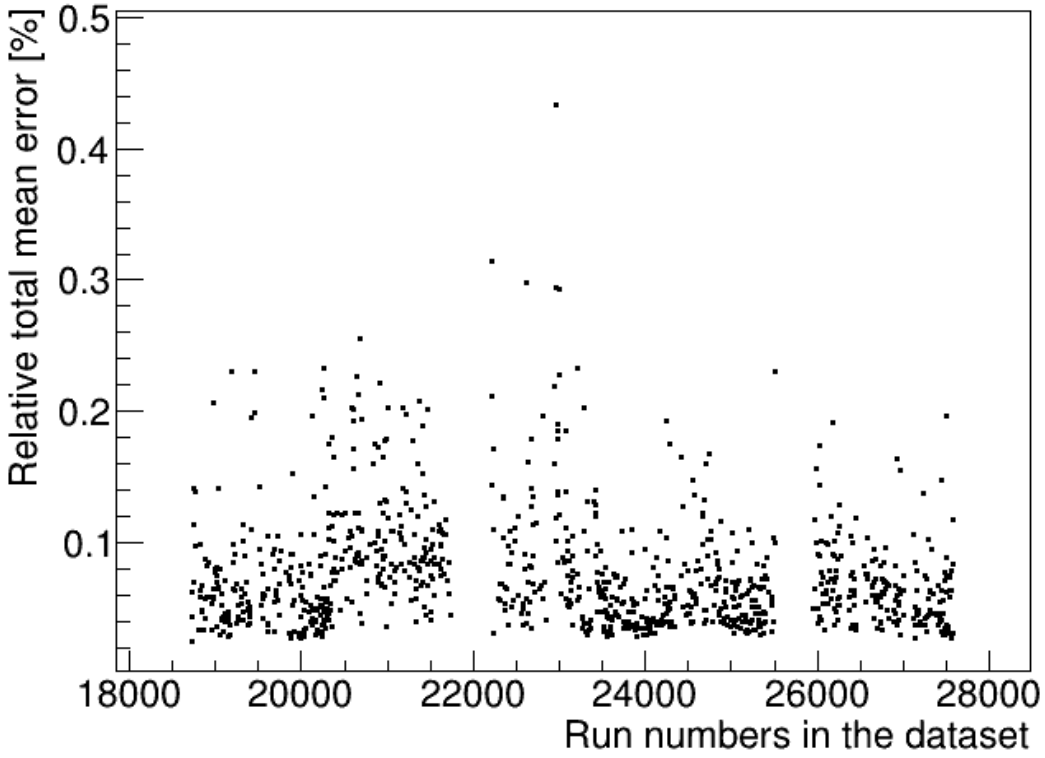

Figure 6.12: The relative total mean error (statistical + systematic errors from equation (6.4), and equation (6.5) respectively) from the mean of the LY ratio for different run numbers in the dataset.

The one-dimensional distribution of the relative error is given in figure 6.13. For the complete understanding of this systematic and its effect on the lifetime of Ar isotope decay, the mean value of the distribution in figure 6.13 is used.

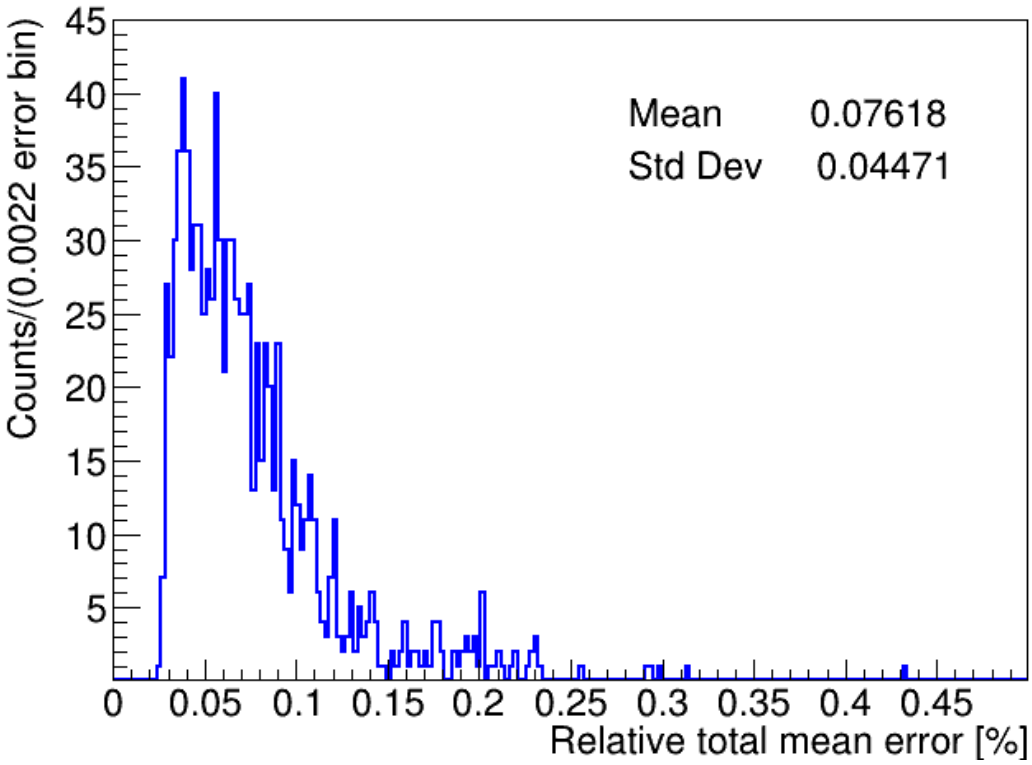

Figure 6.13: The one-dimensional distribution of the relative total mean error from the mean of the LY ratio as calculated in equation (6.6) for different run numbers in the dataset.

The sources of systematic discussed in the above sections could also vary with the time over the period of the dataset. Therefore, to get the complete uncertainty on ^{39}Ar lifetime from this systematic, the deviation of these uncertainties is studied in two ways:

- Allowing for an overall, constant shift in the light yield uncertainty
- Calculating the maximum time-varying shift in the uncertainty

More details for these systematic uncertainties on the lifetime measurement of ^{39}Ar are discussed in the following chapter 7. The uncertainty calculation accounts for both the scenarios mentioned above.

6.5 Energy resolution and variation over time

In addition to the energy corrections based on the small change in the light yield of the detector, studies are performed to estimate the systematic uncertainty from the variation of the energy resolution with time, discussed in section 5.10. The resolution of the energy response parameters is added while convolving the ^{39}Ar spectrum from the keV scale to PE scale by the Gaussian functions where the width of the distribution varied by a small amount based on the energy scale. The function estimated the resolution for a given PE/keV value and then the resolution calculations were scaled to match the width of the Gaussian fits for high energy ^{208}Tl peaks. The width of the Gaussian fits for the high energy gamma peak of ^{208}Tl at energy 2605 keV is measured for all the run numbers and plotted over time as shown in figure 6.14.

Also, the one-dimensional distribution for the standard deviation is given in figure 6.15. The uncertainty in the energy resolution calculated from the one-dimensional distribution in figure 6.15, 11.37 PE is considered in the resolution parameter while convolving the analytical energy spectrum of ^{39}Ar from keV scale to the PE scale. The uncertainty on the resolution is included both by increasing the decreasing the energy resolution by 11.37 PE, and the fraction of the single ^{39}Ar decays in the selected energy region from 700 to 1200 PE is evaluated from the updated full spectrum in PE from the energy resolution effects. The fraction of single ^{39}Ar decays in the ROI from the revised spectrum is,

$$\epsilon_{1,1}^{'} = 0.21 \tag{6.7}$$

Thus, the small uncertainty from the energy resolution resulted in the tiny uncertainty on the fraction of ^{39}Ar triggers in the study. However, the difference in the fraction

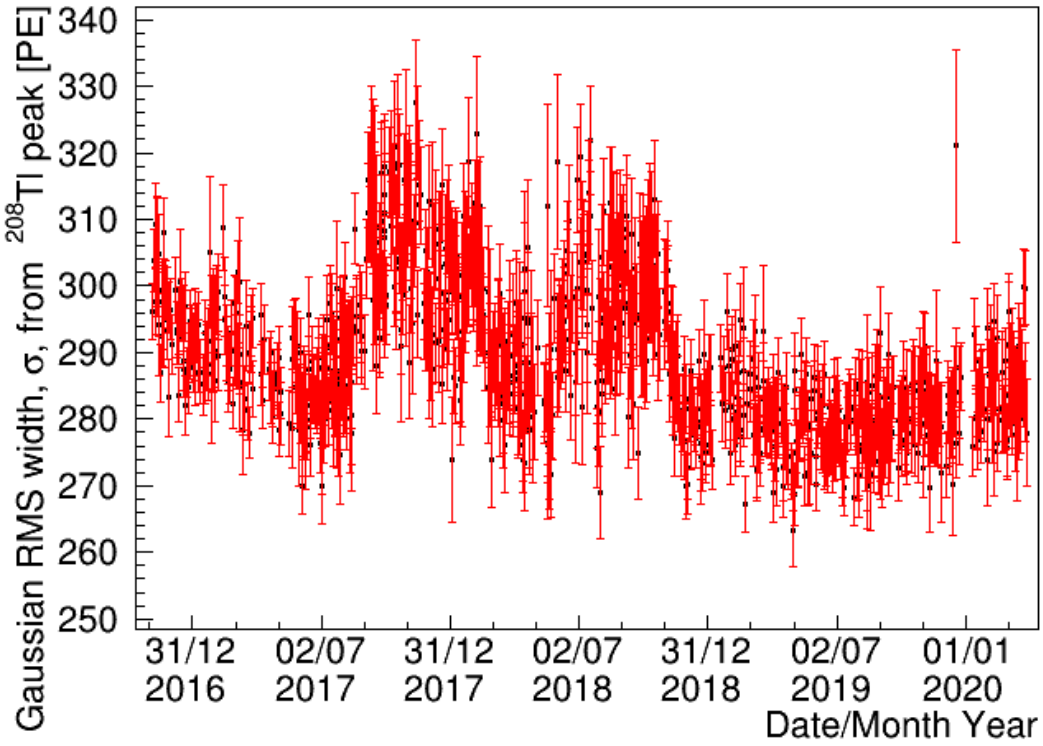

Figure 6.14: The RMS width or standard deviation of the Gaussian fits for the ^{208}Tl gamma peak for all the run numbers considered in the analysis and presented as a function of time.

of single ^{39}Ar from equation (5.26) and with resolution uncertainty is ∼0.12%.

The effect of this systematic uncertainty from the energy resolution on the lifetime measurement of ^{39}Ar is further evaluated in section 7.3.4 for the final systematic uncertainty calculations in the analysis. Also, the effect of energy resolution in the fraction of double and triple ^{39}Ar pile-up in the ROI will be very small and these higher order corrections can be neglected.

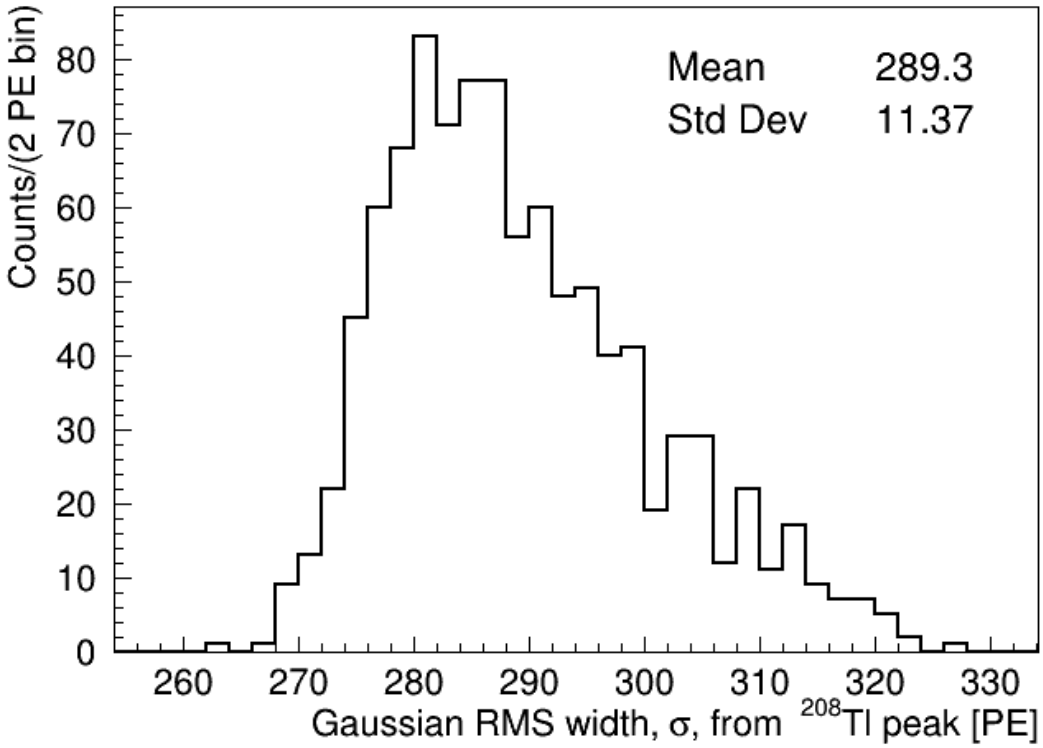

Figure 6.15: The one-distribution of the width for the Gaussian fits on the ^{208}Tl gamma peaks. The average standard deviation from the fits on all the run numbers is 289.3 PE with an uncertainty of 11.37 PE.

6.6 Trigger rate of ^{39}Ar from corrected energies and livetime

In this section, the calculations for the ^{39}Ar trigger rates in the selected ROI are discussed. The rates are reported in the figure 6.16, and are measured from the energy-corrected triggers using the corrected livetime, following the trigger addition criterion as specified in the section 5.7.

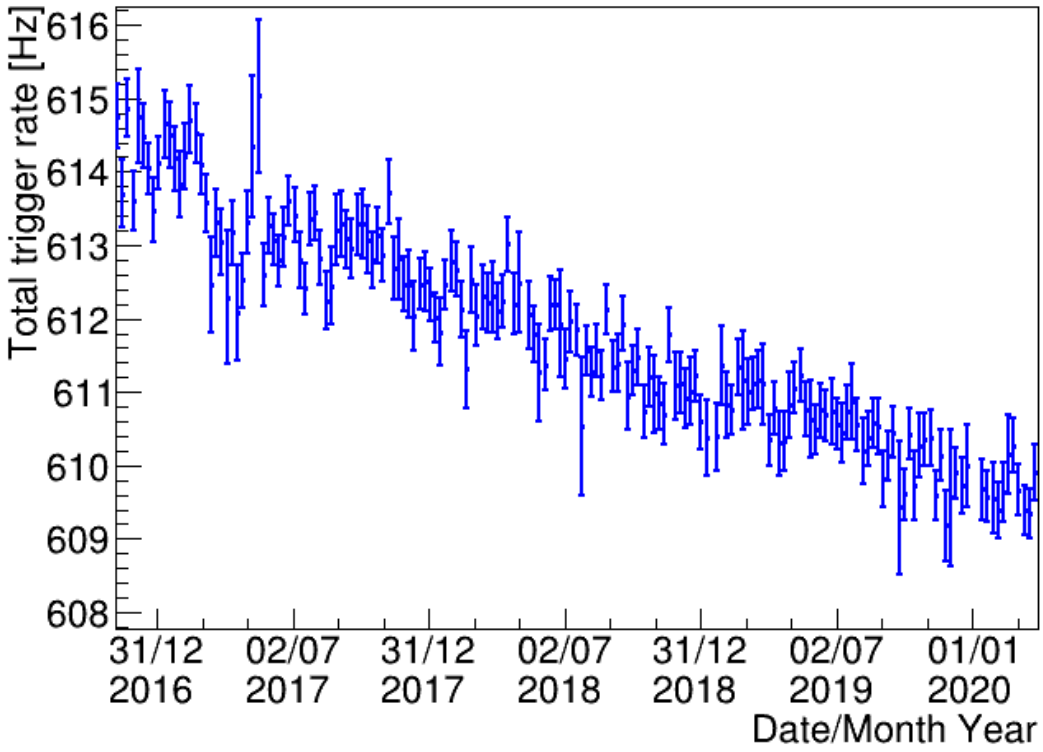

Figure 6.16: Total trigger rate in the ROI with time plotted on the weekly bin basis using the data cleaning cuts and ^{39}Ar selection cuts.

Therefore, using the energy corrections to the trigger energies and corrected livetime information of the run numbers, the rate of the triggers is measured from the physics data, from November 2016 to March 2020 on a weekly bin basis. Each bin point in this figure represents the trigger rates in the week of the year, and we have 177 weeks in the dataset. The data rates are calculated from the ratio of the total trigger counts in each of the weeks in the dataset to the livetime (L_{corr}) of physics data in those week periods. More explicitly, the rates are given by,

$$\text{Total trigger rate (R)} = \frac{NP + P * F}{L_{corr}} \tag{6.8}$$

The statistical uncertainty (σ_R) on the data points is given by the error propagation of equation (6.8) from the first principle, such that,

$$\sigma_R^2 = (\frac{\partial R}{\partial P})^2 * \sigma_P^2 + (\frac{\partial R}{\partial NP})^2 * \sigma_{NP}^2 + (\frac{\partial R}{\partial L_{corr}})^2 * \sigma_{L_{corr}}^2 \tag{6.9}$$

Also, the livetime (L_{corr}) information in the DEAP-3600 DAQ system is very precise, therefore, $\sigma_{L_{corr}} \approx 0$. The statistical uncertainty on trigger rates is dependent only on the uncertainty for P and NP triggers in ROI and since the prescaling is done by the trigger module which works perfectly for selecting trigger types. Thus, the statistical uncertainty is simply given by,

$$\sigma_R^2 = (\frac{100}{L_{corr}})^2 * \sigma_P^2 + (\frac{1}{L_{corr}})^2 * \sigma_{NP}^2 \tag{6.10}$$

Using the Poisson statistics for the trigger count, the uncertainties for the P and NP trigger types can be written as,

$$\sigma_P^2 = P \tag{6.11}$$

$$\sigma_{NP}^2 = NP \tag{6.12}$$

Thus, the statistical uncertainties on the trigger rates are calculated from the square root of the following equation,

$$\sigma_R^2 = (\frac{100}{L_{corr}})^2 * P + (\frac{1}{L_{corr}})^2 * NP \tag{6.13}$$

The one-dimensional distribution for the mean value of the statistical uncertainty on the total trigger rates in ROI is shown in figure 6.17, the mean statistical uncertainty on the total trigger rates from the 177 weeks of physics data is (0.43 $\pm$ 0.12) Hz.

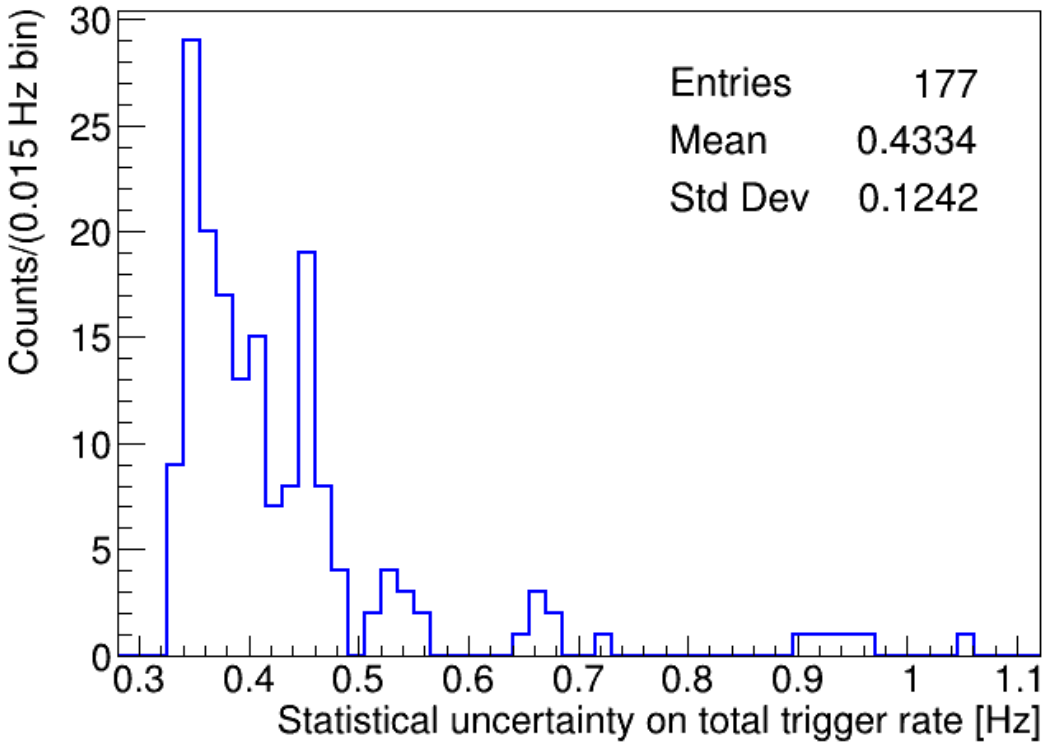

Figure 6.17: The one-dimensional distribution of the statistical uncertainty on the total trigger rates. The mean statistical uncertainty is 0.43 Hz with a 0.12 Hz standard deviation.

Also, the trigger rate calculations are tested with the different deltat values ranging from 32 μs to 110 μs, to verify the dead time corrections to the livetime. It is expected to get the same trigger rate for every deltat cut value since the loss in the trigger count after the deltat cut is equally compensated by the removal of the dead time from the livetime to get the corrected time. The trigger rate for the first week in the dataset is shown in figure 6.18 as the function of the deltat cut value, with the corrected livetime calculations.

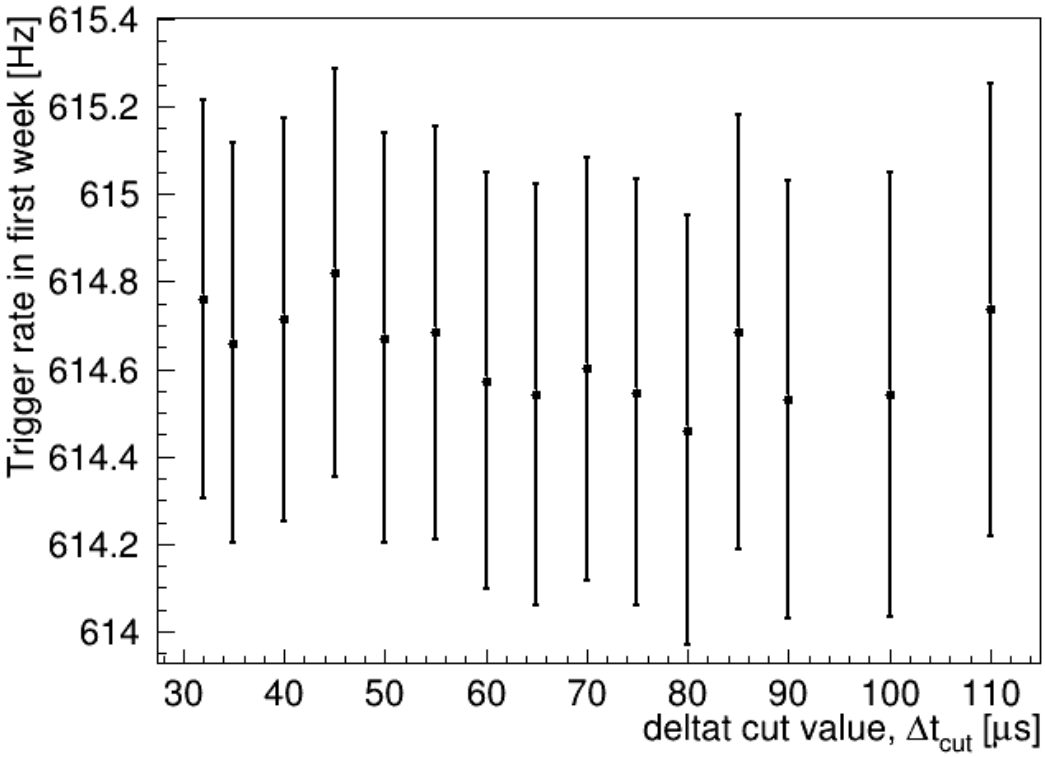

Figure 6.18: The trigger rate in the first week of the dataset calculated from varying the deltat cut values to verify the dead time calculations made from the algorithm (5) in the study. The calculated trigger rates from different deltat cut values and corrected livetime are in good agreement.

The uncertainty on the trigger rates is evaluated from equation (6.13), and dead time corrections are applied following the algorithm (5). The very small deviation seen in the rates is possibly due to a little change in the dead time calculations and has a very negligible effect on the trigger rates.

This confirms the independence of deltat cut in the study, the calculated trigger rates and hence lifetime measurement of ^{39}Ar isotope is not affected by using this additional cut, included to remove pre-scintillation light in the detector while counting the number of PEs.

Thus, the trigger rates are plotted with good precision, the next step is to fit

the derived decay model from equation (5.24) on the calculated rates to measure the lifetime of ^{39}Ar isotope. The results of the fit model on the estimated triggers are discussed in the next chapter 7.

Chapter 7

Analysis of DEAP-3600 detector data for ^{39}Ar lifetime measurement

The results from the lifetime study of ^{39}Ar isotope are discussed in this chapter. The lifetime of ^{39}Ar is obtained by fitting the decay fit model from equation (5.24) to the calculated trigger rates in section 6.6. The effects from various systematic sources mentioned in chapter 5, and 6 are also studied in the detail to calculate the total systematic uncertainty on the measured lifetime.

7.1 Fitting the decay model to the ^{39}Ar rates

The fit model from equation (5.24) represents the rate of triggers in ROI including the efficiency factors from the hardware and software conditions and the contribution of different trigger types. The fitting of the data model is performed in two ways, firstly fixing the ER background rate in ROI, R_{bg}, to 1.65 Hz, which returned the values of the parameters as shown in the figure 7.1.

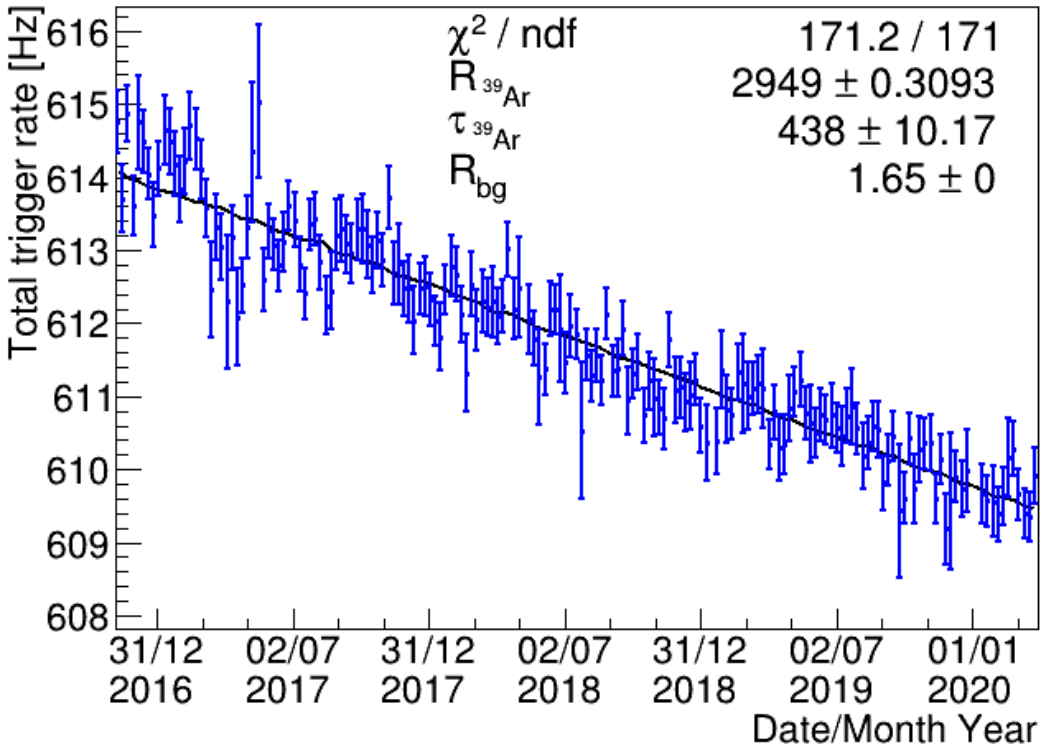

Figure 7.1: Rates of ^{39}Ar triggers with time fitting the decay model fit function derived in section 5.8 in equation (5.24). The ER background contribution is fixed to 1.65 Hz in the fit model.

Therefore, the direct measurement of ^{39}Ar lifetime from DEAP-3600 data is,

$$\tau_{^{39}Ar} = (438.0 \pm 10.2\ (\text{stat}))\ \text{years} \tag{7.1}$$

The lifetime for ^{39}Ar has a statistical uncertainty of 10.2 years. The average activity of ^{39}Ar, $R_{^{39}Ar}$, from the full spectrum at the beginning of the dataset is 2949.3 $\pm$ 0.3 Hz. Moreover, the contribution of the pile-up rates is also investigated further in section 7.2. The activity and lifetime parameter of ^{39}Ar was floated in the fit function with a very large range of 0 to 3600 Hz and 0 to 3600 years respectively, to get an absolute value for these parameters at the global minimum value of the fit model.

In the second case, the rate of the ER background is floated in the fit model which proved the initial activity and background rates in ROI is certainly correlated with each other such that the higher ER background rates in the dataset can return the lower value of the ^{39}Ar recoil rates but the lifetime of ^{39}Ar was not varying significantly. Some cross-checks are performed to validate the value of $\tau_{^{39}Ar}$ from the fit model as discussed in the following section.

7.1.1 Validation of ^{39}Ar lifetime from ER background rate

The ER background rate, R_{bg}, is floated within a large range to verify the value of the $\tau_{^{39}Ar}$ parameter, the lifetime of ^{39}Ar. The limits for R_{bg} were set to 0 to 3600 Hz initially while keeping the same range for the other two independent parameters, $R_{^{39}Ar}$ and $\tau_{^{39}Ar}$, and the fit model from equation 5.24 was again fitted on the calculated rates. The fit output from floating the R_{bg} in 0 to 3600 Hz is shown in figure 7.2.

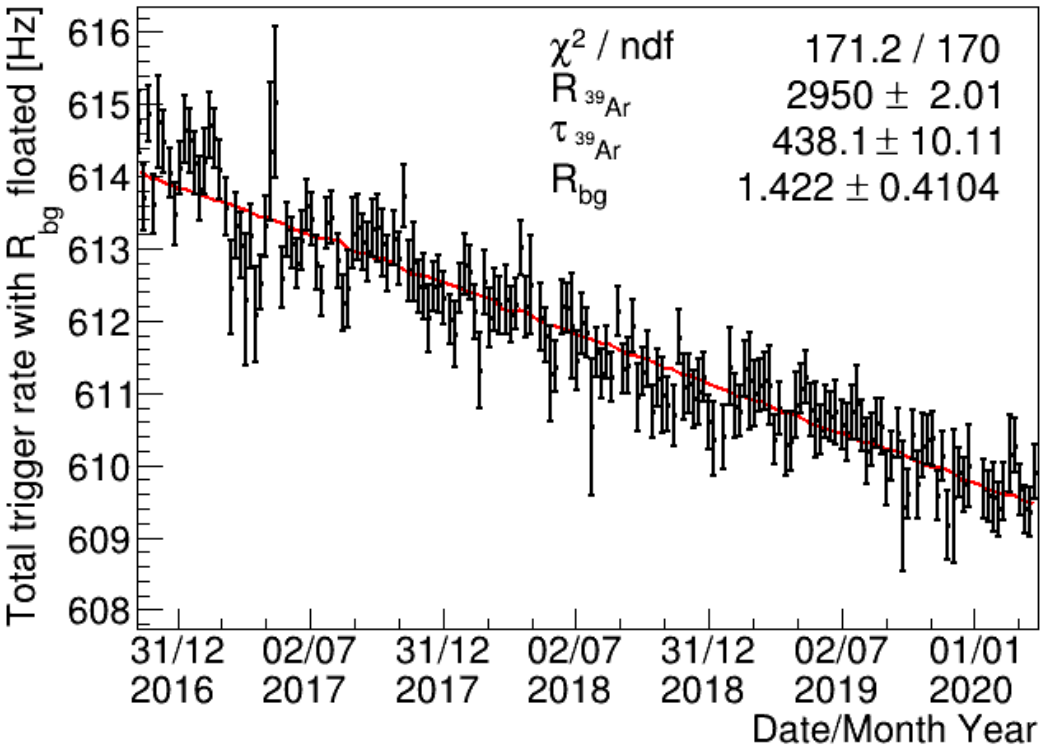

Figure 7.2: Rates of ^{39}Ar triggers with time fitting the decay model fit function derived in section 5.8 in equation (5.24). The ER background contribution is floated between 0 to 3600 Hz in the fit model. The lifetime parameter, $\tau_{^{39}Ar}$ is not varying significantly, however, the dependence of $R_{^{39}Ar}$, and R_{bg} can be clearly inferred.

The fit output with R_{bg} floating in 0 to 3600 Hz results in the $\tau_{^{39}Ar}$ value as 438.1 ± 10.1 (stat) years which does not vary significantly. The background parameter is 1.4 ± 0.4 Hz, and the mean value of $R_{^{39}Ar}$ is changed by 1.12 Hz with the uncertainty of 0.4 Hz. The correlation matrix for the fit parameters is presented in the table 7.1.

Table 7.1: The correlation matrix for $R_{^{39}Ar}$, $\tau_{^{39}Ar}$, and R_{bg} fit parameters from the fit model while floating the background rate between 0 to 3600 Hz.

Fit parameter	$R_{^{39}Ar}$	$\tau_{^{39}Ar}$	R_{bg}
$R_{^{39}Ar}$	1.000	-0.038	-0.988
$\tau_{^{39}Ar}$	-0.038	1.000	-0.094
R_{bg}	-0.988	-0.094	1.000

The dependence of $R_{^{39}Ar}$, and R_{bg} can be understood from the fit output as these two parameters are both presented in the same units. These parameters are strongly anti-correlated but they don't affect the lifetime result. Therefore, defining the value for R_{bg} from ER background model helps to describe the limit for this parameter and $\tau_{^{39}Ar}$ is not varying by a large number in this case. However, the small change in the lifetime from this setting can be included as a systematic uncertainty, such that,

$$\sigma_{ERB} = 0.11 \text{ year} \tag{7.2}$$

Moreover, the background rate parameter is fixed at 1.65 Hz in the analysis for the other systematic studies.

7.1.2 Verification of decay model output from best-fit statistics

To further validate the output from the decay model for the lifetime measurement for ^{39}Ar isotope, the fit model from equation (5.24) is performed several times on the calculated trigger rates (in section 7.9) with the lifetime parameter, $\tau_{^{39}Ar}$, fixed and scanning over a range of values for $\tau_{^{39}Ar}$ varying from 200 years to 600 years. The best-fit statistics hence the lowest value of ratio χ^2 to the number of degrees of freedom for the fit model is obtained for the lifetime value at 438 years, as presented in the figure 7.3.

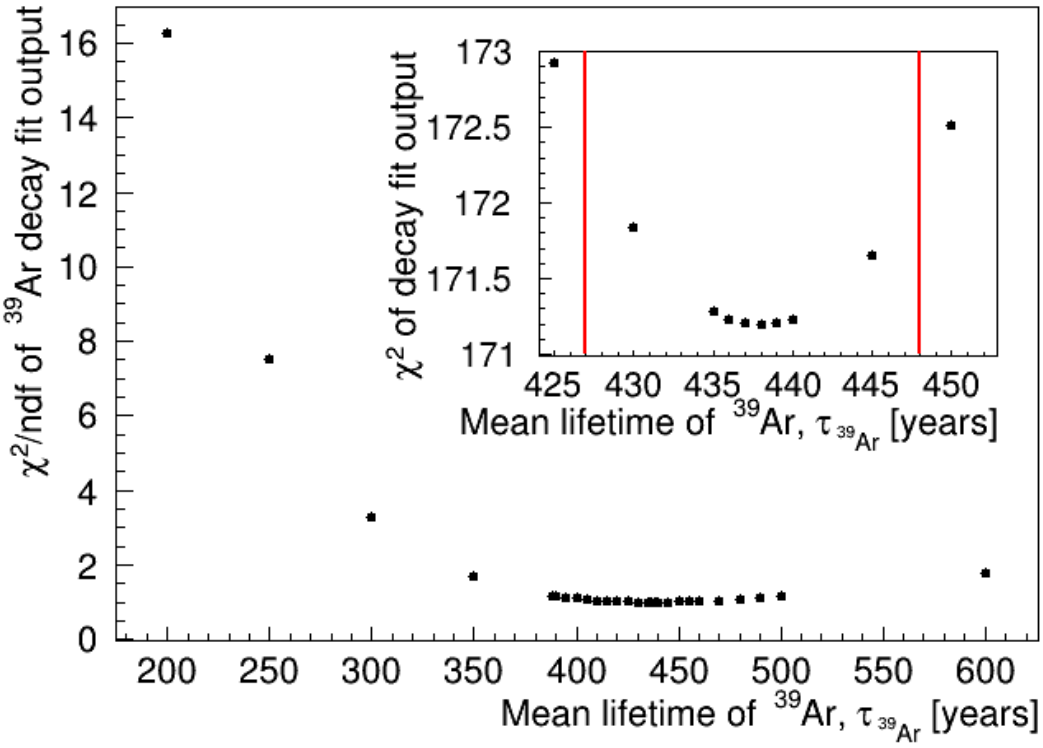

Figure 7.3: The χ^2 to the number of degrees ratio obtained from the fit output of ^{39}Ar decay model for various values of the lifetime, $\tau_{^{39}Ar}$. The global minimum for the fit is obtained for the lifetime value of ^{39}Ar at 438 years. The insert plot shows the absolute χ^2 from the fit model with different lifetime parameters, and the $\chi^2 \pm 1\sigma$ region from the nominal fit solution is highlighted in the red lines.

The absolute value of χ^2 from the output of the fit model by fixing the lifetime parameter to the various values is presented in the inner plot in the above figure. The red lines enclose the region with $\chi^2 \pm 1\sigma$ region from the nominal fit output, which shows the lifetime of ^{39}Ar could only vary from 428 years to 448 years, and the fit statistics are very good for this region as well.

Thus, the decay model from the equation (5.24) returning the lifetime value of ^{39}Ar at 438 years, fits the physics trigger data very well. Also, this can be seen from the best statistics plot in figure 7.3, the data model does not return the best fit χ^2

for the literature value of 388.1 years (indicated in section 3.4), hence the result is in tension with the lifetime measured in the past time from the indirect measurements.

7.1.3 Fit model output from different trigger time cut on rates

The lifetime result and average activity of ^{39}Ar in the detector from the decay model fit output in the figure 5.24 is also confirmed by using the different trigger time deltat cut (Δt_{cut}) values as discussed in the section 5.3, and 6.6. The calculated trigger rates after adding the Δt_{cut}, and making dead time corrections to the estimated livetime are fitted with the decay fit model. The lifetime of ^{39}Ar, $\tau_{^{39}Ar}$ as a function of Δt_{cut} value is shown in figure 7.4.

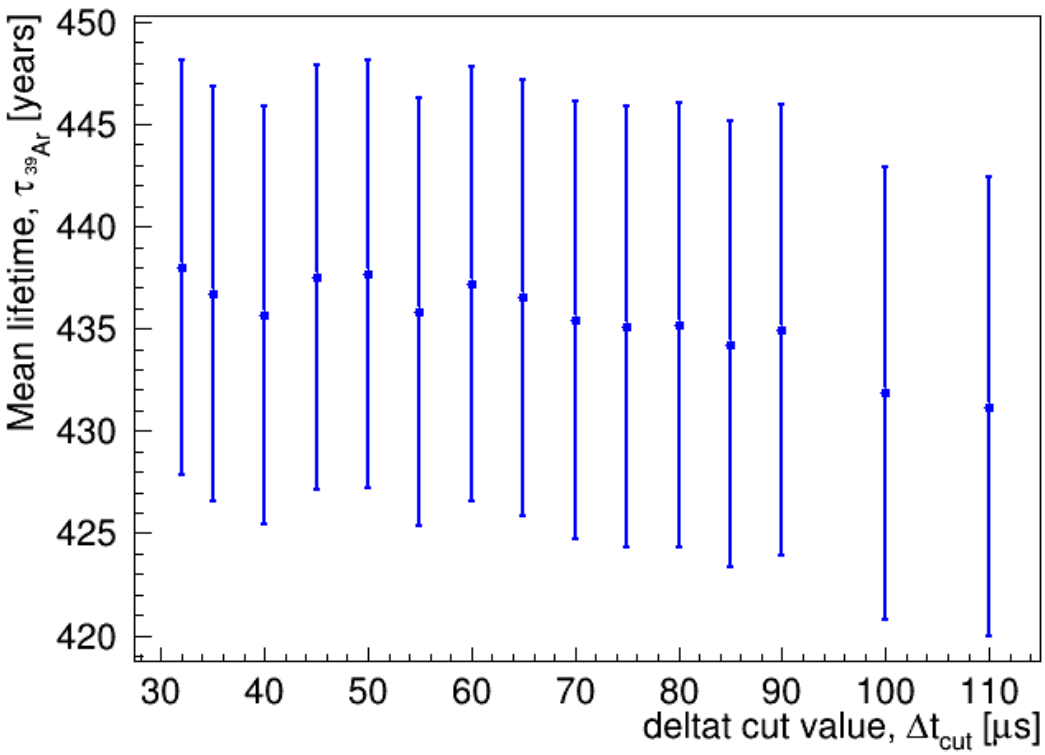

Figure 7.4: The lifetime output of the decay fit model from equation (5.24) fitted on the trigger rates from the dataset calculated from varying the deltat cut values. The measured lifetime of ^{39}Ar is consistent with the different deltat cut values included in the trigger rate calculations.

Similarly, the measured activity of ^{39}Ar, $R_{^{39}Ar}$, plotted as a function of Δt_{cut} values from the fit outcome, which is given in figure 7.5. The measured activity is consistent for different Δt_{cut} values, with a negligible change of 0.5 to 1 Hz, which could be due to the rate of ER backgrounds, R_{bg} kept constant in all the fits for different Δt_{cut} values.

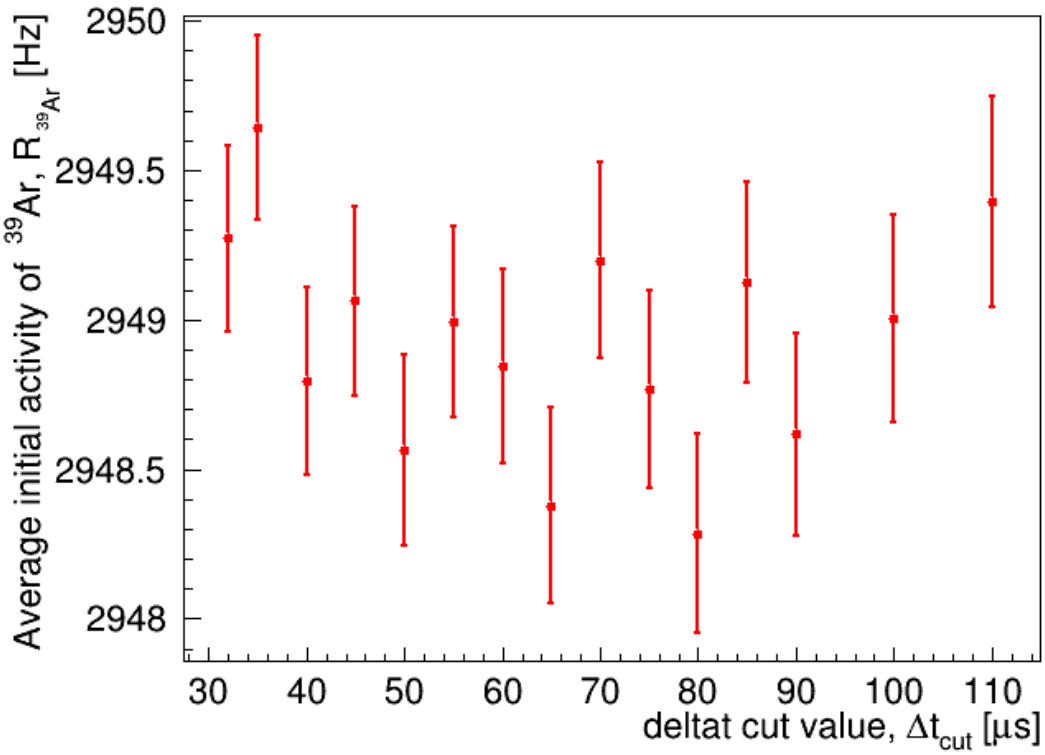

Figure 7.5: The decay fit model outcome for the initial activity of ^{39}Ar, $R_{^{39}Ar}$, obtained by fitting the trigger rates including different deltat cut values and corresponding dead time corrections in the livetime. The activity of ^{39}Ar is consistent for the different deltat cut values, whereas the contribution of the ER background rate, R_{bg} is kept constant for this plot.

7.2 Single and pile-up rate of ^{39}Ar in data from fit model solution

The single ^{39}Ar decay triggers are the dominant trigger type in the ROI. The contribution and decay of the single ^{39}Ar triggers in the total trigger rate can be measured from the equation (7.3), which shows the single ^{39}Ar decay over time as derived from the decay fit model (equation (5.24)) with 100% hardware and software efficiency for

the detector.

$$R_1(t) = R_{^{39}Ar} * \exp(\frac{-t}{\tau_{^{39}Ar}}) * \exp(-(R_{^{39}Ar} * \exp(\frac{-t}{\tau_{^{39}Ar}}) * \delta t)) \tag{7.3}$$

The output of the decay fit model in figure 7.1, specifically the average rate of ^{39}Ar, $R_{^{39}Ar}$, and the measured lifetime, $\tau_{^{39}Ar}$, from the fit model, can be used in the equations (7.3) to get the decay of single ^{39}Ar isotope from the data, which is shown in figure 7.6.

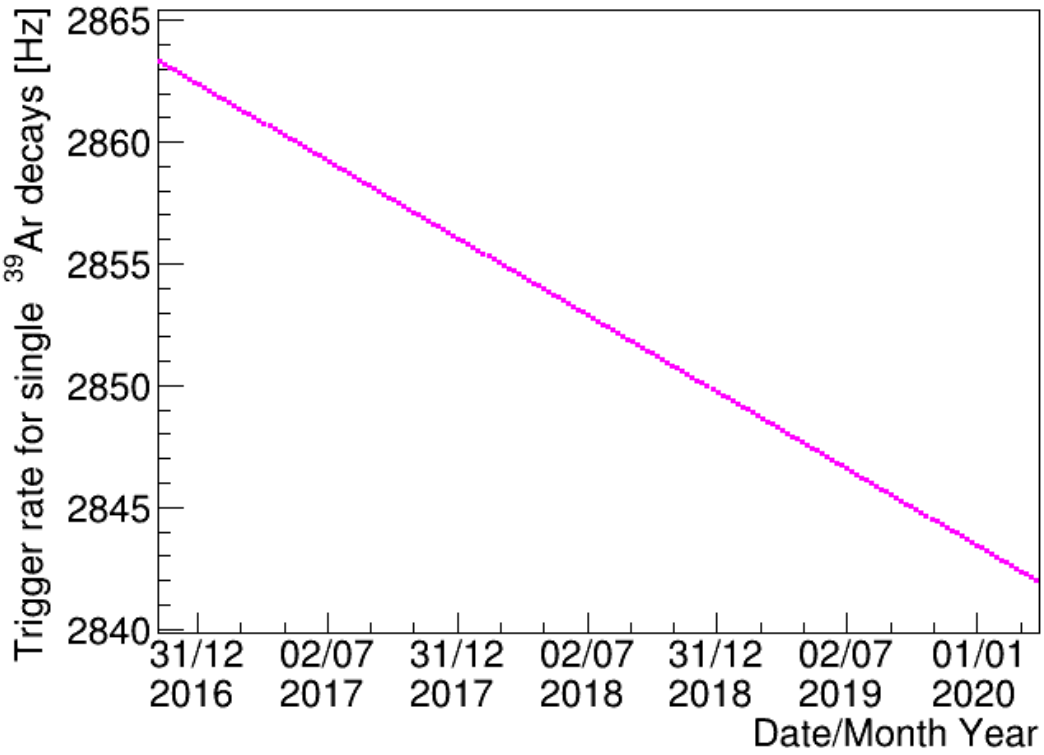

Figure 7.6: The trigger rate and decay of single ^{39}Ar isotopes with time calculated form equation (7.3). The single ^{39}Ar trigger rate decreased by 21 Hz over the time period of the dataset.

The trigger rate from the single ^{39}Ar scintillation light decreased from 2863 Hz in the first week in the dataset to 2842 Hz in the last week, which indicates a change

of 21 Hz over the period of the dataset. Also, for the selected energy region from 700 to 1200 PE, the fraction of single ^{39}Ar triggers decreased from 603 Hz to 598.5 Hz approximately.

There is not much effect expected from the decay of pile-up ^{39}Ar on lifetime measurement, this is because pile-up decay will be decaying with a very long lifetime than the single ^{39}Ar trigger. The expected change in the rates of double and triple pile-up ^{39}Ar from the full pile-up energy spectrum of ^{39}Ar can be investigated from the output of the decay fit model again. Considering the 100% detector efficiency for hardware, and software cuts, the average rate, $R_{^{39}Ar}$, can be used with the measured lifetime of ^{39}Ar in the equations (7.4) and (7.5) to get the values of the double and triple decay trigger rate for ^{39}Ar decays in the start of the dataset. The equations (7.4) and (7.5) are the ^{39}Ar pile-up components with itself in the derived fit model from equation (5.24).

$$R_2(t) = R^2_{^{39}Ar} * \delta t * \exp(\frac{-2t}{\tau_{^{39}Ar}}) * \exp(-(R_{^{39}Ar} * \exp(\frac{-t}{\tau_{^{39}Ar}}) * \delta t)) \tag{7.4}$$

$$R_3(t) = \frac{R^3_{^{39}Ar}}{2} * \delta t^2 * \exp(\frac{-3t}{\tau_{^{39}Ar}}) * \exp(-(R_{^{39}Ar} * \exp(\frac{-t}{\tau_{^{39}Ar}}) * \delta t)) \tag{7.5}$$

The double ^{39}Ar scintillation light rate dropped from 84.37 Hz at the beginning to 83.41 Hz at the end of the dataset, hence the double ^{39}Ar decay rate changed by 0.96 Hz over the period of data taking. Also, for the selected energy region, the fraction of double ^{39}Ar decay triggers decreased from 16.95 Hz to 16.76 Hz approximately including the parameter, $\epsilon_{2,1}$ from equation (5.27). Similarly, the ^{39}Ar trigger rate from the scintillation light where three ^{39}Ar isotopes are simultaneously decaying in the detector is reduced by 0.056 Hz only, starting from 2.504 Hz to the 2.448 Hz at the end of the dataset. Also, including the factor, $\epsilon_{3,1}$, for the selected energy region,

these rates dropped 0.01 Hz only, from 0.468 Hz in beginning to 0.458 Hz when data taking stopped.

The product of efficiency for software selection cuts and event multiplicity factors are not considered here to determine the actual trigger rates in the formulas. Moreover, the residuals for the decay slopes for the single, double, and triple ^{39}Ar decay trigger rates given in equation (7.3), (7.4), and (7.5) respectively from the first week in the dataset is given in the figure 7.7. The gradient for the residuals of single ^{39}Ar decay coincidence trigger rate from the first week is more as expected while the residuals for the double, and triple ^{39}Ar decay rates are slower and slowest as expected.

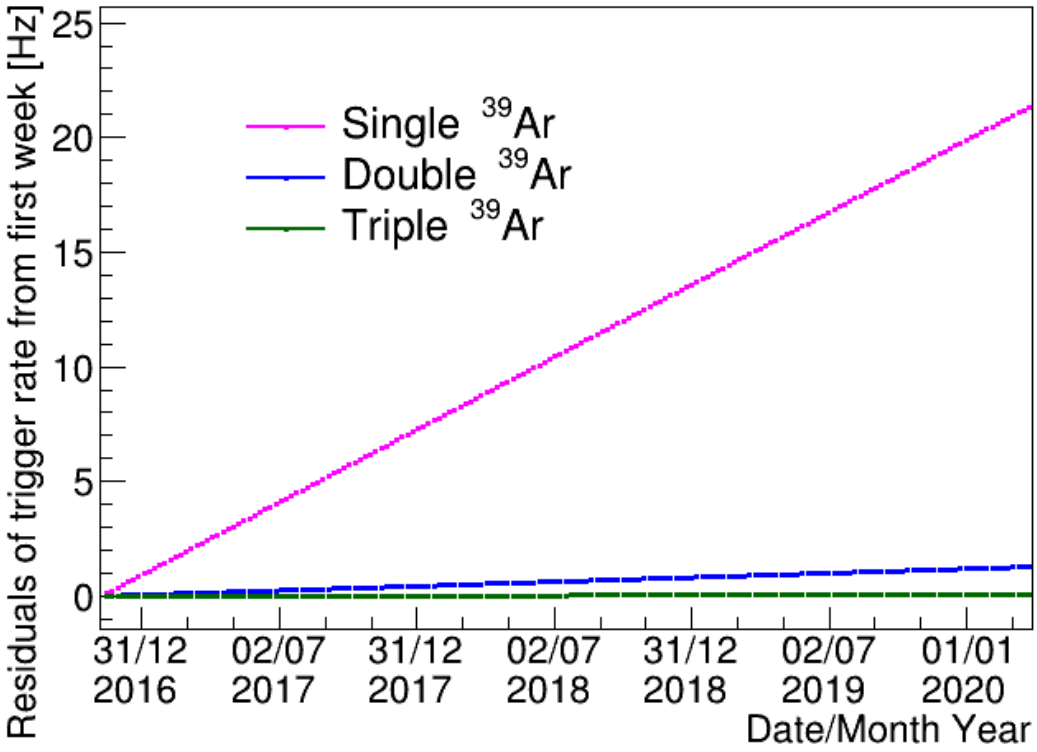

Figure 7.7: The residuals for the different ^{39}Ar trigger rates from the first week in the dataset. The single ^{39}Ar event rate residuals are decaying fastest as predicted by the theoretical definition, following the residuals for the decay of double, and tripe ^{39}Ar decay rates.

To compare the slopes of the different decay rates, the rates for the double and triple ^{39}Ar decay triggers are scaled up with the constant offset of 2778.65 Hz and 2860.82 Hz respectively for the comparison and are shown in figure 7.8.

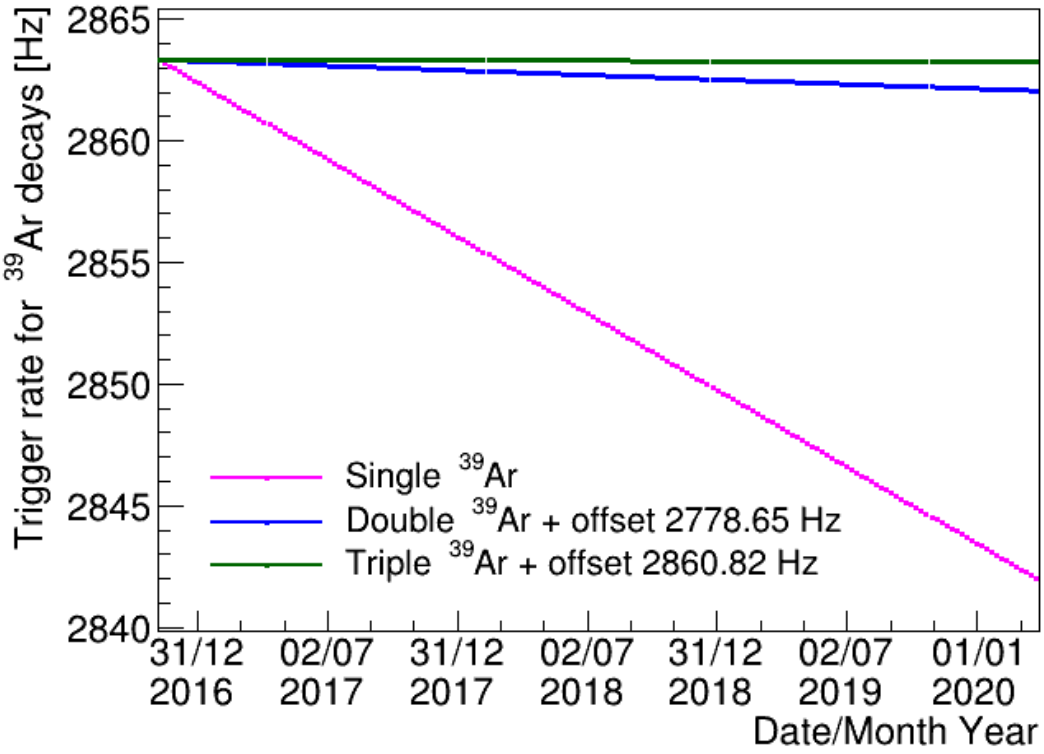

Figure 7.8: The event rate for the decays of single, double, and triple ^{39}Ar isotopes, for comparison the constant offset of event rates 2778.65 Hz and 2860.82 Hz is added to the double and triple ^{39}Ar rates respectively.

Similarly, the pile-up rates for the coincidence of ^{39}Ar decays with low energy Cherenkov light can be calculated from the following equation (7.6) derived from fit model equation (5.24), where the rate of corrected Cherenkov rates for the low threshold from figure 5.20 are used for the estimation of the pile-up rates.

$$R_4(t) = R_{^{39}Ar} * \exp(\frac{-t}{\tau_{^{39}Ar}}) * R_{Cherenkov}(t) * \delta t * \exp(-(R_{Cherenkov}(t) * \delta t)) * \exp(-(R_{^{39}Ar} * \exp(\frac{-t}{\tau_{^{39}Ar}}) * \delta t)) \quad (7.6)$$

The trigger rate for the pile-up of ^{39}Ar with Cherenkov light is also plotted over the

time period of the dataset by using fit output from figure 7.1, and is presented in the figure 7.9.

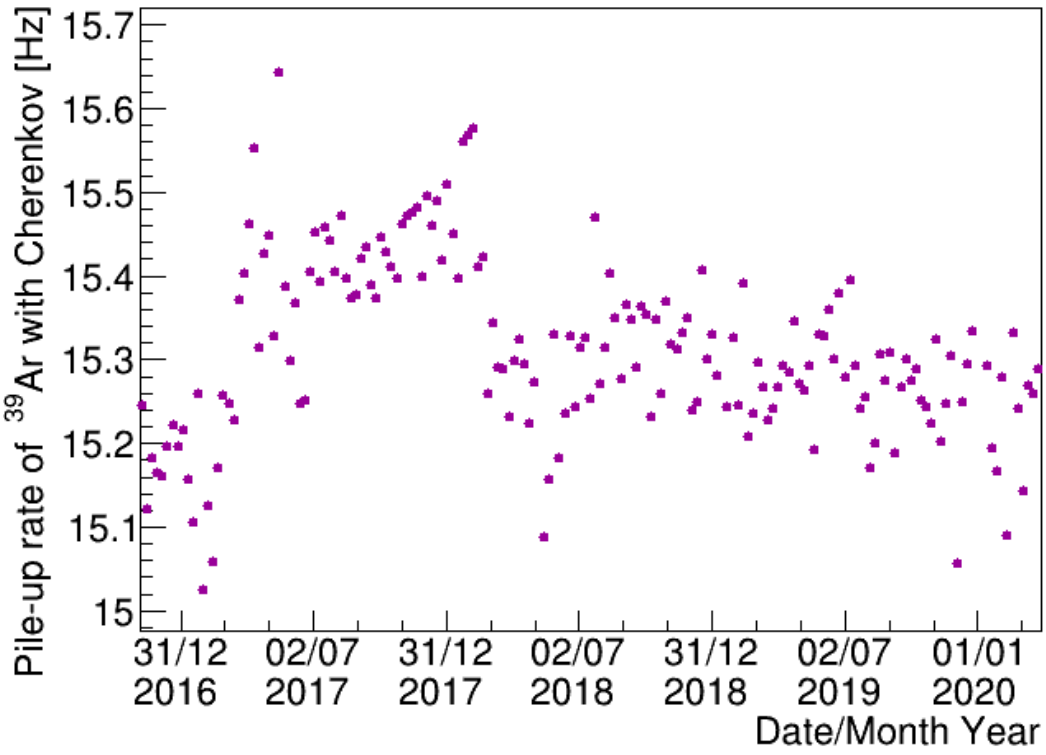

Figure 7.9: The rates for the pile-up of the Ar decay triggers with the low energy Cherenkov light with time.

The trigger rate for the pile-up of ^{39}Ar with low energy Cherenkov scintillation light varied very little over the dataset with the numerical value of 0.64 Hz. The Cherenkov trigger rate is almost constant over time, thus, the lifetime measurement of ^{39}Ar will not be affected by this pile-up.

Thus, by adding the different coincidence event rates from various sources we get the total trigger rates in the detector. The individual pile-up rates from the different coincidence triggers are well-defined and understood from the study. The triggers corresponding to the pile-up of ^{39}Ar with other ^{39}Ar is the dominant of all

the pile-up rates. In addition to the study of different types of triggers in the dataset, the effect of the different systematic (discussed in the section 6.3) is also studied in detail as given in the following sections.

7.3 Systematic uncertainty on lifetime of ^{39}Ar

The fit model output of the evaluated rates from the formula defined in equation (5.24) indicates the statistical uncertainty on the lifetime parameter, $\tau_{^{39}Ar}$ with the value of 10.17 years. However, for the complete measurement of the lifetime of ^{39}Ar isotopes, the effect of the systematic discussed in chapter 6 is also investigated, which is analyzed in this section. The average value of uncertainties from the different systematic is already given in the section 6.3.

7.3.1 Uncertainty from small trigger count difference systematic

The average value of residuals for the small trigger count difference in physics data as predicted from figure 6.4 is $(0.00022 \pm 0.00012)\%$. The effect of this systematic on $\tau_{^{39}Ar}$ is studied by adding an extra constant uncertainty, 0.00022% of trigger rates in the observed error bars in the figure 6.16 and fitting the trigger rates with decay model to get the total uncertainty from statistical and this systematic as already done in the figure 7.1.

The lifetime parameter for the decay of ^{39}Ar does not change significantly, only a change of 0.0026 years is recorded with the addition of this little uncertainty in the estimated errors on the trigger rates, therefore,

$$\sigma_{ecd} = 0.00258 \text{ years} \tag{7.7}$$

Thus, this systematic is not affecting the measurement of $\tau_{^{39}Ar}$ for ^{39}Ar isotope. Moreover, this small systematic uncertainty is a good indication of the precision of the triggers recorded by the detector corresponding to the scintillation of light emitted from the decay of ^{39}Ar.

7.3.2 Uncertainty from small livetime difference systematic

The livetime information for the various triggers in the physics dataset is very precisely and accurately recorded in the database, however with a very little average systematic value of 0.00075% as given in the figure 6.7 it could change the lifetime measurement of ^{39}Ar by some small number. To get the uncertainty from this systematic, a constant uncertainty of 0.00075% of the trigger rates observed in the figure 6.16 is added to the evaluated errors, and then trigger rates containing total uncertainty from statistical and this systematic are fitted with the decay model from equation (5.24).

Adding this extra systematic uncertainty in the trigger rates errors, the value of $\tau_{^{39}Ar}$ for the ^{39}Ar decays only changed by 0.0021 years, hence,

$$\sigma_{ld} = 0.00213 \text{ years} \tag{7.8}$$

Thus, these little systematic for the livetime assessment are not affecting the lifetime measurement under study. Similar to the good precision of event count, the very small value of the livetime difference shows the definite measurement of the time information in the physics data.

7.3.3 Uncertainty from energy correction systematic

The small changes in the energy correction hence the light yield of the detector over the dataset are discussed in section 6.4. The average value for the relative error

propagated from this systematic is given in figure 6.13 with value (0.076 ± 0.044)%. The average value of this error is the highest systematic studied for the analysis. Therefore, in order to get the uncertainty on the ^{39}Ar lifetime measurement from this systematic, the deviation of this relative error overtime is considered in the following three ways,

1. The uncertainty with the average value of 0.076% is constant throughout the dataset.

2. The error decreases uniformly from 0.076% at beginning of the dataset to 0% at the end of the dataset.

3. The error increases uniformly from 0% at the start of the dataset to 0.076% at the end of the dataset in March 2020.

Also, unlike the small event count discrepancy, and livetime measurement, the uncertainty on the energy response correction hence the light yield of the detector is indirectly affecting the trigger rates in the ROI. Therefore, firstly, the uncertainty on the trigger rates in ROI is calculated from the uncertainty on the light yield ratios, and finally, the uncertainty from calculated trigger rates is then studied for the systematic uncertainty on the lifetime parameter. The effect of using the uncertainty in all three cases is discussed as under.

7.3.3.1 Uncertainty from a constant offset in the energy scale

To understand the effect of the average value of systematic on the trigger rates, a constant uncertainty of 0.076% of the light yield ratio is added to the errors bars of the light yield ratios in figure 6.11, which are used for the correction of the energy of triggers (see section 6.4). The trigger rates in the ROI are calculated from two

different corrections, one with the trigger energies corrected from the mean value of light yield ratio, LY_{rm}, and the second with the correction of the trigger energies from the LY_{rm} plus uncertainty, $\mathrm{LY}_{rm+uncertainty}$, where uncertainty is 0.076% times LY_{rm}. More explicitly, this can be written as,

$$\text{Corrected trigger rates } (R_{meanLY}) = \text{Trigger rates where energy of triggers corrected with } LY_{rm} \quad (7.9)$$

and,

$$\text{Corrected trigger rates with uncertainty}(R_{meanLY+uncertainty}) = \text{Trigger rates where energy of triggers corrected with } LY_{rm+uncertainty}(LY_{rm} + 0.076\% * LY_{rm}) \quad (7.10)$$

The difference in the trigger rates, R_{meanLY} and $\mathrm{R}_{meanLY+uncertainty}$ is used as the extra uncertainty on the total trigger rates from this systematic. This additional uncertainty is added to the trigger rates uncertainties in figure 6.16.

The one-dimensional distribution of the relative uncertainties on trigger rates measured from the constant uncertainties on the LY ratios is shown in figure 7.10. The mean value of the relative error from the distribution is $(0.0885 \pm 0.0036)\%$ which is further used to get the uncertainty on the lifetime of ^{39}Ar decay.

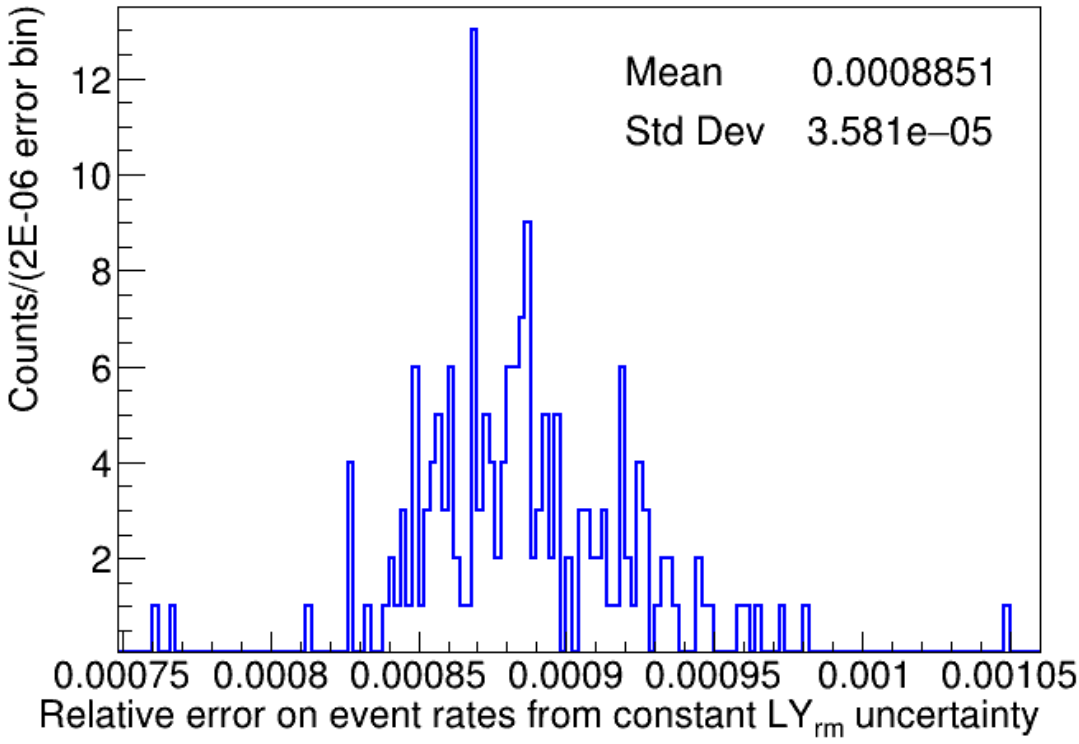

Figure 7.10: The distribution of the relative residuals of uncertainty on the trigger rates corrected with LY_{rm}, and $\mathrm{LY}_{rm+uncertainty}$. The mean value of relative error is 0.088% as indicated in the statistical box.

Also, the uncertainty of the trigger rates is calculated from this systematic in this case by subtracting the extra uncertainty of 0.076% times LY_{rm} from the LY_{rm} correction factor and plotting the relative distribution of trigger rates. This calculation returns the same value of the mean uncertainty of 0.088% over the trigger rates.

The total trigger rates with the new uncertainty (sum of statistical and constant systematic error of 0.088% of trigger rates) are then fitted with the defined fit model from equation (5.24) to get the uncertainty from this systematic by considering it constant throughout the dataset. The result of the fit model showed the lifetime

parameter changes by 3.3 years due to this systematic if considered constant over time.

7.3.3.2 Uniform increase in uncertainty from energy correction systematic

In this section, to investigate the range of the systematic uncertainty from the energy scale corrections on the lifetime parameter, the uniform increment of the energy correction error is considered over the time of the dataset. Since the uncertainty from LY_{rm} is not exactly similar to the uncertainty on trigger rates but it is directly correlated because it affects the excess and leakage of triggers in the ROI. Therefore, the trigger rates are calculated from the two correction factors again, firstly, where the trigger rates corrected from LY_{rm} given by equation (7.9), and secondly, where the trigger energies are corrected from $\mathrm{LY}_{rm+increuncertainty}$, the incre here represents the increment value of error by factor 8.6E-08 over 8862 runs* in the final dataset selected for the study. Also, it can be written as,

$$\text{Corrected trigger rates for } i^{th} \text{ run with increasing uncertainty}(R_{meanLY+increuncertainty}) = \text{Trigger rates where energy of triggers corrected with } LY_{rm+increuncertainty}(LY_{rm} + (i^{th} * 8.6E-08) * LY_{rm}) \quad (7.11)$$

where, i^{th} here represents the integer for the run number like i=1 for first-run number 18721, and i=8862 for last run number 27583.

Again, the difference in the trigger rates, R_{meanLY} and $\mathrm{R}_{meanLY+increuncertainty}$ is used as the uncertainty on the trigger rates from this systematic in this case, and this

*The physics run numbers used in the study are 991 counts, however, the identification number of the runs varies from 18721 to 27583 which gives 8862 steps for the increment.

extra uncertainty is added to the statistical uncertainty from trigger rates in figure 7.1. The one-dimensional distribution of the relative uncertainties on trigger rates measured from the increment of uncertainties on the LY ratios is shown in figure 7.11. The mean value of the relative error from the distribution is $(0.043 \pm 0.026)\%$ which is further used to get the uncertainty on the lifetime of ^{39}Ar decay.

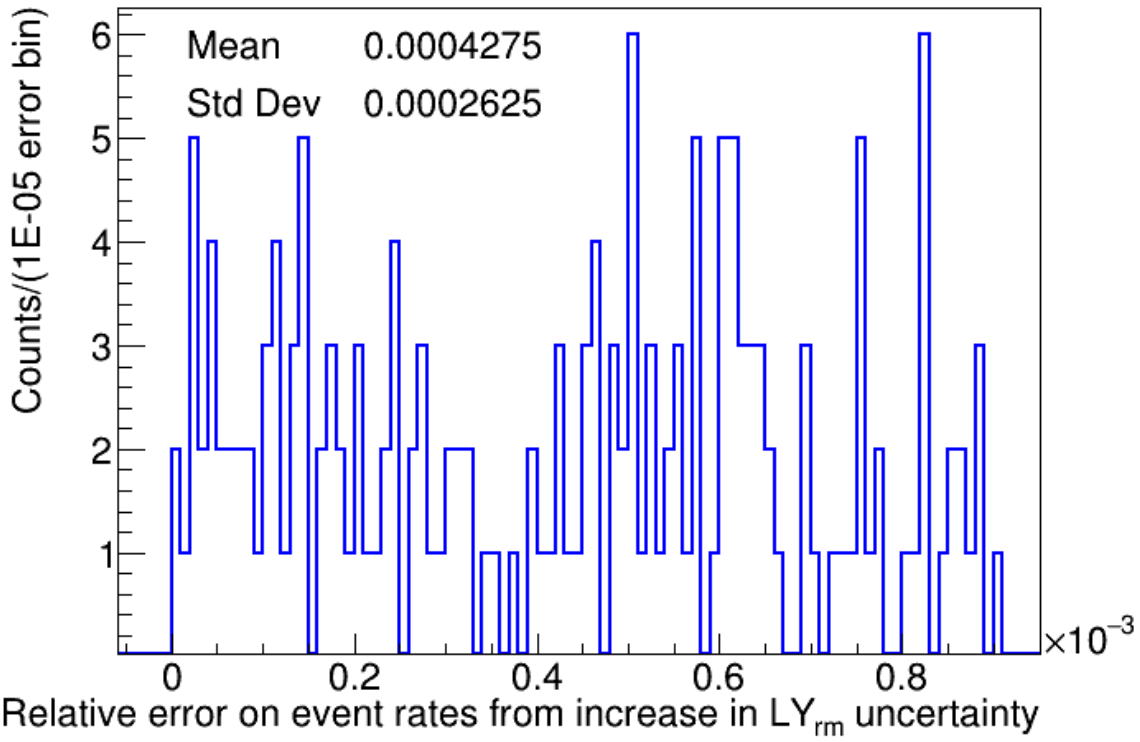

Figure 7.11: The distribution of the relative residuals of uncertainty on the trigger rates corrected with LY_{rm}, and $\mathrm{LY}_{rm+increuncertainty}$. The mean value of relative error is 0.043% as given by the histogram.

In a similar manner, the uncertainty of the trigger rates is also calculated by subtracting the extra uncertainty with the above increment factor from the LY_{rm} correction and plotting the relative distribution of trigger rates. This calculation returns the same value of the mean uncertainty of 0.043% over the trigger rates.

The new systematic uncertainty is then added to the statistical error bars of the trigger rates, and the fit model from equation (5.24) is fitted to the calculated rates to get the uncertainty on the lifetime of ^{39}Ar decay by using the increase in the energy response systematic uncertainty. The fit output returns the lifetime parameter value as 445.38 years. Thus, the lifetime of ^{39}Ar from fit changed by 7.39 years due to this increasing systematic uncertainty with time.

7.3.3.3 Uniform decrease in uncertainty from energy correction systematic

The last deviation studied for the uncertainty on the energy correction systematic if its mean uncertainty decreases uniformly from 0.076% at the beginning of the dataset to 0% till the end of the dataset. Some similar calculations as discussed in the section 7.3.3.2 are done except for the increment of uncertainty for LY_{rm}, its uncertainty value is considered to be uniform decreases with a factor of 8.6E-08 over 8862 runs. The corresponding uncertainty on the trigger rates can be evaluated from the subtraction of trigger rates, R_{meanLY} given in equation (7.9), and ($\mathrm{R}_{meanLY+decreuncertainty}$), where, ($\mathrm{R}_{meanLY+decreuncertainty}$) are the trigger rates in which energies on individual triggers are corrected from $\mathrm{LY}_{rm+decreuncertainty}$. The subscript decre shows the decrement value of error by factor 8.6E-08. Thus, we have,

$$\text{Corrected trigger rates for } i^{th} \text{ run with decreasing uncertainty}(R_{meanLY+decreuncertainty}) = \text{Trigger rates where energy of triggers corrected with } LY_{rm+decreuncertainty}(LY_{rm} - (i^{th} * 8.6E-08) * LY_{rm}) \quad (7.12)$$

where i^{th} has the same representation of the integer number for the runs in the dataset. The distribution of relative uncertainties on trigger rates measured from the uniform

decrement of uncertainties on the LY ratios is shown in figure 7.12. The mean value of the relative error from the distribution is (0.046 ± 0.026)% which is further used to get the uncertainty on the lifetime of ^{39}Ar decay.

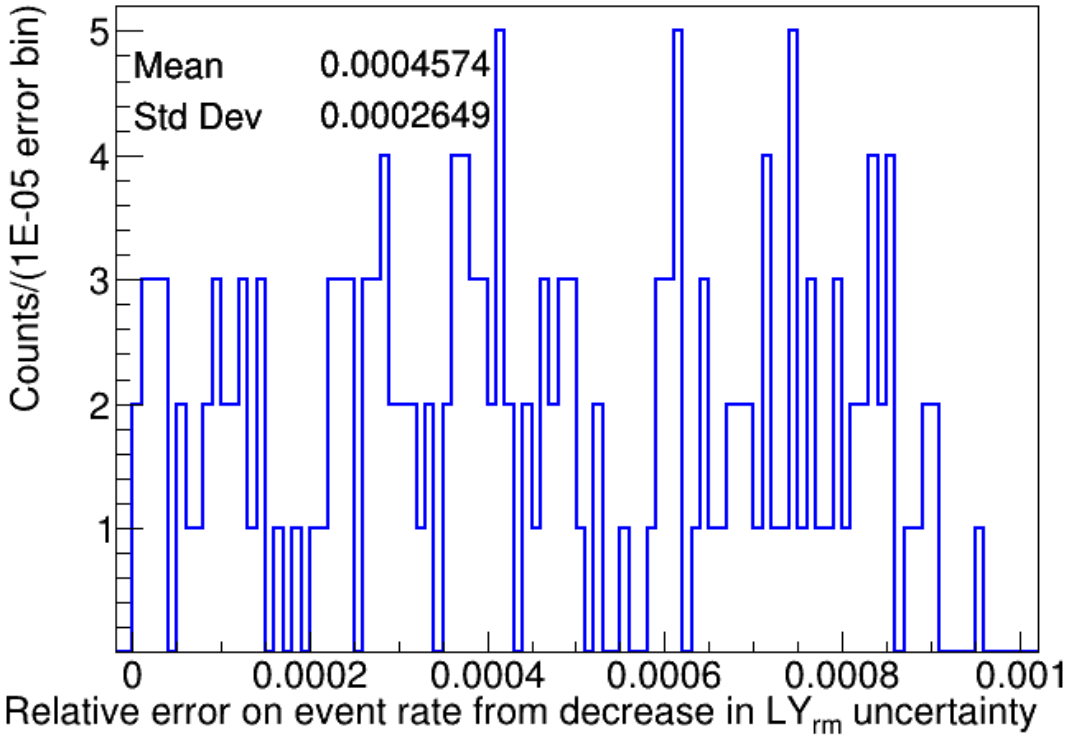

Figure 7.12: The distribution of the relative residuals of uncertainty on the trigger rates corrected with LY_{rm}, and $LY_{rm+decreuncertainty}$. The mean value of relative error is 0.046% as given in the histogram.

As a cross-check, the uncertainty on the trigger rates is also calculated by subtracting the extra uncertainty with the above decrement factor from the LY_{rm} correction. Plotting the relative error distribution for these trigger rates gives the same mean uncertainty of 0.046% for the dataset.

The fit function from equation (5.24) is used for fitting the total trigger rates with the updated uncertainty where the statistical error bars of the trigger rates are

summed with the decreasing value of energy correction systematic uncertainty. The lifetime of ^{39}Ar decay in the new fit results change by 5.14 years with an updated value of 443.12 years. Thus, using the uniform decreasing value of the energy response systematic uncertainty over time, the lifetime parameter varies by 1.2% approximately.

Maximum uncertainty from energy correction systematic To sum up the systematic uncertainty from the energy scale corrections, the maximum uncertainty on the lifetime parameter, $\tau_{^{39}Ar}$ for decay measurement of ^{39}Ar is 7.39 years, which is,

$$\sigma_{esc} = 7.39 \text{ years} \tag{7.13}$$

This is the highest systematic error derived from the deviation of the uncertainties on the differential change of light yield of the detector.

7.3.4 Uncertainty from variation in energy resolution

The systematic uncertainty contributed by the variation in the energy resolution of the detector response over the period of data taking is discussed in section 6.5. To estimate the systematic uncertainty on ^{39}Ar from energy resolution, the new value for the fraction of single ^{39}Ar triggers in the selected energy region derived in equation (6.7) from the updated analytical spectrum with additional error in the energy resolution is used in the fit model from equation (5.24) such that the modified equation for the fit out ^{39}Ar decays look like,

$$R(t) = [R_{^{39}Ar} * \exp(\frac{-t}{\tau_{^{39}Ar}}) * \epsilon^{'}_{1,1} * \prod_{j=2}^{4} \epsilon_{1,j}(t) + R^{2}_{^{39}Ar} * \delta t * \exp(\frac{-2t}{\tau_{^{39}Ar}}) * \prod_{j=1}^{4} \epsilon_{2,j}(t) + \frac{R^{3}_{^{39}Ar}}{2} * \delta t^{2} *$$
$$\exp(\frac{-3t}{\tau_{^{39}Ar}}) * \prod_{j=1}^{4} \epsilon_{3,j}(t) + R_{^{39}Ar} * \exp(\frac{-t}{\tau_{^{39}Ar}}) * R_{Cherenkov}(t) * \delta t * \exp(-(R_{Cherenkov}(t) * \delta t)) *$$

$$\prod_{j=1}^{4} \epsilon_{4,j}] * \exp(-(R_{^{39}Ar} * \exp(\frac{-t}{\tau_{^{39}Ar}}) * \delta t)) + R_{bg} \quad (7.14)$$

where, $\epsilon'_{1,1}$ is 0.209, 0.12% different from nominal fraction, $\epsilon_{1,1}$ calculated in section 5.26. The total trigger rates measured in figure 6.16 are fitted with the modified decay model from equation (7.14). The lifetime parameter for ^{39}Ar, $\tau_{^{39}Ar}$, changed by 0.0032 years only which is a negligible uncertainty from this systematic, which can be written as,

$$\sigma_{erv} = 0.0032 \text{ years} \quad (7.15)$$

Thus, the only way resolution can affect the lifetime measurement is by changing the fraction of single ^{39}Ar in the selected energy window by a small amount which gave insignificant uncertainty on $\tau_{^{39}Ar}$.

7.3.5 Uncertainty from small variation in ER background

The systematic uncertainty from the small variation in the ER background discussed in section 5.13.1 is evaluated in this section. In place of constraining the ER background contribution to 1.65 Hz, the five times the average value of the ^{232}Th rates from figure 5.44 are subtracted from 1.65 Hz. The time-dependent contribution from the ^{232}Th gammas is added to the rest of ER background rates, after scaling the rates from figure 5.42 by a constant multiple of 5. This is because the gamma content in the ROI from the ^{232}Th decay is 5 times the rates in ^{208}Tl peaks. The updated model is then fitted to the calculated ^{39}Ar rates in figure 6.16. The lifetime parameter from the fit output only varied by 0.27 years.

Moreover, using the same approach by varying the ER background rates with respect to the change in the rates of the ^{226}Ra gammas, a daughter of ^{238}U chain over time, the lifetime of the changed by 0.33 years only.

Thus, the maximum systematic uncertainty, σ_{ERtime}, calculated from the time dependence of ER background rates is estimated from the decay of ^{232}Th and ^{238}U chain, and is given by,

$$\sigma_{ERtime} = 0.33 \text{ years} \tag{7.16}$$

7.3.6 Uncertainty from ^{39}Ar selection cuts efficiency

The ^{39}Ar software cuts used in selecting the ROI and its efficiency calculations are already discussed in section 5.5, and 5.11 respectively. The systematic uncertainty from the cut efficiencies is calculated in two different ways, firstly for the change in the average value of efficiencies from the data, and secondly, for the deviation of efficiencies with time which is discussed in the following sections.

7.3.6.1 Uncertainty from the average value of efficiencies

The systematic uncertainty from the average values of the efficiencies is considered if there are no corrections applied to the efficiencies from the MC and discrepancies adopted from the subeventN cut. For the calculation of uncertainty from this systematic effect, the product of efficiencies from the data is included as

$$\prod_{j=2}^{3} \epsilon^{"}_{i,j}(t) = \prod_{j=2}^{3} \epsilon_{i,j_{data}}(t) \tag{7.17}$$

where i varying from 2 to 3, represents the different trigger types (double, or triple pile-up of ^{39}Ar with other ^{39}Ar decays), and j is the number of software selection cuts used in the study (j=2 and 3, for fmaxpe and fprompt cuts respectively). The updated efficiencies are then used in the fitness model from equation (5.24) for double and triple ^{39}Ar, one at a time to estimate the uncertainty on the lifetime measurement for this systematic. For example, the updated fit model with new efficiencies for double

^{39}Ar selection becomes,

$$R(t) = [R_{^{39}Ar} * \exp(\frac{-t}{\tau_{^{39}Ar}}) * \prod_{j=1}^{4} \epsilon_{1,j}(t) + R^2_{^{39}Ar} * \delta t * \exp(\frac{-2t}{\tau_{^{39}Ar}}) * \epsilon_{2,1} * \epsilon_{2,4} * \prod_{j=2}^{3} \epsilon^{"}_{2,j}(t) +$$
$$\frac{R^3_{^{39}Ar}}{2} * \delta t^2 * \exp(\frac{-3t}{\tau_{^{39}Ar}}) * \prod_{j=1}^{4} \epsilon_{3,j}(t) + R_{^{39}Ar} * \exp(\frac{-t}{\tau_{^{39}Ar}}) * R_{Cherenkov}(t) * \delta t *$$
$$\exp(-(R_{Cherenkov}(t) * \delta t)) * \prod_{j=1}^{4} \epsilon_{4,j}] * \exp(-(R_{^{39}Ar} * \exp(\frac{-t}{\tau_{^{39}Ar}}) * \delta t)) + R_{bg} \quad (7.18)$$

The use of the average efficiencies from the data-driven approach in the fit model for the double ^{39}Ar changed the lifetime output, $\tau_{^{39}Ar}$ by 0.38 years only, therefore,

$$\sigma_{eda} = 0.38 \text{ years} \quad (7.19)$$

Similarly, the new average values of the triple ^{39}Ar cut efficiencies from data only in the fit model decreased the lifetime, $\tau_{^{39}Ar}$ by 0.013 years, which can be presented by,

$$\sigma_{eta} = 0.013 \text{ years} \quad (7.20)$$

Also, to include the effect of deviation in the efficiencies over time, and this systematic uncertainty in the lifetime measurement for ^{39}Ar isotope, a similar procedure adopted for the energy response systematic uncertainty is followed. The only difference is that uncertainty on the efficiency is directly related to the trigger rates of individual trigger types.

The uncertainty on the lifetime measurement of ^{39}Ar isotope from this systematic is calculated by using the updated efficiencies for selecting different event types (single, double, and triple ^{39}Ar pile-up) in the fit model from equation (5.24) where

the efficiencies are increased or decreased with errors, such that,

$$\prod_{j=2}^{3} \epsilon'_{i,j}(t) = \prod_{j=2}^{3} (\epsilon_{i,j} \pm \sigma_{\epsilon_{i,j}})(t) \tag{7.21}$$

where i varying from 1 to 3, represents the different trigger types (single ^{39}Ar decay trigger, or double, or triple pile-up of ^{39}Ar with other ^{39}Ar decays), and j is the number of software selection cuts used in the study (j=2 and 3, for fmaxpe and fprompt cuts respectively). The uncertainty, $\sigma_{\epsilon_{i,j}}(t)$, for these software efficiencies, is further varied in the following three ways again,

1. The uncertainty with the average value from each type of trigger (single or pile-up) is kept constant throughout the dataset and added to the efficiency value to get the updated efficiency in the fit model.

2. The average value of error on the efficiency of each trigger is considered to decrease uniformly from the maximum percentage at beginning of the dataset to 0% at the end of the dataset, and then added to the efficiency value to get the updated efficiency in the fit model.

3. The average uncertainty for each trigger type is increased uniformly from 0% at the start of the dataset to the maximum value at the end of the dataset and then added to the efficiency value to get the updated efficiency in the fit model.

As an example, for the updated software cut efficiencies for selecting single ^{39}Ar decay triggers, the fit model from equation (5.24) becomes,

$$R(t) = [R_{^{39}Ar} * \exp(\frac{-t}{\tau_{^{39}Ar}}) * \epsilon_{1,1} * \epsilon_{1,4} * \prod_{j=2}^{3} \epsilon'_{1,j}(t) + R^2_{^{39}Ar} * \delta t * \exp(\frac{-2t}{\tau_{^{39}Ar}}) * \prod_{j=1}^{4} \epsilon_{2,j}(t) +$$

$$\frac{R^3_{^{39}Ar}}{2} * \delta t^2 * \exp(\frac{-3t}{\tau_{^{39}Ar}}) * \prod_{j=1}^{4} \epsilon_{3,j}(t) + R_{^{39}Ar} * \exp(\frac{-t}{\tau_{^{39}Ar}}) * R_{Cherenkov}(t) * \delta t *$$
$$\exp(-(R_{Cherenkov}(t) * \delta t)) * \prod_{j=1}^{4} \epsilon_{4,j}] * \exp(-(R_{^{39}Ar} * \exp(\frac{-t}{\tau_{^{39}Ar}}) * \delta t)) + R_{bg} \quad (7.22)$$

Only the addition of uncertainty to the mean efficiency for the different types is considered to get the maximum change (one at a time for three efficiencies); however, the cross-checks have been made by subtracting the uncertainty from the mean efficiency which results in the similar error on the lifetime parameter. A similar treatment is done for getting the systematic uncertainty from new double and triple efficiency terms in the fit function. More details for the uncertainty calculation from this systematic are discussed in the following section.

7.3.6.2 Uncertainty from deviation in single ^{39}Ar efficiency over time

The one-dimensional distribution for the efficiency of software cuts used to separate the single ^{39}Ar decay triggers are given in figure 5.31 which has 100% mean value and, a sigma of 0.000079%. This very small value of the standard deviation shows the accuracy of the trigger selection cuts used in the study. However, to study the effect of this uncertainty on the lifetime of ^{39}Ar, additional uncertainty is added to the mean efficiency in the three different methods.

The constant systematic uncertainty with value 0.000079% is added with the mean efficiency, and the total trigger rates from figure 6.16, are fitted with the updated efficiency of single ^{39}Ar triggers. The new fit model returns a change in the lifetime parameter by 0.0014 years.

Also, including the additional uncertainty with a uniform increment of factor 4.46E-09 corresponding to 177 weeks of the dataset, with the efficiency term and then fitting the total trigger rates with the new model from equation (7.22) gives

the maximum change of 0.047 years in the lifetime parameter. The same variation in the $\tau_{^{39}Ar}$ is observed even if the uncertainty on the single ^{39}Ar selection efficiency decreases uniformly from maximum value 0.000079% at the start of the data period to the 0% at the end of the data period. Thus, the uncertainty from the efficiency of cuts used to select single ^{39}Ar triggers is,

$$\sigma_{es} = 0.04687 \text{ years} \tag{7.23}$$

7.3.6.3 Uncertainty from deviation in double ^{39}Ar efficiency over time

The efficiency of selection cuts for the double ^{39}Ar decay triggers is given in the distribution from figure 5.34. The mean value for this efficiency is (0.9099 ± 0.0033), and to measure the uncertainty from this systematic on the lifetime of ^{39}Ar, similar treatment as discussed in the section 7.3.6.2 is done.

In the constant uncertainty approach, the additional error of 0.33% is added to the efficiency factors for selecting double Ar decay triggers using software cuts, $\prod_{j=2}^{3} \epsilon_{2,j}(\mathrm{t})$ and then updated fit model is applied to the calculated trigger rates. The lifetime of Ar isotope from the fit model returns a change of 0.022 years.

Similarly, adding the uniform increment, and also the uniform decrement in the efficiency for selecting the double ^{39}Ar decay triggers, affects the lifetime parameter, $\tau_{^{39}Ar}$ by 2.61 years, and 2.63 years respectively. The constant factor for the overall deviation on the uncertainty is 1.847E-05 for the 177 weeks of the dataset. The uncertainty from the efficiency of cuts used in the selection of double ^{39}Ar decay triggers is,

$$\sigma_{ed} = 2.631 \text{ years} \tag{7.24}$$

7.3.6.4 Uncertainty from deviation in triple ^{39}Ar efficiency over time

The last systematic uncertainty studied from the efficiency term for the selection of the triple ^{39}Ar decays. The equivalent procedure is followed where the effect of constant average uncertainty and uniform deviation of uncertainty (either increase or decrease in the uncertainty) is used with the efficiency factor, $\prod_{j=2}^{3} \epsilon_{3,j}(\mathrm{t})$.

The distribution of efficiency for selecting triple ^{39}Ar is already discussed and shown in figure 5.37. The constant uncertainty of 3.93% is when added to the efficiency term, $\prod_{j=2}^{3} \epsilon_{3,j}(\mathrm{t})$, the lifetime, $\tau_{^{39}Ar}$ changed with 0.005 years only which is a negligible divergence from this systematic uncertainty. Also, if the efficiency for triple ^{39}Ar decay triggers is either uniformly increased or decreased with a factor of 0.000022, the lifetime of ^{39}Ar varied by 0.28 years in both cases. Consequently, the uncertainty from the efficiency of cuts for triple ^{39}Ar decays is,

$$\sigma_{et} = 0.2838 \text{ years} \tag{7.25}$$

Maximum uncertainty from the efficiency of trigger selection cuts Therefore, the maximum systematic uncertainty on the lifetime of ^{39}Ar from the software efficiency of different trigger selection cuts is 2.6 years. This systematic error derived from the deviation of the uncertainties on the efficiencies is lower than the energy correction systematic which has the maximum uncertainty of 7.4 years on the, $\tau_{^{39}Ar}$, lifetime of ^{39}Ar isotope.

7.3.7 Uncertainty from the fraction of different trigger types in fit model

The fraction of different trigger types in the selected energy region including the single, and pile-up of ^{39}Ar decay light with itself and low energy Cherenkov light is constrained in the fit model from the analytical spectrum which is also verified from the simulated MC spectra. Though, to estimate the systematic uncertainty expected from the small variations in these parameters are studied for the complete understanding of uncertainty in the fit model. The fraction parameters corresponding to different ^{39}Ar trigger types are varied from 1% to 5%, and updated values are used in the decay model from equation (5.24) to get uncertainty on $\tau_{^{39}Ar}$. The results from the effect of changing the various fraction parameters by a maximum 5% change are shown in table 7.2.

Table 7.2: Uncertainty on the ^{39}Ar lifetime measurement from the other fit model parameters used to describe the decay of the isotope from DEAP-3600 data.

Fit Parameter	Nominal value used in the analysis	New value with 5% uncertainty	Uncertainty on $\tau_{^{39}Ar}$ [years]
$\epsilon_{1,1}$	0.2106	0.2606	$\sigma_{\epsilon_{1,1}} = 0.31$
$\epsilon_{2,1}$	0.20114	0.25114	$\sigma_{\epsilon_{2,1}} = 1.60$
$\epsilon_{3,1}$	0.18698	0.23698	$\sigma_{\epsilon_{3,1}} = 0.015$
$\epsilon_{4,1}$	0.20846	0.25846	$\sigma_{\epsilon_{4,1}} = 0.0611$

7.3.8 Uncertainty from other time-dependent sources

In this section, the uncertainty on the lifetime measurement of ^{39}Ar is estimated from other sources of systematic which are varying with time, from assuming the presence of other backgrounds in the region of interest, decaying with different lifetimes. For

example, the activity of ^{85}Kr decaying in the detector, production of decay of some other unknown isotopes in the detector with time.

7.3.8.1 ^{85}Kr contribution to the systematic uncertainty

There is no evidence for the presence of ^{85}Kr isotope in the LAr target of the detector (as discussed in section 5.8.1) but there is some uncertainty on the fraction that may be present in the argon. To evaluate the effect of having ^{85}Kr in the argon, a constant upper limit of ^{85}Kr with the different values is used as one-dimensional systematic uncertainty for the measurement of the lifetime of ^{39}Ar isotope. The upper limit for ^{85}Kr is tested at 0.4 mBq/kg, 1.5 mBq/kg, 5 mBq/kg, and 10 mBq/kg. Since the half-life of the lifetime of ^{85}Kr isotope (10.7 years as predicted by [71]) is very shorter than the lifetime of ^{39}Ar, the beta decay of ^{85}Kr isotope (if any present) in the detector can change the measurement of the activity of ^{39}Ar by some percent.

The theoretical analytical spectrum for the beta decay of ^{85}Kr is taken from the publication Haselschwardt et al [71]. The spectrum is calculated in the scale of PE (using the same energy response model from section 5.10) and is shown in figure 7.13. About 17.54% of the total beta decay spectrum lies in the selected ROI, highlighted in the red lines.

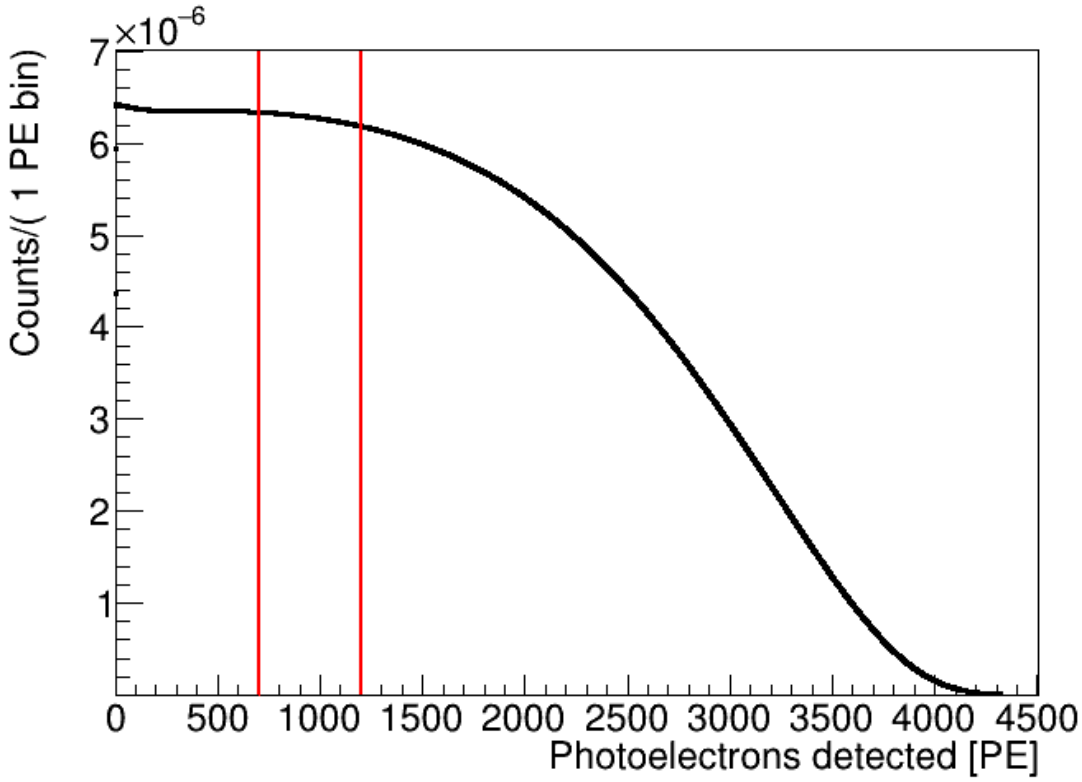

Figure 7.13: Analytical beta decay spectrum of ^{85}Kr isotopes in the scale of PE detected after using the energy response model of the detector (discussed in section 5.10). The selected ROI for the study is shown in the red lines.

To investigate the value of systematic from the upper limit of ^{85}Kr uncertainty, an additional exponential term corresponding to the decay of ^{85}Kr with the constant lifetime of 15.4 years (calculated from the half-life of 10.7 years[†]) is added to the fit model from equation (5.24), as given under,

$$R(t) = [R_{^{39}Ar} * \exp(\frac{-t}{\tau_{^{39}Ar}}) * \prod_{j=1}^{4} \epsilon_{1,j}(t) + R^2_{^{39}Ar} * \delta t * \exp(\frac{-2t}{\tau_{^{39}Ar}}) * \prod_{j=1}^{4} \epsilon_{2,j}(t) + \frac{R^3_{^{39}Ar}}{2} * \delta t^2 *$$

$$\exp(\frac{-3t}{\tau_{^{39}Ar}}) * \prod_{j=1}^{4} \epsilon_{3,j}(t) + R_{^{39}Ar} * \exp(\frac{-t}{\tau_{^{39}Ar}}) * R_{Cherenkov}(t) * \delta t * \exp(-(R_{Cherenkov}(t) * \delta t)) *$$

[†]From radioactive decay model of the nucleus, lifetime = $\frac{\text{half life}}{\ln 2}$

$$\prod_{j=1}^{4} \epsilon_{4,j}] * \exp(-(R_{^{39}Ar} * \exp(\frac{-t}{\tau_{^{39}Ar}}) * \delta t)) + R_{bg} + R_{^{85}Kr} * \exp(\frac{-t}{15.4}) \quad (7.26)$$

where $R_{^{85}Kr}$ is the activity of ^{85}Kr at the start of the physics dataset in November 2016.

The activity of ^{85}Kr is constrained to the various upper limits mentioned above at the beginning of the dataset. The trigger rates are evaluated for the different values of this activity limits from the complete spectrum of ^{85}Kr decay (if the total trigger rates from DEAP data is 3282 Hz). Also, from the beta decay spectrum of ^{85}Kr in the ROI for individual activities, the contribution of trigger rates during the first week in the dataset is very small. The output of fit parameters for the trigger rates using equation (7.26), and its effect on the lifetime of ^{39}Ar isotope, $\tau_{^{39}Ar}$ is shown in the table 7.3.

Table 7.3: The various upper limits for the activity of ^{85}Kr considered in the study and corresponding one-sided systematic uncertainty on the lifetime of ^{39}Ar.

Activity of ^{85}Kr at the first week [mBq/kg]	Trigger rate from the activity ($R_{^{85}Kr}$) in ROI [Hz]	Increase recorded in $\tau_{^{39}Ar}$ parameter [years]
0.4	0.23	4.5
1.5	0.86	16.0
5	2.87	58.7
10	5.75	134.0

Thus, the maximum systematic uncertainty on the lifetime measurement increases with an increase in the upper limit of ^{85}Kr. Also, the decay and lifetime contribution of ^{85}Kr in the fit model from equation (7.26) will shift and correct the lifetime, $\tau_{^{39}Ar}$ in the right direction. Therefore, a precise estimation of ^{85}Kr from the DEAP-3600 detector is needed to finalize the uncertainty from this systematic, however, any amount of ^{85}Kr will only increase the lifetime of ^{39}Ar hence the tension

in the results from this analysis and literature value still exists.

7.3.8.2 Uncertainty from unknown isotope decaying with long lifetime

The ER background rate in the selected region of interest is constrained in the study from the detailed understanding of the ER background model in the experiment as discussed in the section 5.13. However, to evaluate the systematic uncertainty of any unknown isotope which is exponentially decaying in the detector with a long lifetime, the additional unknown background term is added to the fit model as indicated in the equation (7.27).

$$R(t) = [R_{^{39}Ar} * \exp(\frac{-t}{\tau_{^{39}Ar}}) * \prod_{j=1}^{4} \epsilon_{1,j}(t) + R^2_{^{39}Ar} * \delta t * \exp(\frac{-2t}{\tau_{^{39}Ar}}) * \prod_{j=1}^{4} \epsilon_{2,j}(t) + \frac{R^3_{^{39}Ar}}{2} * \delta t^2 * \exp(\frac{-3t}{\tau_{^{39}Ar}}) * \prod_{j=1}^{4} \epsilon_{3,j}(t) + R_{^{39}Ar} * \exp(\frac{-t}{\tau_{^{39}Ar}}) * R_{Cherenkov}(t) * \delta t * \exp(-(R_{Cherenkov}(t) * \delta t)) * \prod_{j=1}^{4} \epsilon_{4,j}] * \exp(-(R_{^{39}Ar} * \exp(\frac{-t}{\tau_{^{39}Ar}}) * \delta t)) + R_{bg} + R_{unknown} * \exp(\frac{-t}{\tau_{unknown}}) \quad (7.27)$$

where $R_{unknown}$ is the rate for any unknown background exponentially decaying in the detector at the start of the physics dataset, and $\tau_{unknown}$ is the long lifetime of the background. There are two cases tested for the unknown background with a lifetime of 500 years and 1000 years with floated the activity of the backgrounds. The lifetime measurement of ^{39}Ar varied by 0.38 years and 2.11 years only with the addition of the unknown background with a lifetime of 500 years and 1000 years respectively, and fit output resulted in the ∼5.4 Hz for the activity of unknown background in the ROI in both cases. Thus, any long-lived unknown component in the detector will contribute to the very small systematic uncertainty that falls within the 1σ value of the statistical uncertainty.

7.3.8.3 Uncertainty from ^{210}Po alphas

The ER background rate included in the decay fit model has every known contribution from the other beta decay in the detector. The physics data analysis from the different studies in the experiment shows the risks of the leaking of the long-lived alphas decay from the ^{210}Po isotope in the lower energy region from 18000 to 22000 PE [6]. This isotope is present in the AV surface at LAr/TPB interface, at TPB/AV interface, and at some inner surfaces of the detector in the bulk amount. The leaking of these alphas can be explained by the action of the TPB, however, not all the alpha decay in the detector results in the triggers.

The leakage probability of these alphas in the ROI is really small or even negligible. Anyhow, the effect of these long-lived alphas is studied from the growth rate of ^{210}Po for the additional systematic analysis since the ^{210}Po with a half-life of 138 days is the primary source of these alphas from the inner surface in AV. ^{210}Po comes later in the ^{222}Rn decay chain as indicated in the figure 4.8. It may appear out of equilibrium with other isotopes on the detector surfaces. In addition to this, the combined activity of ^{210}Po on the different sources within the detector results in the total trigger rates of 3.13 mHz as shown in the table 7.4 from DEAP publication [6].

Table 7.4: The different components in the detector with the corresponding activity and event rate that result in the long-lived alpha decay from ^{210}Po isotope.

Component in the detector with ^{210}Po	Activity/Rate in the detector
TPB and AV surface	(0.26 ± 0.02) mBq/m^2
AV bulk	(2.82 ± 0.05) mBq
Inner flow guide, inner surface in neck region	(14.1 ± 1.3) μHz
Inner flow guide, outer surface in neck region	(16.8 ± 1.4) μHz
Outer flow guide, inner surface in neck region	(22.7 ± 1.6) μHz

Though the exact fraction of these alphas in the ^{39}Ar ROI is not known, the

contribution of a few percent varying from 1 mHz to 500 mHz out of the total event rates are analyzed for the uncertainty on ^{39}Ar lifetime measurement from this systematic. The trigger rates from figure 6.16 are fitted with the fit model in equation (7.28) that account for the growth rate of ^{210}Po in the detector.

$$R(t) = [R_{^{39}Ar} * \exp(\frac{-t}{\tau_{^{39}Ar}}) * \prod_{j=1}^{4} \epsilon_{1,j}(t) + R_{^{39}Ar}^{2} * \delta t * \exp(\frac{-2t}{\tau_{^{39}Ar}}) * \prod_{j=1}^{4} \epsilon_{2,j}(t) + \frac{R_{^{39}Ar}^{3}}{2} * \delta t^{2} * \exp(\frac{-3t}{\tau_{^{39}Ar}}) * \prod_{j=1}^{4} \epsilon_{3,j}(t) + R_{^{39}Ar} * \exp(\frac{-t}{\tau_{^{39}Ar}}) * R_{Cherenkov}(t) * \delta t * \exp(-(R_{Cherenkov}(t) * \delta t)) * \prod_{j=1}^{4} \epsilon_{4,j}] * \exp(-(R_{^{39}Ar} * \exp(\frac{-t}{\tau_{^{39}Ar}}) * \delta t)) + R_{bg} + (R_{^{210}Po} * (1 - \exp(\frac{-t}{\tau_{^{210}Po}})))$$

(7.28)

where $R_{^{210}Po}$ is the activity of ^{210}Po in the ROI, and $\tau_{^{210}Po}$ is the lifetime of the ^{210}Po, fixed to 0.55 years since the half-lifetime of this isotope is 138 years from the literature. The various values of ^{210}Po are included in the fit model at the start time of the dataset, and the output from the decay fit equation with the effect on the ^{39}Ar lifetime measurement is presented in the table 7.5.

Table 7.5: The various activity values of ^{210}Po isotope to account for the leakage of alphas considered in the ROI with the change in the $\tau_{^{39}Ar}$ given in the second column given that the contamination occurred at the start of the dataset.

Trigger rate in the ROI, $R_{^{210}Po}$ with growth started in November 2016 [Hz]	Decrease recorded in the $\tau_{^{39}Ar}$ parameter from fit output [years]
0.001	0.0615
0.0035	0.215
0.010	0.614
0.100	6.064
0.200	11.954
0.300	17.692
0.400	23.280
0.500	28.726

Thus, for the non-realistic case with 500 mHz of ^{210}Po alpha rate in the ROI, the $\tau_{^{39}Ar}$ can decrease by $\sim$29 years. However, for the exact uncertainty from this systematic, the proper leakage of alphas in the 700 to 1200 PE should be estimated. The actual rate of events from ^{210}Po alphas in the ROI is less than 10 mHz. However, the exponential growth curve for the ^{210}Po with time for the extreme case of 500 mHz can be seen in figure 7.14. Also, the average activity of ^{39}Ar from the fit output as a function of ^{210}Po activity is indicated in the figure 7.15.

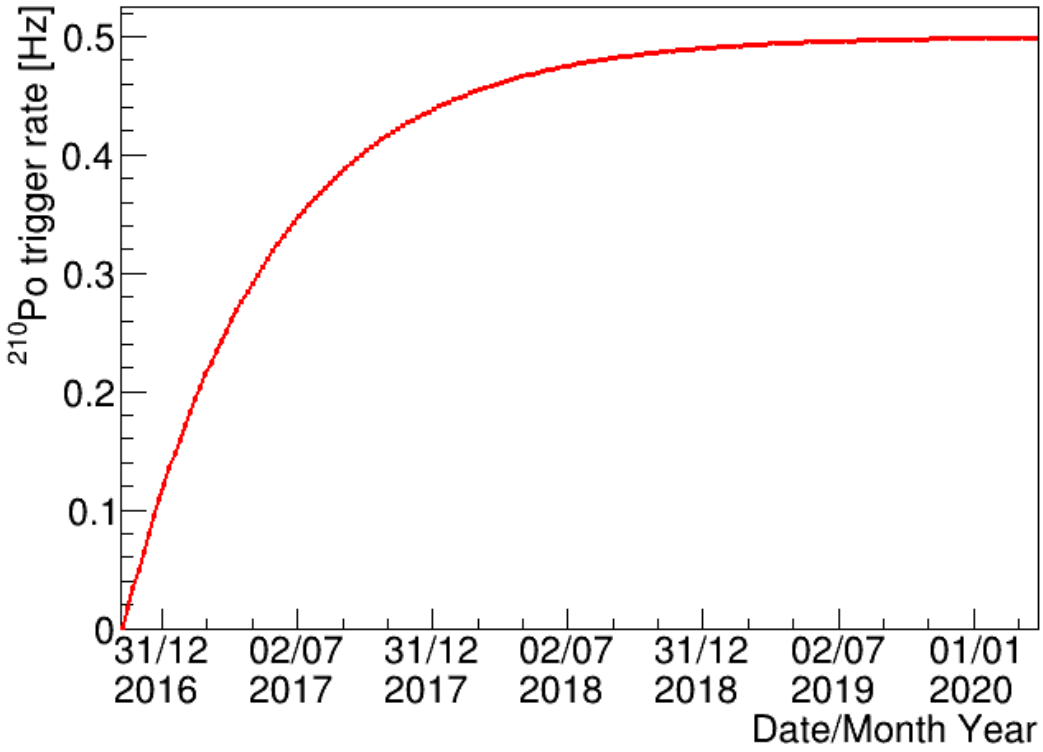

Figure 7.14: The growth curve for the trigger rate corresponding to raise of ^{210}Po on the various surfaces of the detector with the total trigger rate saturated to 500 mHz after the two years in the dataset given that the initial contamination occurred at the beginning of the dataset.

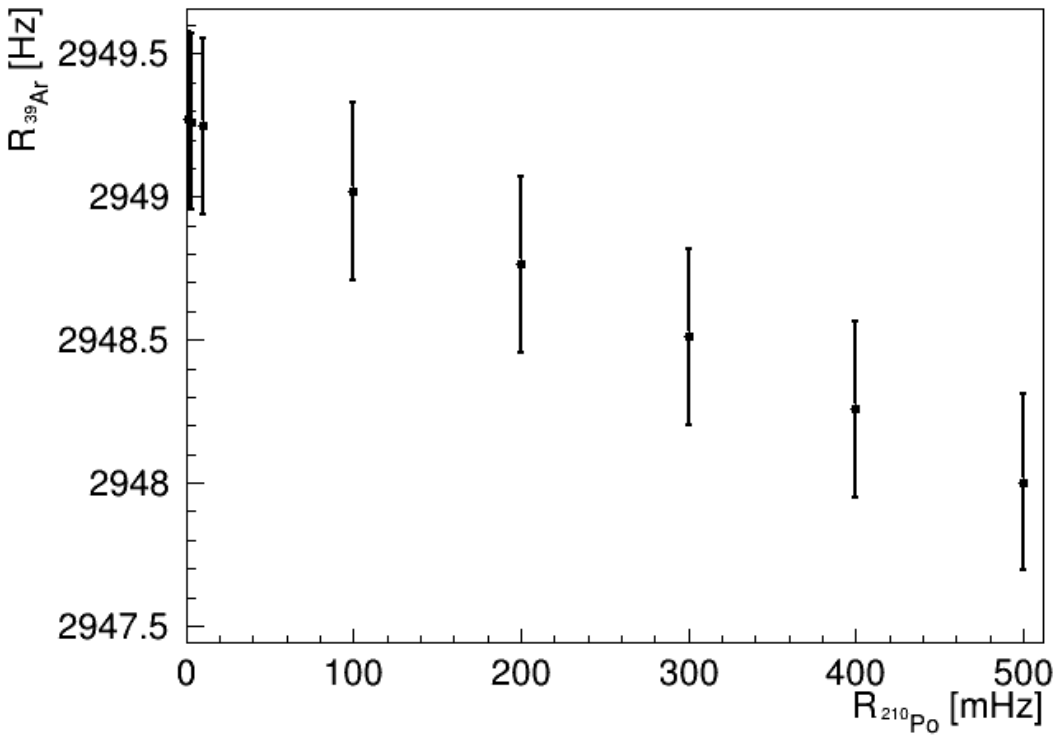

Figure 7.15: The average activity of ^{39}Ar from the full spectrum predicted by the fit output versus the activity of ^{210}Po accounted in the selected energy region.

Moreover, if the Po210 activity is considered to start from the second year of the dataset, from 1 January 2018, the table 7.5 will be updated with negligible effects on the ^{39}Ar lifetime measurement and is shown in the table 7.6.

Table 7.6: The various activity values of ^{210}Po isotope to account for the leakage of alphas considered in the ROI with the change in the $\tau_{^{39}Ar}$ given in the second column given that the growth of ^{210}Po occurred in the start of the second year in the data taking, on 1 January 2018.

Trigger rate in the ROI, $R_{^{210}Po}$ with growth started in January 2018 [Hz]	Decrease recorded in the $\tau_{^{39}Ar}$ parameter from fit output [years]
0.001	0.00081
0.0035	0.00261
0.010	0.00751
0.100	0.07011
0.200	0.14171
0.300	0.21581
0.400	0.28361
0.500	0.35371

Since the ^{210}Po isotope almost saturates to the stable ^{208}Pb isotope in two years, the maximum activity is attained at the end of the dataset in this case as well, however, there is no contribution of trigger rates from ^{210}Po to the total trigger in the beginning for more than one year in this case, and there is very small uncertainty expected in this case.

Similarly, if the contamination of lead, ^{210}Pb, had occurred in the detector during an assembly of different parts of the detector underground sometime from 2014 to 2015, before the start of physics taking, the corresponding growth of ^{210}Po alphas and its effect from the start date of November 2014 and November 2015. The variation in $\tau_{^{39}Ar}$ from the different activity of ^{210}Po alphas in the selected energy region from November 2014 and November 2015 is shown in table 7.7 and 7.8 respectively.

Table 7.7: The various activity values of ^{210}Po isotope to account for the leakage of alphas considered in the ROI with the change in the $\tau_{^{39}Ar}$ if the growth of ^{210}Po occurred on 1 November 2014.

Trigger rate in the ROI, $R_{^{210}Po}$ with growth started in November 2014 [Hz]	Decrease recorded in the $\tau_{^{39}Ar}$ parameter from fit output [years]
0.001	0.00226
0.0035	0.00791
0.010	0.02265
0.100	0.22159
0.200	0.44449
0.300	0.66947
0.400	0.88864
0.500	1.10953

Table 7.8: The activity values of ^{210}Po isotope for the leakage of alphas and change in the $\tau_{^{39}Ar}$ if the growth of ^{210}Po started on 1 November 2015.

Trigger rate in the ROI, $R_{^{210}Po}$ with growth started in November 2015 [Hz]	Decrease recorded in the $\tau_{^{39}Ar}$ parameter from fit output [years]
0.001	0.01016
0.0035	0.03553
0.010	0.10147
0.100	1.00815
0.200	2.01331
0.300	3.01474
0.400	4.00714
0.500	5.0007

Therefore, the exact value of the uncertainty from the leakage of the ^{210}Po alphas in the ROI is still questionable. With the small leakage for 3.5 Hz to the total trigger rate at the start of the dataset, there are 0.2 years of uncertainty on the estimated $\tau_{^{39}Ar}$. Moreover, if there is a leakage of 500 mHz this uncertainty can be increased to 29 years.

7.4 Total systematic uncertainty on $\tau_{^{39}Ar}$

The systematic uncertainties from the small event count discrepancy, livetime difference, energy corrections, and resolution studied for the lifetime measurement of ^{39}Ar are summarised in the table 7.9.

Table 7.9: The mean value of the different detector systematic including the small event count discrepancy, livetime difference, and energy response parameters over ∼3.4 years of the dataset, the systematical uncertainty on the trigger rates and lifetime measurement of ^{39}Ar is also listed in the table.

Systematic uncertainty source	Uncertainty average value	Uncertainty on trigger rate	Uncertainty on $\tau_{^{39}Ar}$ [years]
Event count discrepancy (σ_{ecd})	0.00022%	0.00022%	0.00258
Livetime difference (σ_{ld})	0.00075%	0.00075%	0.00213
Absolute energy scale corrections (σ_{esc})	a) Constant over dataset 0.076%	0.088%	3.263
	b) Uniform shift in light yield uncertainty from 0% to 0.07%	0.043%	7.391
	c) Uniform shift in light yield uncertainty from 0.07% to 0%	0.046%	5.138
Energy resolution variation (σ_{erv})	0.12%	0.00019%	0.0032
ER background rate variation (σ_{ERtime})	0.17%	0.00028%	0.33

Also, the uncertainty on the lifetime parameter from the different fit parameters used in the analysis is summed up in the table 7.10, for the definitions of the various parameters refer to table 5.3.

Table 7.10: List of fit parameters used to model the decay of ^{39}Ar isotope with the average uncertainty and systematic uncertainty on $\tau_{^{39}Ar}$.

Fit model parameters	Uncertainty symbol	Uncertainty source	Uncertainty average value	Uncertainty on $\tau_{^{39}Ar}$ [years]
R_{bg}	σ_{ERB}	Floating the parameter	0.24 Hz	0.11
$\epsilon_{1,1}$	$\sigma_{\epsilon_{1,1}}$	If fraction of single ^{39}Ar in ROI changed by 5.0%	0.050	0.31
$\epsilon_{1,2}(t)$ and $\epsilon_{1,3}(t)$	σ_{es}	Deviation in single ^{39}Ar decay efficiencies with time	a) Constant over dataset 0.000079% b) Uniform shift in efficiency uncertainty from 0% to 0.000079% c) Uniform shift in efficiency uncertainty from 0.000079% to 0%	0.00141 0.04687 0.04684
$\epsilon_{2,1}$	$\sigma_{\epsilon_{2,1}}$	If fraction of double ^{39}Ar in ROI changed by 5.0%	0.050	1.60
$\epsilon_{2,2}(t)$ and $\epsilon_{2,3}(t)$	σ_{eda}	Difference in average value of efficiency for double ^{39}Ar cuts in data and MC	6.0%	0.38
$\epsilon_{2,2}(t)$ and $\epsilon_{2,3}(t)$	σ_{ed}	Deviation in double ^{39}Ar decay efficiencies with time	a) Constant over dataset 0.33% b) Uniform shift in efficiency uncertainty from 0% to 0.33%	0.02231 2.61151

Continuation of Table 7.10				
Fit model parameters	Uncer-tainty symbol	Uncertainty source	Uncertainty average value	Uncer-tainty on $\tau_{^{39}Ar}$ [years]
			c) Uniform shift in efficiency uncertainty from 0.33% to 0%	2.63086
$\epsilon_{3,1}$	$\sigma_{\epsilon_{3,1}}$	If fraction of triple ^{39}Ar in ROI changed by 5.0%	0.050	0.015
$\epsilon_{3,2}$(t) and $\epsilon_{3,3}$(t)	σ_{eta}	Difference in average value of efficiency for triple ^{39}Ar cuts in data and MC	12%	0.013
$\epsilon_{3,2}$(t) and $\epsilon_{3,3}$(t)	σ_{et}	Deviation in triple ^{39}Ar decay efficiencies with time (σ_{et})	a) Constant over dataset 3.9% b) Uniform shift in efficiency uncertainty from 0% to 3.9% c) Uniform shift in efficiency uncertainty from 3.9% to 0%	0.00549 0.27664 0.28381
$\epsilon_{4,1}$	$\sigma_{\epsilon_{4,1}}$	If fraction of ^{39}Ar and Cherenkov pile-up in ROI changed by 5.0%	0.050	0.0611

The overall systematic uncertainty on the lifetime, $\tau_{^{39}Ar}$, is thus evaluated from their maximum possible values of these different systematic uncertainties (discussed section 7.3), and adding them in quadrature since the different sources of systematic uncertainties are uncorrelated. The systematic uncertainties can be added as follows,

$$\sigma_{\tau_{^{39}Ar}}(\text{syst}) =$$

$$\sqrt{\sigma^2_{ERB} + \sigma^2_{ecd} + \sigma^2_{ld} + \sigma^2_{esc} + \sigma^2_{erv} + \sigma^2_{eda} + \sigma^2_{eta} + \sigma^2_{es} + \sigma^2_{ed} + \sigma^2_{et} + \sigma^2_{\epsilon_{1,1}} + \sigma^2_{\epsilon_{2,1}} + \sigma^2_{\epsilon_{3,1}} + \sigma^2_{\epsilon_{4,1}}} \tag{7.29}$$

$$\sigma_{\tau_{^{39}Ar}}(\text{syst}) = 8.03 \text{ years} \tag{7.30}$$

Therefore, the lifetime of ^{39}Ar from its decay measurement is,

$$\tau_{^{39}Ar} \pm \sigma_{\tau_{^{39}Ar}} = (438 \pm 10(\text{stat}) \pm 8(\text{syst})) \text{ years} \tag{7.31}$$

Also, the presence of ^{85}Kr in the detector can increase the average value of the lifetime measurement for ^{39}Ar. In the future steps of the study, in order to estimate the exact lifetime of ^{39}Ar, a detailed understanding of the detector data is required for the activity of ^{85}Kr beta decays. Similarly, the growth rate of ^{210}Po can decrease the estimated lifetime by a couple of years but the correct leakage of these alphas in the selected energy range is need to be evaluated, which is the other step needed for this analysis. Any long-lived unknown isotope decay in the selected energy window will not affect the lifetime measurement for ^{39}Ar isotope from the DEAP-3600 dataset. Thus, the measurement of the lifetime of ^{39}Ar is very precisely done including all the uncertainties from different systematic effects and neglecting any sources of errors. The selection for the ROI is precisely done while rejecting the very low and high energy regions from the spectrum, however, only the stable energy region as validated in the section 5.6 is used for this analysis.

Chapter 8

Sensitivity studies for annual modulation in DEAP

The annual modulation in the nuclear recoil signal due to the relative motion of Earth in the WIMP halo is a powerful tool for dark matter detection [40]. Many direct detection experiments with the target materials, solid crystals, and liquid Xenon have looked for the annual modulation event rates of their signals. Some collaborations have claimed the existence of this modulation with strong evidence, however, their results are still under discussion for various reasons, and there are many experiments that proved the null results for any modulation in the signal [43].

There is no information available for the annual modulation sensitivity of dark matter detectors using LAr as the target material. In this chapter, we will study the possibility of detection of annual modulation in the argon and estimate the sensitivity of the DEAP detector for this signal. The calculations are performed without considering any background contribution to the event rates since this analysis is providing the starting point for the annual modulation possibility with argon as a target material in direct detection experiments using PSD technique. However, the background

for the modulation studies in the argon can be reduced by using underground argon that is isotropically depleted in the ^{39}Ar. Also, the position reconstruction can be used to remove the external source gammas for these studies.

In addition, the systematic studies performed in the earlier chapters are well motivated by evaluating the sensitivity to annual modulation. The comparisons are made in the expected modulation rate and the current detector systematics to conclude the sensitivity for future generation experiments with LAr target. The perspective sensitivities are further evaluated for different detector thresholds. However, the systematics are needed to re-evaluate at the lower thresholds since there are several backgrounds added up in the data taking at the low energies. The systematic uncertainties from the other low-energy ER backgrounds, selection cut efficiencies and their consistency over time are significantly important which can also change for these thresholds. The light yield of the detector is expected to not vary much at the lower energies if the data and energies are properly modeled and explained from the calibration sources but it can be a dominant systematic which can change by the thermodynamic conditions and stability of the detector.

8.1 Nuclear recoil rates in LAr

The method of combining the WIMP model with the DEAP-3600 detector model for the recoil event rate calculations is taken from Lewin and Smith [40], and McCabe [44]. The study of the WIMP model with ^{40}Ar nucleus is originally done by Shawn Westerdale with the contribution from the collaboration to define the exclusion curves from the physics data for WIMP analysis where an average value of the speed of Earth was used. This chapter shows the calculation of the WIMP model for the DEAP-3600 detector with the variations in the velocity of the Earth, to get the sensitivity for the

annual modulation in signal. Following the details of the WIMP model discussed in section 2.3.3, the coupling of WIMP particles with LAr is studied through the WIMP velocity model, the form factor for ^{40}Ar, and hence calculating the event rates in DEAP detector are discussed in the following sections.

8.1.1 Velocity model

The velocity model of the WIMP and nuclear interactions are estimated from the velocity profile model used by McCabe's treatment in [44]. The Standard Halo Model assumes the isothermal, isotropic, and spherical halo of dark matter following a Maxwellian distribution of velocities in the galactic rest frame. The cut-off velocity or the escape velocity (v_{esc}) is set to the value of the 544 km/s, such that if a WIMP particle with a velocity greater than this escape velocity, it will not be bound in the galaxy, hence will not be seen in the detector. The velocity distribution of the WIMPs is given by,

$$f(\vec{v},t) = \begin{cases} \frac{1}{k}[e^{(-(\vec{v}+\vec{v_E}(t))^2/v_0^2)} - e^{(-v_{esc}^2/v_0^2)}] & if\ |\vec{v}+\vec{v_E}(t)| < v_{esc} \\ 0 & if\ |\vec{v}+\vec{v_E}(t)| > v_{esc} \end{cases} \tag{8.1}$$

Here, v_0 is the velocity of the sun with respect to the galactic rest frame, $\vec{v}$ is the WIMP velocity in the Earth's rest frame, $\vec{v_E}$(t), and v_{esc} are the velocity of Earth, and galactic escape velocity respectively, where,

$$v_0 = 232 \text{ km/s} \tag{8.2}$$

The velocity of Earth in the galaxy is not constant over a year, it varies due to the small velocity of the Earth around the Sun. Therefore, as a function of the day of

the year, t, it can be written from [80], and [81] as follows,

$$v_E(t) = v_0 + (v_{orb} * \cos\gamma * \cos(\omega(t - t_0))) \tag{8.3}$$

with $v_{orb} = 29.8$ km/s is the orbital speed of Earth around the Sun, $\gamma \sim 60°$ is the inclination of Earth's orbit with respect to the Sun's trajectory in galactic rest frame which gives $\cos\gamma = 0.49$. Also, $\omega = (2\pi/365.25 \text{ days})$ is the angular frequency and t_0 is the time when this velocity is maximum, such that, $t_0 = 152.25$ days on June 2. The normalization constant, k, normalize the speed distribution for WIMP velocity distributions extending to the escape velocity,

$$k = k_0[erf(v_{esc}/v_0) - \frac{4}{\sqrt{\pi}} e^{(-v_{esc}^2/v_0^2)}(\frac{v_{esc}}{2v_0} + \frac{v_{esc}^3}{3v_0^3})] \tag{8.4}$$

Also, k_0 normalizes the speed distribution for extending to infinite velocity,

$$k_0 = (\pi v_0^2)^{\frac{3}{2}} \tag{8.5}$$

The WIMP speed distribution can be obtained by integrating equation (8.1) over all the angles,

$$f(v,t) = \int_0^{2\pi} d\phi \int_0^{\pi} \sin\theta d\theta \int_0^{\infty} v^2 f(\vec{v},t) dv \tag{8.6}$$

with θ, and ϕ as polar and azimuthal angles respectively.

If we only average over all the angles to get the distribution of the WIMP speeds relative to the Earth assuming no angular momentum relative to the motion of the Sun. The speed distribution for the WIMPs can be written in form of a piecewise

function from equation (8.8), where the parameter $\alpha(v,t)$ can be defined as,

$$\alpha(v,t) = \frac{v_{esc}^2 - v^2 - v_E^2(t)}{2vv_E(t)} \tag{8.7}$$

$$f(v,t) = \begin{cases} 0 & \text{if } \alpha < -1 \\ \frac{2\pi}{k}[\frac{v_0^2 v}{2v_E(t)}(e^{-(\frac{v-v_E(t)}{v_0})^2} - e^{\frac{-2\alpha v v_E(t) - v^2 - v_E^2(t)}{v_0^2}} - (1+\alpha)v^2 e^{-(\frac{v_{esc}}{v_0})^2}] & \text{if } -1 \leq \alpha \leq 1 \\ \frac{2\pi}{k}[\frac{v_0^2 v}{2v_E(t)}(e^{-(\frac{v-v_E(t)}{v_0})^2} - e^{(\frac{v+v_E(t)}{v_0})^2} - 2v^2 e^{-(\frac{v_{esc}}{v_0})^2}] & \text{if } \alpha > 1 \end{cases} \tag{8.8}$$

The first case in the velocity distribution in equation 8.8 accounts for the condition where the velocity of WIMP speed relative to the Earth is more than the escape velocity even if the WIMP is moving parallel to the Earth. The third case is the state where velocity is below the escape velocity. The centered term connects these two cases, and velocity distribution is accessible due to the motion of the earth.

The speed distribution of the WIMPs evaluated from these equations by including the speed of the Earth for the month of June, and December is shown in figure 8.1.

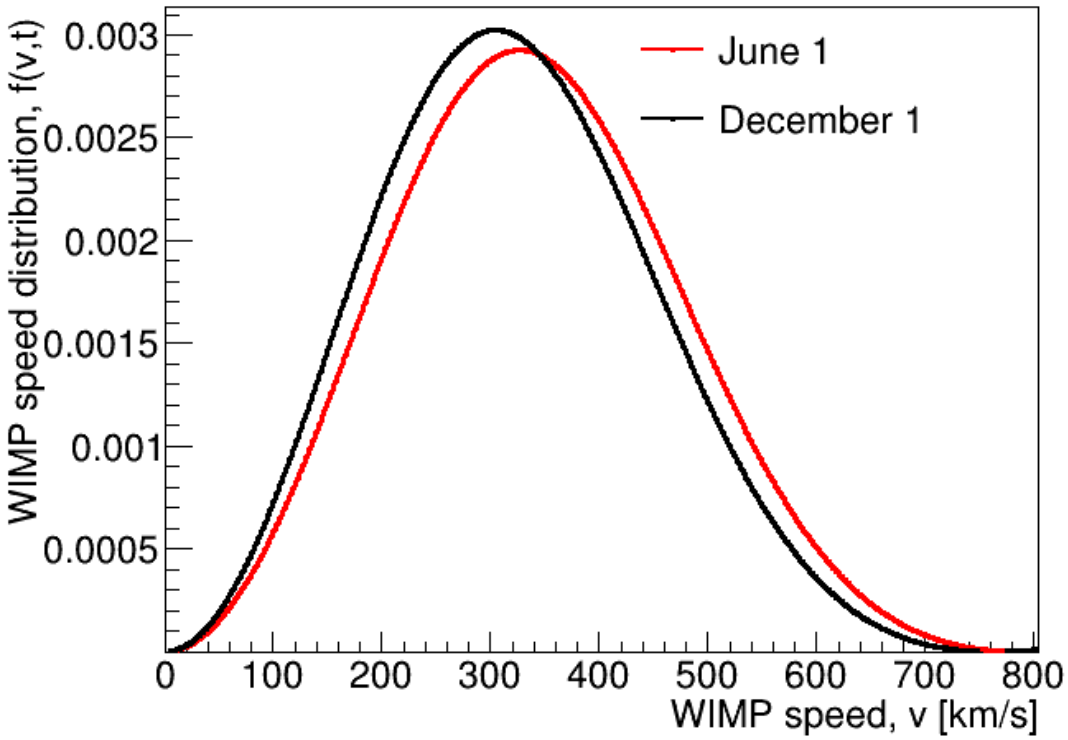

Figure 8.1: The velocity distribution for the WIMPs following the Maxwell-Boltzmann profile assumed by the Standard Halo Model. The Earth's velocity is calculated from the equation (8.3) for the month of June and December when Earth is moving in parallel and opposite to the direction of the Sun respectively.

The difference in the velocity distribution is clearly seen in the month of June and December which will further add to the total nuclear recoil rate of the WIMP interaction with target nuclei and hence contribute to the annual modulation of the recoil rate.

8.1.2 Nuclear form factor

The nuclear form factor is the function of the momentum transfer, q, in the interaction. It is the property of the target nucleus and the ways in which WIMPs can interact with the target. The nuclear form factor can be calculated by adding the

interaction operator for all the nucleons in the nucleus with radius, r_n, and in the spin-independent case, this is approximately equal to the Fourier transform of the nucleon distribution.

The Helm form factor model is suggested in research papers [40], and [44] that assumes the spherical charge distribution softened by a Gaussian skin with some skin thickness, s, where the WIMP-nucleus interactions are independent of spin and angular momentum, such that the WIMPs couples equally to protons and neutrons. The form factor is,

$$F(q) = \frac{3j_1(qr_n)}{qr_n} e^{-\frac{(qs)^2}{2}} \tag{8.9}$$

The skin thickness fit by Lewin and Smith is, s≈0.9 fm, and $j_1(qr_n)$ is a spherical Bessel function given by,

$$j_1(x) = \frac{\sin x - x\cos x}{x^2} \tag{8.10}$$

The nuclear radius from McCabe treatment and parameterization,

$$r_n = \sqrt{c^2 + \frac{7}{3}(\pi a)^2 - 5s^2} \tag{8.11}$$

where, $a = 0.52$, and $c = 1.23A^{\frac{1}{3}} - 0.60$ fm Using the mass number, A = 40, for the ^{40}Ar nucleus, the nuclear radius for the DEAP-3600 detector becomes, r_n =3.89669 fm. Also, the momentum transfer equation as indicated by Lewin and Smith [40],

$$q = \sqrt{2ME_R} \tag{8.12}$$

where, E_R is the nuclear recoil energy, and M is the mass of the nucleus, which can

be written in the form of the mass of a nucleon, m_n, as,

$$M = m_n * A = 0.932 * A \tag{8.13}$$

The equation (8.12) makes form factor recoil energy dependent. The Planck's constant, $\hbar$ (=197.3 MeV fm), is used for the mass-energy conversion, such that,

$$qr_n(\text{dimensionless}) = \frac{qr_n}{\hbar} = 0.00692 * \sqrt{AE_R} * 3.896 \tag{8.14}$$

Moreover, qs = s*q/$\hbar$. The Helm form factor for ^{40}Ar in the detector settings is shown in figure 8.2 for the range of nuclear recoil energies from 0 to 1 MeV$_{nr}$.

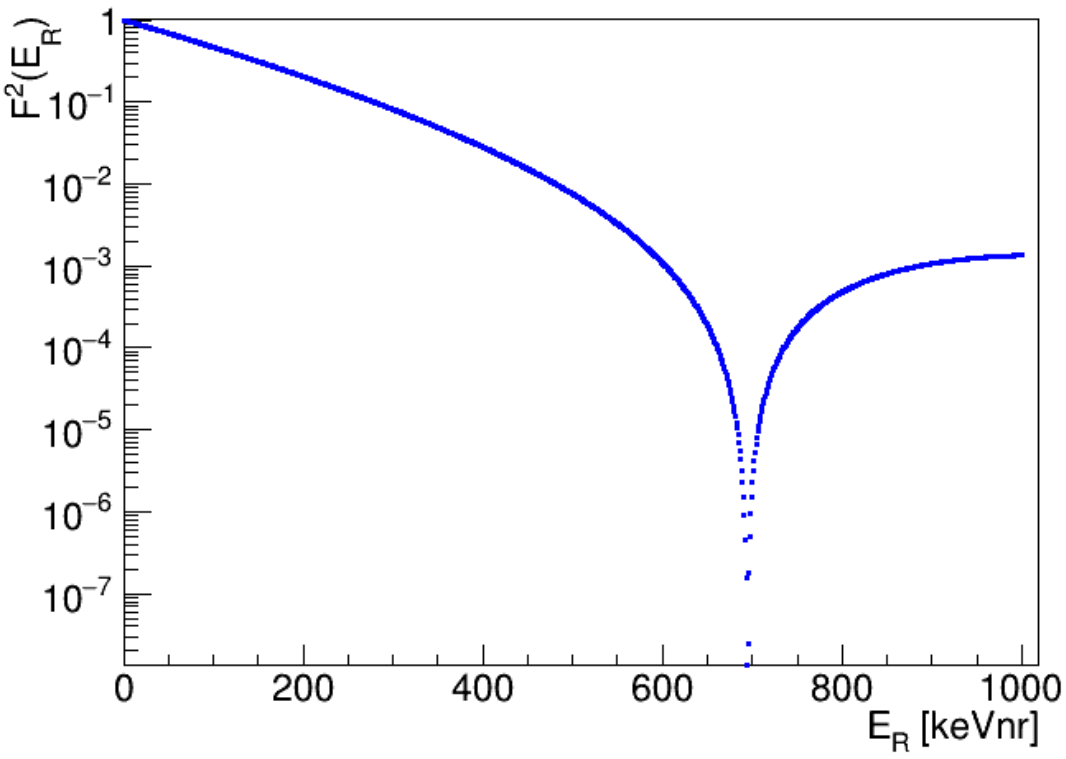

Figure 8.2: The Helm form factor for the ^{40}Ar nucleus characteristics, calculated for the different nuclear recoil energies.

8.1.3 Quenching model

The quenching factor, $\mathcal{L}_{eff}$, accounts for the detector response to the recoils of the argon nucleus such that no suppression and non-linearity is taken into account for the nuclear recoils calculation of the energies as indicated in equation (2.7). The quenching model described by the SCENE collaboration [82] is used in the analysis to calculate the nuclear recoil energies and hence recoil rates.

The quenching model from this paper as shown in figure 2.7, is based on the Lindhard-Birks model which factors in the energy loss if some of the ionized argon atoms fail to recombine at a relevant time scale and the rate of recombination loss depends on the nature of the track left by the recoiling factor. The quenching factor diverges at the high energies, the highest recoil energy relevant to the WIMP-^{40}Ar scattering at energies $\sim$500 keVnr.

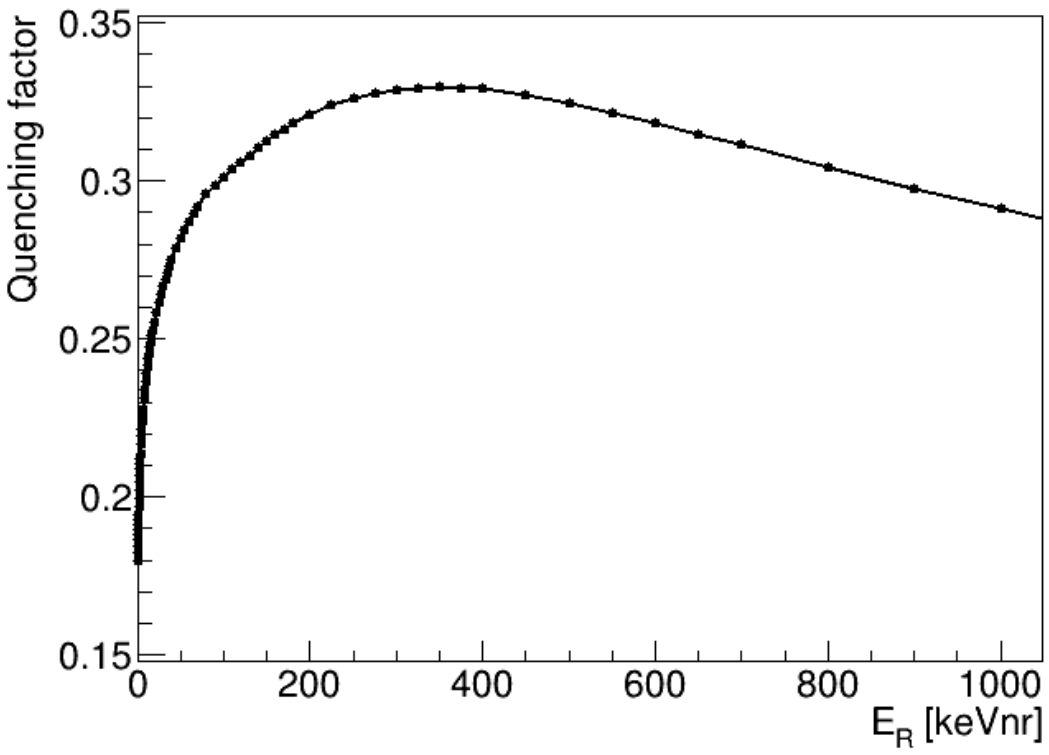

Figure 8.3: The quenching factor, $\mathcal{L}_{eff}$, measurements from the SCENE experiment used for the conversion of energy from keVee (keV electron equivalent) to keVnr (keV nuclear recoil).

8.1.4 Recoil spectrum model

The recoil energy distribution for the WIMP-nucleus system can be derived from the WIMP velocity distribution and nuclear form factor for any given cross-section. In the elastic scattering of WIMP with nucleon where the recoils are isotropic in the center of mass frame, the recoil energy is uniformly distributed between 0 to E_R^{max}, where the E_R^{max} is the maximum energy transferred from a WIMP of mass, m_χ and kinetic energy, E_χ to the target nucleus of Mass, M in a single scatter. Using the kinematics equations for a non-relativistic two-body elastic scattering interaction, the

maximum recoil energy is,

$$E_R^{max} = E_\chi r = E_\chi \frac{4M_\chi M}{(M_\chi + M)^2} \tag{8.15}$$

The kinematic factor, r, describes the maximum fraction of kinetic energy that the target nucleus can get from the WIMPs.

The differential recoil rate, $\frac{dR}{dE_R}$ per unit fiducial mass of the WIMPs recoiling with energy E_R as explained earlier in equation (2.5) can be written as,

$$\frac{dR}{dE_R} = \frac{N_A}{A}\frac{\rho}{m_\chi}\int_{v_{min}}^{\infty} v f(\vec{v},t)\frac{d\sigma}{dE_R}d^3\vec{v} \tag{8.16}$$

where N_A is Avogadro's number with value 6.022E+23, the velocity distribution of WIMPs defined in equation (8.8), the minimum velocity a WIMP must have to recoil with energy E_R is,

$$v_{min} = v_0\sqrt{\frac{E_R}{E_0 r}} \tag{8.17}$$

Also,

$$E_0 = \frac{1}{2}m_\chi v_0^2 \tag{8.18}$$

The $\frac{d\sigma}{dE_R}$ is the differential cross section given by,

$$\frac{d\sigma}{dE_R} = \frac{1}{2v^2}\frac{M\sigma_0}{\mu^2}A^2F^2(E_R) \tag{8.19}$$

The v is the velocity of WIMPs, σ_0 is the nuclear cross section when zero momentum is transferred from WIMP to nucleon, and μ is the reduced mass of the system given in equation (2.4). Using the equation (8.19) in the differential recoil rate from equation

(8.16), the recoil rate becomes,

$$\frac{dR}{dE_R} = \frac{N_A m_n}{2\mu^2}\frac{\rho}{m_\chi}\sigma_0 F^2(E_R)A^2\int_{v_{min}}^{\infty}\frac{f(v,t)}{v}dv \tag{8.20}$$

Moreover,

$$\frac{dR}{dE_R} = \frac{N_A m_n}{2\mu^2}\frac{\rho}{m_\chi}\sigma_0 F^2(E_R)A^2\zeta(E_R,t) \tag{8.21}$$

where $\zeta(E_R,t)$ is the analytical solution to the integral part of the equation. Also, using the integral from the equation (8.8),

$$\zeta(E_R,t) = \begin{cases} \frac{\pi^{\frac{3}{2}}v_0^3}{2kv_E(t)}[erf(\frac{v_{min}+v_E(t)}{v_0}) - erf(\frac{v_{min}-v_E(t))}{v_0}) & \text{if } v_{min} < v_{esc} - v_E(t) \\ -\frac{4v_E(t)}{v_0\sqrt{\pi}}e^{-\frac{v_{esc}^2}{v_0^2}}(1+(\frac{v_{esc}}{v_0})^2 - \frac{1}{3}(\frac{v_E(t)}{v_0})^2 - (\frac{v_{min}}{v_0})^2)] & \\ \frac{\pi^{\frac{3}{2}}v_0^3}{2kv_E(t)}[erf(\frac{v_{esc}}{v_0}) - erf(\frac{v_E(t)-v_{min}}{v_0}) & \text{if } v_{min} > v_{esc} - v_E(t) \\ -\frac{2}{v_0\pi}e^{-v_{esc}^2}(v_{esc}+v_E(t)-v_{min} & \text{and } v_{min} < v_E(t) + v_{esc} \\ -\frac{1}{3v_0^2}(v_E(t)-2v_{esc}-v_{min})(v_{esc}+v_E(t)-v_{min})^2)] & \\ \frac{1}{v_E(t)} & \text{if } v_{min} < v_E(t) - vesc \\ 0 & \text{if } v_{min} > v_{esc} + v_E(t) \end{cases} \tag{8.22}$$

The differential recoil rate spectrum for different WIMP masses calculated from the above set of equations is shown in figure 8.4. The cross-section of the WIMP-^{40}Ar nucleus scattering considered in the calculation is 10^{-44} cm^2, such that, $\sigma_0 = 10^{-44}$ cm^2, and the local WIMP density, ρ, considered is 0.3 GeV/cm^3.

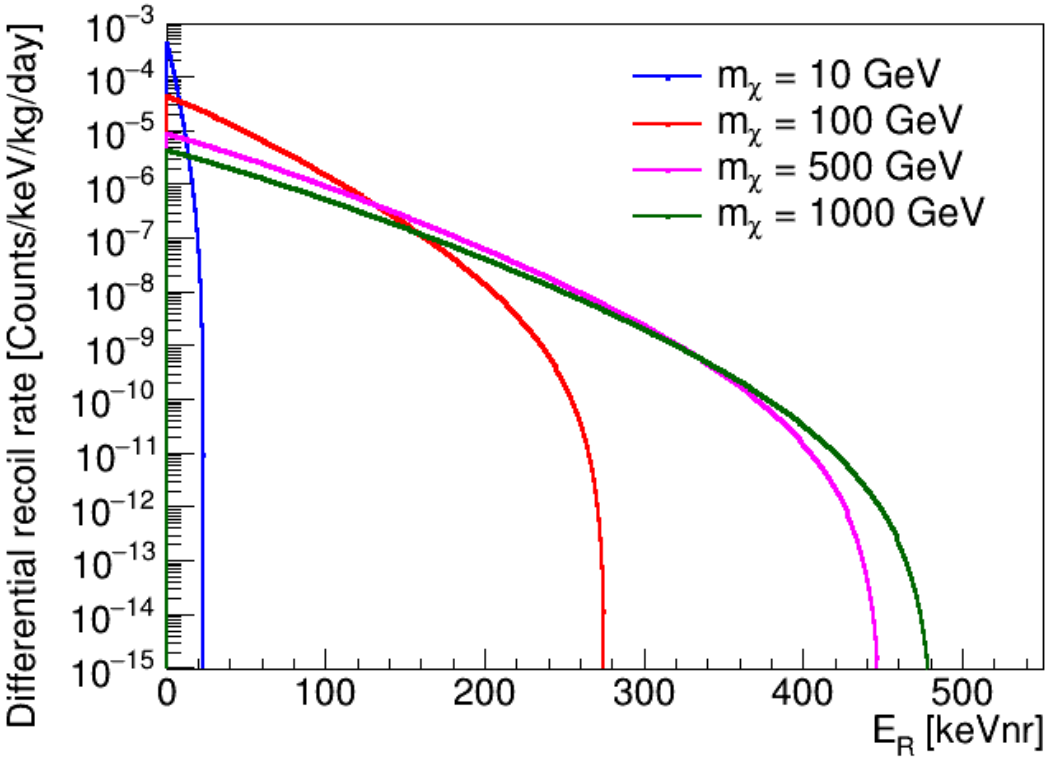

Figure 8.4: The recoil rate spectra for different WIMP masses as a function of recoil energy. The scattering cross-section, $\sigma_0 = 10^{-44}$ cm^2 is used for the calculation of the spectra.

Also, the differential recoil rate is compared for the month of June and December for the WIMP mass of 10 GeV keeping the σ_0 at 10^{-44} cm^2, and ρ at 0.3 GeV/cm^3 as shown in the figure 8.5. The small change in the recoil rates for two months is contributed by the time-dependent component of Earth's velocity as discussed in the above sections.

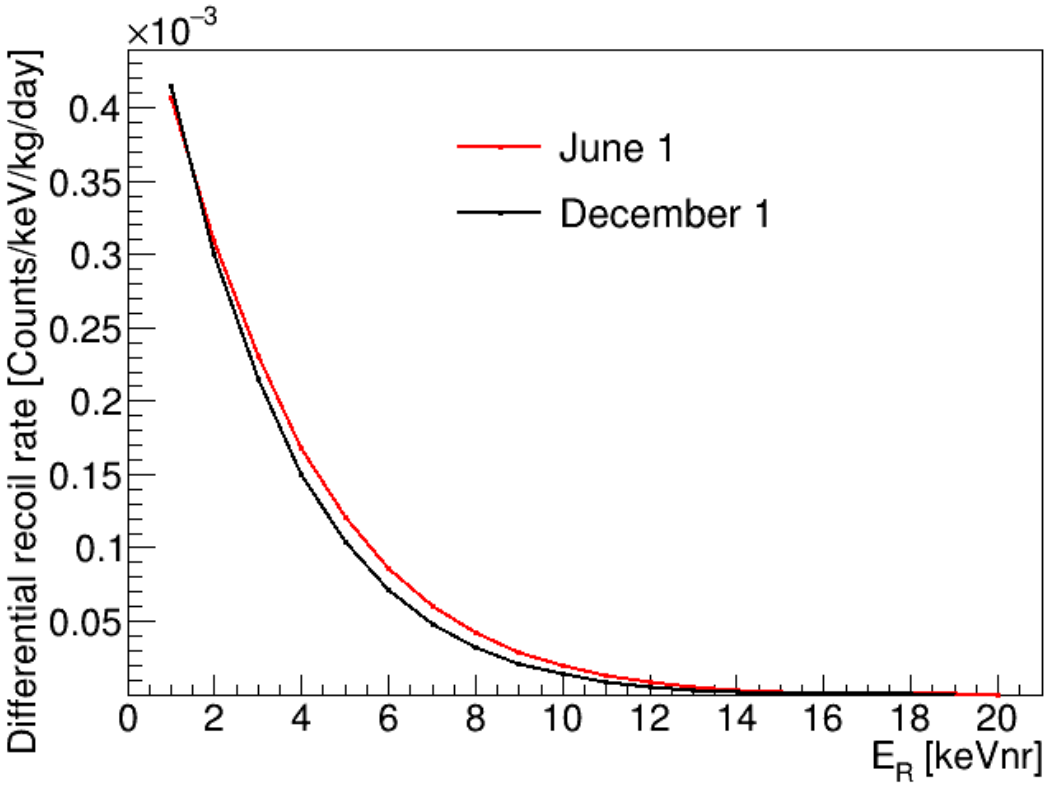

Figure 8.5: The recoil rate spectra for the WIMP particle with mass 10 GeV as a function of recoil energy in the month of June and December. The scattering cross-section, $\sigma_0 = 10^{-44}$ cm^2 is used for the calculation of the spectra.

Furthermore, the differential recoil rate as a function of the detector threshold energy can be calculated by using the quenching factor for energy conversion as discussed in section 8.1.3. Figure 8.6 shows the minimum detector threshold needed at 5 keV at most to record the nuclear recoil modulation signal in the month of June and December.

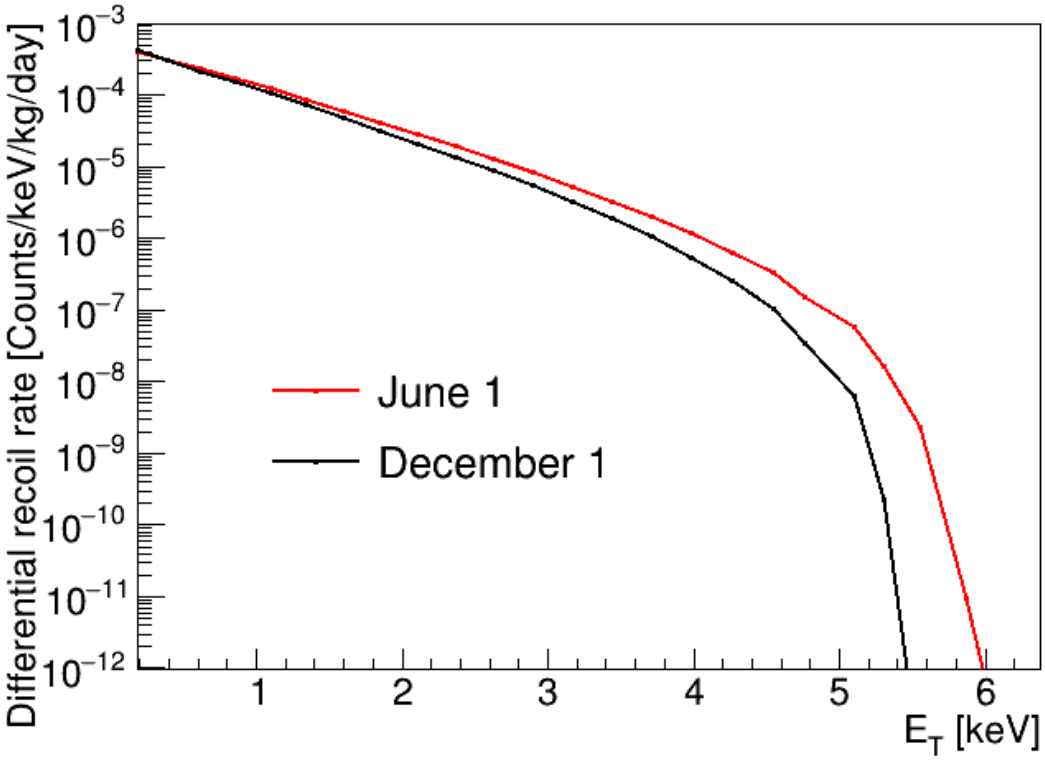

Figure 8.6: The recoil rate spectra for the WIMP particle with mass 10 GeV as a function of detector threshold energy in the month of June and December. The scattering cross-section, $\sigma_0 = 10^{-44}$ cm^2 is used for the calculation of the spectra.

8.2 Total recoil rates in DEAP-3600

The total nuclear recoil rates for the WIMP-^{40}Ar interactions can be estimated for any WIMP particle of the known mass and cross section by the integration of the differential recoil rates from equation (8.21) within the limits from any energy threshold to the higher overall possible recoil energies, which gives,

$$R(t, m_\chi, \sigma_0) = \int_{E_T}^{\infty} \frac{N_A m_n}{2\mu^2} \frac{\rho}{m_\chi} \sigma_0 F^2(E_R) A^2 \zeta(E_R, t) dE_R \tag{8.23}$$

Therefore, the total recoil rates are calculated for the elastic scattering with

cross-section, $\sigma_0 = 10^{-44}$ cm^2 for the 10 GeV WIMPs with the ^{40}Ar nucleus to test the different energy thresholds needed to observe the annual modulation in the recoil signal in liquid argon as presented in figure 8.8. The total recoil rate calculations show the detector threshold of at least 5 keV needed to record the annual modulation in the signal with the magnitude of order 10^{-8}.

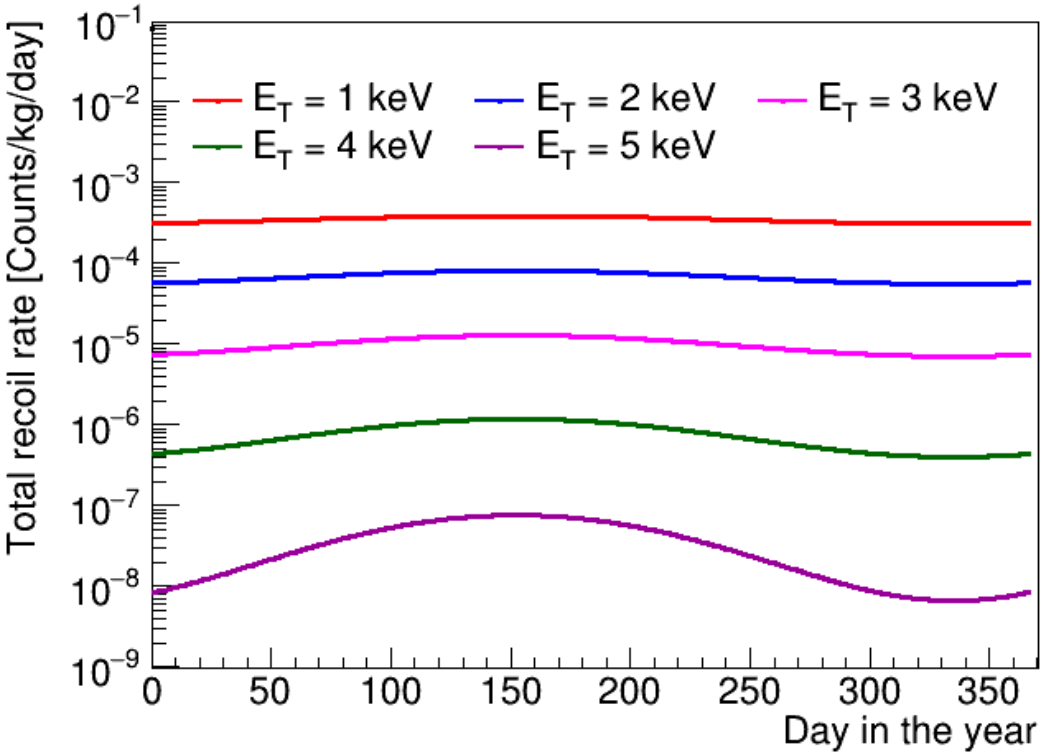

Figure 8.7: The annual modulation in the total recoil rate of WIMP scattering with a mass of 10 GeV with the ^{40}Ar nucleus at the scattering cross-section of 10^{-44} cm^2 with different detector thresholds.

To determine the sensitivity of the DEAP-3600 detector to record the annual modulation in the total recoil signal with the 3600 kg of LAr as the target material, the total recoil rates from equation (8.23) are multiplied by a factor of 3600 such that at a detector threshold of 1 keV, DEAP-3600 will be sensitive to record average rate

of more than 1.2 events per day. The calculated total recoil rates with the fiducial volume of the DEAP-3600 detector at the different detector thresholds are shown in figure 8.8 with $\sigma_0 = 10^{-44}$ cm^2 and WIMP mass constrained to 10 GeV.

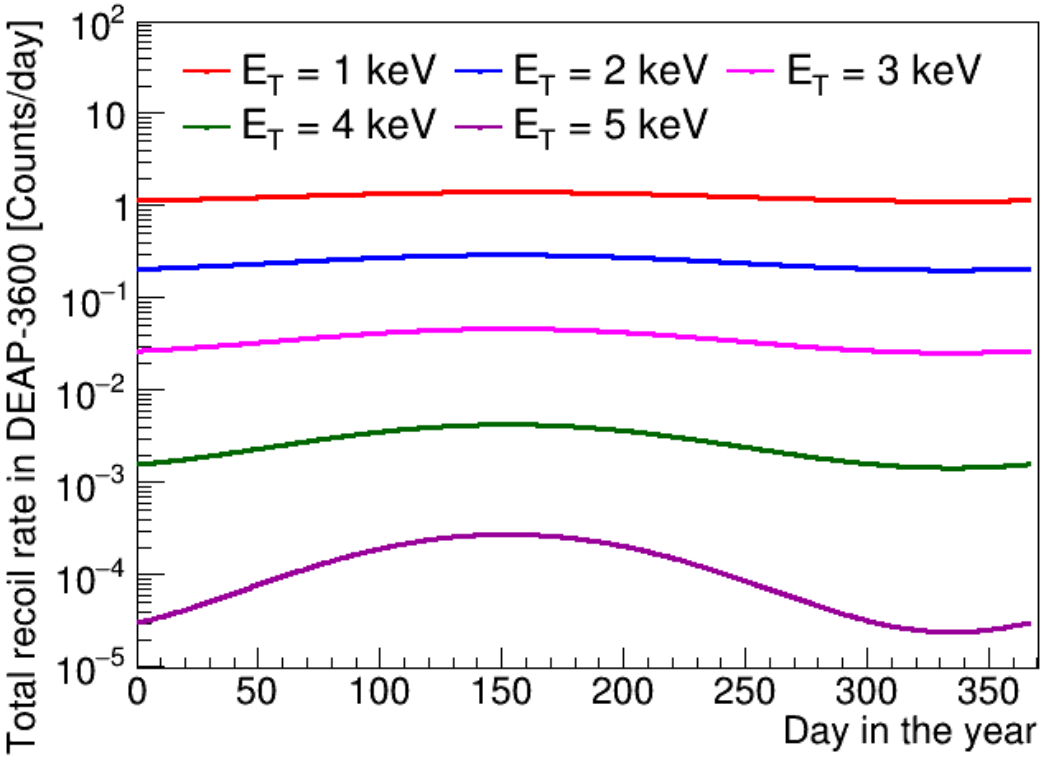

Figure 8.8: The annual modulation of the total recoil rate expected in the DEAP-3600 experiment fiducial volume for a WIMP with the mass of 10 GeV with the ^{40}Ar nucleus at the scattering cross-section of 10^{-44} cm^2 with different detector thresholds.

The total recoil rates are presented in the non-logarithmic scale in the simple non-logarithmic scale is shown in figure 8.9.

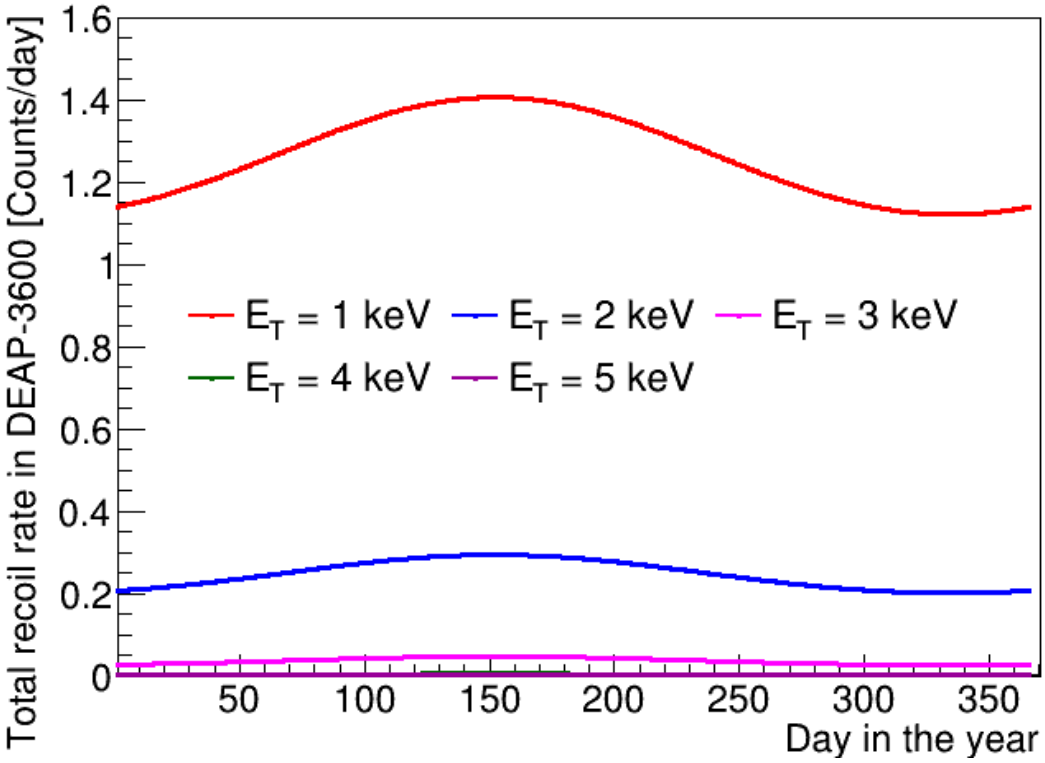

Figure 8.9: The total recoil rate in the DEAP-3600 detector fiducial volume for a WIMP with the mass of 10 GeV at the scattering cross-section of 10^{-44} cm^2 with different detector thresholds where the recoil rates are presented in the non-logarithmic scale.

Also, with the minimum detector threshold needed in LAr to record annual modulation, DEAP-3600 will be sensitive to record a very negligible event count per day. The calculated total recoil rates with respect to the time of the year can be fitted with the model from equation (8.24) as Fourier expansion suggested by [83] for the isotropic and halo component of dark matter to determine the time-averaged rate and modulation amplitude rate in the LAr for the DEAP-3600 experiment fiducial mass.

$$R(t, m_\chi, \sigma_0) \approx S_0(E_R) + S_m(E_R) \cos \omega(t - t_0) \tag{8.24}$$

where $S_0(E_R)$ is the time-averaged rate, $S_m(E_R)$ is the modulation amplitude rates, such that, $|S_m| \ll S_0$. The time-averaged total recoil rate and modulation amplitude for the recoil rates in figure 8.8 can be seen in figure 8.10, and 8.11 respectively.

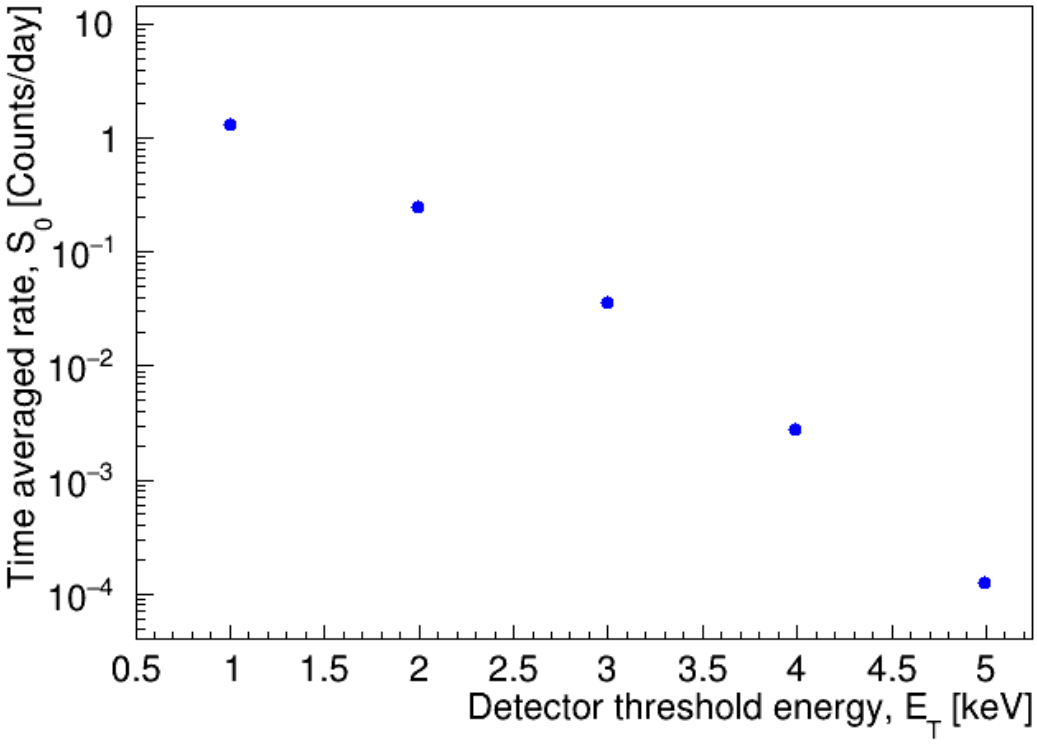

Figure 8.10: The time-averaged total recoil rate expected in the DEAP-3600 experiment fiducial volume for a WIMP with the mass of 10 GeV with the ^{40}Ar nucleus at the scattering cross-section of 10^{-44} cm^2 with different detector thresholds.

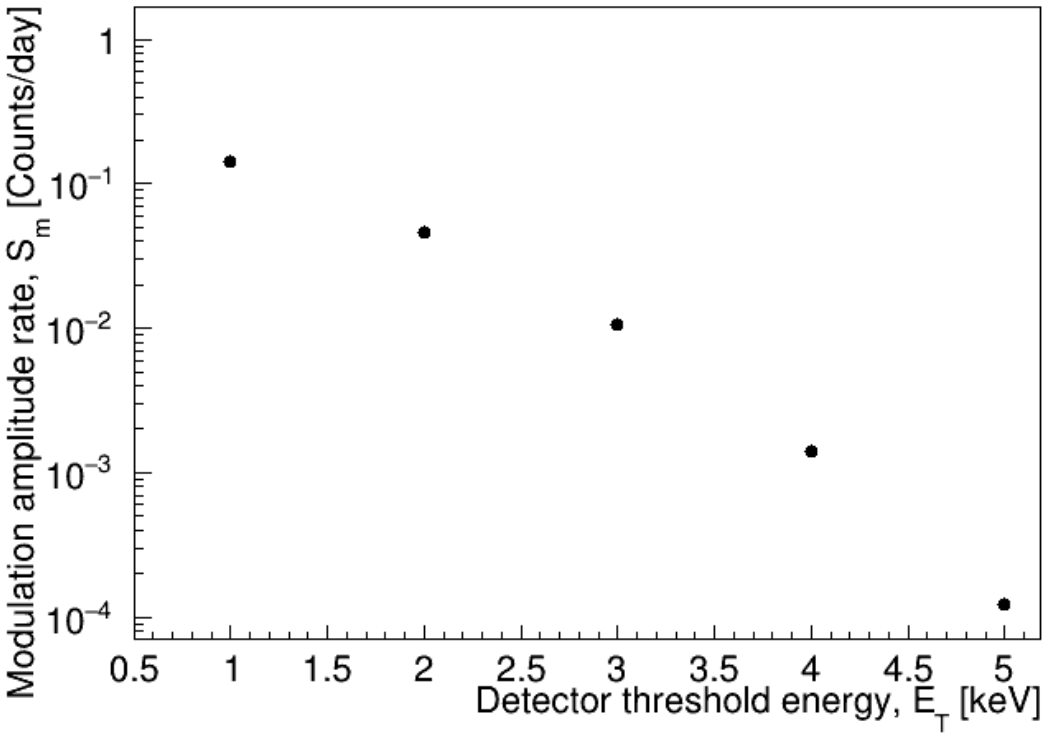

Figure 8.11: The modulation amplitude expected in the DEAP-3600 detector fiducial volume for a WIMP with the mass of 10 GeV with the ^{40}Ar nucleus at the scattering cross-section of 10^{-44} cm^2 with different detector thresholds.

8.3 Current Status of dark matter experiments

The current status of the several experiments looking for the direct detection of the dark matter particle can be referred from the exclusion curve plot in figure 8.12.

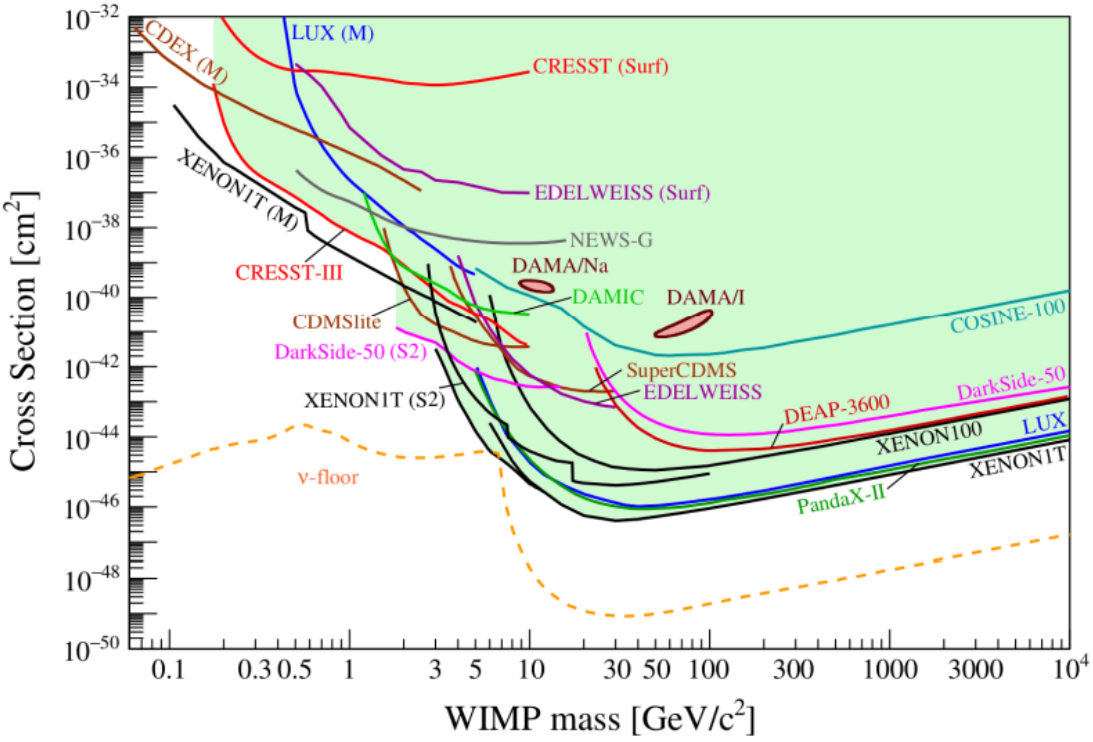

Figure 8.12: The current status of dark matter experiments as described by the [33]. These limits are derived based on the searches for the elastic spin-independent WIMP-nucleus scattering assuming the standard parameters for an isothermal WIMP halo.

These exclusion curves are taken from the different experimental data [33] and show the lower limit of a WIMP-nucleon cross-section sensitivity of the experiment as a function of WIMP masses. The upper region of the exclusion curves is ruled out by the experiments since no events are detected for the WIMP nuclear recoil signal in these regions. The neutrino floor in the orange dotted line shows the lowest limit for the WIMP discovery where the sensitivity for coherent neutrino scattering becomes very large which is the dominant background in the experiments and thus most of the data will be thrown out. Also, the region for the annual modulation sensitivity is at the very low mass of WIMP masses from $\sim$0.1 GeV/c^2 up to around 10 GeV/c^2. The strong limit in the region above WIMP mass of 110 MeV/c^2 is currently

obtained by the XENON1T [84] experiment. The DAMA/NaI experiment from the DAMA/LIBRA collaboration is the only experiment presently claiming the results of annual modulation in their data [85] which was taken in two phases as shown in figure 8.13. The superimposed curve in the figure 8.13 shows the cosinusoidal function, $A\cos\omega(t - t_0)$ fitted to data with a period T=$\frac{2\pi}{\omega}$=1 year, a phase t_0=152.5 days (June 2) and A is the modulation amplitude obtained by the best fit on the data points. However, the other collaborations, like the COSINE-100 experiment using the same technique for the detection of annual modulation signal published the null results from their dataset and analysis [86].

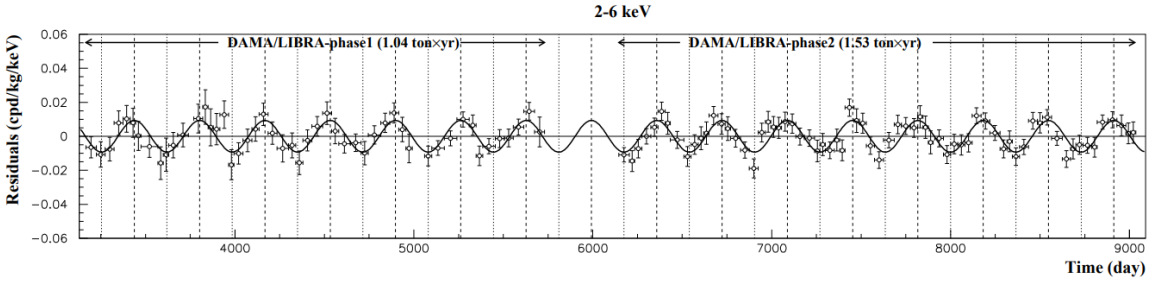

Figure 8.13: The residual rates in the experimental data measured by the DAMA/LIBRA-phase1 and DAMA/LIBRA-phase2 for the energy intervals of 2 to 6 keV as a function of time [85].

The current low acceptance in the DEAP-3600 experiment is shown on the right side of the graph which is determined from the one year of the dataset with an exposure of 231 days. The result indicates the sensitivity of the DEAP-3600 experiment to 100 GeV/c^2 massive WIMPs at the WIMP-nucleon scattering of 3.9 x 10^{-45} cm^2. This result is published in 2019 [6] that shows the world-leading limit for the sensitivity of the DEAP-3600 experiment in all the single-phase LAr dark matter detectors. The sensitivity studies from the current analysis will define the perspective limit for the DEAP-3600 experiment for the sensitivity of the detector for the annual modulation signal on the left side of the exclusion limit plot for low WIMP masses.

8.4 Predicted sensitivities for future dark matter experiments with LAr

The amplitude of the modulation in the signal presented in figure 8.11 can also be calculated in percentage from the following equation (8.25),

$$\text{Modulation percentage } = \frac{R_{max} - R_{min}}{R_{avg}} * 100 \tag{8.25}$$

where R_{max}, R_{min}, and R_{avg} are the maximum, minimum, and average recoil rates respectively calculated for any detector threshold energy. The amplitude of modulation in percentage is plotted as a function of threshold energy as shown in figure 8.14 where the red line shows the limit for the maximum uncertainty on the event rates calculated from the DEAP-3600 detector systematic studies as presented in table 7.9 in previous chapter 7. This systematic uncertainty of 0.09% is contributed by the absolute energy scale calculations and corrections. The physics data in the DEAP-3600 detector was taken for the period of November 2016 to March 2020, and a good understanding of detector systematics is already discussed in the chapter 6.

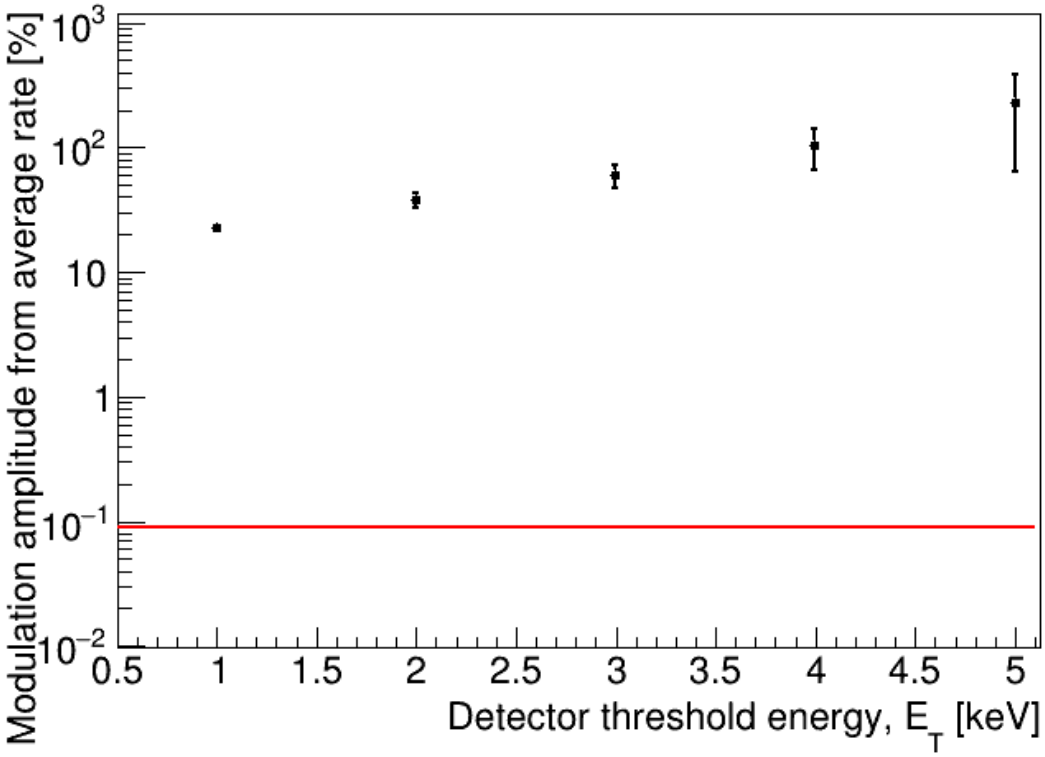

Figure 8.14: The modulation amplitude in percentage for total recoil rate expected in the DEAP-3600 experiment fiducial volume for a WIMP with the mass of 10 GeV with the ^{40}Ar nucleus at the scattering cross-section of 10^{-44} cm^2 with different detector thresholds. The red line represents the maximum systematic uncertainty in DEAP-3600 event rates from the absolute energy scale.

Therefore, for the lowest detector threshold energy at 5 keV, the DEAP-3600 experiment will be able to detect the annual modulation in the nuclear recoil signal with great control over the systematic uncertainty of the event rates. However, the signal is very small due to limited statistics and the smaller average recoil rate at this threshold value. The systematic uncertainty of 0.09% on event rates is however independent of detector mass and for better statistics, a large detector can be made with more fiducial volume to get a high value of average recoil rate and hence modulation amplitude. Also, the preliminary calculations showed that detector threshold

at 3 keV, the DEAP-3600 experiment will be able to discriminate the event rate in the month of June and December by 2σ difference at the WIMP-nucleus scattering cross-section of 7.6 x 10^{-44} cm^2 with an exposure of 3 months given there are no backgrounds in the data. The sensitivity of the detector can be affected by the presence of any background in the data however, the use of underground argon will get the detector results close to this sensitivity. In the context of the global experiments, the DEAP-3600 detector can place its world-leading sensitivity limits at the WIMP mass of 10 GeV for the annual modulation signal by lowering its threshold to 3 keV.

The above conclusions are made for the small WIMP particle with mass 10 GeV, and scattering cross section for WIMP and ^{40}Ar is included in calculations at 10^{-44} cm^2. Moreover, using the higher value of scattering cross section at 10^{-41} cm^2 as used by the XMass-I collaboration [87] to search for the search of annual modulation in liquid Xenon, the sensitivity for the annual modulation in total recoil signal for DEAP-3600 is greatly increased as suggested by equation (8.23). The total recoil rates at scattering cross-section of 10^{-41} cm^2 for a WIMP of mass 10 GeV in the DEAP-3600 detector at various detector thresholds will be increased by a factor of 3. The DEAP-3600 detector will be sensitive to record about 1000 events/day at the energy threshold of 1 keV to detect annual modulation in the total recoil rate. Similarly, the detector threshold at 5 keV shows the sensitivity to detect more than 1 event per day. Thus, the bigger detector with more argon mass volume will be a suitable option for the threshold at 5 keV to detect annual modulation in signal.

To recapitulate, the energy threshold required for any dark matter experiment using the liquid argon as the target material to record the annual modulation signal should be less than or equal to 5 keV as estimated in the section 8.2. The higher values of the scattering cross-section between WIMPs and ^{40}Ar increases the responsiveness

of the detector towards annual modulation which also amplifies for the heavier masses of WIMPs. In addition to the sensitivity of the detector towards annual dark matter, the perfect understanding of the backgrounds in the detector is needed to a greater extent. The rate of the backgrounds per day in any experiment can be subtracted from the total recorded recoil rate to get the sensitivity for the dark matter signal through the indirect criteria of annual modulation. Moreover, a good knowledge of detector systematics is also required to neglect any type of background. Although the detector data was recorded at a higher threshold than 5 keV the best background model of the DEAP-3600 detector [6] makes it a suitable experiment to detect the annual modulation signal for dark matter in the liquid argon using the Pulse-shape discrimination technique. The DEAP detector would need to collect new data at the lower hardware threshold of 5 keV or less, and a more complete understanding of the detector backgrounds would be required. In future dark matter experiments planned with tonnes of liquid argon like Darkside-20k and Argo, the energy threshold can be kept at the lowest possible values to obtain the sensitivity for the indirect evidence of the dark matter through the annual modulation signal.

Chapter 9

Conclusion

The existence of dark matter is highly suggested by various pieces of evidence collected over the last many decades. There are many dark matter aspirants predicted by the theorists but WIMPs are considered as the possible candidate. The dark matter searches are ongoing in three independent ways in which either the experiments are looking for the creation of the dark matter or annihilation signal from the dark matter producing the standard model particles to inherit its properties and through the direct searches to record the energy imparted by the dark matter with the weak interaction with the target nucleus resulting in the elastic scattering and generation of the recoil energy signals. The other popular theory for the existence of dark matter proposed the annual modulation in the nuclear recoil signal over the period of the year due to the relative velocity of the Sun and hence around the galactic center in the halo of dark matter.

DEAP-3600 experiment is designed to detect the dark matter signal through the direct detection technique which uses ∼3279 kg of argon as the target material. The scintillation properties of argon make it an ideal nucleus to record the recoil energy. Also, the PSD method used by the DEAP collaboration returns perfect

discrimination from the electron recoils and dominant backgrounds in the detector. In addition to this, the stability of the DEAP-3600 detector over more than 3 years of data taking meets the criteria of event rate studies for the search of annual modulation, an alternate method to detect the existence of dark matter.

9.1 Measured lifetime of ^{39}Ar

The event rate studies supplement the lifetime measurement for the ^{39}Ar isotope from the physics data in the detector by fitting the rates with the fit model describing the data. The decay fit equation is derived as a part of this study to fit the radioactive decay rates of ^{39}Ar such that all the possibilities of the pile-up of the ^{39}Ar with itself and other low energy backgrounds triggers are included from the theory, Poisson statistics and detector response model. Various data variables are used in this analysis to select different types of triggers and the software cut efficiencies and hardware efficiencies are considered in the fit equation, the variation in the software efficiencies is also studied with time, however, the hardware efficiencies are fixed as no changes are made to the detector and DAQ system throughout the period of data taking. There is about 21% of the total single ^{39}Ar beta spectrum is taken in the study, while the ∼20% and ∼18% of the beta spectrum corresponding to the simultaneous decay of the double and triple ^{39}Ar isotopes are contained in the ROI, that is mainly obtained due to the shifting in the pile-up spectra to the low energy side and high fprompt because of the 10.028 μs length of the trigger window. These efficiencies and acceptance values are confirmed from both MC and data-driven approaches.

The well-defined energy region selected for the study is about 700 to 1200 PE which is equivalent to 114.19 keV to 195.76 keV in the beta spectrum. The lower bound for the energy is set to neglect any systematics from the prescaling in the

DAQ system, and also it checks any low energy triggers to get accounted for in the study that may have otherwise triggered or non-triggered by the detector due to threshold conditions. The upper bound of the energy window rejects any uncertainty in the energy variable and hence PE calculation that could have occurred because of saturation and clipping in the LAr PMTs for the high energy ^{39}Ar triggers in the detector.

A rate algorithm is developed for this work to determine the rates of different types of events in the data from the trigger count and livetime information. This algorithm plots the trigger rates on a weekly bin basis to take into account more statistics from the dataset. For the validation of the algorithm, the rates of the calibration triggers, called periodic triggers in the DEAP-3600 experiment are plotted first since these triggers are injected into the DAQ system to calibrate the PMT performance with a known frequency. The output of the algorithm returned the rates of 1 Hz with an uncertainty of 2.2 μHz on average for this trigger type as expected. In addition to this, these rates are verified with the use of a trigger time cut in the analysis such that the triggers separated by a certain time distance are considered and equitable corrections are applied to the livetime calculations to include the correct time for the triggers. The periodic trigger rates are consistent for various trigger time cuts included except for some residuals reported for the very high cut values which can be explained from the biasing of data itself because of low statistics at large trigger cut values. These residuals could also have occurred due to some small systematic in the calculation of the trigger time variable that is being added for higher cut values. This issue is under investigation by the experiment. However, this will not affect the rate calculations and present results from the analysis. The rate of low-energy Cherenkov triggers is also estimated from the rate algorithm for the Cherenkov energies corrected

for the detector threshold to 150 ADC. The rates of Cherenkov triggers are recorded to be 538.1 ± 3.9 Hz in the full dataset. These rates are further included in the fit model to measure ^{39}Ar from the derived decay equation.

The detailed study is performed for the selection of a good dataset for the ^{39}Ar isotope from the full dataset, and there are only 991 run numbers out of 1280 total runs analyzed. There is special care taken with various cross-checks so that the exact number of triggers and livetime information is recorded by the DAQ and processed data files. The very small uncertainties noticed for the trigger count is 0.00012% over all the run numbers, and the negligible uncertainty in the livetime details is 0.00075% which shows the precise storage of data in the DEAP-3600 system that rejects any uncertainties on the rate calculations but these numbers are further included to study the systematic effect of these errors on the lifetime measurement of ^{39}Ar isotope. Furthermore, the detector energy response is studied in great detail over time for the light yield study that can be affected by a number of factors. The light yield of values calculated from different sources with time and quite a good stability is recorded with a small change of 0.3 PE/keV over more than 3 years. However, for the rate calculations of ^{39}Ar isotope, the corrections are applied to the energies on the trigger level basis such that the corrected energy of the trigger is considered in the study to maintain the energy region constraint. The corrections are applied for the deviation in the light yield since the first run number in the dataset. The total uncertainty from the energy corrections is measured to be 0.076% which is the dominant systematic from the detector in the study, and fixes are already applied for this systematic. Moreover, the uncertainty evaluated from the energy resolution parameter is 0.12% which indirectly affects the fraction of triggers in the selected energy region by a very small amount.

The trigger rates for the ^{39}Ar decay are then plotted with the same algorithm by considering some data selection cuts for these triggers. A constant factor of 100 is multiplied with the triggers that are prescaled for the same statistics that of non-prescaled that could have entered into the selected energy region. There are ∼177 weeks of ^{39}Ar data plotted with time and a clear decay of the trigger rates is obtained. The trigger rates for the selected energy region decayed from ∼615 Hz to ∼609 Hz with an average statistical uncertainty of 0.43 Hz. The trigger rates for the ^{39}Ar trigger type are also cross-checked by adding the additional trigger time, deltat cut at different values, and dead time corrections are considered in livetime while plotting rates which shows the consistent calculations for the rates. However, for the nominal result, a trigger time cut at 32 μs is fixed in the study to reject any pre-scintillation light in the trigger energies. The next step in the analysis is to fit the calculated trigger rates with the fit model that shows, the result for the lifetime of ^{39}Ar as 438.0 ± 10.2 (stat) years. Also, the average activity of ^{39}Ar in the fit solution is 2949.3 ± 0.3 Hz. The ER background contribution in the fit model is fixed at 1.65 Hz from the ER background model since this model includes all the possible ER backgrounds in the selected energy region from the detector setup.

The fit output for the lifetime is also verified by floating the ER background parameter in the fit model, and the lifetime parameter does not change, and fit returns the ER background at 1.42 ± 0.41 Hz. Another cross-check performed for the fit output is the calculation of the best-fit statistics by fixing the lifetime parameter to the different values, the global minimum for the fit is obtained for the lifetime of 438 years as expected. Moreover, the fit model output for the different trigger cuts is estimated which resulted in the insignificant change in the lifetime of ^{39}Ar parameter. The decay slopes for the single and pile-up ^{39}Ar are also extracted from the fit model

by substituting the fit output back in the decay equation. The decay curve for the single ^{39}Ar went down very fast in comparison to the pile-up rate. The rate of single ^{39}Ar triggers changed by 21 Hz which is 0.73% of the total single rates over the entire dataset. The trigger rates for double and triple pile-ups changed only by 0.96 Hz and 0.056 Hz respectively.

For the systematic uncertainty on the lifetime of ^{39}Ar from the small trigger count difference and livetime difference, the standard deviation from the average values are added to the trigger count and livetime calculations respectively. There are very small uncertainties of 0.0026 years and 0.0021 years for the trigger count and livetime difference respectively. The systematic uncertainty from energy response corrections is studied in three ways by keeping the uncertainty constant, and uniformly increasing and decreasing uncertainty over time to get the maximum possible error on the lifetime of ^{39}Ar from this systematic. The maximum shift in the lifetime parameter noted from this systematic is 7.39 years. Also, for the systematic uncertainties from the software cut efficiencies, a similar is adopted approach by keeping the uncertainty the same throughout the dataset, or by changing the uncertainty over time, the lifetime of ^{39}Ar varied by 0.047 years, 2.63 years, and 0.3 years for the single, double and triple ^{39}Ar selection cut efficiencies respectively. Moreover, changing the mean values of cut efficiencies from the difference in the data-driven approach and MC does not significantly change the lifetime measurement for ^{39}Ar. The maximum uncertainty from the change in the mean cut efficiencies is 0.38 years. The systematic uncertainty is also included by changing the fraction of different types of ^{39}Ar by maximum which returned the uncertainty of 1.6 years from double ^{39}Ar trigger type and negligible uncertainty from other trigger types.

The one-sided systematic uncertainty from the contribution of ^{85}Kr is analyzed

for various activity values of this isotope as the current fit model is only sensitive to the return activity of ^{39}Ar isotope only. The upper limit of ^{85}Kr activity with a value of 10 mBq/kg can increase the lifetime measurement of ^{39}Ar by 134 years. However, the exact estimate for the activity of ^{85}Kr still needs to be evaluated in the experiment. Also, the smallest increase of ^{39}Ar lifetime is 16 years with 1.5 mBq/kg of ^{85}Kr. The cross-checks are done if there are any unknown backgrounds in the detector decaying with the long life in the selected energy window. The maximum uncertainty recorded on $\tau_{^{39}Ar}$ is 2.11 years from the unknown background with a lifetime of 1000 years. Also, there are any alphas leaked to the ROI from the decay of ^{210}Po in the low fprompt region, the systematic uncertainty on $\tau_{^{39}Ar}$ is at most 30 years if rate for ^{210}Po alphas in ROI assumed to be 500 mHz which is 3σ away from the mean value of the measurement but for smaller leakage probabilities, the uncertainty is less than one year.

To recapitulate, there are several corrections investigated and applied to estimate the trigger rates of ^{39}Ar decay in the detector data, and various sources of systematic uncertainties are studied. Also, the software cuts are tuned over time to minimize the systematic uncertainties occurring from various sources. The dominant systematics in the study change in the energy scale corrections from the light yield response of the detector, ^{85}Kr contribution, pile-up rate of ^{39}Ar scintillation light with other ^{39}Ar triggers and with low energy Cherenkov light in the detector, and the software cut acceptances. The lifetime of ^{39}Ar measured in the $\sim$3.4 years of DEAP-3600 dataset is,

$$\tau_{^{39}Ar} \pm \sigma_{\tau_{^{39}Ar}} = (438 \pm 10(\text{stat}) \pm 8(\text{syst}))\ \text{years} \tag{9.1}$$

The result obtained from the analysis is different from the literature value of 388 $\pm$

4 years measured indirectly by Stoenner et al in the year 1965 [3].

9.1.1 Future steps for final measurement

The main outstanding work in this analysis is to include the correct ^{85}Kr activity in the fit model that will only increase the average value of the measured lifetime by a couple of years. A detailed study of the energy response of the detector is needed especially in the endpoint region of ^{85}Kr. The pile-up is mainly present in the energy region of ^{85}Kr which makes it a little hard to distinguish the different trigger types in that part of the spectrum. However, strong efficient cuts can be used to reject the pile-up in this energy window to estimate and fit the peak corresponding to the beta decays from ^{85}Kr which will return the exact quantity of isotope. The presence of ^{85}Kr in the detector cannot be ruled out from the analysis performed by other collaborators, therefore it is expected for the average value of lifetime for ^{39}Ar by some number of years but the tension with literature value will be further increased with this last step in the analysis.

In addition to this, any leakage of ^{210}Po alphas to the lower energy region in the study will decrease the lifetime measurement for ^{39}Ar which can compensate for the effect of ^{85}Kr by some percent. However, the leakage probabilities of the low-energy region are very low and there is an insignificant effect on the ^{39}Ar lifetime from this systematic.

9.2 DEAP-3600 sensitivity to detect annual modulation

The possibility of the annual modulation in the nuclear recoil rate with the solid crystals and liquid Xenon target medium is discussed by many experiments. The

existence of annual modulation in dark matter is claimed by some of the collaborations, these results are still under dialogue for various grounds. There is no literature available on the sensitivity of LAr for the detection of annual modulation in the recoil signal of dark matter. Thus, the nuclear recoil rate calculations are performed with argon as a target nucleus in this study.

The Standard Halo Model is considered for the velocity calculations and the clear distinction in the WIMP speed distribution is observed in the month of June, and December where the respective direction of the velocity of Earth is expected to be opposite, and in alignment with the WIMP wind velocity. Also, the nuclear form factor calculations are done for the ^{40}Ar nucleus, and the quenching model predictions for the WIMP-^{40}Ar scattering from the SCENE experiment as inserted in the analysis. The differential recoil rates plotted for different WIMP masses are plotted with scattering cross section at 10^{-44} cm^2, which show higher recoil energies for the heavier masses. The differential recoil rate is also estimated for a WIMP of mass 10 GeV in the month of June and December, which can be distinguished for the lower recoil energies below 14 keVnr.

The total recoil rates are estimated in the DEAP-3600 detector by considering the fiducial volume of the detector at different values of energy thresholds to measure the detector sensitivity for the annual modulation in LAr. The differential recoil rates are integrated with limits from any set energy threshold to the higher possible recoil energy. This measurement shows the minimum detector threshold needed at 5 keV to observe the modulation in the WIMP signal with the maximum modulation amplitude and highest absolute rates observed at the threshold value of 1 keV. The time-averaged rate and modulation amplitude are evaluated by fitting the calculated rates with the Fourier expansion where the modulation parameter is considered with

a periodic Cos function. DEAP-3600 will be sensitive to record modulation of 0.1 events per day with the scattering cross-section of 10^{-44} cm^2 for a WIMP mass of 10 GeV at an energy threshold of 1 keV, and a much smaller value of modulation rate at 5 keV. Therefore, the statistics hence a bigger detector with more volume of target mass of liquid argon is required to detect modulation signal at the lower threshold values. Moreover, for the higher scattering cross-section at 10^{-41} cm^2, the modulation amplitude shows the sensitivity of 140 events per day at the detector threshold of 1 keV, and this amplitude decreases with an increase in the threshold energy. For the comparison of the sensitivity of DEAP-3600 with other dark matter experiments, the preliminary calculations show that the DEAP-3600 experiment can place its world-leading sensitivity limits at WIMP mass of 10 GeV for the annual modulation signal by lowering its threshold to 3 keV, giving 2σ difference in the event rates from the month of June and December.

In the DEAP-3600 detector, the different detector systematics which could create some uncertainty in the rate measurements are already under control. The calculated systematic uncertainty is 0.09% on event rates. Therefore, for the predicted sensitivities towards the annual modulation signal, DEAP-3600 will be limited by statistics although systematics are understood to great extent, and a large detector with more volume of target mass is needed for the annual modulation study. Moreover, the DEAP experiment would need to record new data at the detector hardware threshold of 5 keV or less, and a perfect investigation of the detector backgrounds would be needed.

Appendix A

DEAP-3600 detector stability

This section contains all the information relevant to the stability of the detector over the full second-fill physics dataset, from November 2016 through March 2020. The detector stability is examined in detail as a part of event rate analysis. The trend lines for different detector stability parameters are analyzed for the sanity checks to depict any time dependence of data on the different detector components and instrumental and systematic effects. Having prepared this technical document for the collaboration helped me a lot to get a deep understanding of detector systematics. The excellent stability of the DEAP-3600 experiment during more than 3 years of data taking can be verified from the various parameters. These parameters are grouped thematically in the following way: DAQ parameters, slow control parameters, PMT parameters, LAr parameters, and high-level parameters. Each parameter is briefly explained in the following sections.

A.1 DAQ

Runtime for physics data The runtime is the cumulative real-time for all runs from the following L2 run lists that finalized for the different analyses based on the data quality studies:

- PhysicsTrigger_November2016ToDecember2017_L2
- PhysicsTrigger_OpenData2018_L2
- PhysicsTrigger_BlindData2018_L2
- PhysicsTrigger_OpenData2019_L2
- PhysicsTrigger_BlindData2019_L2
- PhysicsTrigger_OpenData2020_L2
- PhysicsTrigger_BlindData2020_L2

These run lists include 878.547 live days of data. The dead time correction of 20 μs trigger window the run time reduces to 822.884 live days of data, a typical run time curve for physics data is shown in figure A.1.

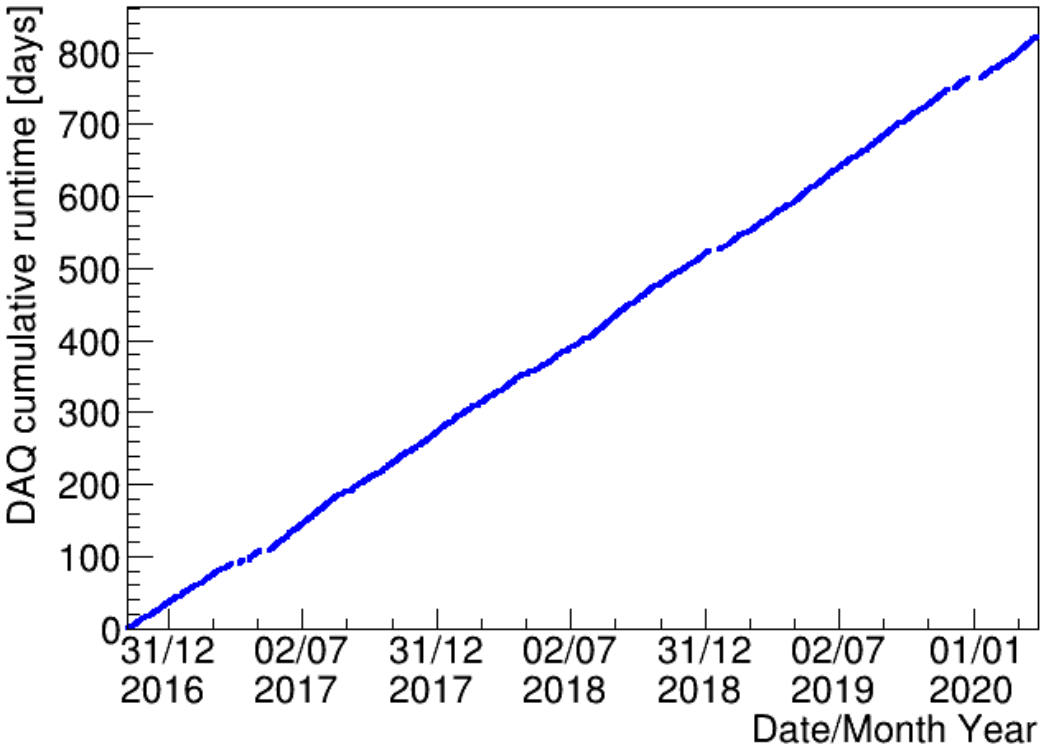

Figure A.1: The cumulative runtime from the DAQ with a deltat cut of 20 μs in the trigger time over the full physics dataset.

A.2 Slow controls

The data from the slow control sensors is recorded using the DeltaV system and stored in a PostgreSQL database that mirrors the internal DeltaV database.

AV temperature and pressure The changes in these variables could lead to changes in LAr convection or bubble formation. The AV pressure values are recorded from two different sensors at the top of the cooling coil at in and outlet positions. Figure A.2 shows the trend lines for pressure changes in the AV.

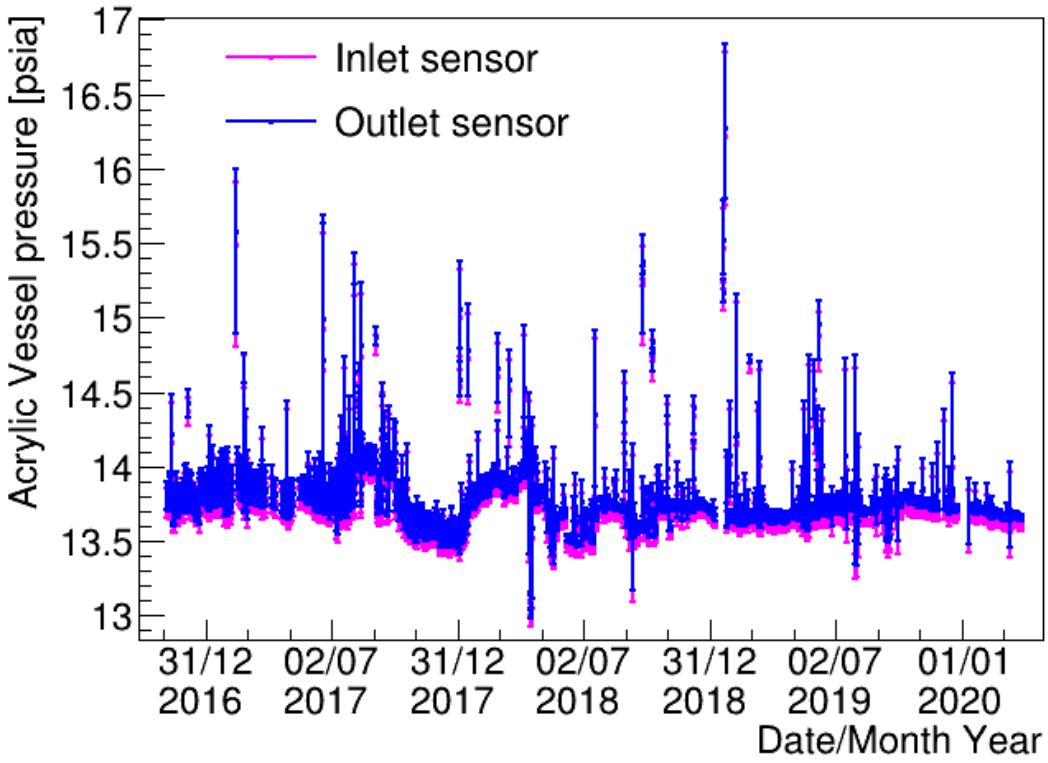

Figure A.2: AV pressures from two different temperature sensors coil with the time of the dataset.

The temperature of the Gaseous Argon (GAr) is also recorded from the temperature sensor at the same location and its trend line is given in figure A.3.

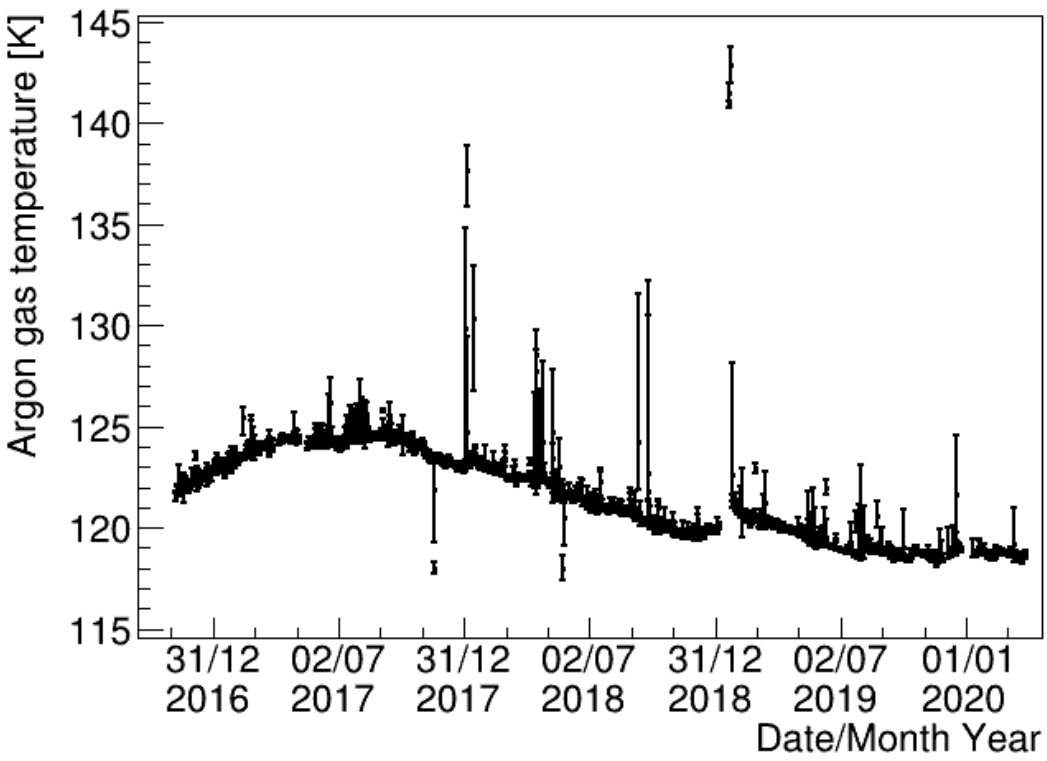

Figure A.3: Variation in Gaseous Argon temperature over time.

Water tank fill level and temperature The level and temperature of the water in the water tank are recorded in the database by using sensors located around the steel shell and are shown in figure A.4 and figure A.5 respectively. It is important to keep track of these parameters since they influence the shielding efficiency of the water tank and PMT temperatures and help to keep the LAr cold.

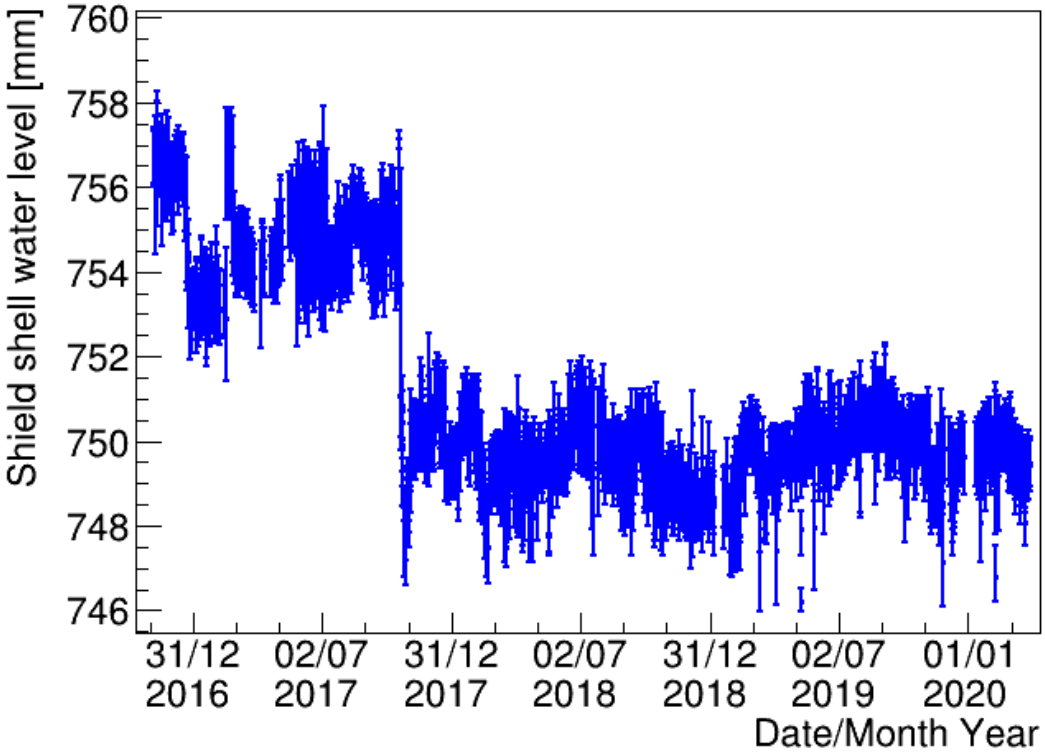

Figure A.4: Changes in steel shell water level over the data taking. The water level was changed once in the data taking time for some improvements to the detector conditions.

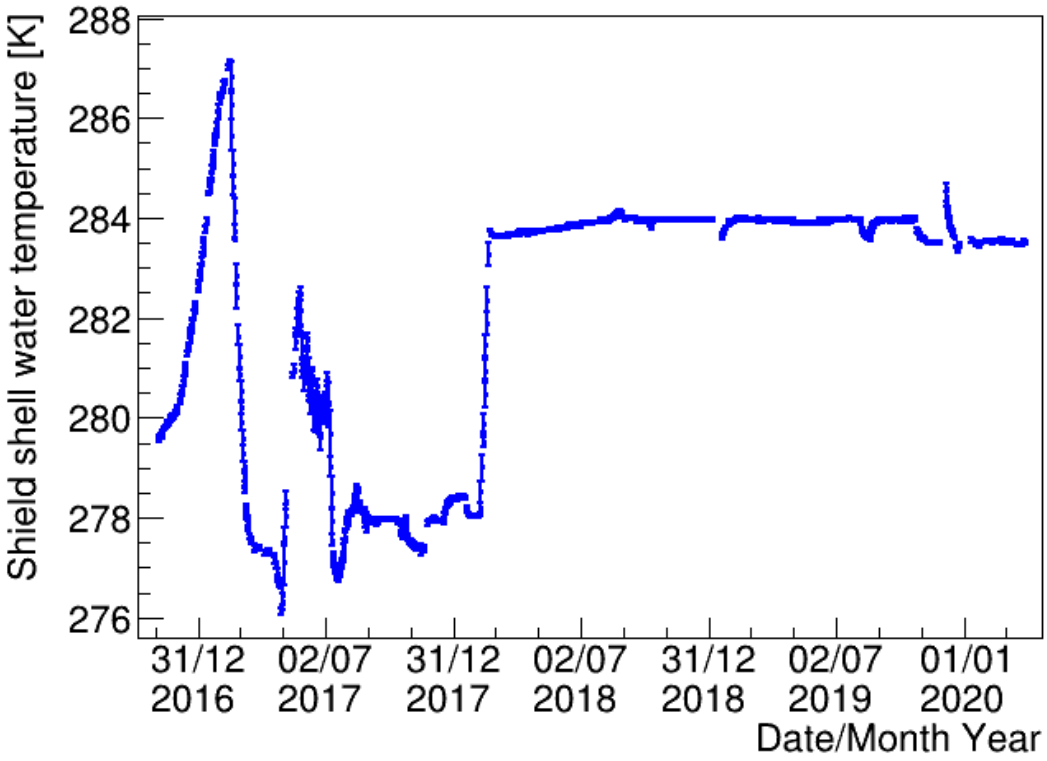

Figure A.5: Water temperature trendline over time which could have affected the performance of PMTs hence the light yield of the detector.

Cooling coil temperatures To keep track of the temperatures around the cooling coil, the output of three different sensors was recorded and is shown in figure A.6. There are two sensors on the inlet and one at the outlet of the cooling coil.

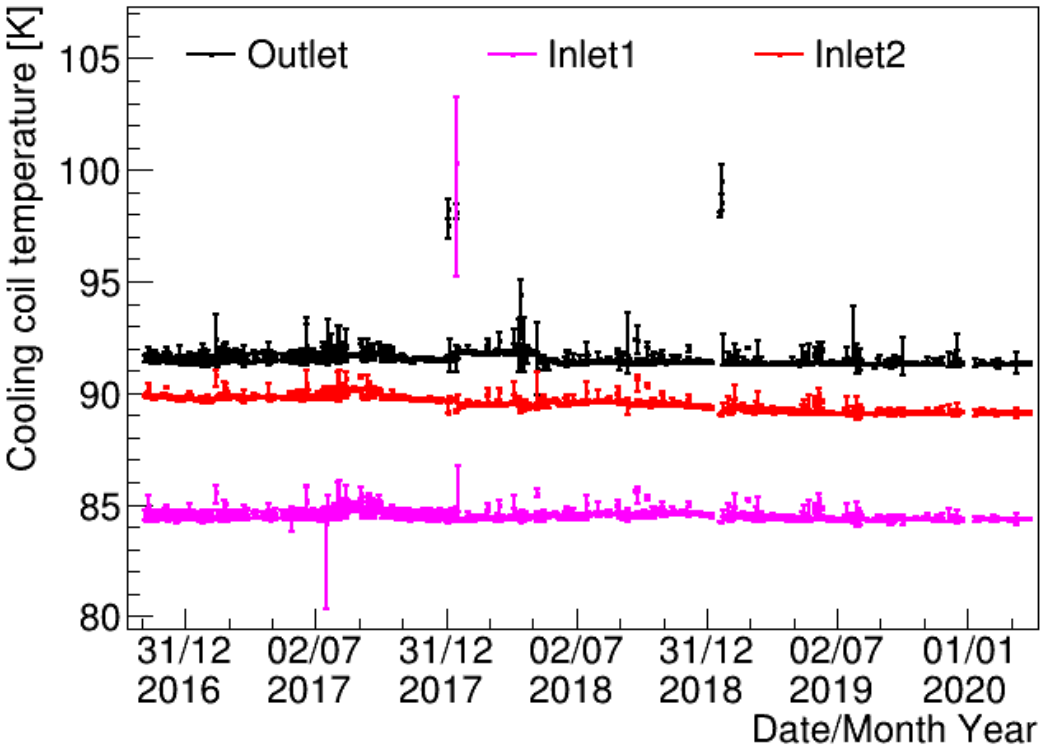

Figure A.6: Temperature of the cooling coil from three different sensors located at the inlet and outlet positions of the coil.

Steel shell The trend plot in figure A.7 shows the pressure in the outer steel shell and its variation over time.

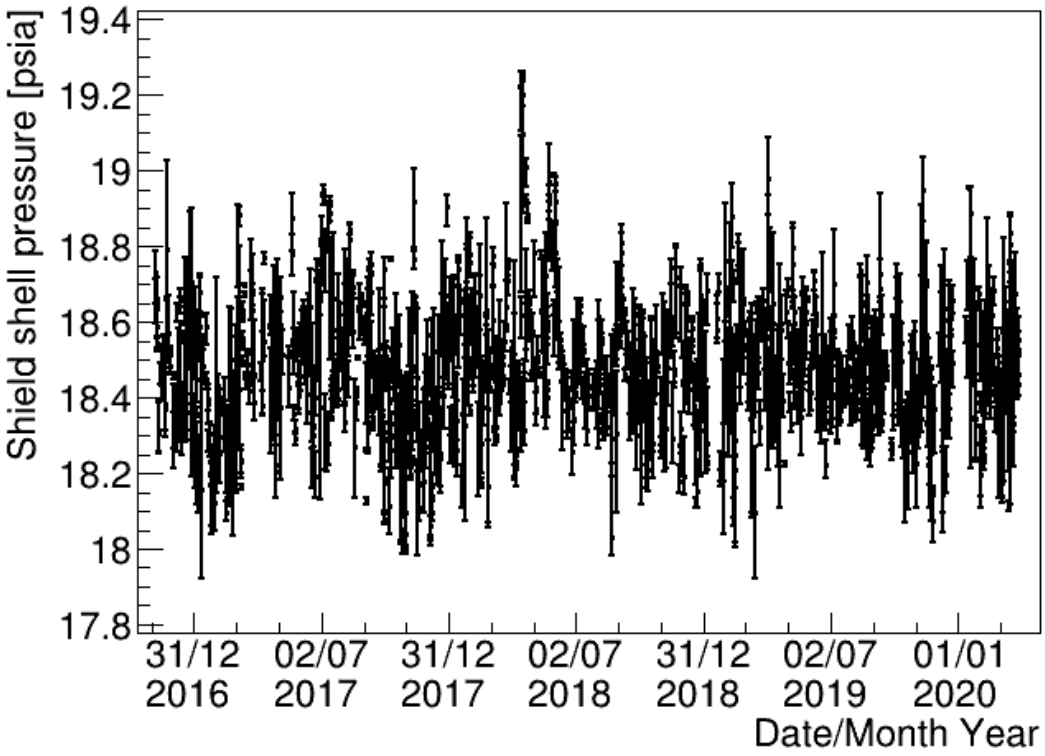

Figure A.7: The outer steel shell pressure measured over time from the sensor shows the stability of the pressure of the shell.

Compensation coil current The compensation coils around the detector cancel the Earth's magnetic field so that the PMTs operate under zero-field conditions. Changes in the currents in these coils can lead to changes in PMT gain and efficiency. The recorded values of the compensation coil currents are in figure A.8.

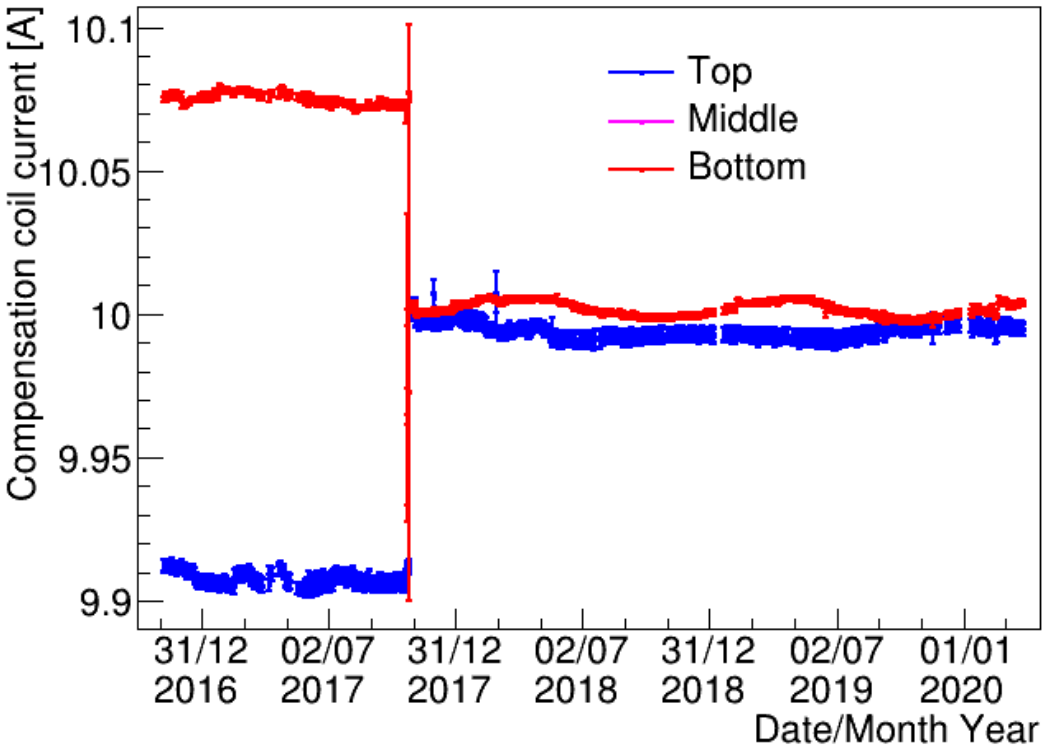

Figure A.8: The trendline for the compensation coil current at different positions of the detector with the time. There are very minor changes in the coil currents around October 2017, and currents are then matched for all the positions.

Glove box The pressure in the glove box is recorded using the sensors to keep the track of pressure at the top of the neck. The trend line for the glove box pressure is given in figure A.9.

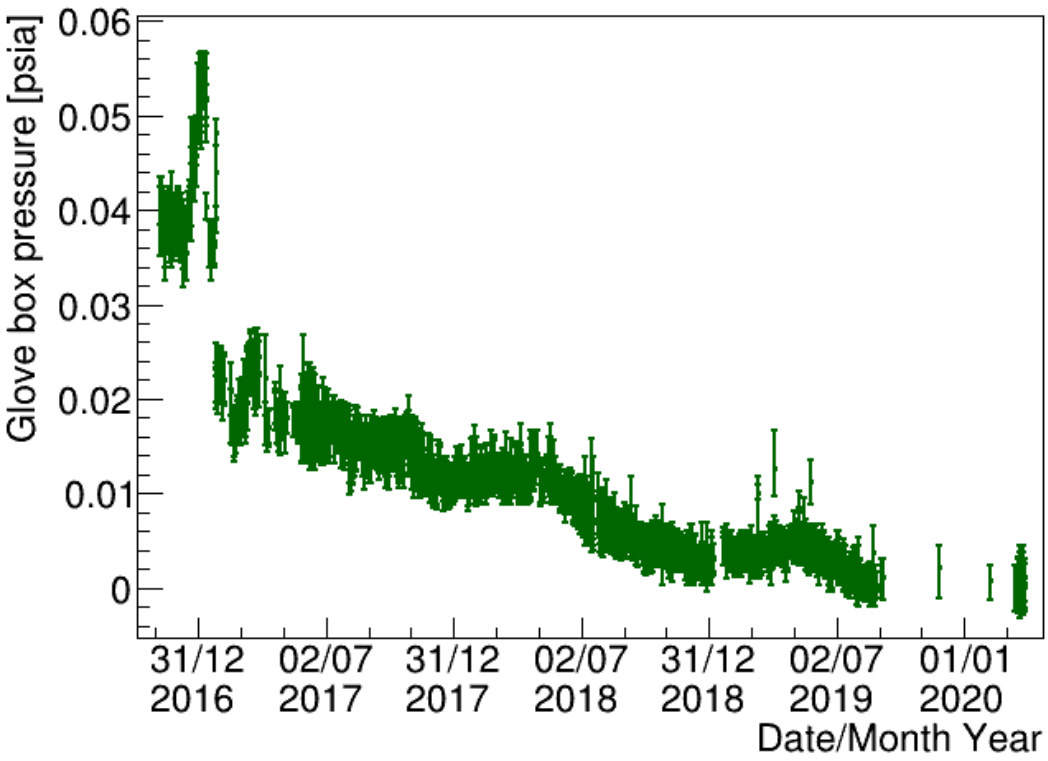

Figure A.9: The glove box pressure reading variations with the time of the data taking. The pressure a very little as indicated by the plot.

A.3 PMTs

Single-photoelectron charge distribution mean The mean SPE charges for all PMTs are stored in the database and are calibrated daily. These values are only updated in the database in response to physical detector events such as PMT ramping, or when the SPE charge mean in a time window is significantly different from the charge mean at earlier times. Figure A.10 shows the average mean SPE charge across all PMTs. The mean SPE charges have been drifting up on average for an unknown reason. This could be contributed to the fining of the edges or refinement of the impurities with time.

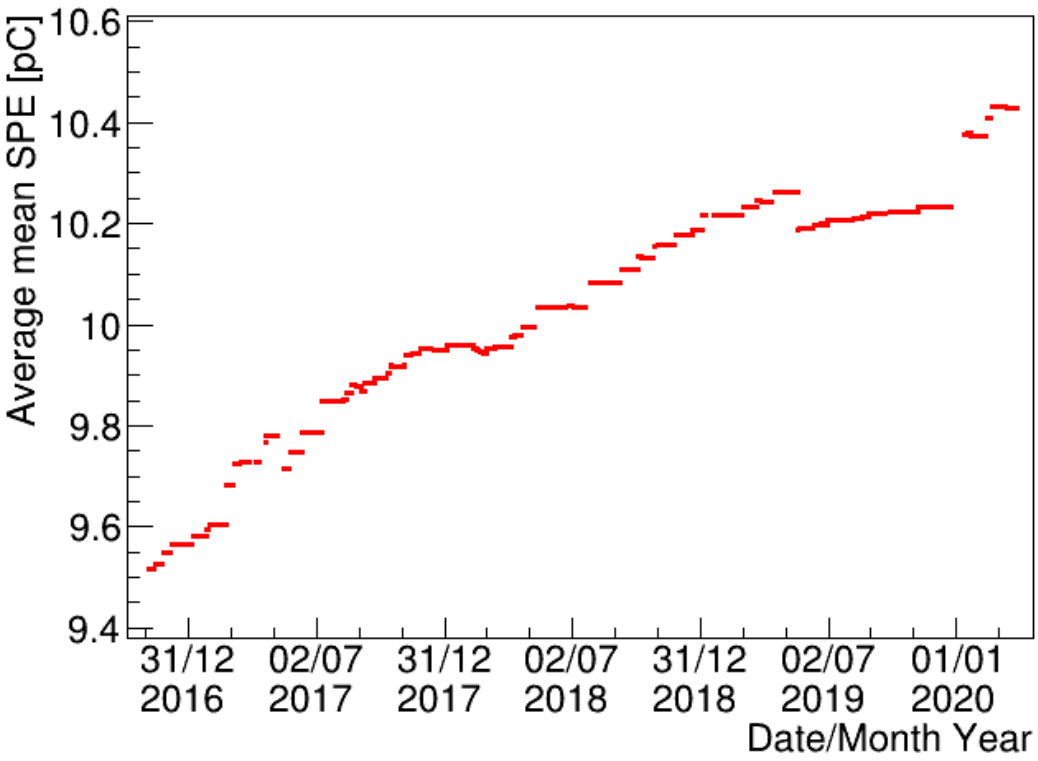

Figure A.10: The average of the mean SPE charges recorded from all the LAr PMTs over time. The slight increase in the mean charges is still unknown in the experiment.

Afterpulsing rates Afterpulsing occurs when the residual gas in the PMTs becomes ionized by the moving electrons. The late pulses don't produce any secondary electrons in the scattering of the photoelectron on the dynode. The afterpulsing rates can be calculated from two methods: i) The AARF calibration method used before the LAr fill. ii) The average ^{39}Ar pulseshape. Due to the high ^{39}Ar coincidence rate, method i) is unreliable when the detector is filled. The results shown in figure A.11 are from method ii).

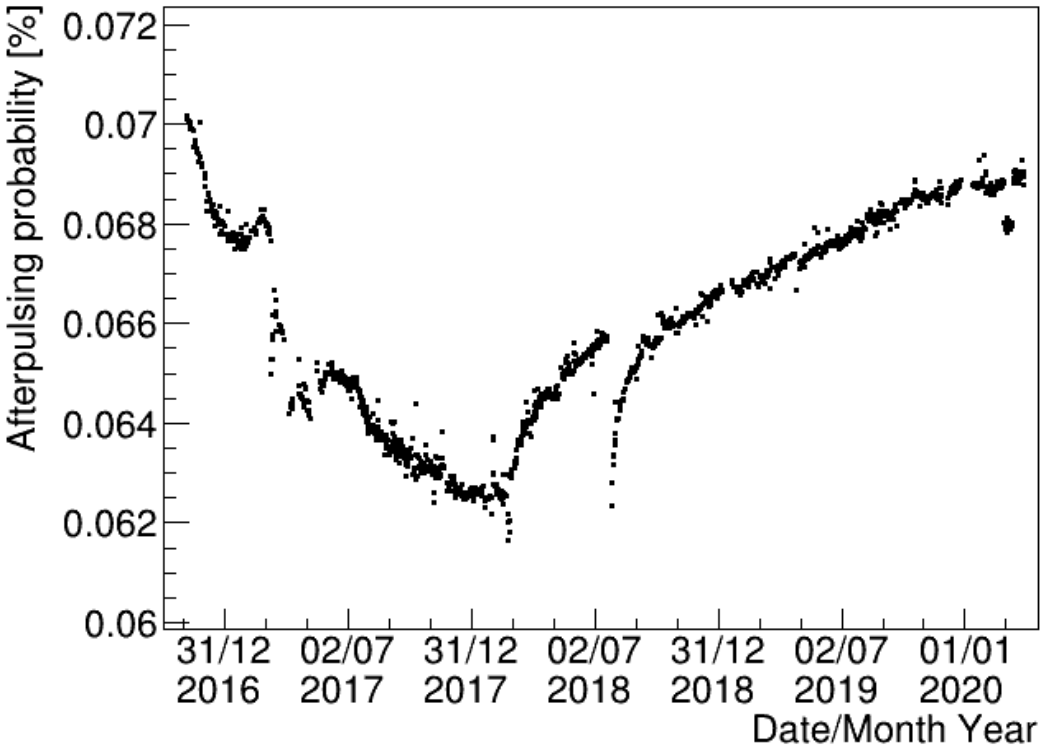

Figure A.11: The afterpulsing probability calculated from the average ^{39}Ar pulse shape fitting. The probability varied very little over time.

Stray light level The pre-event light level or stray light level is measured from the pulse rate in physics events at times before the peak of the event. It accounts for the dark noise of PMTs and the very late TPB emission from previous events, hence it is sensitive to PMT temperature and to the total event rate and spectrum in the detector. It also includes events with very small energies that can't trigger, this light component is very late TPB light of the event. The trendline in figure A.12 gives the trend line of stray light level in physics data.

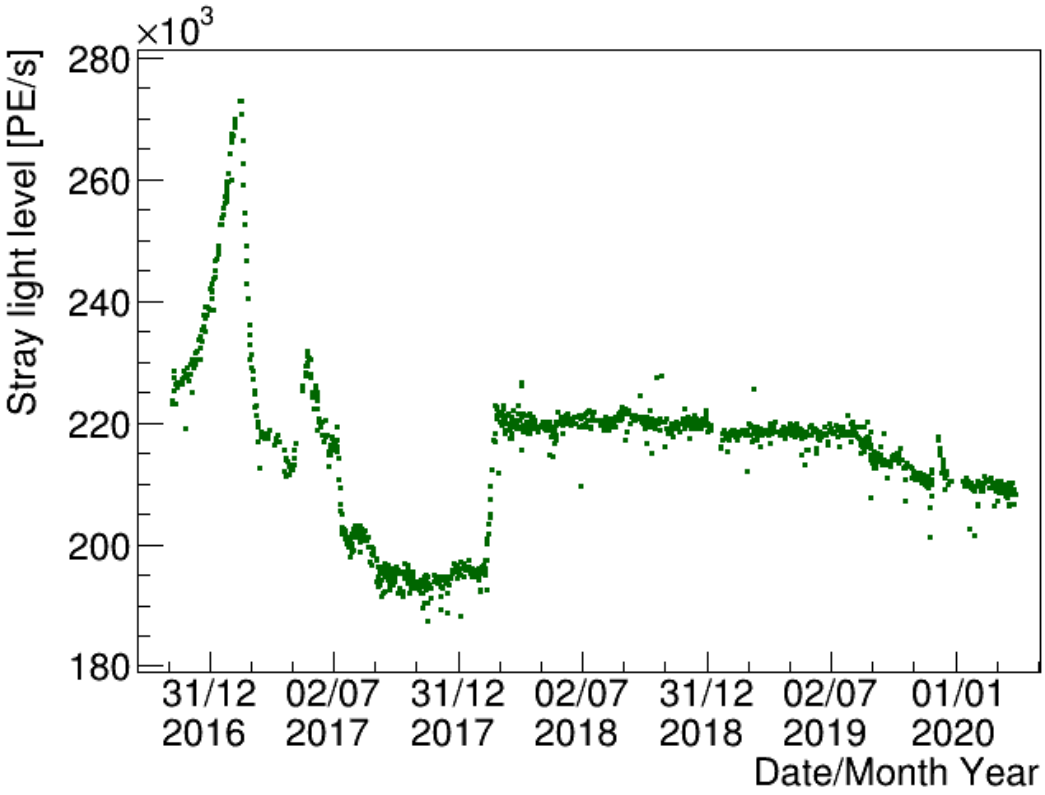

Figure A.12: The Stray light level rate and its variation over time. The trendline in the stray light rate can be directly correlated to the changes in the PMT temperatures.

Efficiency The efficiencies of all PMTs are plotted for the whole data set and these efficiencies are almost stable with time but there are a few exceptional PMTs like 125, 204, 240, 250, and 254 where efficiency is varying slightly for various run numbers. The major concern is related to PMT 204 which is LAr PMT and it is decided to not include the data collected by this PMT for the physics analysis. In figure A.13 we can see the variation in the average efficiency for all the PMTs with time.

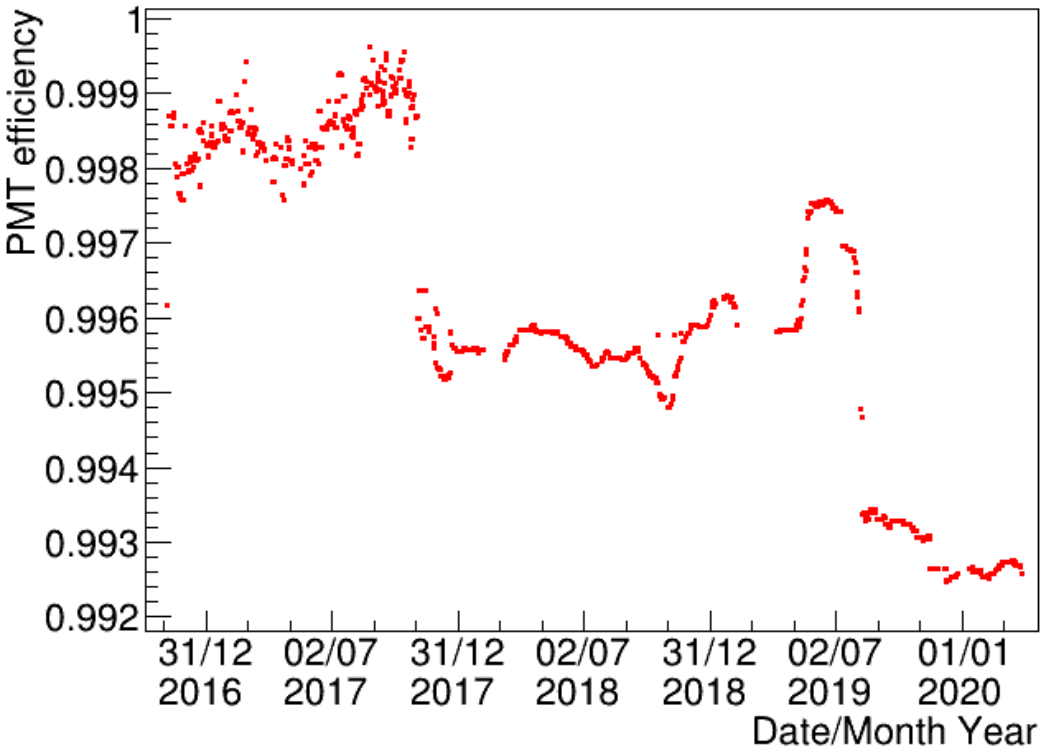

Figure A.13: The average calculated for the efficiency of all the LAr PMTs over time. The physics data from any of the PMTs acting badly in any range of the run numbers is excluded from the processing so that only good data is included in the physics analyses.

Temperature The trend lines for the temperature of three different LAr PMTs located that the top, middle, and bottom of the detector with PMT numbers 0, 130, and 253 respectively are given in figure A.14. As expected the trendline for the temperature of PMTs varies in a similar way as shield water temperature.

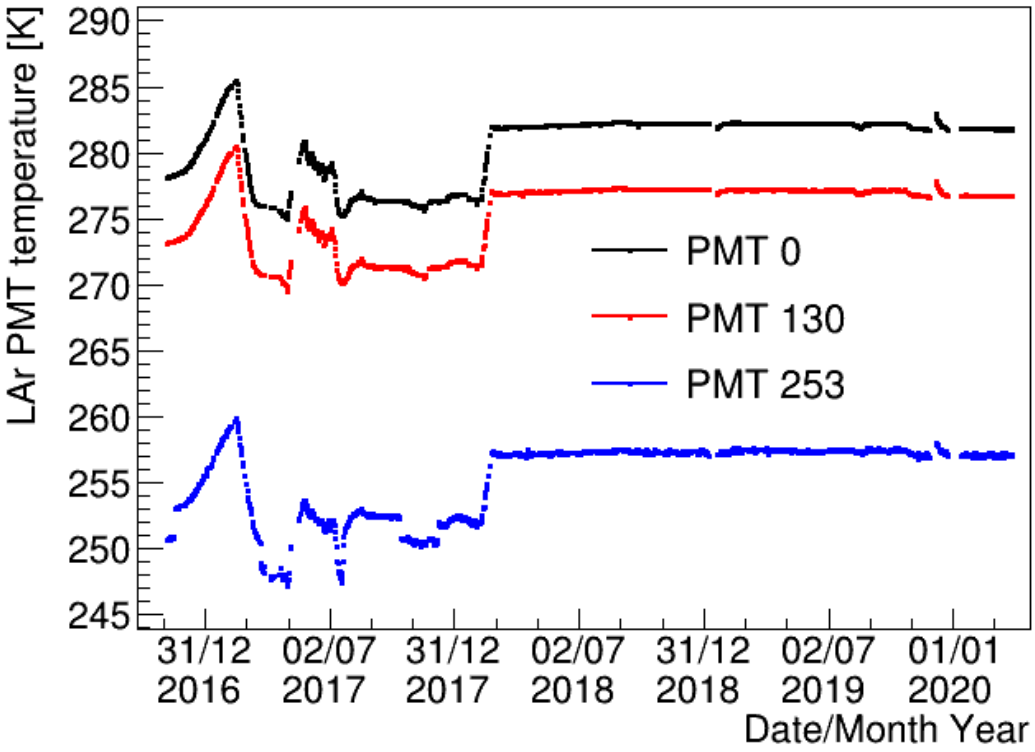

Figure A.14: The changes in the temperature of the LAr PMTs at three different locations of the detector. The fluctuations in the PMT temperatures correspond to the variations in the outer water tank temperatures.

Moreover, there are several temperature sensors present at the different locations of filler blocks and many of these sensors are close to the PMT array. These are attached to the copper short, so they do not the exact temperature of PMTs itself but it is the possible closest value. The variations in possible temperatures of different sensors over time are presented in figure A.15.

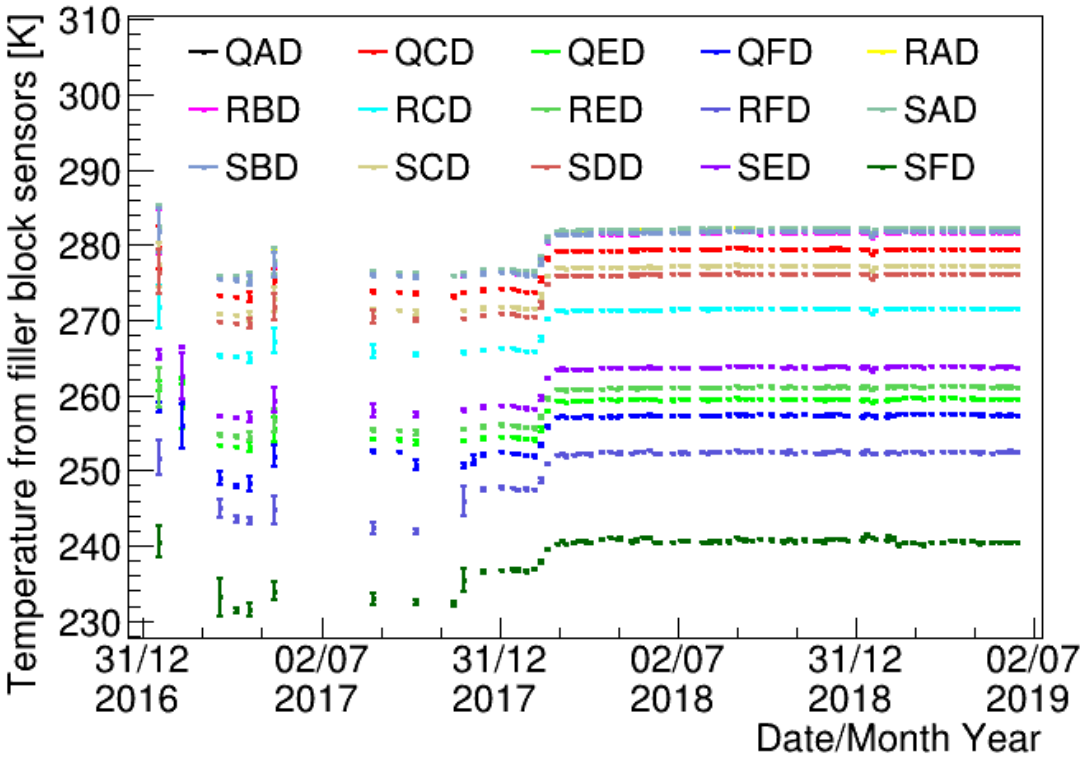

Figure A.15: The readings from the temperature sensors in the filler blocks with time provides the closest temperature value of the PMTs at various positions of the detector.

A.4 LAr

LAr fill level The fill level estimates the level of LAr in the detector. The amount of argon in the detector is the same but due to the continuous condensation of GAr to LAr and vaporization of LAr to GAr, the liquid level is expected to vary by a few millimeters. Any change in the fill level would lead to changes in the optics, coincidence rates, etc. Therefore, it is important to keep track of the LAr fill level. These values are estimated from the pulse rates of different PMTs since the PMTs which are close to the LAr level will see more light because of total internal reflection in liquid than PMT facing GAr. The trend line plot for the fill level of LAr is shown

in figure A.16 plotted from values stored in the database.

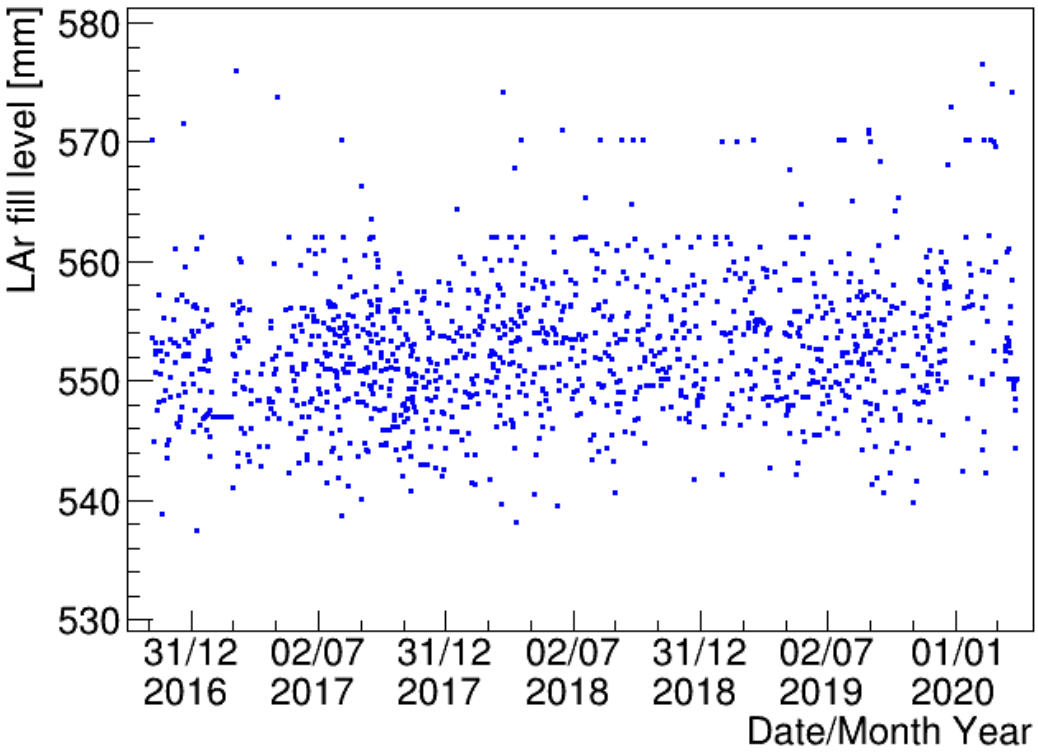

Figure A.16: The LAr fill level in the detector with time estimated from the pulse rates in the different PMTs.

Long livetime The long livetime is the lifetime τ one gets from fitting a simple model from equation (A.1) to the average ^{39}Ar pulse shape (for events that pass cuts and fall between 100 to 300 PE) in the range of 100 ns to 4000 ns. This captures three effects: The LAr triplet state lifetime, the AP rates, and the TPB delayed emission time constants.

$$I(t) = a + b \cdot exp(-t/\tau) \tag{A.1}$$

The trendline for the variation of the long lifetime parameter is given in figure A.17.

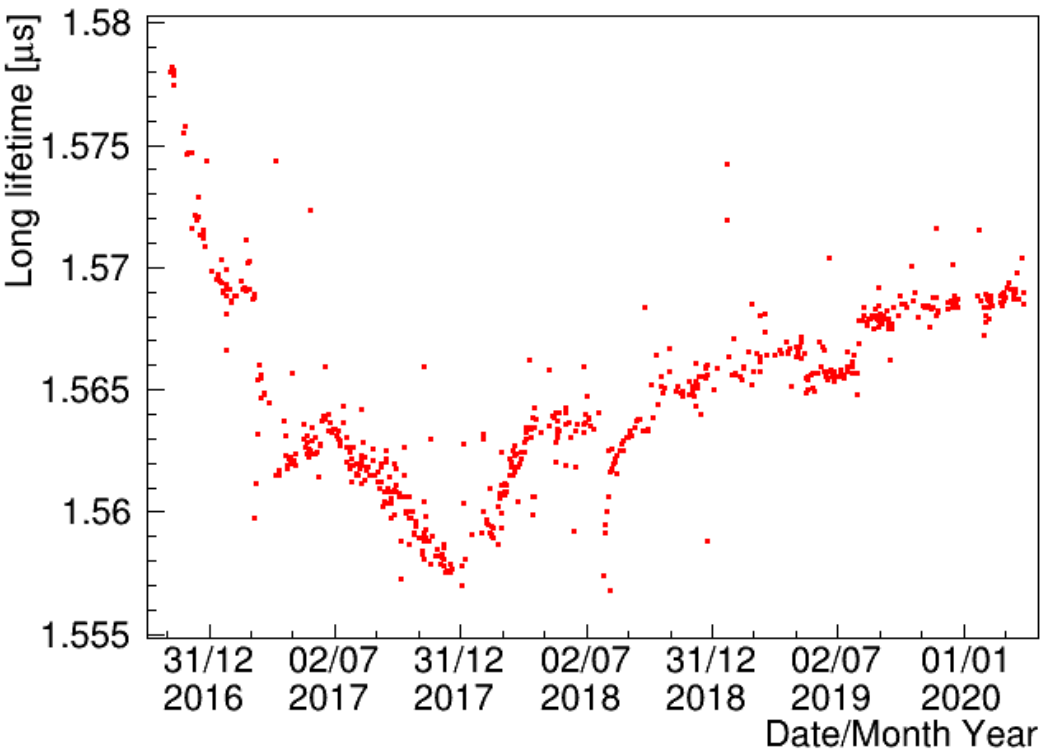

Figure A.17: Variations in a long lifetime parameter with time determined by fitting the average ^{39}Ar pulse shape for low energy region in the short time range.

Triplet lifetime The triplet lifetime is obtained from the fits to each run's data using the full pulse shape model and its trendline is given in figure A.18. This parameter is a convolution of the decay constant of the argon triplet dimer state and late TPB emission.

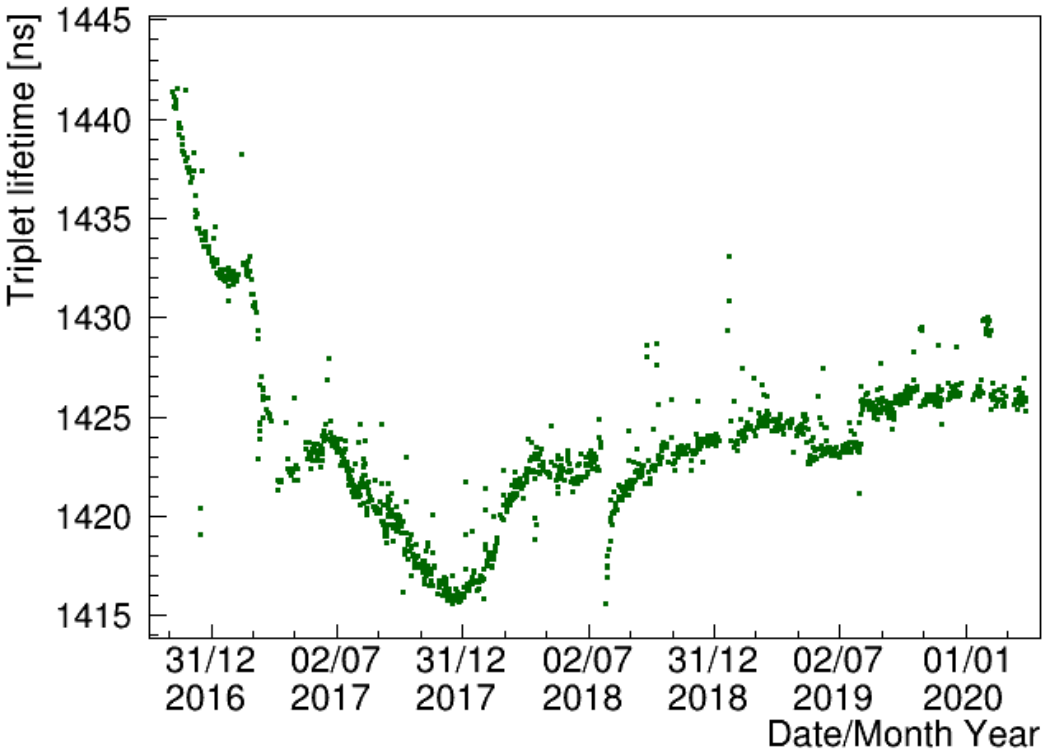

Figure A.18: The value of the long lifetime parameter plotted over time shows the stability of the detector and PSD calculations.

Light yield The trend line for LY in figure 6.9 also allows one to keep track of detector stability over time.

References

[1] **DEAP Collaboration**, R. Ajaj et al., *Electromagnetic backgrounds and potassium-42 activity in the DEAP-3600 dark matter detector*, *Physical Review D* **100** (Oct, 2019).

[2] R. Saldanha et al., *Cosmogenic production of ^{39}Ar and ^{37}Ar in argon*, *Physical Review C* **100** (Aug, 2019).

[3] R. W. Stoenner, O. A. Schaeffer, and S. Katcoff, *Half-Lives of Argon-37, Argon-39, and Argon-42*, *Science* **148** (1965), no. 3675 1325–1328.

[4] **DEAP Collaboration**, P. Adhikari et al., *Precision measurement of the specific activity of ^{39}ar in atmospheric argon with the deap-3600 detector*, 2023.

[5] S. Profumo, L. Giani, and O. F. Piattella, *An Introduction to Particle Dark Matter*. arXiv, 2019.

[6] **DEAP Collaboration**, R. Ajaj et al., *Search for dark matter with a 231-day exposure of liquid argon using deap-3600 at snolab*, *Phys. Rev. D* **100** (Jul, 2019) 022004.

[7] F. Zwicky, *On the Masses of Nebulae and of Clusters of Nebulae*, *Astrophys. J.* **86** (Oct, 1937) 217. Provided by the SAO/NASA Astrophysics Data System.

[8] F. Zwicky, *Nebulae as gravitational lenses*, *Phys. Rev.* **51** (Feb, 1937) 290–290.

[9] F. Zwicky, *On the large scale distribution of matter in the universe*, *Phys. Rev.* **61** (Apr, 1942) 489–503.

[10] V. C. Rubin and W. K. Ford; Jr., *Rotation of the Andromeda Nebula from a Spectroscopic Survey of Emission Regions*, *Astrophys. J.* **159** (Feb, 1970) 379. Provided by the SAO/NASA Astrophysics Data System.

[11] V. C. Rubin, W. K. Ford; Jr., and N. Thonnard, *Extended rotation curves of high-luminosity spiral galaxies. IV. Systematic dynamical properties, Sa through Sc.*, *Astrophys. J.* **225** (Nov, 1978) L107–L111. Provided by the SAO/NASA Astrophysics Data System.

[12] V. C. Rubin, W. K. Ford; Jr., and N. Thonnard, *Rotational properties of 21 SC galaxies with a large range of luminosities and radii, from NGC 4605 (R=4kpc) to UGC 2885 (R=122kpc).*, *Astrophys. J.* **238** (Jun, 1980) 471–487. Provided by the SAO/NASA Astrophysics Data System.

[13] V. C. Rubin, W. K. Ford; Jr., N. Thonnard, and D. Burstein, *Rotation velocities of 16 SA galaxies and a comparison of Sa, SB, and SC rotation properties.*, *Astrophys. J.* **289** (Feb, 1985) 81–104. Provided by the SAO/NASA Astrophysics Data System.

[14] T. S. van Albada, J. N. Bahcall, K. Begeman, and R. Sancisi, *Distribution of dark matter in the spiral galaxy NGC 3198.*, *Astrophys. J.* **295** (Aug, 1985) 305–313. Provided by the SAO/NASA Astrophysics Data System.

[15] R. Garner, *NASA's Webb Delivers Deepest Infrared Image of Universe Yet*, Jul, 2022.

[16] Y. Friedman and J. M. Steiner, *Gravitational deflection in relativistic newtonian dynamics*, *EPL (Europhysics Letters)* **117** (Mar, 2017) 59001.

[17] M. Markevitch et al., *Direct constraints on the dark matter self-interaction cross section from the merging galaxy cluster 1e0657-56*, *The Astrophysical Journal* **606** (May, 2004) 819–824.

[18] D. Clowe et al., *A direct empirical proof of the existence of dark matter*, *The Astrophysical Journal* **648** (Aug, 2006) L109–L113.

[19] R. Massey, T. Kitching, and J. Richard, *The dark matter of gravitational lensing*, *Reports on Progress in Physics* **73** (Jul, 2010) 086901.

[20] **Planck Collaboration**, R. Adam et al., *Planck 2015 results - I. Overview of products and scientific results*, *Astronomy & Astrophysics* **594** (Sep, 2016) A1.

[21] G. Bertone, D. Hooper, and J. Silk, *Particle dark matter: evidence, candidates and constraints*, *Physics Reports* **405** (2005), no. 5 279–390.

[22] J. L. Feng, *Dark matter candidates from particle physics and methods of detection*, *Annual Review of Astronomy and Astrophysics* **48** (2010), no. 1 495–545.

[23] G. Jungman, M. Kamionkowski, and K. Griest, *Supersymmetric dark matter*, *Physics Reports* **267** (Mar, 1996) 195–373.

[24] **DEAP Collaboration**, P. Adhikari et al., *First direct detection constraints on planck-scale mass dark matter with multiple-scatter signatures using the DEAP-3600 detector*, *Physical Review Letters* **128** (Jan, 2022).

[25] C. Alcock et al., *The MACHO project: Microlensing results from 5.7 years of large magellanic cloud observations*, *The Astrophysical Journal* **542** (Oct, 2000) 281–307.

[26] D. S. Graff and K. Freese, *The mass function of low-mass halo stars: Limits on baryonic halo dark matter*, *The Astrophysical Journal* **467** (Aug, 1996) L65–L68.

[27] E. A. Baltz, *Dark matter candidates*, 2004.

[28] F. Chadha-Day, J. Ellis, and D. J. E. Marsh, *Axion dark matter: What is it and why now?*, 2021.

[29] L. Bergström, *Dark matter candidates*, *New Journal of Physics* **11** (Oct, 2009) 105006.

[30] **Super-Kamiokande Collaboration**, Y. Fukuda et al., *Evidence for oscillation of atmospheric neutrinos*, *Physical Review Letters* **81** (Aug, 1998) 1562–1567.

[31] **SNO Collaboration**, Q. R. Ahmed et al., *Direct evidence for neutrino flavor transformation from neutral-current interactions in the sudbury neutrino observatory*, *Physical Review Letters* **89** (Jun, 2002).

[32] B. W. Lee and S. Weinberg, *Cosmological lower bound on heavy-neutrino masses*, *Phys. Rev. Lett.* **39** (Jul, 1977) 165–168.

[33] B. Billard et al., *Direct detection of dark matter—APPEC committee report*, *Reports on Progress in Physics* **85** (Apr, 2022) 056201.

[34] L. Barak et al., *SENSEI: Direct-detection results on sub-GeV dark matter from a new skipper CCD*, *Physical Review Letters* **125** (Oct, 2020).

[35] **LIGO Scientific Collaboration, Virgo Collaboration**, B. Abbott et al., *Observation of gravitational waves from a binary black hole merger*, *Physical Review Letters* **116** (Feb, 2016).

[36] S. Giagu, *WIMP Dark Matter Searches With the ATLAS Detector at the LHC*, *Frontiers in Physics* **7** (2019).

[37] F. Donato, *Indirect searches for dark matter*, *Physics of the Dark Universe* **4** (2014) 41–43. DARK TAUP 2013.

[38] D. G. Cerdeño and A. M. Green, *Direct detection of WIMPs*, in *Particle Dark Matter*, pp. 347–369. Cambridge University Press, Jan, 2010.

[39] S. Magni, *Astrophysical aspects of dark matter direct detection.* Theses, Université Montpellier, Nov, 2015.

[40] J. Lewin and P. Smith, *Review of mathematics, numerical factors, and corrections for dark matter experiments based on elastic nuclear recoil*, *Astroparticle Physics* **6** (1996), no. 1 87–112.

[41] P. Agnes et al., *Measurement of the liquid argon energy response to nuclear and electronic recoils*, *Physical Review D* **97** (Jun, 2018).

[42] **COSINE collaboration**, *Annual modulation image*, 2022.

[43] K. Freese, M. Lisanti, and C. Savage, *Annual modulation of dark matter: A review*, *Reviews of Modern Physics* **85** (Nov, 2013) 1561–1581.

[44] C. McCabe, *Astrophysical uncertainties of dark matter direct detection experiments*, *Physical Review D* **82** (Jul, 2010).

[45] M. Boulay and A. Hime, *Technique for direct detection of weakly interacting massive particles using scintillation time discrimination in liquid argon*, *Astroparticle Physics* **25** (2006), no. 3 179–182.

[46] S. Kubota et al., *Evidence of the existence of exciton states in liquid argon and exciton-enhanced ionization from xenon doping*, *Phys. Rev. B* **13** (Feb, 1976) 1649–1653.

[47] T. Heindl et al., *The scintillation of liquid argon*, *EPL (Europhysics Letters)* **91** (Sep, 2010) 62002.

[48] M. Roush, M. Wilson, and W. Hornyak, *Pulse shape discrimination*, *Nuclear Instruments and Methods* **31** (1964), no. 1 112–124.

[49] P. Benetti et al., *Measurement of the specific activity of ^{39}Ar in natural argon*, *Nuclear Instruments and Methods in Physics Research Section A: Accelerators, Spectrometers, Detectors and Associated Equipment* **574** (Apr, 2007) 83–88.

[50] J. Calvo et al., *Backgrounds and pulse shape discrimination in the ArDM liquid argon TPC*, *Journal of Cosmology and Astroparticle Physics* **2018** (Dec, 2018) 011–011.

[51] A. R. Brosi, H. Zeldes, and B. H. Ketelle, *$^{39}Argon$ beta-spectrum*, *Phys. Rev.* **79** (Sep, 1950) 902–902.

[52] M. L. Pool, J. M. Cork, and R. L. Thornton, *A Survey of Radioactivity Produced by High Energy Neutron Bombardment*, *Phys. Rev.* **52** (Aug, 1937) 239–240.

[53] G. T. Seaborg and I. Perlman, *Table of isotopes*, *Rev. Mod. Phys.* **20** (Oct, 1948) 585–667.

[54] H. Zeldes, B. H. Ketelle, A. R. Brosi, C. R. Fultz, and R. F. Hibbs, *Half-Life and Mass Assignment of Argon 39*, *Phys. Rev.* **86** (Jun, 1952) 811–811.

[55] R. W. Stoenner, O. A. Schaeffer, and R. D. Jr, *Meteorites as space probes for testing the spatial constancy of cosmic radiation*, *Journal of Geophysical Research (1896-1977)* **65** (1960), no. 10 3025–3034.

[56] C. E. Melton, W. . Massey, and B. . N. Abels, *The Isotopic Abundance of Neon, Argon and Krypton*, *Zeitschrift für Naturforschung A* **26** (1971), no. 7 1241–1242.

[57] A. K. Baksi, D. A. Archibald, and E. Farrar, *Use of a double-spike to determine the half-life of 39Ar and the operating characteristics of a mass spectrometer used in geochronological studies*, *Canadian Journal of Physics* **74** (1996), no. 5-6 263–266.

[58] J. Chen, *Nuclear Data Sheets for A=39*, *Nuclear Data Sheets* **149** (Mar, 2018).

[59] S. Heinitz, I. Kajan, and D. Schumann, *How accurate are half-life data of long-lived radionuclides?*, *Radiochimica Acta* **110** (2022), no. 6-9 589–608.

[60] **DEAP Collaboration**, P.-A. Amaudruz et al., *Design and construction of the DEAP-3600 dark matter detector*, *Astroparticle Physics* **108** (Mar, 2019) 1–23.

[61] *SNOLAB User's Handbook, rev. 2.* published online, 2006.

[62] **SNO Collaboration**, B. Aharmim et al., *Combined analysis of all three phases of solar neutrino data from the Sudbury Neutrino Observatory*, *Phys. Rev. C* **88** (Aug, 2013) 025501.

[63] *The nobel prize in physics 2015*, Oct, 2015.

[64] C. Jillings, *The SNOLAB Science Program*, *Journal of Physics: Conference Series* **718** (May, 2016) 062028.

[65] J. Hall, *The SNOLAB underground laboratory*, *Journal of Physics: Conference Series* **1468** (Feb, 2020) 012252.

[66] K. Clark, C. Jillings, C. Kraus, J. Saffin, and S. Scorza, eds., *Photomultiplier Tube R5912 Datasheet.* 1998.

[67] M. Bodmer et al., *Measurement of optical attenuation in acrylic light guides for a dark matter detector*, *Journal of Instrumentation* **9** (Feb, 2014) P02002–P02002.

[68] B. Littlejohn, K. M. Heeger, T. Wise, E. Gettrust, and M. Lyman, *UV degradation of the optical properties of acrylic for neutrino and dark matter experiments*, *Journal of Instrumentation* **4** (Sep, 2009) T09001–T09001.

[69] *Photomultiplier Tubes: Basics and Applications.* third edition, 2007 ed., July, 2017.

[70] I. M. Frank and I. E. Tamm, *Coherent visible radiation of fast electrons passing through matter*, *Compt. Rend. Acad. Sci. URSS* **14** (1937), no. 3 109–114.

[71] S. J. Haselschwardt and J. Kostensalo and X. Mougeot, and J. Suhonen, *Improved calculations of decay backgrounds to new physics in liquid xenon detectors*, *Phys. Rev. C* **102** (Dec, 2020) 065501.

[72] **DEAP Collaboration**, P.-A. Amaudruz et al., *First results from the DEAP-3600 dark matter search with argon at SNOLAB*, *Physical Review Letters* **121** (Aug, 2018).

[73] *Thoron decay chain by internachi*, Sep, 2022.

[74] *Uranium-238 decay chain by internachi*, Sep, 2022.

[75] S. Agostinelli et al., *Geant4—a simulation toolkit*, *Nuclear Instruments and Methods in Physics Research Section A: Accelerators, Spectrometers, Detectors and Associated Equipment* **506** (2003), no. 3 250–303.

[76] T. Boltan et al., *RAT (is an Analysis Tool) User's Guide.* arXiv, 2018.

[77] R. Brun and F. Rademakers, *Root — an object oriented data analysis framework*, *Nuclear Instruments and Methods in Physics Research Section A: Accelerators, Spectrometers, Detectors and Associated Equipment* **389** (1997), no. 1 81–86. New Computing Techniques in Physics Research V.

[78] J. Kostensalo, J. Suhonen, and K. Zuber, *Spectral shapes of forbidden argondecays as background component for rare-event searches*, *Journal of Physics G: Nuclear and Particle Physics* **45** (Dec, 2017) 025202.

[79] J. R. Klein and A. Roodman, *Blind analysis in nuclear and particle physics*, *Annual Review of Nuclear and Particle Science* **55** (2005), no. 1 141–163.

[80] P. Belli et al., *Extending the DAMA annual-modulation region by inclusion of the uncertainties in astrophysical velocities*, *Physical Review D* **61** (Dec, 1999).

[81] R. W. Schnee, *Introduction to dark matter experiments*, in *Theoretical Advanced Study Institute in Elementary Particle Physics: Physics of the Large and the Small*, pp. 775–829, WORLD SCIENTIFIC, Mar, 2011.

[82] **SCENE Collaboration**, H. Cao et al., *Measurement of scintillation and ionization yield and scintillation pulse shape from nuclear recoils in liquid argon*, *Phys. Rev. D* **91** (May, 2015) 092007.

[83] F. Froborg and A. R. Duffy, *Annual modulation in direct dark matter searches*, *Journal of Physics G: Nuclear and Particle Physics* **47** (Jul, 2020) 094002.

[84] **XENON1T Collaboration**, E. Aprile et al., *Search for light dark matter interactions enhanced by the migdal effect or bremsstrahlung in XENON1t*, *Physical Review Letters* **123** (Dec, 2019).

[85] R. Bernabei et al., *The dark matter: DAMA/LIBRA and its perspectives*, 2021.

[86] G. Adhikari et al., *Strong constraints from COSINE-100 on the DAMA dark matter results using the same sodium iodide target*, *Science Advances* **7** (nov, 2021).

[87] **XMASS Collaboration**, K. Abe et al., *Direct dark matter search by annual modulation with 2.7 years of XMASS-I data*, *Physical Review D* **97** (May, 2018).